Fraunhofer ITWM

Fraunhofer Institute for Industrial Mathematics ITWM

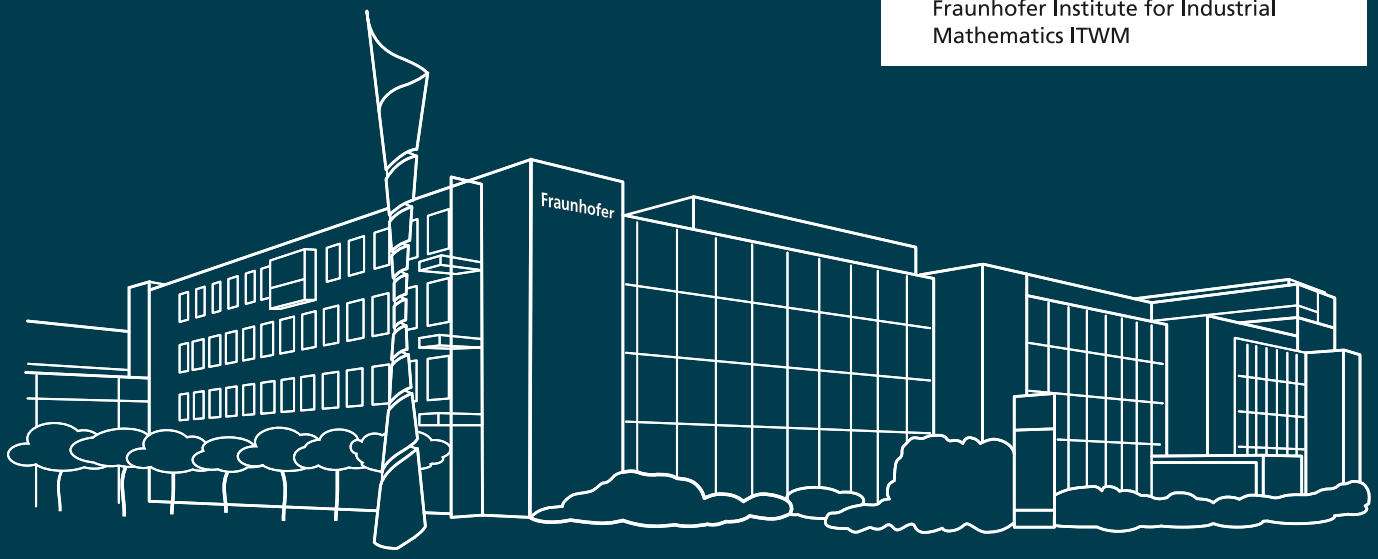

HFSS 2025 – September 22nd to 26th, 2025
Fraunhofer ITWM Kaiserslautern

2nd International Conference on Highly Flexible Slender Structures

ECCOMAS Thematic Conference and IACM Special Interest Conference, supported by ECMI

ECCOMAS Thematic Conference

IACM SPECIAL INTEREST CONFERENCE

ECMI EUROPEAN CONSORTIUM FOR MATHEMATICS IN INDUSTRY

Table of Contents

Mini Symposia

MS-1 CONSTITUTIVE MODELLING FOR FLEXIBLE SLENDER STRUCTURES

MS-2 CONTACT AND FRICTION IN MECHANICS OF FLEXIBLE SLENDER STRUCTURES

MS-6 NONLINEAR DYNAMICS OF SLENDER STRUCTURES

MS-7 MULTIPHYSICS COUPLED PROBLEMS IN SLENDER STRUCTURES

MS-8 TEXTILES AND OTHER MACROSCOPIC STRUCTURES, BUILT OF FLEXURAL 1D OBJECTS

MS-9 ADVANCED MODELS AND NUMERICAL FORMULATIONS FOR THE INTERACTION OF BEAMS AND THE COUPLING OF BEAMS WITH SOLIDS

MS-10 INDUSTRIAL APPLICATION OF SIMULATION METHODS FOR FLEXIBLE SLENDER STRUCTURES AND THEIR CHALLENGES

Welcome to HFSS 2025

September 2025

Dear Participants,

On behalf of the organizers and the scientific committee I want to welcome you cordially to the 2nd edition of the International Conference on Highly Flexible Slender Structures at Fraunhofer ITWM in Kaiserslautern.

Some of you will certainly remember our first conference that has taken place two years ago in Rijeka. While the original motivation for that conference had been to set up a final event for the European doctoral network THREAD, the organizers already then hoped to attract a wider audience of researchers beyond the THREAD network. With about 80 participants and 7 of 8 keynotes contributed by speakers outside the THREAD community, these hopes were fortunately fulfilled beyond the organizers' expectations.

For HFSS 2025 we widened the topical scope of the conference, and we also shifted its focus a bit, as reflected in some novel subjects addressed in several of the thematic mini-symposia and in particular the invited lectures. Hosting the conference at ITWM as one of the founding institutions of the European Consortium of Mathematics in Industry (ECMI), having "more mathematics" was one aspect to shape the conference agenda. On the other hand, as a Fraunhofer institute the actual impact (vs. a merely potential applicability) of novel developments in modelling and numerical simulation on real applications in industry is of utmost importance and a main aspect of our mission. This will be showcased in a dedicated mini-symposium. We wanted to direct more attention towards data based methods using AI techniques for computational mechanics applications. Nevertheless, classical aspects of the nonlinear mechanics of flexible slender structures still provide the scientific core of the subject and the majority of contributions to the conference.

We observed in recent years that physics based mathematical models for flexible slender structures and related numerical algorithms to simulate their quasistatic and fully dynamic behaviour are subjects of interest in several communities, which up to date seem to have little connection and scientific exchange. Having visited two larger conferences earlier this year – ESMC in Lyon, and the Eccomas Thematic Conference on Multibody Dynamics in Innsbruck – with dedicated mini-symposia on the Mechanics and Physics of Structures and on Flexible Multibody Dynamics respectively, one finds that despite the large number of contributions, both had hardly any overlap among the participants. This reinforces our intention to provide an opportunity for scientists of these communities to meet in a workshop-like atmosphere with a single-track program to meet and discuss their latest results in the current and future editions of HFSS. Two years ago in Rijeka we already took first steps in this direction, and I think we managed to do an even larger one in the present conference.

With this in mind, I wish us all an interesting conference, with many exciting discussions, inspiration for our own research activities, and possibly the spark that ignites fruitful cooperation across borders in the future.

Joachim Linn
Fraunhofer ITWM

Committee

Scientific Committee

- **Martin Arnold**
  Martin Luther University Halle-Wittenberg
- **Olivier Brüls**
  University of Liège
- **Elena Celledoni**
  National Technical University of Norway Trondheim
- **José Escalona**
  University of Seville
- **Johannes Gerstmayr**
  University of Innsbruck
- **Gordan Jelenić**
  University of Rijeka
- **Sigrid Leyendecker**
  Friedrich Alexander University Erlangen-Nürnberg
- **Joachim Linn**
  Fraunhofer ITWM Kaiserslautern
- **Vanessa Dörlich**
  Fraunhofer ITWM Kaiserslautern
- **Sina Ober-Blöbaum**
  University of Paderborn
- **Edita Papa Dukić**
  University of Rijeka
- **Sébastien Neukirch**
  Sorbonne University
- **Aki Mikkola**
  Lappeenranta University of Technology
- **Christoph Meier**
  Technical University Munich
- **Yury Vetyukov**
  Technical University Vienna

Local Organising Committee at Fraunhofer ITWM

- **Joachim Linn**
- **Vanessa Dörlich**
- **Quirin Hoesch**
- **Christine Rauch**
- **Caroline Wasser**
- **Olena Buchbinder**
- **Esther Packullat**
- **Gesa Ermel**
- **Antonia Rinck**
- **Steffen Grützner**

Information for Participants

Binding Rules During Your Visit

- Participants must be registered for the conference when they come to the Fraunhofer institute.
- During the visit, the conference badge must be worn in a clearly visible manner.
- Follow the instructions of the Fraunhofer ITWM staff.
- Please note that the main entrance of ITWM closes at 6 pm on each day. You will not be able to enter the building on your own afterwards. Please inform any ITWM colleague, if you need to leave the building and plan to come back after 6 pm.

ECCOMAS Thematic Conference and IACM Special Interest Conference
Highly Flexible Slender Structures (HFSS 2025)
22–26 September 2025, Kaiserslautern, Germany

Hamiltonian Generative Adversarial Network

Christine Allen-Blanchette

Princeton University, {yy0555, ca15}@princeton.edu

Keywords: Hamiltonian Neural Networks; Generative Adversarial Networks; Physics-Guided Learning

1. Introduction

Learning generative models of video that are both physically plausible and interpretable remains a core challenge in machine learning. High-dimensional videos often arise from low-dimensional dynamical systems, yet most generative approaches focus primarily on perceptual realism without guaranteeing physical consistency. This lack of structure limits their usefulness in downstream tasks such as prediction, control, and scientific modeling. The Hamiltonian formalism offers a principled inductive bias for dynamical systems: it ensures conservation of energy, constrains trajectories to evolve on a phase-space manifold, and provides interpretable coordinates for describing system dynamics. Embedding this structure into machine learning models can therefore improve both the realism of generated trajectories and the interpretability of learned latent spaces.

Recent works have integrated Hamiltonian neural networks (HNNs) [1] into variational autoencoder (VAE) [2] pipelines to guide video generation. These methods use Hamilton's equations to enforce physically meaningful transitions in latent space, yielding trajectories that better reflect the underlying system dynamics. However, they rely critically on the specification of a prior distribution for the latent space. Gaussian priors provide flexibility but often result in poor reconstruction fidelity and weak interpretability, while structured priors improve interpretability but require prior knowledge of the configuration space, which is rarely available in practice. This tension restricts the generality of existing methods.

To address these challenges, we introduce the Hamiltonian GAN (HGAN), the first adversarial video generation framework that integrates Hamiltonian structure. Unlike VAE-based methods, GANs learn latent distributions implicitly during training, eliminating the need to specify priors in advance. HGAN combines this advantage with a Hamiltonian motion model, a configuration-space mapping, and a physics-inspired regularization scheme to generate videos that are both visually realistic and consistent with underlying dynamical laws.

2. Methodology

The Hamiltonian GAN builds on the motion–content decomposition used in prior GAN-based video generators but adds three critical innovations. First, a *configuration-space mapping* transforms Gaussian noise samples into an interpretable latent representation that serves as the initial condition of the dynamical system. This module allows the model to infer the geometry of the configuration space directly from data rather than requiring hand-crafted assumptions. Second, latent trajectories are evolved using a *Hamiltonian motion model*. Instead of relying on recurrent neural networks to propagate motion vectors in discrete time, HGAN employs a Hamiltonian neural network to integrate Hamilton's equations forward in time. This guarantees continuous and conservative dynamics in the motion subspace, ensuring that the latent representation respects conservation laws inherent to the system. Third, a *cyclic-coordinate regularization term* is introduced during training. Inspired by the observation that conjugate momenta corresponding to cyclic coordinates are conserved, this penalty encourages the model to identify redundant or ignorable coordinates in the latent representation. The result is a more compact and interpretable latent structure that reveals conserved quantities and underlying

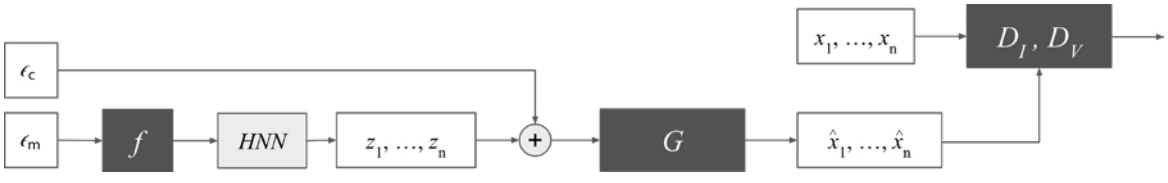

Figure 1: HGAN video generation pipeline.

system symmetries. The outputs of the Hamiltonian motion model are concatenated with content vectors and passed through a generator network to produce video frames. As in standard GAN pipelines, adversarial discriminators evaluate both individual frames and video sequences, guiding the generator to produce outputs that are both realistic and temporally coherent.

3. Experiments

We evaluate HGAN on the Hamiltonian Dynamics Suite Toy Physics dataset [3], which provides video renderings of canonical dynamical systems such as the mass–spring, pendulum, double pendulum, two-body, and three-body problems. Each system is rendered under different conditions, including variations in physical parameters and color schemes, enabling systematic evaluation of model performance. In our experiments, we focus on two dataset variants: (i) CCC: constant physical parameters and constant colors; (ii) CCV: constant parameters but varied colors across trajectories. We compare HGAN against three baselines. Hamiltonian Generative Networks (HGN) [4] represent the VAE-based approach, where latent dynamics are propagated using Hamilton's equations but priors must be chosen in advance. MoCoGAN [5] represents a widely used GAN-based video generation pipeline that separates motion and content but does not enforce physical structure. Finally, an HNN-GAN variant ablates the configuration-space mapping, isolating the impact of this component.

Quantitative evaluation We measure perceptual quality using the Frechet Video Distance (FVD). On the CCC dataset, HGAN achieves the best or second-best performance in four of the five benchmark systems. In particular, HGAN significantly improves results on pendulum and two-body dynamics, where temporal coherence is crucial. On the CCV dataset, HGAN matches or exceeds the baselines in most tasks, demonstrating robustness to changes in visual appearance.

Qualitative evaluation Visual inspection of generated sequences confirms that HGAN produces more realistic and stable trajectories. For example, pendulum and double-pendulum systems exhibit smooth periodic or chaotic motion consistent with physical expectations, while MoCoGAN outputs often drift or lose coherence over time. Visualization of the learned latent manifold using dimensionality reduction further highlights the advantage of HGAN: whereas baselines produce scattered or unstructured latent spaces, HGAN discovers compact, low-dimensional manifolds that correspond closely to the true configuration spaces of the systems.

These results demonstrate that HGAN not only improves perceptual quality but also yields interpretable and physically faithful representations of dynamical systems.

4. Conclusion and Outlook

The Hamiltonian GAN demonstrates that adversarial generative models can be enhanced by embedding physical structure. By combining implicit distribution learning with Hamiltonian dynamics, HGAN generates videos that are both visually plausible and consistent with fundamental conservation laws. The learned configuration-space representations are compact and interpretable, providing a foundation for downstream tasks that require understanding of system dynamics.

References

[1] Samuel Greydanus, Misko Dzamba, and Jason Yosinski. Hamiltonian neural networks. *Advances in Neural Information Processing Systems*, 32, 2019.

[2] Diederik P Kingma and Max Welling. Auto-encoding variational bayes. *arXiv preprint arXiv:1312.6114*, 2013.

[3] Aleksandar Botev, Andrew Jaegle, Peter Wirnsberger, Daniel Hennes, and Irina Higgins. Which priors matter? benchmarking models for learning latent dynamics. 2021.

[4] Peter Toth, Danilo Jimenez Rezende, Andrew Jaegle, Sébastien Racanière, Aleksandar Botev, and Irina Higgins. Hamiltonian generative networks. *arXiv preprint arXiv:1909.13789*, 2019.

[5] Sergey Tulyakov, Ming-Yu Liu, Xiaodong Yang, and Jan Kautz. Mocogan: Decomposing motion and content for video generation. In *Proceedings of the IEEE conference on computer vision and pattern recognition*, pages 1526–1535, 2018.

ECCOMAS Thematic Conference and IACM Special Interest Conference
Highly Flexible Slender Structures (HFSS 2025)
22–26 September 2025, Kaiserslautern, Germany

A Journey Through the World of Frictionless Sliding Sleeves Systems

Francesco Dal Corso

DICAM, University of Trento, Italy, francesco.dalcorso@unitn.it

Keywords: Configurational mechanics; Actuation; Contact mechanics; Self-tuning dynamics; Variable-length systems.

1. Introduction

A frictionless sliding sleeve is a mechanical constraint that allows only relative sliding motion between the sleeve and the constrained element, creating an effective system with variable length. When the flexibility of the constrained component is considered, a curvature discontinuity typically arises at the sleeve exit and a tangential concentrated force, nonlinear and repulsive, is generated there.
In this presentation, I will summarize key findings from the past decade on fundamental structural systems involving this simple yet distinctive constraint.

2. Showcase of the earliest results

After its introduction by Eshelby [1] to motivate the motion of defects within solids, the concept of configurational forces has been recently extended to structural mechanics by considering variable-length systems. The variable length is the configurational parameter of the system and is attained through the insertion of a structural element, for example, within a frictionless sliding sleeve. This specific constraint has been shown theoretically and experimentally to generate a non-null reaction, parallel to the sliding direction [2] (Fig. 1, left). This concept has been so far exploited to display unexpected quasi-static response [3, 4] and to analyze propulsion [5, 6] (Fig. 1, center), and divergent motion [7] (Fig. 1, right).

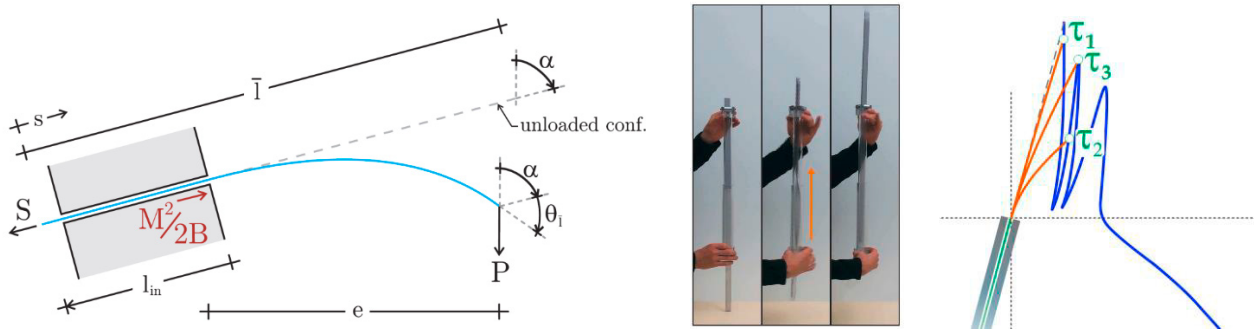

Figure 1. The non-null tangential and outward reaction at the sliding sleeve exit (left). Torsional locomotion (center). Divergent motion for a falling rod (right).

3. The latest results

3.1. Elastic solids under frictionless rigid contact

With a strong analogy to fracture mechanics, for a homogeneous elastic solid in frictionless contact against a rigid and rectilinear constraint, ending with a rounded or sharp corner, it is shown that (i.) a path-independent *J*-integral can be defined, (ii.) which is equal to the energy release rate *G* associated with an infinitesimal growth in the size of the frictionless constraint and thus gives the value of the configurational force component along the sliding direction [8]. It is found that (iii.) such a configurational sliding force is the Newtonian force component exerted by the elastic solid on the constraint at the frictionless contact.
Assuming the kinematics of a Euler-Bernoulli rod for an elastic body of rectangular shape, the results (i.)-(iii.) lead to a new interpretation from a nonlinear solid mechanics perspective of the configurational forces disclosed for one-dimensional structures of variable length.

Approximate but closed-form solutions (validated with finite element simulations) are exploited to provide further insight into the effect of configurational forces. Two applications show that a transverse compression can lead to Eulerian buckling (Fig. 2, left) or to longitudinal dynamic motion, both realizing novel examples of soft actuation mechanisms.

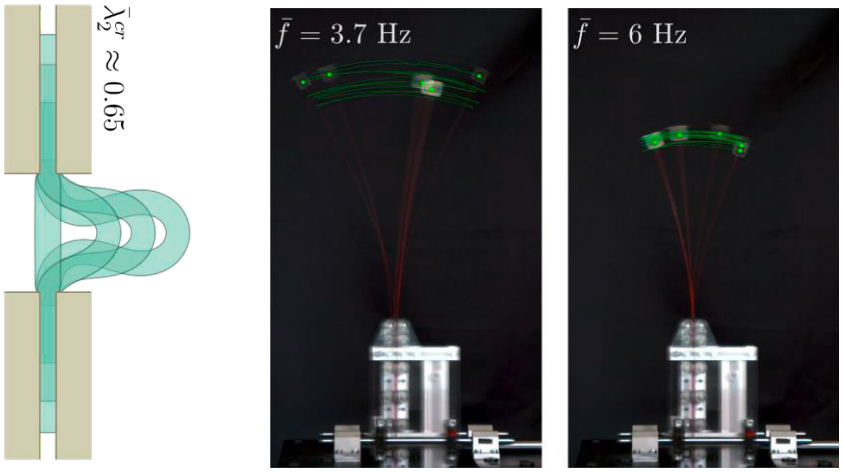

Figure 2. Euler buckling through transverse compression (left). Self-tuning variable-length system through transverse oscillation of the sliding sleeve constraint (right).

3.2. The self-tuning resonant system

The dynamics is addressed for an elastic rod, straight in its undeformed state, having a mass attached at one end and a variable length, due to a constraint at the other end by a frictionless sliding sleeve [9]. The constraint is arranged with the sliding direction parallel to a gravity field, in a way that the rod can freely slip inside of the sleeve, when the latter is not moving. In this case, the free fall of the mass continues until the rod is completely injected into the constraint. However, when the sliding sleeve is subject to a harmonic transverse vibration, it is shown that the fall of the mass and the rod injection are hindered by the presence of a configurational force developing at the sliding sleeve and acting oppositely to gravity. During the dynamic motion, such a configurational force is varying in time because it is associated with the variable bending moment at the sleeve entrance. It is (experimentally, analytically, and numerically) demonstrated that, in addition to the states of complete injection or ejection of the elastic rod (for which the mass falls down or is thrown out), a stable sustained oscillation around a finite height can be realized. This 'suspended motion' is the signature of a new attractor, that arises by the constraint oscillation. This behaviour shares similarities with parametric oscillators, as for instance the Kapitza inverted pendulum. However, differently from the classical parametric oscillators, the 'suspended' configuration of the rod violates equilibrium and the stabilization occurs through a transverse mechanical input, instead of a longitudinal one. By varying the sliding sleeve oscillation amplitude and frequency within specific sets of values, the system spontaneously adjusts the sustained motion through a self-tuning of the rod's external length (Fig. 2, right).
Furthermore, the effect of viscous damping on the nonlinear planar dynamics of a paradigmatic variable-length structural system has been theoretically analyzed [10]. The analysis reveals the potential for unique or multiple periodic responses, depending on system parameters and damping levels. Stability analysis via Floquet theory identifies conditions for monostable or bistable dynamic responses, showing that viscous damping can stabilize or, somewhat unexpectedly, destabilize the system, akin to other dynamic instability problems.
Finally, this analysis has been recently extended to the case of a heavy rod (without any lumped mass) showing multiple modal self-tuning and mode-jumping at the decrease of frequency [11]. When a critical frequency value is reached, a switch of the system oscillating at the n*th* mode occurs through its self-tuning towards the (n-1)*th* mode, depending on the amount of system dissipation.

3.3. The elastica sling

The planar equilibrium is analyzed for a flexible elastic rod constrained at its edges by a pair of sliding sleeves. The equilibrium configuration is found to have shape defined only by the inclination of the two constraints, while their distance is responsible only for scaling the size. By extending the theoretical stability criterion available for systems under isoperimetric constraints to the case of variable domains, the existence of no more than one stable equilibrium solution is revealed. The set of sliding sleeves' inclination pairs for which the stability is lost are identified. Such critical conditions allow the indefinite ejection of the flexible rod from the sliding sleeves, thus realizing an elastica sling (Fig. 3, left).

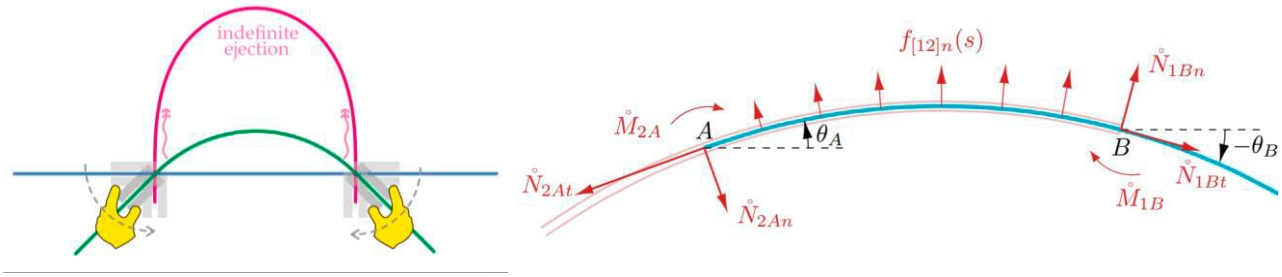

Figure 3. The elastica sling (left). Distributed and concentrated interaction forces along a flexible frictionless sliding sleeve (right).

3.4. The flexible frictionless sliding sleeve

The original concept introduced by Yury Vetyukov (TU Wien) at HFSS2023 in Rijeka [13] laid the foundation for a new line of research into frictionless sliding sleeve constraints. Building directly on this idea, a joint research effort with him and Sébastien Neukirch (Sorbonne University) has extended the theoretical framework of frictionless sliding sleeves to include systems where the constraint itself is also flexible [14]. The application of variational and micromechanical approaches disclosed the equilibrium conditions and the closed form expressions for evaluating the interaction (concentrated and distributed) forces along the overlapping length (Fig. 3, right). Quasi-static and dynamic mechanisms for attaining the maximum bearing capacity are found to be displayed by the flexible sleeves.

Acknowledgements

The author gratefully acknowledges financial support from the European Research Council (ERC) under the European Union's Horizon Europe research and innovation programme, Grant agreement No. ERC-ADG-2021-101052956-BEYOND.

References

[1] J.D. Eshelby. *The continuum theory of lattice defects*. Solid State Physics, 3 (1956) 79-144.
[2] D. Bigoni, F. Dal Corso, F. Bosi F., D. Misseroni. *Eshelby-like forces acting on elastic structures: theoretical and experimental proof*. Mechanics of Materials, 80 (2015) 368-374.
[3] D. Bigoni, F. Bosi, F. Dal Corso, D. Misseroni. *Instability of a penetrating blade*. Journal of the Mechanics and Physics of Solids, 64 (2014) 411-425.
[4] F. Bosi, D. Misseroni, F. Dal Corso, S. Neukirch, D. Bigoni. *Asymptotic self-restabilization of a continuous elastic structure*. Physical Review E, 94 (6) (2016), 063005.
[5] F. Dal Corso, D. Misseroni, N.M. Pugno, A.B. Movchan, N.V. Movchan, D. Bigoni. *Serpentine locomotion through elastic energy release*. Journal of the Royal Society Interface, 14 (2017): 20170055.
[6] D. Bigoni, F. Dal Corso, D. Misseroni, F. Bosi. *Torsional locomotion.* Proceedings of the Royal Society A, 470 (2014), 20140599.
[7] C. Armanini, F. Dal Corso, D. Misseroni, D. Bigoni. *Configurational forces and nonlinear structural dynamics*. Journal of the Mechanics and Physics of Solids, 130 (2019), 82-100.

[8] F. Dal Corso, M. Amato, D. Bigoni. *Elastic solids under frictionless rigid contact and configurational force*. Journal of the Mechanics and Physics of Solids, 188 (2024) 105673.
[9] P. Koutsogiannakis, D. Misseroni, D. Bigoni, F. Dal Corso. *Stabilization of an elastic rod through an oscillating sliding sleeve*. Journal of the Mechanics and Physics of Solids, 181 (2023) 105452.
[10] G. Migliaccio, F. D'Annibale, P. Koutsogiannakis, F. Dal Corso. *Viscous damping stabilization and destabilization of resonant self-tuning variable-length structures*. Submitted for publication (2025).
[11] P. Koutsogiannakis, D. Misseroni, D. Bigoni, F. Dal Corso. *Multiple modal self-tuning stabilization and mode-jumping of an oscillating variable-length rod*. In preparation (2025).
[12] A. Cazzolli, F. Dal Corso. *The elastica sling*. European Journal of Mechanics / A Solids, 105 (2024): 105273.
[13] Y. Vetyukov, A. Humer. *Sliding flexible rods: non-material finite elements and configurational forces*, ECCOMAS Thematic Conference and IACM Special Interest Conference Highly Flexible Slender Structures (HFSS 2023), 25-29 September 2023, Rijeka.
[14] S. Neukirch, F. Dal Corso, Y. Vetyukov. *The frictionless flexible sliding sleeve*. Submitted for publication (2025).

ECCOMAS Thematic Conference and IACM Special Interest Conference
Highly Flexible Slender Structures (HFSS 2025)
22–26 September 2025, Kaiserslautern, Germany

1D models for slender hyperelastic structures based on a two-scale approach

Helen Le Clézio [1], Claire Lestringant [2]

[1] ETH Zürich, helen.leclezio@mavt.ethz.ch
[2] Sorbonne Université, claire.lestringant@sorbonne-universite.fr

Keywords: finite elasticity, hyperelastic material, dimension reduction, non-linear effects

1. Motivation and context

The rapid evolution of structural engineering towards designing flexible and soft structures challenges classical 1D models based on Kirchhoff's equations and fosters a growing need for new 1D models capable of accurately capturing the mechanics of structures having complex, nonlinear deformations in their cross-section, such as thin-walled beams, beams with large, incompatible pre-strains or sharp elastic contrasts in their cross-sections. In this presentation, we will focus on hyperelastic materials and discuss a range of structures featuring nonlinear effects coming from their geometry or constitutive behavior.

Asymptotic dimension reduction offers a rigorous constructive method to derive accurate nonlinear 1D models. Assuming a separation of scales between the structure's length and its cross-sectional dimensions, it splits the 3D kinematics into an effective 1D description of the center-line and a set of 3D cross-sectional microscopic displacements that can be slaved to the 1D kinematics by solving a series of micro-scale problems set on the structure's cross-section [1]. Applying this formal approach to a hyperelastic structure results in a nonlinear 1D kinematic description that closely resemble the one underlying Kirchhoff's equations, associated with a constitutive behavior that depends on the solutions of 2D nonlinear cross-sectional problems [2, 3, 4]. Closed-form solutions to the 2D microscopic problems exist for simple geometries [5, 4, 6]. However, there is no general analytical solution for arbitrary cross-sections and hyperelastic constitutive laws: the dimension reduction procedure thus needs to be numerically implemented [2, 3, 7].

In this talk, we start by presenting the main steps of the two-scale dimension reduction procedure in a general finite elasticity setting. After showing a few cases for which explicit or semi-explicit solutions exist, we discuss its numerical implementation and demonstrate its capacities on a set of examples that include comparisons with predictions from full 3D hyperelastic models.

2. Formal nonlinear dimension reduction for hyperelastic structures

We consider a hyperelastic slender prismatic solid of length L and cross-section Ω. We denote $\mathbf{T}$ its cross-sectional and S its axial coordinates in the undeformed configuration. A 3D finite deformation of the solid is described by its deformed configuration $\mathbf{x}(S,\mathbf{T})$, that we decompose as

$$\mathbf{x}(S,\mathbf{T}) = \mathbf{r}(S) + y_i(S,\mathbf{T})\mathbf{d}_i(S), \tag{1}$$

where $\mathbf{r}(S) = \langle \mathbf{x}(S,\cdot)\rangle$ is the deformed position averaged over the cross-section (capturing the structure's effective center-line position) and $(y_i(S,\mathbf{T}))_{i\in\{1,2,3\}}$ captures the 3D microscopic deformation of the cross-section.

In Equation (1) and following [2, 4], we express the microscopic displacement in the local orthonormal material frame associated to the structure's center-line position $(\mathbf{d}_1(S),\mathbf{d}_2(S),\mathbf{d}_3(S))$ with $\mathbf{d}_3 = \mathbf{r}'(S)/|\mathbf{r}'(S)|$. With this definition, the macroscopic stretch $\varepsilon(S)$ is defined through the relation $\mathbf{r}'(S) = (1+\varepsilon(S))\mathbf{d}_3(S)$. The cross-section's rotation gradient $\boldsymbol{\kappa}(S)$ is further defined by the relation $\mathbf{d}_i'(S) = \boldsymbol{\kappa}(S)\times\mathbf{d}_i(S)$ for $i\in\{1,2,3\}$. Thus $\boldsymbol{\kappa}(S) = \kappa_1(S)\mathbf{d}_1(S) + \kappa_2(S)\mathbf{d}_2(S) + \kappa_3(S)\mathbf{d}_3(S)$ captures the macroscopic bending $\kappa_1(S),\kappa_2(S)$ and twisting $\kappa_3(S)$ strains.

Adopting a variational view [1, 2, 4], we define the structure's 3D energy as

$$\Phi[\varepsilon,\boldsymbol{\kappa};\mathbf{y}] = \int_0^L \left(\iint_\Omega \mathscr{W}(\mathbf{E}(\varepsilon,\boldsymbol{\kappa};\mathbf{y}))\mathrm{d}\mathbf{T} \right) \mathrm{d}S, \tag{2}$$

where $\mathscr{W}$ denotes the material's energy strain density and $\mathbf{E}$ is the 3D Green-Lagrange strain tensor. The goal of the formal dimension reduction procedure is to slave the microscopic displacement $\mathbf{y}$ to the macroscopic strains

$(\boldsymbol{\varepsilon}, \boldsymbol{\kappa})$ by solving the following energy stationarity problem for a given distribution of $(\boldsymbol{\varepsilon}(S), \boldsymbol{\kappa}(S))$

$$\frac{\partial \Phi}{\partial \mathbf{y}}[\boldsymbol{\varepsilon}, \boldsymbol{\kappa}; \mathbf{y}] \cdot \hat{\mathbf{y}} = 0 \quad \forall \hat{\mathbf{y}}. \tag{3}$$

Seeking solutions of (3) as a series expansion in powers of a small parameter $\eta \ll 1$ (typically defined as the ratio of the cross-sectional dimension over the length L) yields an approximation of the solution $\mathbf{y}^\star[\boldsymbol{\varepsilon}, \boldsymbol{\kappa}](\mathbf{T})$ in the form

$$\mathbf{y}^\star[\boldsymbol{\varepsilon}, \boldsymbol{\kappa}](\mathbf{T}) = \mathbf{y}_{[0]}[\boldsymbol{\varepsilon}, \boldsymbol{\kappa}](\mathbf{T}) + \eta \mathbf{y}_{[1]}[\boldsymbol{\varepsilon}, \boldsymbol{\kappa}](\mathbf{T}) + \eta^2 \mathbf{y}_{[2]}[\boldsymbol{\varepsilon}, \boldsymbol{\kappa}](\mathbf{T}) + \mathscr{O}(\eta^3), \tag{4}$$

where the functions $\mathbf{y}_{[i]}[\boldsymbol{\varepsilon}, \boldsymbol{\kappa}](\mathbf{T})$ are obtained by solving a cascade of nonlinear elasticity problems set on a reference cross-section for a given set of macroscopic strains $(\boldsymbol{\varepsilon}, \boldsymbol{\kappa})$. Replacing this solution into the 3D energy in Equation (2) yields an effective energy depending on the macroscopic strains only, defined as $\Phi^\star[\boldsymbol{\varepsilon}, \boldsymbol{\kappa}] = \Phi[\boldsymbol{\varepsilon}, \boldsymbol{\kappa}; \mathbf{y} = \mathbf{y}^\star]$. By further integrating over the cross-section and expanding in terms of successive powers of η this yields

$$\Phi^\star[\boldsymbol{\varepsilon}, \boldsymbol{\kappa}] = \int_0^L \left(W_0(\boldsymbol{\varepsilon}, \boldsymbol{\kappa}) + \begin{pmatrix} \boldsymbol{\varepsilon}' \\ \boldsymbol{\kappa}' \end{pmatrix} \boldsymbol{B}(\boldsymbol{\varepsilon}, \boldsymbol{\kappa}) \begin{pmatrix} \boldsymbol{\varepsilon}' \\ \boldsymbol{\kappa}' \end{pmatrix} \right) \mathrm{d}S + \mathscr{O}(\eta^3). \tag{5}$$

In (5), $W_0(\boldsymbol{\varepsilon}, \boldsymbol{\kappa}) = \iint_\Omega \mathscr{W}(\mathbf{E}(\boldsymbol{\varepsilon}, \boldsymbol{\kappa}; \mathbf{y}_{[0]}) \mathrm{d}\mathbf{T}$ is a nonlinear effective energy density and $\mathbf{B}(\boldsymbol{\varepsilon}, \boldsymbol{\kappa})$ is a matrix of gradient moduli. When truncating the expansion in (5) at order η^0, one obtains the leading order asymptotic 1D model. The axial gradients $\boldsymbol{\varepsilon}'$ and $\boldsymbol{\kappa}'$ scale as η and the second term in the expansion is thus of order η^2. In our talk, we will mainly focus on the leading order effective model. We will show that the gradient contribution can help regularize the model when localization occurs in the structure.

3. Numerical implementation

By the above dimension reduction method, solving a macroscopic (initial) boundary value problem ((I)BVP)—making use of the effective strain energy potential (5)—at leading order involves solving a series of local 2D problems (3) on the cross-section for each local combination of strains $\boldsymbol{\varepsilon}(S)$, $\kappa_1(S)$, $\kappa_2(S)$, and $\kappa_3(S)$ at each S. These 2D elasticity problems lend themselves naturally to be solved using conventional finite elements. This can be done on the fly at every load/time step and for every macroscale coordinate S (in an FE^2 fashion), which, however, comes at a high computational cost [2, 3, 8].

We discuss two approaches to increase the efficiency of the microscale simulations: The effective energy can be computed a priori for a catalog of macroscopic strain combinations for a given cross-sectional geometry and hyperelastic constitutive law(s) of the base material(s) within the cross-section. By introducing a third-order 4D interpolation, an approximate albeit smooth and differentiable energy landscape is obtained, which then serves as the material model for the macroscale simulation [7]. Alternatively, the microscale simulations are substituted with a surrogate model based on a machine-learned neural network [8, 9].

In both cases, at the cost of an initial effort, we save significant computational costs when solving the macroscopic (I)BVP. We use a discrete beam formulation based on discrete elastic rods to solve the structural (I)BVP on the macroscale, following the implementation of [10] and using the open-source C++ library *UtoBeams* [11].

4. Results

To illustrate the nonlinear effects captured by our numerical implementation, we consider a hollow tube with a thin-walled circular cross-section subjected to bending and compare this to a fully resolved 3D finite element simulation. The deformed beam obtained from the 3D FE analysis compares excellently with the center-line obtained from our nonlinear 1D model, as shown in Fig. 1 [7]. To highlight the significantly nonlinear behavior due to the Brazier effect, the linear response resulting from classical Euler-Bernoulli 1D beam theory is included in Fig. 1. Small deviations between the nonlinear 1D model and the 3D FE analysis are due to boundary effects, as the beam is fully clamped. Here, the leading-order reduced model accurately captures the nonlinear effects, owing to the slenderness of the beam, even in the presence of boundary effects.

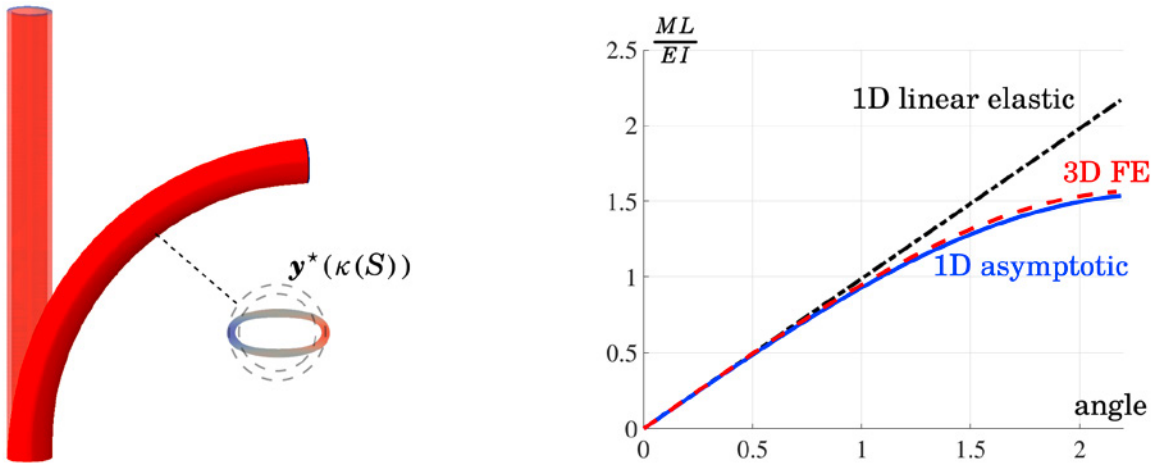

Figure 1: Simulation of a cantilever tube (fully clamped on one end) with a rotation applied to the free end. The reaction moment at the fully clamped end of the beam is shown in for our numerical reduced-order hyperelastic beam model, full 3D FE analysis, and Euler-Bernoulli beam theory.

References

[1] VL Berdichevskii. On the energy of an elastic rod. *Journal of Applied Mathematics and Mechanics*, 45(4):518–529, 1981.

[2] Fang Jiang and Wenbin Yu. Nonlinear variational asymptotic sectional analysis of hyperelastic beams. *AIAA journal*, 54(2):679–690, 2016.

[3] Abhishek Arora, Ajeet Kumar, and Paul Steinmann. A computational approach to obtain nonlinearly elastic constitutive relations of special cosserat rods. *Computer Methods in Applied Mechanics and Engineering*, 350:295–314, 2019.

[4] Basile Audoly and Claire Lestringant. Asymptotic derivation of high-order rod models from non-linear 3d elasticity. *Journal of the Mechanics and Physics of Solids*, 148:104264, 2021.

[5] Derek E Moulton, Thomas Lessinnes, and Alain Goriely. Morphoelastic rods iii: Differential growth and curvature generation in elastic filaments. *Journal of the Mechanics and Physics of Solids*, 142:104022, 2020.

[6] Basile Audoly and Sébastien Neukirch. A one-dimensional model for elastic ribbons: a little stretching makes a big difference. *Journal of the Mechanics and Physics of Solids*, 153:104457, 2021.

[7] Helen Le Clézio, Claire Lestringant, and Dennis M Kochmann. A numerical two-scale approach for nonlinear hyperelastic beams and beam networks. *International Journal of Solids and Structures*, 276:112307, 2023.

[8] Helen Le Clézio, Konstantinos Karapiperis, and Dennis M. Kochmann. Nonlinear two-scale beam simulations accelerated by thermodynamics-informed neural networks. *Extreme Mechanics Letters*, 73:102260, 2024.

[9] Jasper O. Schommartz, Dominik K. Klein, Juan C. Alzate Cobo, and Oliver Weeger. Physics-augmented neural networks for constitutive modeling of hyperelastic geometrically exact beams. *Computer Methods in Applied Mechanics and Engineering*, 435:117592, 2025.

[10] Claire Lestringant, Basile Audoly, and Dennis M. Kochmann. A discrete, geometrically exact method for simulating nonlinear, elastic and inelastic beams. *Computer Methods in Applied Mechanics and Engineering*, 361(2002), 2020.

[11] UtoBeams. Mechanics and Materials Lab, ETH Zurich. `https://doi.org/10.5905/ethz-1007-238`, 2020. Accessed: Aug, 2022.

ECCOMAS Thematic Conference and IACM Special Interest Conference
Highly Flexible Slender Structures (HFSS 2025)
22–26 September 2025, Kaiserslautern, Germany

Geometric numerical integration for data-driven system identification

Christian Offen [1,2]

[1] University of Birmingham, School of Mathematics, Edgbaston, Birmingham, B15 2TT, UK
[2] Paderborn University, Warburger Str. 100, 33098 Paderborn, Germany, christian.offen@uni-paderborn.de

Keywords: System identification, uncertainty quantification, physics informed machine learning, structure preservation, numerical integration

1. Introduction

The simulation and optimisation of physical or technical processes requires reliable and efficient models of the underlying dynamical systems. When the equations of motions are unknown, efficient surrogate models need to be identified from data. This also applies when equations of motions are known in principle but too computationally complex to simulate efficiently [1].

The use of prior geometric knowledge in the identification of models of dynamical systems from data has been advocated in various contexts [2, 3, 4]. Here we will consider fundamental geometric structures, in particular, Hamiltonian and Lagrangian dynamical systems as well as systems with continuous symmetries, such as rotational or translational symmetries.

A data-driven context assumes that observations $\{(x^{(j)},\dot{x}^{(j)})\}_j$ of trajectories of a dynamical systems are available. The machine learning task is to infer the underlying unknown first order differential equation

$$\dot{x} = f(x) \tag{1}$$

from the data with a generic ansatz for the vector field, such as a neural network $f = f_\Theta$. Training then involves optimising parameters Θ such that the loss $\ell_\Theta = \sum_{j=1}^N \|\dot{x} - f_\Theta(x)\|^2$ is minimised.

Often prior knowledge of the form of (1) is known. *Hamiltonian neural networks* (HNN) parametrise f as

$$f_\Theta(x) = J^{-1}(x)\nabla H_\Theta(x) \tag{2}$$

for a known symplectic structure J such that only a scalar valued Hamiltonian function needs to be identified from data [2]. Hamiltonian structure is related to energy conservation (conservation of H). This is an important qualitative aspect of the dynamical system which Hamiltonian data-driven models capture by design. Gaussian processes have been used as models for H as well [4, 5, 6] and extensions are available for systems with forcing terms [7], Poisson structure, or pde character [8].

Another geometric assumption is that (1) is the first order formulation of a (non-degenerate) Lagrangian ordinary differential equation

$$0 = \ddot{q}^\top \frac{\partial^2 L}{\partial\dot{q}\partial\dot{q}}(q,\dot{q}) + \dot{q}^\top \frac{\partial^2 L}{\partial q\partial\dot{q}}(q,\dot{q}) - \frac{\partial L}{\partial q}(q,\dot{q}), \tag{3}$$

where L is a scalar valued function (Lagrangian) that is non-degenerate, i.e. the matrix $\frac{\partial^2}{\partial\dot{q}\partial\dot{q}}L(q,\dot{q})$ is invertible. The approach is called *Lagrangian neural network (LNN)*, when $L = L_\Theta$ is parametrised as a neural network [3]. Gaussian processes can be used as well [9, 10]. Next to covering conservative mechanical systems, generalisations of (3) can govern electromagnetic field equations or Schrödinger equation and have been considered in a machine learning context as well [11, 12, 13, 14]. Other generalisation include forcing terms [10].

Apart from assuming prior knowledge that the system is Hamiltonian or Lagrangian, no further assumptions are made about the structure of the Hamiltonian or Lagrangian function. Indeed, a framework for very general Hamiltonians H and Lagrangians L without further structural assumptions is required when the evolution of the system is described in some (partial) measurement variables that describe a projection of the dynamical system. In contrast, when the full state can be observed, then a more informed ansatz is often possible such as $H_\Theta(q,p) = \frac{1}{2}p^\top M^{-1}p + V_\Theta(q)$ or $L_\Theta(q,\dot{q}) = \frac{1}{2}\dot{q}^\top M\dot{q} - V_\Theta(q)$ with mass matrix M and a data-driven potential V_Θ for mechanical systems.

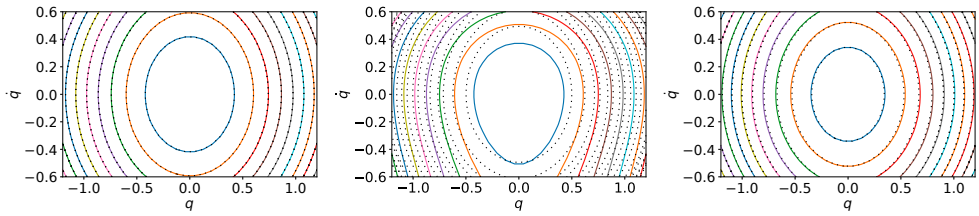

Figure 1: Left: Motions of a data-driven model (solid lines) for the mathematical pendulum match motions of an analytic model (dotted). Centre: Numerically computed motions of the data-driven model are surprisingly inaccurate despite using a small step-size. Right: Applying the same numerical integrator to a true analytic model yield much more accurate results. (Figure taken from [15, Fig. 6].)

2. Challenges for geometric data-driven models

A critical aspect of data-driven models of dynamical systems is their behaviour, when they are employed as surrogate models in numerical simulations or optimisation pipelines. For this, machine learned models do not just need to fit the training data and have good extrapolation properties, they also need to be suitable for numerical integration.

The identification of a Lagrangian function from data is a highly ill-posed inverse problem. Indeed, observed motions do *not* determine the Lagrangian uniquely, even in the infinite data limit. Instead, many Lagrangian govern the same motions, i.e. many functions L can yield the same or equivalent differential equations (3). Similar issues exist on the Hamiltonian side, when the Hamiltonian $H = H_\Theta$ and symplectic structure $J = J_\Theta$ are both data-driven and learned simultaneously. Here we will focus on the Lagrangian description.

Without a careful set-up, a machine learning-based method may identify a Lagrangian L that, while consistent with the data, yields equations of motions that are numerically ill-conditioned and amplify numerical errors. This is demonstrated in fig. 1: while a Lagrangian model is learnt to high accuracy and its exact motions coincide with motions of the true dynamical system (left), a numerical integration shows amplified and unbalanced discretisation errors (middle). However, the issue is not with the numerical integrator: when the same integrator with the same step-size is applied to a true, analytical Lagrangian, then the integration errors are tiny (right). This demonstrates that while a data-driven Lagrangian can be correct in the sense that it governs the dynamics to high accuracy, it can be badly suited for numerical integration.

The following approaches tackle these issues:

- *Regularisation:* Carefully designed regularisation approaches for neural network based learning methods [13, 12] or Gaussian processes [9, 14] seek to optimise the regularity of the machine learned Lagrangian while not restricting the generality of the ansatz. An approach relates to normalising the value, momentum, and symplectic volume at one point of the phase space [9, Appendix B]. Another approach seeks to optimise the numerical regularity of (3) using the regularisation term

$$\ell_{\mathrm{reg}} = \int \left\| \left(\frac{\partial^2 L_\Theta}{\partial \dot{q} \partial \dot{q}} (q, \dot{q}) \right)^{-1} \right\|$$

  or computationally efficient approximations of this idea [13].

- *Discrete models:* Rather than learning a continuous Lagrangian or Hamiltonian, one can learn a discretised model directly. In this way, numerical integration errors are eliminated from the problem by design [11, 13]. In many cases, this corresponds to learning a generating function of the symplectic flow map [6, Appendix A] as done in [18, 17]. Moreover, the symplectic flow map can be learned directly using SympNets [16]. Techniques based on numerical backward error analysis [19, 20, 21] can be used to reconstruct the continuous Hamiltonian or Lagrangian from the learned discrete quantities [6, 22, 15].

- *Symmetry:* The centre plot of fig. 1 indicates that the learned Lagrangian is unsymmetric. While non-symmetric Lagrangians can govern symmetric motions, surprisingly large, unbalanced numerical errors

can show up (centre) in numerical variational integration. This motivates to design approaches that do not just identify any Lagrangian but the most symmetric Lagrangian that is consistent with the data. Next to numerical advantages of highly symmetric Lagrangians or Hamiltonians, benefits are seen in extrapolation properties, both in methods that assume that invariances are known a priori [23, 24, 25] and in those that seek to learn symmetries along with the Lagrangian or Hamiltonians, respectively, using a Lie group based framework [26, 27]. Indeed, learning of symmetries can be interpreted as a regularisation as well, as it pushes the identified Hamiltonian or Lagrangian into the most symmetric representation that is consistent with the data. As an additional benefit, the identified symmetries can be related to conservation laws by Noether's theorem, which is of interest for system identification and gives some structural information on the behaviour of the machine learned dynamics.

3. Quantification of model uncertainty for geometric data-driven models

When making dynamical predictions based on limited data, it is important to quantify model uncertainty of the prediction, especially in safety-critical applications. As outlined in the previous section, geometric models can suffer from ambiguities in their representation: there is an abundance of Lagrangians L that yield the same or equivalent Euler–Lagrange equations (3). Analogously, when the symplectic structure $J = J_\Theta$ and the Hamiltonian $H = H_\Theta$ in a Hamiltonian systems are both data-driven, many combinations of Hamiltonian and symplectic structures yield equivalent equations of motions. This has the following implications for the quantification of model uncertainty (UQ).

- It does not make sense to quantify the uncertainty of the learned quantity L (or H and J) directly: UQ for these quantities would include the ambiguity of the model's representation, which has no dynamical effect and is, therefore, not of interest.
- We need to design regularisation strategies that (a) do not restrict the generality of the ansatz, (b) render dynamically significant quantities unique, such as the equations of motions or conserved energy. (c) Additionally, for efficient UQ the dynamical quantities of the previous point need to have a simple dependence (ideally linear dependence) on the geometric quantity that is data-driven (the Lagrangian). In such a case, expensive sampling strategies can be substituted by more efficient analytic estimates.

In [9] corresponding regularisation strategies are developed for learning Lagrangians or discerete Lagrangians from data using Gaussian Processes. Under non-degeneracy conditions on the underlying dynamics, it is shown that normalisation conditions exist that render the equations of motions, the symplectic structure, and the Hamiltonian function unique. By interpreting these as linear observables of the Lagrangian L one can efficiently compute their a posteriori distribution as Gaussian processes.

Figure 2 shows an experiment, where a Lagrangian L of a coupled harmonic oscillator is identified from dynamical data of the form $(q, \dot{q}, \ddot{q})$ using models based on Gaussian processes. Once L is identified, the Hamiltonian can be computed as $H = \dot{q}^\top \frac{\partial L}{\partial \dot{q}} - L$. As this is a linear expression in L, H is again a Gaussian process whose variance indicates model uncertainty. The figure shows experiments with 80 and 300 observation points. As the UQ is derived from a Gaussian process framework, it can be computed by with solving linear equations only. While the computational complexity grows cubically in the number of data points, the approach avoids expansive sampling methods. Moreover, various approaches exists to compute efficient approximations [28, 29, 30, 31].

4. Summary

For successful identification of dynamical systems from data, it is crucial to take aspects of numerical analysis, geometry, and statistics into account. In this talk, I will focus on machine learning of dynamical systems that are governed by Hamilton's equations or Euler–Lagrangian equations. The equations of motions are *un*known a priori and need to be identified from data.

Numerical aspects. Important aspects are the numerical properties of the machine-learned dynamical models for efficient employment in numerical simulations. I will show that numerical aspects need to be taken into account already in the design stage of data-driven models and that classical techniques from Numerical Analysis, such as backward error analysis, prove useful in this context.

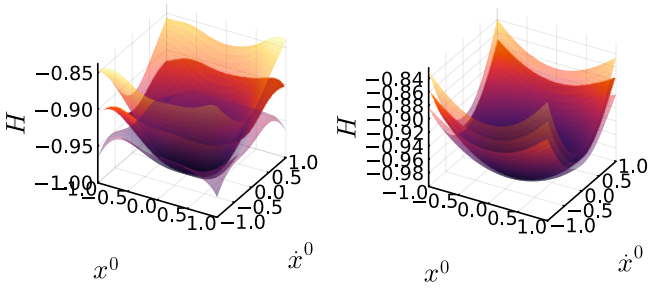

Figure 2: Identification of the Lagrangian L of a coupled harmonic oscillator from dynamical data. The identified mean of H plus/minus 20% standard deviation are displayed for 80 (left) and 300 (right) data points. (Figure taken from [9, Fig. 4].)

Symmetries. Further benefits can be derived from exploiting symmetries, even when these are not explicitly known a priori but are identified from data along the equations of motions. Indeed, I will show approaches to learn Lie group symmetries and dynamical systems simultaneously and how symmetry identification can be interpreted as a regularisation that pushes the identified quantities into their most symmetric representations.

Regularisation. Many Lagrangian functions can govern the same motions. This proves challenging in a machine learning context as it implies that identifying a Lagrangian from observations of motions is a highly ill-posed inverse problem. I will show the main ideas behind geometric regularisation strategies that optimise numerical performance or eliminate model uncertainty that is due to artificial ambiguity of the model's representation rather than limited data.

Uncertainty Quantification (UQ). The statistics-informed regularisation opens up interesting opportunities for including UQ in geometric data-driven machine learning methods. Indeed, especially in the limited data regime, for which inclusion of prior geometric knowledge is assumed to be most helpful, it is important to quantify prediction errors of machine learned models based on well-founded statistical techniques. By telling users when to doubt a data-driven prediction, we aim to increase users' trust into data-driven models in the cases when sufficient data is available for highly accurate predictions. I will show approaches to UQ in this context that overcome the ill-posedness of the geometric problem in a way that one can even prove convergence in the infinite data limit. Indeed, once a statistical model for UQ is established, one can compare the effect of geometric prior knowledge on model uncertainty quantitatively. This provides a systematic framework to analyse the benefit of geometry in machine learning.

References

[1] Slawomir Koziel and Anna Pietrenko-Dabrowska. *Performance-Driven Surrogate Modeling of High-Frequency Structures*. Springer International Publishing, 2020.

[2] Samuel Greydanus, Misko Dzamba, and Jason Yosinski. Hamiltonian Neural Networks. In H. Wallach, H. Larochelle, A. Beygelzimer, F. d'Alché Buc, E. Fox, and R. Garnett, editors, *Advances in Neural Information Processing Systems*, volume 32. Curran Associates, Inc., 2019.

[3] Miles Cranmer, Sam Greydanus, Stephan Hoyer, Peter Battaglia, David Spergel, and Shirley Ho. Lagrangian neural networks. ICLR 2020 Deep Differential Equations Workshop, 2020.

[4] Tom Bertalan, Felix Dietrich, Igor Mezić , and Ioannis G. Kevrekidis. On learning Hamiltonian systems from data. *Chaos*, 29(12):121107, dec 2019.

[5] Jianyu Hu, Juan-Pablo Ortega, and Daiying Yin. A structure-preserving kernel method for learning Hamiltonian systems. *Math. Comp.*, 2025.

[6] Christian Offen and Sina Ober-Blöbaum. Symplectic integration of learned Hamiltonian systems. *Chaos*, 32(1):013122, 1 2022.

[7] Juan-Pablo Ortega and Daiying Yin. Learnability of linear port-Hamiltonian systems. *Journal of Machine Learning Research*, 25:1–56, 2 2024.

[8] Sølve Eidnes and Kjetil Olsen Lye. Pseudo-Hamiltonian neural networks for learning partial differential equations. *Journal of Computational Physics*, 500:112738, 2024.

[9] Christian Offen. Machine learning of continuous and discrete variational odes with convergence guarantee and uncertainty quantification. *Math. Comp. (In Press., Preprint: arXiv:2404.19626)*, 2025.

[10] Giulio Evangelisti. *Physically Consistent Gaussian Processes for Learning-based Control of Euler-Lagrange Systems*. PhD thesis, Technische Universität München, 2025.

[11] Hong Qin. Machine learning and serving of discrete field theories. *Scientific Reports*, 10(1):19329, 11 2020.

[12] Christian Offen and Sina Ober-Blöbaum. Learning discrete Lagrangians for variational pdes from data and detection of travelling waves. In Frank Nielsen and Frédéric Barbaresco, editors, *Geometric Science of Information*, volume 14071, pages 569–579, Cham, 2023. Springer Nature Switzerland.

[13] Christian Offen and Sina Ober-Blöbaum. Learning of discrete models of variational PDEs from data. *Chaos*, 34:013104, 1 2024.

[14] Christian Offen. Machine learning of discrete field theories with guaranteed convergence and uncertainty quantification. arxiv:2407.07642, 2024.

[15] Sina Ober-Blöbaum and Christian Offen. Variational learning of Euler–Lagrange dynamics from data. *Journal of Computational and Applied Mathematics*, 421:114780, 2023.

[16] Pengzhan Jin, Zhen Zhang, Aiqing Zhu, Yifa Tang, and George Em Karniadakis. SympNets: Intrinsic structure-preserving symplectic networks for identifying Hamiltonian systems. *Neural Networks*, 132:166–179, 2020.

[17] Renyi Chen and Molei Tao. Data-driven prediction of general Hamiltonian dynamics via learning exactly-symplectic maps. In Marina Meila and Tong Zhang, editors, *Proceedings of the 38th International Conference on Machine Learning*, volume 139 of *Proceedings of Machine Learning Research*, pages 1717–1727. PMLR, 18–24 Jul 2021.

[18] Katharina Rath, Christopher G. Albert, Bernd Bischl, and Udo von Toussaint. Symplectic Gaussian process regression of maps in Hamiltonian systems. *Chaos*, 31(5):053121, 05 2021.

[19] Ernst Hairer, Christian Lubich, and Gerhard Wanner. *Geometric Numerical Integration: Structure-Preserving Algorithms for Ordinary Differential Equations*. Springer Series in Computational Mathematics. Springer Berlin Heidelberg, 2013.

[20] Benedict Leimkuhler and Sebastian Reich. *Simulating Hamiltonian Dynamics*. Cambridge Monographs on Applied and Computational Mathematics. Cambridge University Press, 2005.

[21] Mats Vermeeren. Modified equations for variational integrators. *Numerische Mathematik*, 137(4):1001–1037, 6 2017.

[22] Marco David and Florian Méhats. Symplectic learning for Hamiltonian neural networks. *Journal of Computational Physics*, 494:112495, 2023.

[23] Eva Dierkes and Kathrin Flaßkamp. Learning Hamiltonian systems considering system symmetries in neural networks. *IFAC-PapersOnLine*, 54(19):210–216, 2021. 7th IFAC Workshop on Lagrangian and Hamiltonian Methods for Nonlinear Control LHMNC 2021.

[24] Miguel Vaquero, Jorge Cortés, and David Martín de Diego. Symmetry preservation in hamiltonian systems: Simulation and learning. *Journal of Nonlinear Science*, 34(6):115, Oct 2024.

[25] Mingkun Li, Zaijiu Shang, Peng Wang, Hongkun Zhang, and Junjie Fan. Universal-basis neural ode modeling of the discrete sine-gordon system. 2025.

[26] Eva Dierkes, Christian Offen, Sina Ober-Blöbaum, and Kathrin Flaßkamp. Hamiltonian neural networks with automatic symmetry detection. *Chaos*, 33(6):063115, 06 2023. 063115.

[27] Yana Lishkova, Paul Scherer, Steffen Ridderbusch, Mateja Jamnik, Pietro Liò, Sina Ober-Blöbaum, and Christian Offen. Discrete Lagrangian neural networks with automatic symmetry discovery. *IFAC-PapersOnLine*, 56(2):3203–3210, 2023. 22nd IFAC World Congress.

[28] Carl Edward Rasmussen and Christopher K. I. Williams. *Gaussian Processes for Machine Learning*. The MIT Press, 11 2005.

[29] Michalis Titsias. Variational learning of inducing variables in sparse gaussian processes. In David van Dyk and Max Welling, editors, *Proceedings of the Twelfth International Conference on Artificial Intelligence and Statistics*, volume 5 of *Proceedings of Machine Learning Research*, pages 567–574, Hilton Clearwater Beach Resort, Clearwater Beach, Florida USA, 16–18 Apr 2009. PMLR.

[30] Joaquin Quiñonero-Candela and Carl Edward Rasmussen. A unifying view of sparse approximate Gaussian process regression. *Journal of Machine Learning Research*, 6(65):1939–1959, 2005.

[31] Florian Schäfer, Matthias Katzfuss, and Houman Owhadi. Sparse Cholesky factorization by Kullback–Leibler minimization. *SIAM Journal on Scientific Computing*, 43(3):A2019–A2046, 2021.

ECCOMAS Thematic Conference and IACM Special Interest Conference
Highly Flexible Slender Structures (HFSS 2025)
22–26 September 2025, Kaiserslautern, Germany

Embedding slender structures in continua: Theory, numerical methods, and applications

Ignacio Romero[1,2], David Portillo[1]

[1] Technical University of Madrid, ignacio.romero@upm.es
[2] IMDEA Materials, ignacio.romero@imdea.org

Keywords: Nonlinear Structures, Mixed-dimensionality Problem, Embedded Structures

1. Introduction

Bodies with embedded reinforcements are extremely common in both nature and technology. For example, the human skin is a connective tissue that uses collagen fibers as a means of providing it with strength. In turn, reinforced concrete uses steel rebars to increase stiffness and strength in large structures, especially where subject to tensile stresses.

Modeling this kind of composites — with either point-, line-, or surface-type reinforcements — is difficult because of the disparity of the geometries in the involved bodies. When developing numerical methods to approximation their joint mechanical behavior, severe difficulties appear from the start: the solution spaces are different and often impossible to compare. For example, the displacement in three-dimensional bodies belongs to a Hilbert space that is not defined on any curve. As a result, one can not embed a fiber on a deformable solid simply by constraining their two displacements to be the same.

In this talk a new and general approach to connect continua and structural bodies will be presented. First, a general *model* for deformable bodies with embedded structures will be described. Then, a numerical method to approximate their collective solution will be introduced. Our formulation builds upon the Arlequin method [1, 2], a technique introduced two decades ago and employed to connect deformable bodies that share a non-empty region. In our work, we extend the Arlequin method to encompass bodies with different dimensions. We are able to show the well-posedness of the continuous and discrete formulations.

The methods advocated in our work and described in the talk are suitable for linking rigid bodies, bars, beams, plates, membranes, and shells to deformable bodies. Although all convergence results are for linear elastic cases, the ideas can be extended to the geometrically nonlinear regime and to inelastic materials. We will present examples to illustrate the generality and robustness of the approach.

2. Deformable solids, structures, and their link

In classical elasticity, a deformable body is a smooth domain $\Omega \in \mathbb{R}^3$ with displacement field $u \in X := [H^1_\partial(\Omega)]^3$, the Hilbert space of square-integrable functions with square-integrable derivatives that vanish on $\partial_D\Omega$. The equilibrium solution of such a body is the minimizer of the potential energy $V_{LE} : X \to \mathbb{R}$, that is

$$u = \arg \inf_{w \in E} V_{LE}(w) \ . \tag{1}$$

In linear problem the potential V_{LE} is quadratic and there exists a linear form $a_{LE} : X \times X \to \mathbb{R}$ and a linear form $f_{LE} : X \to \mathbb{R}$ such that

$$V_{LE}(u) = \frac{1}{2} a_{LE}(u,u) - f_{LE}(u) \ . \tag{2}$$

A structure is deformable body $\mathscr{S}$ with two crucial features. First, its geometry admits a representation as the direct product of a base manifold $\mathscr{C}$ and a fiber $\mathscr{F}$. Hence, every $x \in \mathscr{S}$ has base coordinates σ and fiber coordinates ξ. The dimension of each of these two spaces depends on the specific structural model. For example, the fiber of a beam is the two-dimensional cross section at every point of the curve of centroids, which is the base manifold. In the case of a plate, the base manifold is the midsurface and the fiber is the one-dimensional segment piercing the structure at every point of the midsurface. By this construction, every point $x \in \mathscr{S}$ can be projected onto $\mathscr{C} \times \mathscr{F}$ and we write $(\sigma, \xi) = \Pi(x)$. Likewise, from the coordinates (σ, ξ), a point in $\mathbb{R}^3$ can be obtained using $x = \mathscr{E}(\sigma, \xi)$, with $\Pi \circ \mathscr{E} = Id$.

The second important feature of every structural model is that the displacement of every point of coordinates (σ, ξ) can be written in the form

$$\Psi(\sigma,\xi) = \Sigma(\sigma) + \Theta(\sigma) * \xi \ , \tag{3}$$

where the notation '$*$' is used to indicate some linear map. Since it is clear that the displacement depends on the fields Σ, Θ we will denote, henceforth, as $[\Sigma, \Theta]$ any function of the form (3) and define as Y the admissible functional space for pairs $[\Sigma, \Theta]$.

In every structural model, its solution $[\Sigma, \Theta] \in Y$ is the minimizer of a potential energy $V_{ST} : Y \to \mathbb{R}$ which is of the form

$$V_{ST}(\Upsilon, \beta) = \frac{1}{2} a_{ST}(\Upsilon, \beta; \Upsilon, \beta) - f_{ST}(\Upsilon, \beta) \ . \tag{4}$$

where $a_{ST} : Y \times Y \to \mathbb{R}$ and $f_{ST} : Y \to \mathbb{R}$ are, respectively, bilinear and linear forms defined differently for each structure.

Finally, let us introduce the inner product on functions defined on $\mathscr{C} \times \mathscr{F}$:

$$\langle\langle U, V \rangle\rangle = \int_{\mathscr{C}} \int_{\mathscr{F}} \left(U(\sigma,\xi) \cdot V(\sigma,\xi) + \ell^2 \, DU(\sigma,\xi) \cdot DV(\sigma,\xi) \right) \mathrm{d}\mathscr{F} \, \mathrm{d}\mathscr{C} \ . \tag{5}$$

Then, a deformable solid has displacement $u \in X$ that is compatible with an embedded structure with generalized displacement field $[\Sigma, \Theta] \in Y$ if it satisfies

$$\inf_{u \in X, [\Sigma,\Theta] \in Y} \sup_{\gamma \in Y} \left[V_{LE}(u) + V_{ST}(\Psi) + \langle\langle \gamma, [\Sigma, \Theta] - u \circ \mathscr{E} \rangle\rangle \right] \ . \tag{6}$$

This is a constrained minimization problem. However, and in contrast with standard formulations where the constraints are enforced by L^2-pairing them with Lagrange multipliers, in Eq. (6) the inner product (5) is employed. This operation enforces the constraint in a more subtle way than standard inner products since also first order derivatives are included.

The optimality conditions of this problem are: find the displacements $u \in X$, $[\Sigma, \Theta] \in Y$ and the multipliers $[\gamma, \mu] \in Z$ such that

$$\begin{aligned} a(u, \Sigma, \Theta; v, \Gamma, \beta) + b(v, \Gamma, \beta; \gamma, \mu) &= f(v, \Gamma, \beta) \\ b(u, \Sigma, \Theta; \alpha, \zeta) &= 0 \end{aligned} \tag{7}$$

for all $v \in X$, $[\Gamma, \beta] \in Y$ and $[\alpha, \zeta] \in Z$. Here, the bilinear forms $a(\cdot,\cdot)$ and the force term $f(\cdot)$ collect, respectively, the bilinear forms and the force terms of the continuum solid and the structure. The bilinear form $b(\cdot,\cdot)$ is responsible for the constraint. Specifically, we employ

$$\begin{aligned} a(u, \Sigma, \Theta; v, \Gamma, \beta) &:= a_{LE}(u, v) + a_{ST}(\Sigma, \Theta; \Gamma, \beta) \ , \\ b(u, \gamma, \mu; \alpha, \zeta) &:= \langle\langle [\alpha, \zeta], [\gamma, \mu] - u \circ \mathscr{E} \rangle\rangle \ , \\ f(v, \Gamma, \beta) &:= f_{LE}(v) + f_{ST}(\Gamma, \beta) \ . \end{aligned} \tag{8}$$

The analysis of this mixed problem shows that it is well-posed under standard assumptions on the continuum body and the structure.

3. Finite element discretization of solids with embedded structures

The finite element discretization of problem (7) is straightforward. To build it, it suffices to define finite dimensional spaces $X^h \subset X$ and $Y^h \subset Y$. Then, the solution is the functions $u_h \in X^h$ and $[\Sigma_h, \Theta_h] \in Y^h$ and the multipliers $[\alpha_h, \zeta_h] \in Y^h$

$$\begin{aligned} a(u_h, \Sigma_h, \Theta_h; v_h, \Gamma_h, \beta_h) + b(v_h, \Gamma_h, \beta_h; \gamma_h, \mu_h) &= f(v_h, \Gamma_h, \beta_h) \ , \\ b(u_h, \Sigma_h, \Theta_h; \alpha_h, \zeta_h) \ , &= 0 \end{aligned} \tag{9}$$

hold for all $v_h \in X^h, [\Gamma_h, \beta_h] \in Y^h$ and $[\alpha_h, \zeta_h] \in Y^h$. This problem is always well-posed.

The evaluation of the integrals that appear in Eq. (7) demand some care. The base manifold $\mathscr{C}$ of the structure is partitioned into elements and on each element, $Q_{\mathscr{C}}$ are selected. If $Q_{\mathscr{F}}$ quadrature points are selected on each fiber, a total number of $Q_{\mathscr{C}} \times Q_{\mathscr{F}}$ quadrature points have to be evaluated for the inner product $\langle\langle \cdot, \cdot \rangle\rangle$. At each of these points the displacement of the three-dimensional body needs to be evaluated and compared with the generalized displacement of the structure. The location of these points on the structure and the continuum solid needs to be calculated just once and thus its computational cost is negligible.

3.1. Extension to the finite strain regime

The extension of the models of Section 2. and the finite element approximations of Section 3. to the finite strain regime is fairly straightforward, in contrast with its analysis, which is extremely complex.

Standard finite strain models for continuum mechanics can be combined with fully nonlinear geometrically exact structures, such as rods and shells. In these cases, the easiest way to formulate robust numerical methods of nonlinear linked bodies is to impose the energetic compatibility of the solid and structural displacement incrementally.

4. Numerical examples

In this section we present one example to illustrate the kind of coupling that can be obtained with the methods introduced in this article. We refer the readers to a more comprehensive text [3] where several other examples can be found.

In the proposed example we consider the compression of a fiber-reinforced elastic block in non-dimensional units. The cube has volume 1 and the fibers have length 0.2 and radius 0.005. A set of 63 fibers have been randomly placed inside the cube occupying, approximately, 0.1% of the total volume of the composite. The cube has Young's modulus $E = 10^3$ and zero Poisson's ratio, while the fibers have $E = 10^5$ and their Poisson's ratio is also zero. Figure 1 depicts the initial configuration of the composite body, whose finite element mesh employs 20^3 hexahedral elements for the continuum body and 15 beam elements for each fiber.

Figure 2 shows the displacement magnitude of both the fibers and the solid. Although it is difficult to see clearly due to the number of fibers, the compatibility of motion between the solid and the fibers can be observed. Additionally, Figure 3 displays the Von Mises stress, which, as seen, is not uniform, with a maximum value of 117.72, a minimum of 93.80, and an average of 105.67.

5. Summary

This document summarizes our work in the formulation of models and finite element approximations of deformable solids with structural reinforcements. We showed that the method, for all structural types, can be cast into the form of a saddle point minimization. Moreover, it can be shown that both the continuum problem as well as the finite element discretizations are stable for all types of reinforcements under mild restrictions. The proposed methodology can serve as template for the analysis of large reinforced structural members (for example, reinforced concrete beams), but also for composite materials with particle and fiber inclusions.

References

[1] H. B. Dhia and G. Rateau. Analyse mathématique de la méthode Arlequin mixte. *Comptes Rendus de l'Académie des Sciences - Series I - Mathematics*, 332(7):649–654, Apr 2001.

[2] H. B. Dhia and G. Rateau. The Arlequin method as a flexible engineering design tool. *International Journal for Numerical Methods in Engineering*, 62(11):1442–1462, 2005.

[3] D. Portillo and I. Romero. Embedding structures in continua: linear models and finite element discretizations. *Submitted for publication*, 2025.

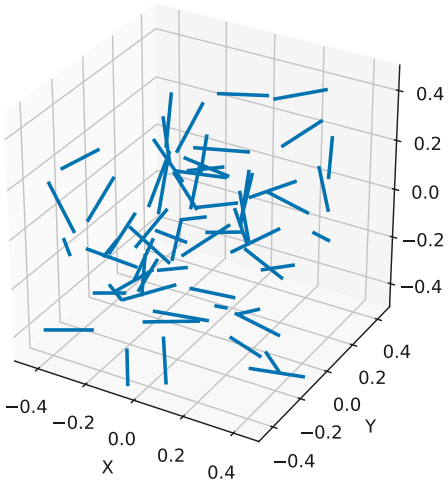

Figure 1: Fiber-reinforced brick. Fiber placement.

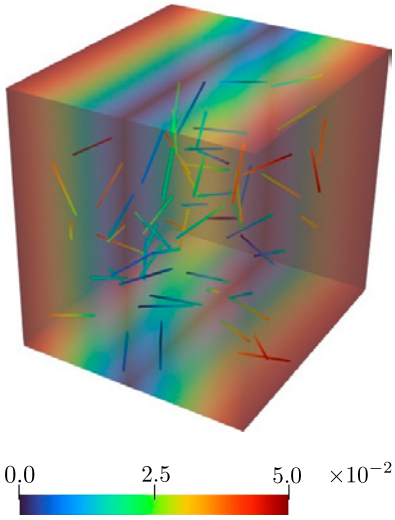

Figure 2: Fiber-reinforcement displacement magnitude.

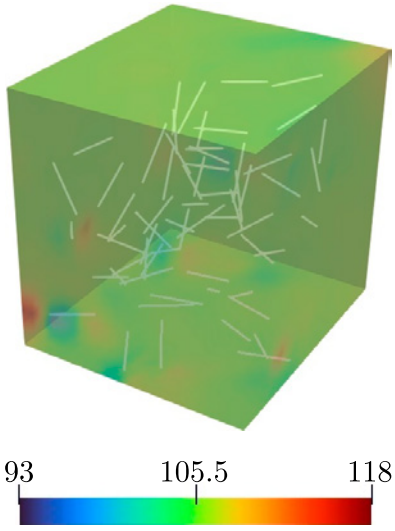

Figure 3: Fiber-reinforcement Von Mises stress.

ECCOMAS Thematic Conference and IACM Special Interest Conference
Highly Flexible Slender Structures (HFSS 2025)
22–26 September 2025, Kaiserslautern, Germany

Parametric Model Order Reduction in the Multi-Scale Material Setting

Theron Guo[1*], Ondrej Rokos[2], Varvara G. Kouznetsova[2], Marc G.D. Geers[2], Karen Veroy[2]

[1] Massachusetts Institute of Technology, t_guo@mit.edu
[2] Eindhoven Institute of Technology,
o.rokos@tue.nl, v.g.kouznetsova@tue.nl, m.g.d.geers@tue.nl, k.p.veroy@tue.nl

Keywords: Physics-Based Model Order Reduction, Digital Twins, Computational Homogenization, Parametrized Partial Differential Equations

1. Introduction

Physics-based model order reduction presents great potential for digital twins [1], providing highly accurate yet efficient approximations to solutions of parametrized partial differential equations. However, embedding such physics-based reduced order models in digital twin frameworks poses significant challenges. We consider some of these challenges particularly in the context of two-scale materials simulations.

Two-scale simulations are often employed to analyze the effect of the microstructure on a component's macroscopic properties. It is well known that understanding these structure–property relations is essential in the optimal design of materials, or to enable (for example) estimation of microstructure parameters through macroscale measurements. Unfortunately, the high computational costs of such multiscale simulations in computational homogenization often render the solution of design, optimization, or inverse problems in digital twins infeasible. To address this issue, we explore and develop parametric model order reduction (MOR) techniques to construct inexpensive surrogates for parametrized microscale problems. The method is specifically well-suited for multiscale simulations since the coupled simulation is decoupled into two independent problems: (1) solving the microscopic problem for different parameters (describing, e.g., loading, material, or geometric properties) and learning a surrogate model from the data; and (2) solving the macroscopic problem with the learned model.

We summarize several works on developing such reduced order models to construct inexpensive surrogates for parametrized microstructures in the *data-poor* regime, i.e., for applications in which the amount of data (obtained through measurements or simulations) to be used for training must be economized due to scarcity or cost. In addition to recent developments, we highlight limitations, challenges, and opportunities for parametric MOR in the multi-scale materials setting.

2. First-Order Computational Homogenization

In [2,3], we present a non-intrusive reduced basis method to construct approximations for the microscopic stress field. The method is based on combining proper orthogonal decomposition (POD) and regression [4]. In the case of geometric parameters [3], an auxiliary problem is also used to treat the geometric transformations. The method permits accurate and efficient prediction of the microscopic stress field for a wide range of parameters, and can be readily used in design and optimization tasks. Numerical results show that the method achieves high accuracy and efficiency.

In [5], we present intrusive reduced basis methods that permit the treatment of more complex behaviors. We present a method based on POD and the empirical cubature method [6] capable of treating nonlinear history-dependent behaviors. Numerical tests illustrate the significant speed-ups and accuracies achieved while observing good extrapolation behavior.

3. Second-Order Computational Homogenization

For more complex microstructures, enriched schemes such as second-order computational homogenization are required to fully capture the nonlinear behaviour that arises from nonlocal interactions due to the buckling or patterning of the microstructure. In [7], we present a technique that combines reduced basis methods with

[*] T. Guo worked on this project while he was affiliated with the Department of Mathematics and Computer Science at Eindhoven University of Technology.

second-order computational homogenization, thus allowing more complex nonlinear behaviors to be captured. The proposed method uses POD and a hyperreduction method that is specifically tailored for this problem and was inspired by the empirical cubature method [6].

Numerical examples compare the performance of the reduced-order model with respect to direct numerical simulations and the full second order computational homogenization model. Results show that the reduced order model is able to approximate the full second-order model well, and that any remaining errors with respect to the direct numerical simulation can be attributed to the inherent approximation errors in the computational homogenization scheme.

4. Conclusions

The works described above show that surrogates constructed via physics-based MOR techniques can be effectively used to significantly accelerate two-scale materials simulations. The methods provided accurate and rapid predictions for complex nonlinear behaviours simulated using first- and second-order computational homogenization techniques. Furthermore, the numerical results show that the methods are especially effective for data-poor contexts that occur in many digital twins applications. In particular, the methods are capable of constructing accurate and reliable surrogates using only a fraction of the training data typically required by, e.g., machine learning techniques. Such methods are thus suitable for digital twin applications in which training data must be economized due to scarcity or cost, or in which the surrogate model must be rapidly adapted to new data.

Acknowledgements

These results are part of a project that has received funding from the European Research Council (ERC) under the European Union's Horizon 2020 Research and Innovation Programme (Grant Agreement No. 818473).

References

[1] National Academies of Sciences, Engineering, and Medicine. *Foundational Research Gaps and Future Directions for Digital Twins*. The National Academies Press, Washington, DC, 2024.

[2] T. Guo, O. Rokoš, K. Veroy. *Learning constitutive models from microstructural simulations via a non intrusive reduced basis method*. Computer Methods in Applied Mechanics and Engineering. 384 (2021) pp. 113924.

[3] T. Guo, F. Silva, O. Rokoš, K. Veroy. *Learning constitutive models from microstructural simulations via a non-intrusive reduced basis method: Extension to geometrical parameterizations*. Computer Methods in Applied Mechanics and Engineering. 401 (2022) pp. 115636.

[4] M. Guo, J.S. Hesthaven. *Reduced order modeling for nonlinear structural analysis using Gaussian process regression*. Computer Methods in Applied Mechanics and Engineering. 341 (2018) 807–826,

[5] T. Guo, O. Rokoš, & K. Veroy. *A reduced order model for geometrically parameterized two-scale simulations of elasto-plastic microstructures under large deformations*. Computer Methods in Applied Mechanics and Engineering. 418 (2024) pp. 116467.

[6] Hernandez, J., Caicedo, M. & Ferrer, A. *Dimensional hyper-reduction of nonlinear finite element models via empirical cubature*. Computer Methods in Applied Mechanics and Engineering. 313 (2017) pp. 687-722.

[7] T. Guo, V.G. Kouznetsova, M.G.D. Geers, K. Veroy, O. Rokoš. *Reduced-Order Modeling for Second-Order Computational Homogenization With Applications to Geometrically Parameterized Elastomeric Metamaterials*. International Journal For Numerical Methods In Engineering. (2024) pp. e7604

ECCOMAS Thematic Conference and IACM Special Interest Conference
Highly Flexible Slender Structures (HFSS 2025)
22–26 September 2025, Kaiserslautern, Germany

Advanced material modeling for 3D beams

Oliver Weeger [1]

[1] TU Darmstadt, Cyber-Physical Simulation, weeger@cps.tu-darmstadt.de

Keywords: Geometrically exact beams, Elasto-visco-plasticity, Hyperelasticity, Machine learning, Multiphysics

1. Introduction

Classical beam and shell theories for modeling slender structures typically employ linear elastic material models to express the constitutive relationship between the strain and stress measures. However, when finite strains occur within slender structures, e.g., due to large stretches in soft polymer lattice structures [1], when stresses exceed yield limits or the material behavior is strongly rate-dependent, e.g., in stiff, metallic or polymeric lattices [2], or multiphysical effects such as thermo- or chemo-mechanical couplings are important, e.g., in batteries or thermo-elastic generators [3], linear elastic material modeling is not sufficient anymore. In this talk, we will thus introduce different concepts for establishing more advanced constitutive models within structural theories, in particular focusing on geometrically exact, shear-deformable 3D beams.

2. Inelastic material models with internal variables

We demonstrate inelastic material models for beams with elasto-visco-plasticity and damage [4]. The models are formulated in terms of the strain measures of the beam theory (axial, shear, curvature, and torsion strains) and additional internal variables for viscoelastic and plastic strains, isotropic and kinematic hardening variables, or damage parameters. By representing an effective internal energy density in terms of these variables and accompanying evolution equations in the typical fashion similar to 1D rheological and 3D continuum models (Coleman-Noll procedure), the approach is thermodynamically consistent. The approach is verified in comparison to 1D examples as well as reference results for 3D beams. Interestingly, also high accuracy in comparison to experimental measurements of lattice structures is achieved, even when the parameters of these material models are only characterized by 1D experiments [2], see Figure 1.

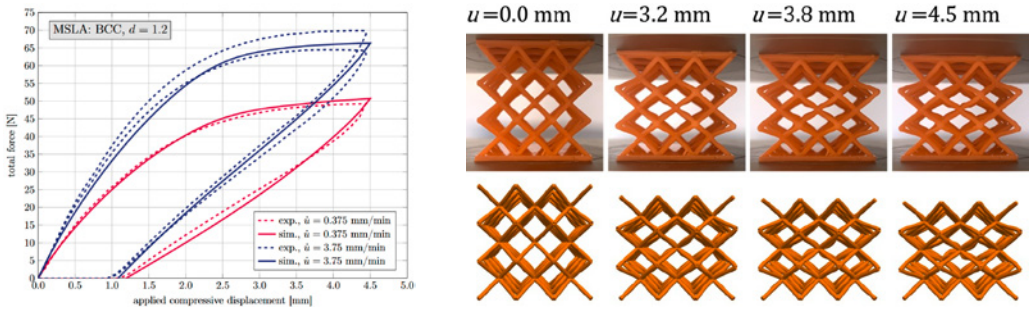

Figure 1: Inelastic beam simulation of additively manufactured lattice structure [2]

3. Physics-augmented neural network models for hyperelasticity

We present neural network-based constitutive models for hyperelastic geometrically exact beams [5], see Figure 2. The proposed models are physics-augmented, i.e., they fulfill important mechanical conditions by construction, which improves accuracy and generalization. Strains and curvatures of the beam are used as input for feed-forward neural networks that represent the effective hyperelastic beam potential. Forces and moments are received as the gradients of the beam potential, ensuring thermodynamic consistency. Additionally, we introduce a parameterization with a scalar parameter to represent ring-shaped cross-sections with different ratios between the inner and outer radii. This highly flexible but physically reasonable model enables efficient constitutive surrogate modeling for geometrically exact beams with nonlinear material behavior and cross-sectional deformation, which otherwise would require computationally much more expensive methods. The models are calibrated and tested with data generated for beams with circular and ring-shaped hyperelastic deformable cross-sections at varying inner and outer radii, showing excellent accuracy and generalization. The applicability of the proposed point symmetric model is further demonstrated by applying it in beam simulations.

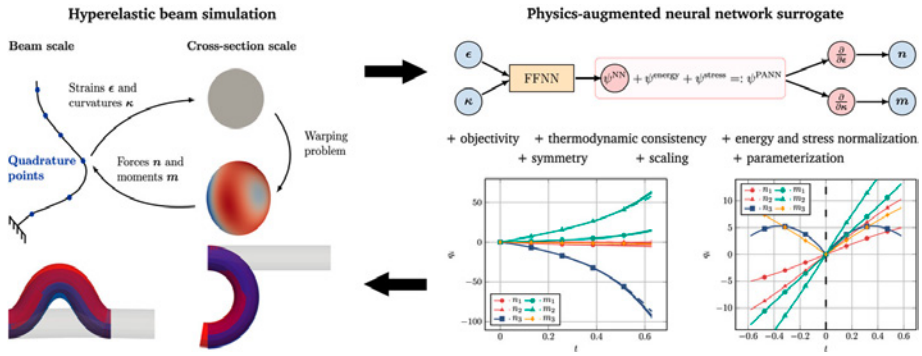

Figure 2: Overview of physics-augmented neural network modeling framework for hyperelastic beams [5]

4. Finite swelling beam model with axial and radial diffusion

We introduce a geometrically exact 3D beam model that incorporates axial and radial swelling strains resulting from a rotationally symmetric, thermal or chemical diffusion [6]. As major novelties, the presented method relates beam theory, and consequently small elastic strains, with large swelling deformation stemming from anisotropic diffusion phenomena, as it considers also radial diffusion. Isogeometric collocation is employed to discretize both the mechanical momentum balances and the axis-symmetric, steady-state 2D diffusion equation along the beam. The resulting coupled nonlinear problem for displacements, rotations, and temperatures or concentrations is solved using a staggered scheme, see Figure 3 (left). The model is validated against 3D continuum models in various numerical examples and proven to be both accurate and numerically efficient, see Figure 3 (right). Ultimately, this novel finite swelling beam model can present the starting point for the efficient modeling of lattice structures under diffusion conditions, such as microstructured Li-ion electrodes or thermoelectric semiconductors.

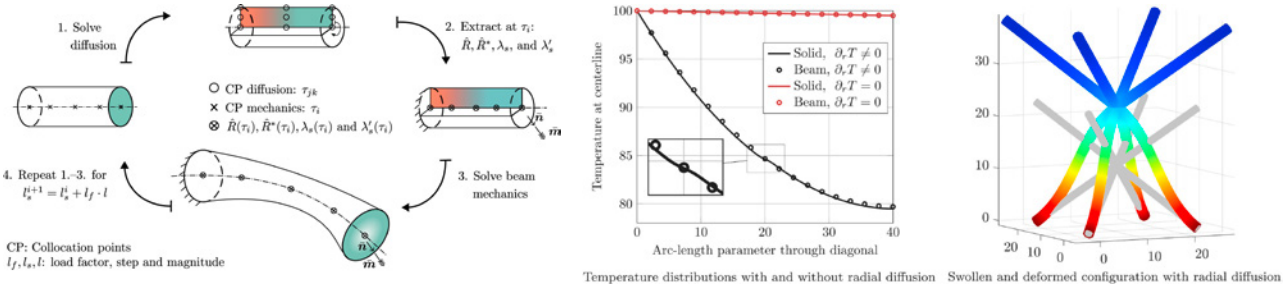

Figure 3: Illustration of the coupling of diffusion with mechanics through swelling (left) and results that highlight the importance of considering radial diffusion (right) [6]

5. Conclusions

We have demonstrated the development of advanced material models for 3D beam theory, considering inelastic (linear elasto-visco-plastic), hyperelastic, and chemo/thermo-mechanically coupled behaviors.

References

[1] O. Weeger, N. Boddeti, S.-K. Yeung, S. Kajima, M.L. Dunn. *Digital Design and Nonlinear Simulation for Additive Manufacturing of Soft Lattice Structures*, Addit. Manuf., 25 (2018), 39–49

[2] O. Weeger, I. Valizadeh, Y. Mistry, D. Bhate. *Inelastic finite deformation beam modeling, simulation, and validation of additively manufactured lattice structures*, Addit. Manuf. Lett., 4 (2022), 100111

[3] X. Xia, A. Afshar, H. Yang, C.M. Portela, D.M. Kochmann, C.V. Di Leo, J.R. Greer. *Electrochemically reconfigurable architected materials*. Nature, 573.7773 (2019), 205–213

[4] O. Weeger, D. Schillinger, R. Müller. *Mixed isogeometric collocation for geometrically exact 3D beams with elasto-visco-plastic material behavior and softening effects*, Comput. Methods Appl. Mech. Eng., 399 (2022), 115456

[5] J. Schommartz, D.K. Klein, J.C. Alzate Cobo, O. Weeger. *Physics-augmented neural networks for constitutive modeling of hyperelastic geometrically exact beams*, Comput. Methods Appl. Mech. Eng., 435 (2025), 117592

[6] J.C. Alzate Cobo, X.-L. Peng, B.-X. Xu, O. Weeger. *A finite swelling 3D beam model with axial and radial diffusion*, Comput. Methods Appl. Mech. Eng., 441 (2025), 117983

ECCOMAS Thematic Conference and IACM Special Interest Conference
Highly Flexible Slender Structures (HFSS 2025)
22–26 September 2025, Kaiserslautern, Germany

On Convolution based Variational Integrators for Fractional Lagrangians

Khaled Hariz [1], Fernando Jiménez [2], Sina Ober-Blöbaum [1]

[1] Paderborn University, hariz@math.upb.de, sinaober@math.upb.de
[2] Technical University of Madrid, fernando.jimenez.alburquerque@upm.es

Keywords: Convolution quadrature, fractional variational integrators, restricted calculus of variations.

1. Introduction

Some physical phenomena, as in anomalous damping and deformations, may not be accurately captured by classical models. The fractional calculus plays an important role in describing such phenomena. The main reason why fractional differential equations (FDEs) are being used to model real phenomena is that they are nonlocal in nature, that is, a realistic model of a physical phenomenon depends not only on the actual time but also on the previous one. The analytic solutions of FDEs are however not always available. Dealing with dynamical systems subject to fractional damping, a novel approach was proposed in [4] to formulate it in a purely variational way. We derive higher-order fractional variational integrators for this approach using Rung-Kutta convolution quadratures (RKCQs) and some numerical tests are provided.

1.1. Fractional integrals and convolution quadrature methods

Let $\alpha \in [0,1]$ and $f : [0,T] \to \mathbb{R}$ be a AC^2- function. The Riemann-Liouville α-fractional integrals of f are

$$I_-^\alpha f(t) = \frac{1}{\Gamma(\alpha)} \int_0^t \frac{f(\tau)}{(t-\tau)^{1-\alpha}}\, d\tau, \quad t \in (0,T], \quad I_+^\alpha f(t) = \frac{1}{\Gamma(\alpha)} \int_t^T \frac{f(\tau)}{(\tau-t)^{1-\alpha}}\, d\tau, \quad t \in [0,T). \tag{1}$$

Focusing on the *retarded* fractional integral, $I_-^\alpha f(t)$, it is easy to see that it may be written as a convolution

$$I_-^\alpha f(t) = \left(\kappa^{(\alpha)} * f\right)(t) := \int_0^t \kappa^{(\alpha)}(t-\tau) f(\tau) d\tau, \quad \text{where} \quad \kappa^{(\alpha)}(t) = \frac{t^{\alpha-1}}{\Gamma(\alpha)}. \tag{2}$$

An approximation of the convolution (2) was introduced by [1, 2] using the so-called CQ method. It is a special quadrature rule based on the Laplace transforms of the kernel $\kappa^{(\alpha)}$ and a linear multistep method (LMM). The CQ is defined by

$$\left(\kappa^{(\alpha)} * f\right)(t_k) \approx \mathfrak{J}_-^\alpha f_k := \sum_{n=0}^{k} \omega_n(h) f_{k-n} = \sum_{n=0}^{k} \omega_{k-n}(h) f_k, \quad (h \in \mathbb{R}_+ \text{ the time step}). \tag{3}$$

The *CQ weights* ω_n are defined as the coefficients of the generating power series

$$K^{(\alpha)}\left(\frac{\gamma(z)}{h}\right) = \sum_{n=0}^{\infty} \omega_n z^n, \qquad |z| \quad \text{small}, \tag{4}$$

where $\gamma(z)$ is the generating polynomials of a LMM for $y' = f(y)$. A CQ is convergent of order p (to I_σ^α) if

$$I_\sigma^\alpha t^{\beta-1} - \mathfrak{J}_\sigma^\alpha t^{\beta-1} = O(h^\beta) + O(h^p) = O(h^{\min\{\beta,p\}}), \quad \text{for all} \quad \beta \in \mathbb{C},\ \beta \neq 0, -1, -2, \cdots. \tag{5}$$

Another method to approximate (2) is to use CQ based on RKCQ [3]. This leads to an arbitrary order of accuracy. Under appropriate assumptions of an m-stage implicit RK method $\begin{array}{c|c} \mathbf{c} & A \\ \hline & \mathbf{b}^\top \end{array}$, $A \in \mathbb{R}^{s\times s}$, $\mathbf{b}, \mathbf{c} \in \mathbb{R}^s$., the RKCQ is defined by

$$\mathfrak{J}_-^\alpha \mathbf{f}_k = \begin{pmatrix} f_{k1} \\ \vdots \\ f_{km} \end{pmatrix} =: \sum_{n=0}^{k} W_{k-n}^{(\alpha)} \begin{pmatrix} f(t_n) + c_1 h \\ \vdots \\ f(t_n) + c_m h \end{pmatrix}.$$

The analysis of RKCQ method [3] was shown under some assumptions on f and its derivatives to be

$$I_-^\alpha f(t) - \mathfrak{J}_-^\alpha f(t) = O(h^{\min\{p, q+1+\mu\}}), \quad \text{where} \quad \|K(s)\| \leq M \cdot |s|^{-\mu}, \quad \mu > 0. \tag{6}$$

The integration by parts and semigroup properties are crucial in the restricted Hamilton's principle [4]. Such properties are preserved by CQ allowing to derive fractional variational integrators (FVIs) at the discrete level.

2. Fractional variational integrators with RKCQ

A *restricted calculus of variations* [4] is used to obtain the dynamics of a Lagrangian system subject to fractional damping by defining the following action:

$$\mathscr{L}(x,y) = \mathscr{L}^{\text{con}}(x,y) + \mathscr{L}^{\text{frac}}(x,y) = \int_0^T \left(L(x,\dot{x}) + L(y,\dot{y})\right) dt - \rho \int_0^T D_-^\alpha x(t) D_+^\alpha y(t)\, dt. \tag{7}$$

FVIs have been derived with an approximation of order 1 for the fractional derivatives. For a higher-order approximation, we choose a quadrature rule $(b_i, c_i)_{i=1}^r$ for $\mathscr{L}^{\text{con}}$ and a convolution quadrature for $\mathscr{L}^{\text{fra}}$. We consider a discrete series $x_d := \{\mathbf{x}_k\}_{0:N}$ with $\mathbf{x}_k := (x_k^1, \dots, x_k^{s+1})^\top$ (equiv for y_d). Namely

$$\mathscr{L}_d(x_d,y_d) = \mathscr{L}_d^{\text{con}}(x_d,y_d) + \mathscr{L}_d^{\text{frac}}(x_d,y_d) = \sum_{k=0}^{N-1} \left(L_d(x_k) + L_d(y_k)\right) - \rho h \sum_{k=0}^{N} \mathfrak{D}_-^\alpha x_k\, \mathfrak{D}_+^\alpha y_k, \tag{8}$$

where $L_d(x_k) = \sum_{i=1}^r b_i L(x_d(c_i h;k), \dot{x}_d(c_i h;k))$ is the piecewise polynomial on $[k,k+1]$ (equiv. for $y_d(t;k)$). The restricted calculus of variations lead to the so-called fractional variational integrators

$$D_{s+1}L_d(\{x_{k-1}^{0:s}\}) + D_1 L_d(\{x_k^{0:s}\}) - \rho\, h b_s \mathfrak{D}_-^{2\alpha} x_{k-1} - \rho\, h b_1 \mathfrak{D}_-^{2\alpha} x_k = 0, \quad k = 1,\dots,N-1, \tag{9}$$

$$D_i L_d(\{x_k^{0:s}\}) - \rho\, h b_i \mathfrak{D}_-^{2\alpha} x_k = 0, \qquad k = 0,\cdots,N-1, \quad i = 2,\cdots,s. \tag{10}$$

These are numerical schemes corresponding to fractionally damped systems. The equations with respect to y variables can be seen as eqs. (9)-(10) in reversed time, see also [4].

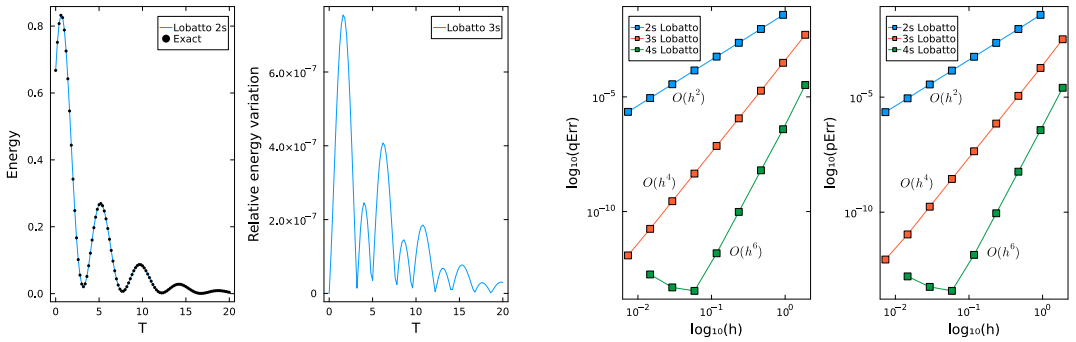

Figure 1: Coupled damped oscillator ($\alpha = 1/2$). Energy decay with error variation and convergence plots.

An important implication of variational structure in a dynamical system is the connection between symmetries and conserved quantities (Noether's theorem). So, incorporating variational structure into learning algorithms for dynamical systems is crucial in order to make sure that the learned model shares important features with the exact physical system [5]. This idea appears unexplored in case of fractional Lagrangians and thus will be our future research.

References

[1] C. Lubich. *Discretized fractional calculus*, SIAM J. Math. Anal., 17(3) (1983) 704-719.

[2] C. Lubich. *Convolution quadrature and discretized operational calculus I and II*, Numer. Math., 52 (1988) 129-145 and 413-425.

[3] C. Lubich and A. Ostermann *Runge-Kutta methods for parabolic equations and convolution quadrature*, Math. Comput. 60(201) (1993), 105-131

[4] F. Jiménez and S. Ober-Blöbaum *Fractional Damping Through Restricted Calculus of Variations*, Journal of Nonlinear Science, 31 (2021).

[5] S. Ober-Blöbaum and C. Offen *Variational learning of Euler–Lagrange dynamics from data*, Journal of Computational and Applied Mathematics, 421 (2023), 11478

ECCOMAS Thematic Conference and IACM Special Interest Conference
Highly Flexible Slender Structures (HFSS 2025)
22–26 September 2025, Kaiserslautern, Germany

Arbitrary Lagrangian–Eulerian Method and its Numerical Stability in Flexible Tether Deployment and Retrieval

Ryo Kuzuno [1], Kanjuro Makihara [2], Keisuke Otsuka [3]

[1] Department of Aerospace Engineering, Tohoku University, ryo.kuzuno.q1@dc.tohoku.jp
[2] Department of Aerospace Engineering, Tohoku University, kanjuro.makihara.e3@tohoku.ac.jp
[3] Department of Aerospace Engineering, Tohoku University, keisuke.otsuka.d6@tohoku.ac.jp

Keywords: Space Tether, Flexible Multibody Dynamics, Arbitrary Lagrangian-Eulerian, Slender Structures

1. Introduction

Flexible structures such as cables, membranes, and booms have attracted attention for application in space structures due to their lightweight and deployable characteristics. These components are deployed from a stowed configuration for mission operations in space. In non-serviceable environments such as outer space, the reliability of deployable systems must be ensured (Figure 1). Nevertheless, their low bending stiffness allows these structures to undergo large deformations and exhibit complex behaviors after deployment or retrieval [1]. Nonlinear finite element methods such as absolute nodal coordinate formulation (ANCF) and geometrically exact beam formulation, have been regarded as promising approaches for analyzing flexible multibody systems, and have been actively developed.

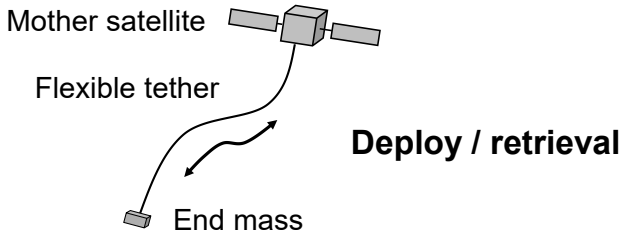

Figure 1. Example of deployable flexible tether used in space: tethered satellite.

The Arbitrary Lagrangian–Eulerian (ALE) method is a computational technique that combines aspects of purely Lagrangian and purely Eulerian descriptions to simulate problems with moving boundaries or large deformations, or fluid-structure interaction. ALE-ANCF has been developed recently [2][3]. On the other hand, ALE-ANCF has faced several challenges in practical numerical simulations. One such issue is numerical instability caused by nodal operations. In particular, when a node is removed, it becomes necessary to represent the interval originally interpolated by two third-order polynomial elements with a single third-order polynomial element. The resulting discontinuity in the interpolation shape before and after node removal can induce numerical instability. This problem becomes more pronounced in structures such as tethers, which undergo large changes in overall length while experiencing complex bending. In this study, we mainly focus on the numerical instability in the retrieval of flexible slender structures and propose a method to mitigate the numerical instability arising from such interpolation discontinuities associated with node removal.

2. Proposed Concept of ALE Node Scheme

In this research, we propose a co-moving node scheme. Conventionally, when the distance l_e between a moving ALE node and its adjacent node becomes less than a certain threshold, the adjacent node is deleted to avoid a singular mass matrix. However, this leads to numerical instability due to discontinuities in the configuration. In the proposed scheme, the adjacent node co-moves along with the originally moving ALE node, as illustrated in Fig. 2. Both schemes can represent tether retrieval, and the proposed scheme can avoid abrupt changes in interpolated shape, thereby mitigating numerical instability.

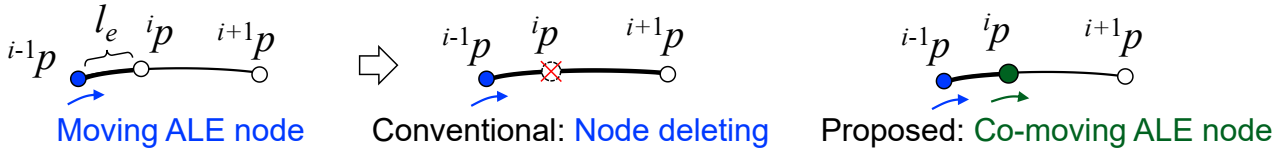

Figure 2. Schematic diagram of the proposed node co-moving scheme.

3. Numerical Results

Flexible pendulum simulation is conducted, and overall shape and energy history is compared with the ALE-ANCF applying node deletion scheme and that applying node co-moving scheme. As shown in Figure 3, the proposed scheme can alleviate unnatural motion and sudden increase of energy caused by node deletion. Note that the total energy is not conserved in this problem, as the retrieval of the pendulum is governed by a prescribed time-dependent function.

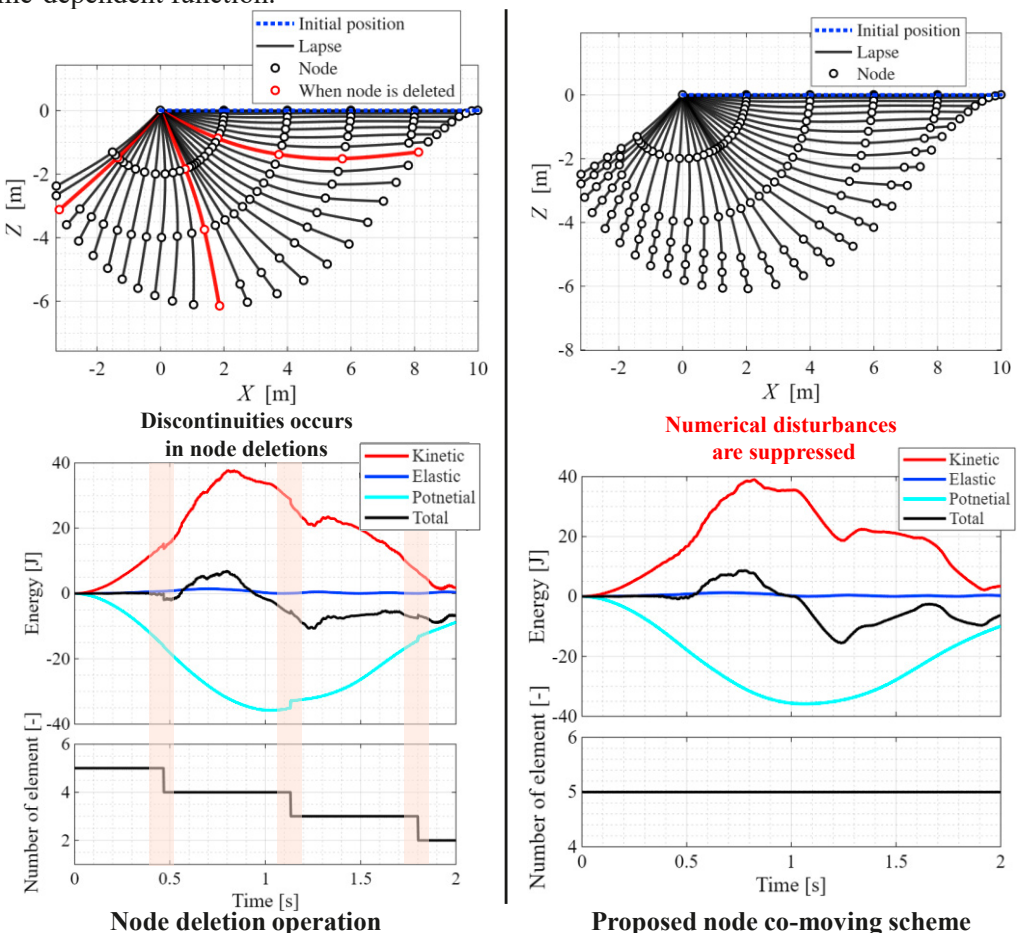

Figure 3. Time lapse and energy history of flexible pendulum problem comparing with two node operation schemes.

4. Conclusions

Numerical instability in analyzing retrieval of highly flexible cable using ALE-ANCF is alleviated by the proposed node operation.

Acknowledgements

This project has received funding from the Japan Society for the Promotion of Science (JSPS) KAKENHI (Grant numbers 24KJ0357) and The Anri Fellowship.

References

[1] R. Kuzuno, S. Dong, Y. Takahashi, T. Okada, C. Xue, K. Otsuka, K. Makihara. *High-Fidelity Flexible Multibody Model Considering Torsional Deformation for Nonequatorial Space Elevator*, Acta Astronautica, 220 (2024) 504–515

[2] J. L. Escalona. *An arbitrary Lagrangian–Eulerian discretization method for modeling and simulation of reeving systems in multibody dynamics*, Mechanism and Machine Theory, 112 (2017) 1–21

[3] M. Pieber, K. Ntarladima, R. Winkler, J. Gerstmayr, *A Hybrid Arbitrary Lagrangian Eulerian Formulation for the Investigation of the Stability of Pipes Conveying Fluid and Axially Moving Beams*, Journal of Computational and Nonlinear Dynamics, 17 (2022) 051006-1–051006-13

ECCOMAS Thematic Conference and IACM Special Interest Conference
Highly Flexible Slender Structures (HFSS 2025)
22–26 September 2025, Kaiserslautern, Germany

Inverse size effect explained through the Cosserat theory of elasticity

Edita Papa Dukić [1], Gordan Jelenić [2]

[1] University of Rijeka, Faculty of Civil Engineering, edita.papa@uniri.hr
[2] University of Rijeka, Faculty of Civil Engineering, gordan.jelenic@uniri.hr

Keywords: size effect, Cosserat theory, microstructure

1. Introduction

The classical Cauchy continuum theory has long provided a robust framework for describing the mechanical behavior of homogeneous solids, such as steel and aluminum [1]. However, carefully conducted experiments on granular, fibrous, and lattice-structured materials, as well as foam beams subjected to torsion and bending, reveal the so-called size effect—a phenomenon unaccounted for by Cauchy's theory [2]. Discrepancies between classical theory and experimental observations also arise in dynamic analyses, thermal studies, and fluid mechanics [1]. Furthermore, Cauchy's theory inherently assumes the symmetry of the stress tensor, limiting its applicability to specific natural boundary conditions consistent with this property.

To address these limitations, several alternative continuum theories have emerged. Among them, the Cosserat continuum theory, also known as the micropolar continuum theory [3], has gained attention for its ability to capture the behavior of certain materials more accurately. The underlying physical motivation for the development of this theory is found in the observation that on a sufficiently small scale all materials eventually cease to be homogeneous owing to an internal structure (on a molecular level or above it).

Despite its theoretical advancements, even the simplest linear elastic, isotropic, and centro-symmetric Cosserat continuum requires six independent material constants—far more than the two (Young's modulus and Poisson's ratio) in the classical Cauchy continuum. These additional parameters correspond to the coupling number, characteristic length for bending, characteristic length for torsion and polar ratio (analogous to Poisson's ratio). Reliable experimental procedures for determining these constants remain a challenge, underscoring the need for further research in this area.

2. Positive and negative size effect

The analytical solution of Gauthier and Jashman [4] predicts the so-called size effect, with the smaller specimens exhibiting stiffer response than the larger ones but their experimental findings for pure bending show exactly the opposite behavior which they called anti-micropolar since the smaller specimens exhibited softer response (both size effects are shown in Figure 1). The circumstances under which the size effect may be inverted have been clarified by Bigoni and Drugan [5] and experimentally demonstrated by [6]. Analysis of the size effect in the so-called direct approach enables us to determine additional micropolar material parameters. One of them is the characteristic length for bending - a material parameter that quantifies the influence of couple stresses on bending deformation and is a measure of how much the bending behavior deviates from classical Cauchy elasticity. For a micropolar beam in pure cylindrical bending, the maximum stress magnitude is [7]

$$\sigma_e = \frac{1}{1+\phi}\frac{M}{W}, \tag{1}$$

with

$$\phi = \frac{24(1-\nu)l_b^2}{h^2}, \tag{2}$$

where ν is Poisson's ratio, h is height of beam, M is bending moment, W is resistance moment and l_b is the characteristic bending length.

3. Discussion

The Gauthier's pure-bending test remains attractive to researchers to present day (e.g. [5, 6, 7]). All of the quoted works regarded this effect as being impossible in Cosserat's theory, as it took some of the material parameters outside of the range necessary for stable material behavior, according to an established methodology for characterization of material instability.

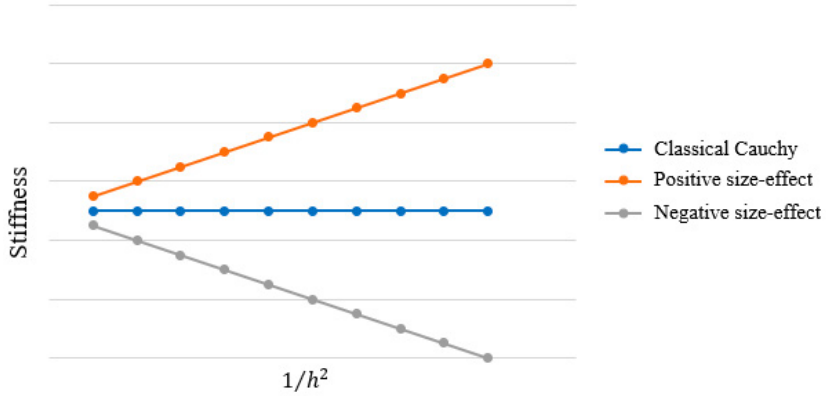

Figure 1: Schematic representation of positive and negative size effect compared to classical behavior of materials with respect to sample height h.

In this work, we will attempt to provide an explanation that the inverse size effect can still be described by Cosserat continuum theory. The analysis will focus on the strain energy accumulated over the entire sample, rather than the strain-energy density at a material point. In this way, we aim to show that the values of material parameters, which may produce negative strain energy at a material point (and are therefore considered invalid), do not necessarily do so at the global level. Consequently, a new definition of legitimate material parameter values may be possible.

Acknowledgments

This research has received funding from the Croatian Science Foundation through the project *Analytical, Numerical and Experimental Methods for Identification of Cosserats' Parameters of Materials.* (HRZZ-IP-2024-05-9904)

References

[1] W. Nowacki. *Theory of micropolar elasticity*, Springer-Verlag, Vienna, 1972.

[2] R.S. Lakes. *Size effects and micromechanics of a porous solid*, Journal of Materials Science, 18 (1983) 2572-2580

[3] E. Cosserat, F. Cosserat. *Theorie des corps deformables*, Herman, Paris, 1909.

[4] R. Gauthier, W.E. Jahsman. *A Quest for Micropolar Elastic Constants*, Journal of Applied Mechanics, 42 (1975) 369-374

[5] D. Bigoni, W.J. Drugan. *Analitical derivation of Cosserat moduli via homogenization of heterogeneous elastic materials*, Trans. ASME J.Appl. Mech., 74 (2007) 741-753

[6] Z. He, H. Zhu, X. Wang, S. Ma. *Experimental investigation on scale effect of mechanical properties of heterogeneous micropolar medium materials*, Composite Structures, 251 (2020) 112667

[7] R. Lakes, W.J. Drugan. *Bending of a Cosserat elastic bar of square cross section - theory and experiment*, Journal of Applied Mechanics, 82 (2015) 091002

[8] E. Papa Dukić, L. Grbac, G. Jelenić. *Characteristic bending length in micropolar materials with periodic internal structure*, Journal of Mechanics of Materials and Structures, 19 (2024) 515-530

ECCOMAS Thematic Conference and IACM Special Interest Conference
Highly Flexible Slender Structures (HFSS 2025)
22–26 September 2025, Kaiserslautern, Germany

The Normal Skeleton

Eugene L. Starostin [1,2], Victor G. A. Goss [1]

[1] School of Engineering, London South Bank University, 103 Borough Rd, London SE1 0AA, UK, staroste@lsbu.ac.uk; gossga@lsbu.ac.uk
[2] Department of Civil, Environmental and Geomatic Engineering, University College London, Gower St, London WC1E 6BT, UK, e.starostin@ucl.ac.uk

Keywords: Skeletonisation, Medial Axis Transform, Normal Axis Transform

1. Introduction

Mechanical studies of slender objects such as animal whiskers, insect antennae, claws, plant stems or other natural structures, are best conducted using accurate geometric descriptions compatible with mechanical models. That is especially important for analysis of large deformations. The widely used mechanics models, e.g. the Kirchhoff elastic rod, rely on defining a centreline that serves as a neutral axis. However, the most common approach in computer graphics and vision, the medial axis transform (MAT) [1], fails to meet mechanical requirements. We introduce the *normal skeleton transform* (NAT), a novel method that defines a centreline passing through the mid-points of orthogonal cross-sections of an object. This orthogonality condition, expressed as a non-holonomic constraint, allows NAT to be consistent with standard engineering models like the Euler-Bernoulli beam and Cosserat rod theories. NAT also provides a more intuitive and computationally efficient representation of an object's shape. This makes NAT particularly useful for studying the mechanics of objects that undergo large deformations, such as slender biological structures.

2. Methodology

The normal skeleton is defined as the locus of midpoints of chords orthogonal to the centreline (Fig. 1,*left*). Given two boundary curves $\boldsymbol{r}_{\pm}(s_{\pm})$ represented by their Whewell equations, the tangential angle $\theta(s)$ of the centreline $\boldsymbol{r}(s)$, and the width function $w(s)$ are found from a system of ordinary differential equations

$$\begin{aligned} w'(s)\sin(\theta_+(s_+(s))-\theta_-(s_-(s))) &= -2\sin(\theta_-(s_-(s))-\theta(s))\sin(\theta_+(s_+(s))-\theta(s)),\\ (1+w(s)\theta'(s))\sin(\theta_+(s_+(s))-\theta_-(s_-(s))) &= 2\cos(\theta_-(s_-(s))-\theta(s))\sin(\theta_+(s_+(s))-\theta(s)),\\ s'_{\pm}(s)\sin(\theta_+(s_+(s))-\theta_-(s_-(s))) &= \pm 2\sin(\theta(s)-\theta_{\mp}(s_{\mp}(s))). \end{aligned}$$

The NAT possesses the property of flexure invariance: the area of the domain remains constant under pure bending of the centreline, consistent with standard engineering rod and beam models (Fig. 1,*right*).

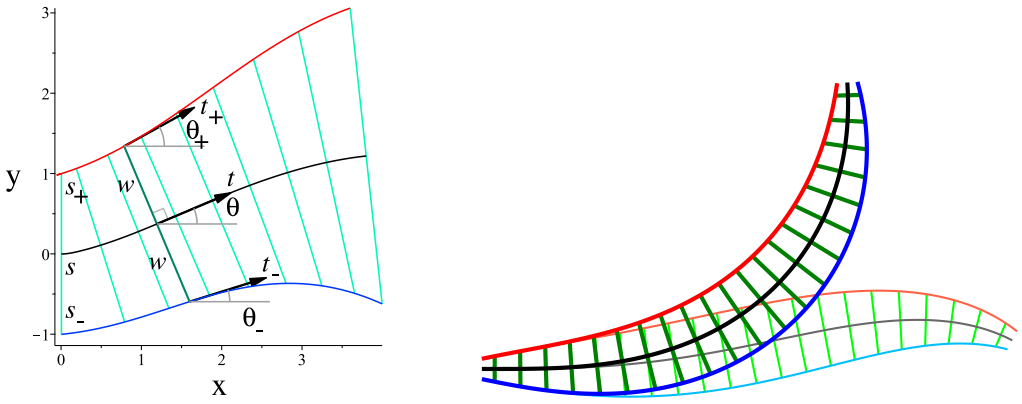

Figure 1: The NAT. *Left:* Two bounding curves (red and blue) define the slender shape. The centreline (black) passes through the mid-points of orthogonal cross-sections (green) of length $2w(s)$, $\boldsymbol{t}(s)$ is the tangent vector, $s, s_{\pm}$ are the arclengths along the axis and boundaries, resp. *Right:* A slender object before (bold) and after deformation, involving pure bending, i.e. the centreline is inextensible and cross-sections remain orthogonal and of same width.

3. Example

We first applied the normal skeleton technique to describe mammal whiskers, in particular those having undulating shapes characteristic for some species of pinnipeds [4]. We also computed normal skeletons of plant prickles and here we present an example of a normal skeleton of an animal's claw. We analysed a lateral image of the unpreserved fifth digit left forepaw claw of a domesticated adult female cat (*Felis catus*) (Fig. 2f of [2]). By employing standard image processing tools we extracted a contour subdivided into the leading and trailing edges. The normal skeleton was computed by numerical integration of the NAT equations from the tip to the base (Fig. 2). The log-log graph of the half-width as a function of centreline arclength deviates significantly from linearity. This is interesting to compare with the linear log-log curve for the average radius of the orthogonal cross-section that was found for the claws of two other species (dinosaur and bear) [3].

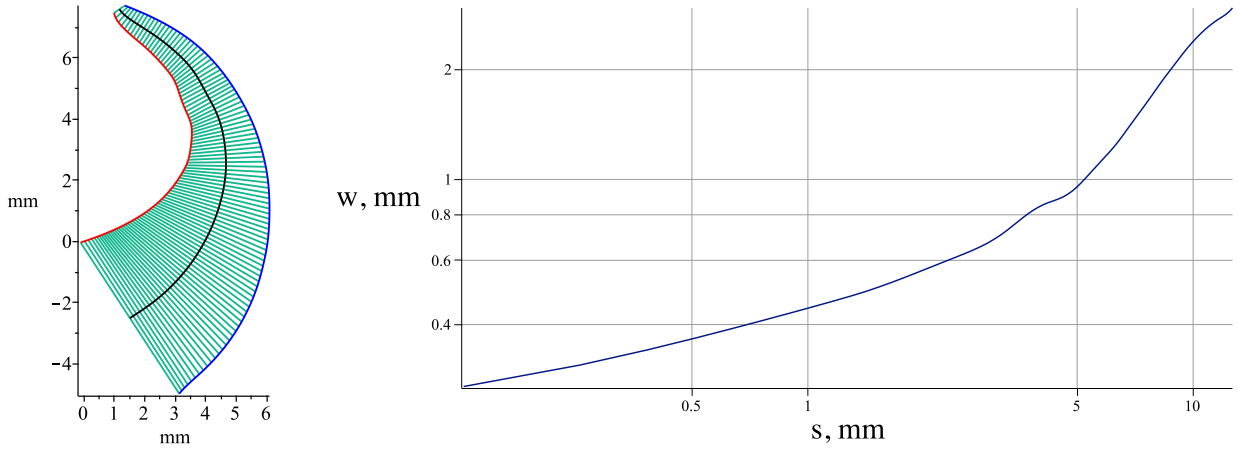

Figure 2: A cat's claw (see Fig. 2f of [2]). *Left:* Normal centreline (black), edges (red and blue), normal cross-sections (green). *Right:* The half-width w as a function of the arclength s (logarithmic scales).

4. Conclusion

The NAT provides a mechanically consistent framework for analyzing slender objects. One key advantage of NAT is its well-defined and easily understood definition of width, which is crucial for many applications. For example, in the study of elastomeric and metal foams, researchers often model the ligaments as 1D beams. However, defining the thickness of these beams is challenging, and traditional methods like MAT tend to overestimate thickness. NAT provides a more accurate definition of thickness, which is essential for reliable mechanical simulations. In biomechanics, NAT can be used to study trabecular bone and cartilage thickness, where accurate measurements are critical. NAT is well-suited for finite element modelling: it allows for natural mesh generation with gridlines orthogonal to the axis. This makes NAT an efficient tool for both shape description and mechanical analysis. Additionally, the normal skeleton accurately models growth kinematics by treating the centreline as a growth timeline. The NAT approach can be generalised to shapes in 3D space.

References

[1] H. Blum. *A transformation for extracting new descriptors of shape*. In W. Dunn, editor, *Models for the Perception of Speech and Visual Form*, volume 4 of *Proceedings of Meeting held Nov. 1964*, MIT Press, Cambridge, 1967, 362–380.

[2] D. G. Homberger et al. *The structure of the cornified claw sheath in the domesticated cat (Felis catus): implications for the claw-shedding mechanism and the evolution of cornified digital end organs.* Journal of Anatomy, **214** (2009) 620–643.

[3] A. R. Evans et al. *A universal power law for modelling the growth and form of teeth, claws, horns, thorns, beaks, and shells.* BMC Biology, **19** (2021) 1–14.

[4] E. L. Starostin et al. *Morphological peculiarities of a harbour seal (Phoca vitulina) whisker revealed by normal skeletonisation.* Bioinspiration & Biomimetics, **17** (2022) 034001.

ECCOMAS Thematic Conference and IACM Special Interest Conference
Highly Flexible Slender Structures (HFSS 2025)
22–26 September 2025, Kaiserslautern, Germany

Hysteretic Bending Response of Slack Metallic Cables

Stefano Corazza[1], Francesco Foti[1], Luca Martinelli[1]

[1]Department of Civil and Environmental Engineering, Politecnico di Milano
stefano.corazza@polimi.it, francesco.foti@polimi.it, luca.martinelli@polimi.it

Keywords: Slack cables, Hysteretic bending behavior, Bouc-Wen model

1. Introduction

Short and slack stranded metallic cables are encountered in several technical applications to connect different structures or different parts of the same structural system. A relevant example is provided by passive damping devices installed on overhead electrical lines, such as Bretelle dampers. Bending behavior of metallic cables is nonlinear and non-holonomic due to the onset and propagation of relative sliding phenomena between the wires. While taut suspended cables have been widely studied in the literature under the classic assumptions of small sag and perfect flexibility, whenever dealing with short and slack cables, the aforementioned hypotheses typically cease to be valid, and the bending stiffness contribution plays a significative role in the determination of the overall structural response. The present work reviews two different modeling strategies for the description of the bending behavior of short and slack stranded cables which have already been presented in [1].
The first (Discrete Bending Model) describes the cable as a composite structural element made of wires, which are individually modeled as curved elastic thin rods interacting through normal and tangential contact forces. The second (Phenomenological Bending Model), instead, relies on a description of the cable bending process based on the well-known Bouc-Wen hysteresis model. Differently than currently available methods to address the bending behavior of taut cables, both modeling approaches herein presented explicitly account for the effect of residual clenching forces induced by manufacturing process. It is indeed shown that these clenching forces control the hysteretic bending behavior of slack cables.

2. Bending behavior of Slack Cables

Whenever a conductor is bent, interactions among adjacent wires occur at internal contact surfaces. Here friction forces tend to contrast relative movement of internal wires, so that transmission of tangential stresses between wires can take place. Under the full-stick kinematic condition the wires are ideally welded together, such that any relative displacement among them is prevented. This condition is associated to a maximum theoretical bending stiffness EI_{max}. When the forces which tend to activate the sliding are greater than the frictional ones, then, a wire can undergo to relative displacement with respect to the neighbors. This process can proceed up to the situation for which all the wires are in the so called full-slip condition, which is associated to a minimum theoretical bending stiffness EI_{min}. The nonlinear transition between the full-stick (small curvatures) and the full-slip (large curvatures) branches of the moment-curvature relation is controlled, for a slack cable, by the value of: (a) the residual normal contact forces induced by the manufacturing process; and (b) the friction coefficient between adjacent wires. In this work, the contact forces induced by the manufacturing process are explicitly accounted for basing on the empirical equation proposed by Rawlins ([2]).

A first strategy to describe the nonlinear bending moment $M(\chi)$ relies on the preliminary evaluation of the axial force induced in each wire by the bending of the cable. This approach will be denoted as Discrete Bending Model (DBM) since the overall response of the cable is obtained by summing up the contribution of each component wire. Basing on the formulation reported in [1], the axial force in each wire of a cable cross section can be numerically evaluated within the framework of an incremental structural analysis, by exploiting a closed-form definition of the wire axial force limit domain:

$$\min(F_{w1}^{lim,+}, F_{w1}^{lim,-}) \leq F_{w1} \leq \max(F_{w1}^{lim,+}, F_{w1}^{lim,-}), \quad \forall \theta \in [0, 2\pi] \tag{1}$$

where $F_{w1}^{lim,\pm}$ are two limit functions which can be expressed in closed-form as well.

The bending moment-curvature ($M - \chi$) law of the cable can be also regarded, in quite general terms, as the input-output relation of a one-dimensional nonlinear hysteretic system. To this aim, a slightly modified

version of the Bouc-Wen model is herein adopted [1] and will be denoted in the following as Phenomenological Bending Model (PBM). This model is computationally cheaper than the DBM and naturally lands itself to experimental calibration of the model parameters (namely EI_{max}, EI_{min} and the transition curvature χ_0, which controls the shape of the hysteresis cycle), without requiring a detailed a-priori knowledge of the mechanical and geometrical properties of the cable cross section.

3. Application Example

In this section, the results of cyclic quasi-static four-point bending test obtained for the All Aluminium Conductor (AAC) Aster 570 are considered (see [3]). The radial contact forces were assumed to be entirely due to the residual stresses of the manufacturing process. Both the DBM and the PBM were applied by considering first a set of "nominal" parameters calculated basing on the sole knowledge of geometrical and mechanical properties of the wires. A back analysis on the model parameters has also been carried out, both for the DBM and the PBM, by solving the nonlinear constrained optimization problem which minimizes the quadratic norm of the distance between the experimentally measured points and the corresponding ones predicted by the proposed bending model (DBM or PBM). The calculated cyclic moment-curvature diagrams are reported in Fig. 1.

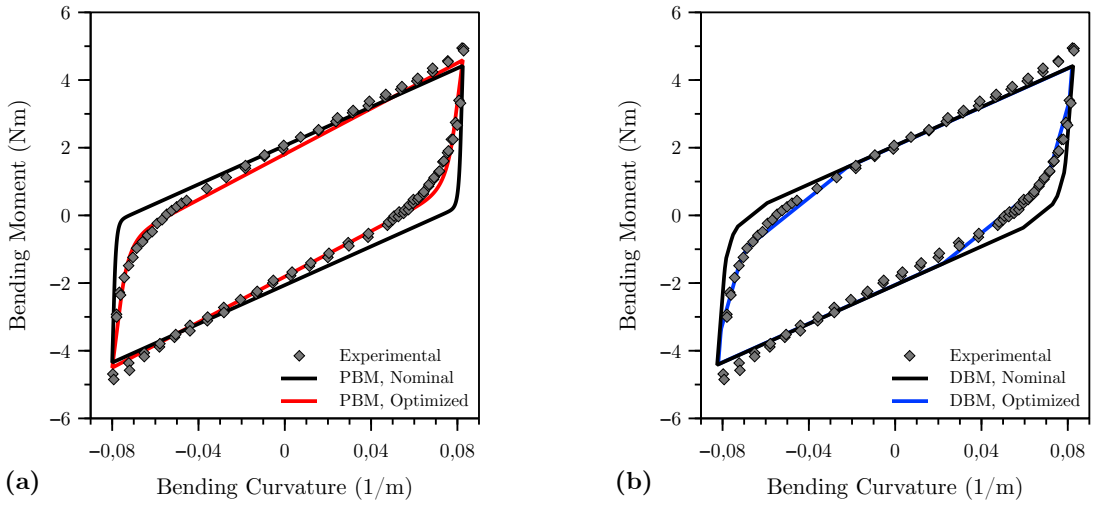

Figure 1: Comparison of the experimental results (see [3]) and the numerical predictions obtained with the PBM (a) and the DBM (b) for both sets of "nominal" and optimized parameters.

4. Conclusions

Differently that most currently available model of the literature, both proposed models allow to explicitly account for the residual stresses induced by the manufacturing processes, which through the normal contact forces between the wires are responsible for the peculiar hysteretic bending behavior of slack cables. The obtained results highlight that both the DBM and the PBM are able to predict the real bending response of short and slack cables, and that the "nominal" values of the parameters allow to obtain a sufficiently precise response for many practical engineering applications.

References

[1] S. Corazza, F. Foti, and L. Martinelli. On the hysteretic bending behavior of slack metallic cables. *Applied Mathematical Modelling*, 139 (115848):23 pp, March 2025.

[2] C.B. Rawlins. *Analytical elements of overhead conductors fabrication*. Fultus Corporation, 2005.

[3] S. Zamanian, S. Langlois, A. Loignon, A.T. Savadkhooi, and Francois M.L.M. Modelling the flexural hysteresis behaviour of bretelle dampers based on a quasi-static bending test. *IEEE Transactions on Power Delivery*, 38:4081–4089, 2023.

ECCOMAS Thematic Conference and IACM Special Interest Conference
Highly Flexible Slender Structures (HFSS 2025)
22–26 September 2025, Kaiserslautern, Germany

Coupled Loading of Cable-like Structures

Muhannad Hawwash [1], Vanessa Dörlich [1], Fabio Schneider-Jung[1], Joachim Linn[1]

[1] Fraunhofer Institute for Industrial Mathematics ITWM, [muhannad.hawwash, vanessa.doerlich, fabio.julian.schneider-jung, joachim.linn]@itwm.fraunhofer.de

Keywords: Cable structures, Coupled loading, Constitutive modeling, Experiments, Finite beam elements

1. Introduction

Cable and cable bundle structures are essential components of automotive applications, providing significant functionality for electrical systems and communication networks. Depending on the specific application, they vary from single conductors to cable bundles, with infinite variants. Such structures often experience coupled loading conditions combining bending and torsion in applications, which define their three-dimensional shape. Thus, understanding the deformation characteristics of cable-like structures under coupled loads is essential e.g. in automotive wiring harness design.
In the work of Dörlich et al. [1], cyclic uncoupled bending and torsion experiments are performed on simple cable specimens. The results show that the effective mechanical response is usually strongly non-linear and inelastic with pronounced hysteresis in bending. Hildebrandt et al. [2] perform free bending experiments coupled with torsion on flexible slender structures. This includes first bending experiments on a coaxial cable under pre-torsion. The authors compared the observed behavior to results from Finite Element (FE) simulations using higher-order finite elements with an anisotropic elastoplastic material model and found good agreement.
This work aims at a deeper understanding of bending-torsion coupling of cable-like structures from single cables to cable bundles depending on the specific structural effects. Therefore, experiments on different types of flexible slender structures ranging in complexity from single wires to multi-wire strands will be performed. The interpretation of experimental results on multi-wire strands will be accompanied by FE simulations based on a previously presented modeling approach for twisted wire strands [3, 4] which has already been successfully validated in comparison with experimental results from bending and torsion of unshielded twisted cable pairs in [5].

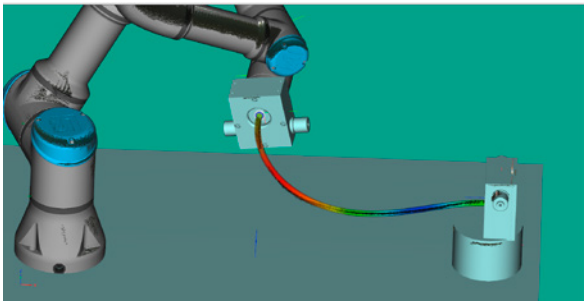

Figure 1: Experimental setup using buckling arm robot to imply coupled load sequences on clamped cable specimens.

2. Coupling Experiments on Cable-Like Structures

In this work, we use an experimental setup which incorporates a buckling arm robot with six degrees of freedom (UNIVERSAL ROBOTS, type UR3e) as actuator, see Figure 1, to apply combined torsion-bending load sequences. One end of the specimen is clamped on the tool tip of the robot. The second end of the specimen is mounted on a six-axis sensor which enables the measurement of all six sectional quantities acting on the end of the specimen. We investigate the influence of torsional loads on the resulting bending behavior by applying pre-torsion in the first load step followed by bending in the second load step. Torsion is applied by rotating the movable specimen end around the global x-axis. Pure bending kinematics are applied by prescribing a trajectory for the tool tip of the robot such that the specimen is bent around the global z-axis as shown in Figure 2. In Figure 2 right, the simulated deformations of a seven-wire strand undergoing torsion and bending is shown as

an example. A series of measurements for different states of pre-torsion allows the investigation of the influence of torsion on the bending characteristics.

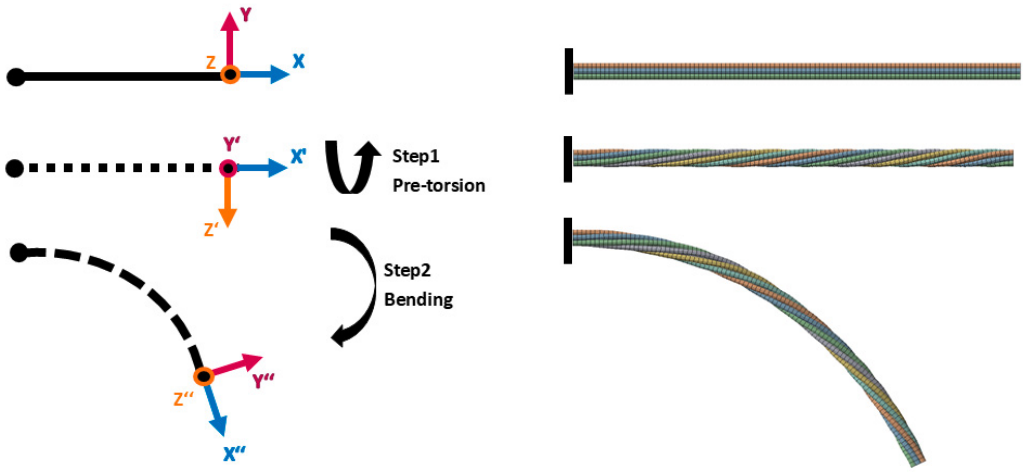

Figure 2: Left: Boundary conditions of bending with pre-torsion of a flexible, slender structure. Right: FE modeling of seven parallel wires

Acknowledgments

This work was supported within the Fraunhofer and DFG transfer programme.

References

[1] V. Dörlich, J. Linn, S. Diebels. Flexible beam-like structures - experimental investigation and modeling of cables. In: Advances in Mechanics of Materials and Structural Analysis, pp. 27 - 46, Springer, 2018.

[2] A. Hildebrandt, P. Sharma, A. Düster, S. Diebels. Experimental and numerical investigation of the deformation behaviour of cables and thin beam-like structures under multi-axial loading. Mathematics and mechanics of solids 27.10, pp. 2314-2337, 2022.

[3] M. Hawwash, V. Dörlich, J. Linn, R. Müller and R. Keller. Effective Inelastic Bending Behavior of Multi-Wire Cables Using Finite Elements Accounting for Wire Contact. In ECCOMAS Thematic Conference on Multibody Dynamics, pp. 369 – 379, Budapest, 2021.

[4] M. Hawwash, V. Dörlich, J. Linn, R. Keller and R. Müller. Modeling the Effective Inelastic Behavior of Multi-Wire Cables Under Mechanical Load Using Finite Elements. In European Congress on Computational Methods in Applied Sciences and Engineering, 2022.

[5] M. Hawwash, V. Dörlich and J. Linn. Bending and Torsion of Twisted Cable Strands Accounting for the Effect of Friction. In ECCOMAS Thematic Conference on Multibody Dynamics, Lisbon, 2023.

ECCOMAS Thematic Conference and IACM Special Interest Conference
Highly Flexible Slender Structures (HFSS 2025)
22–26 September 2025, Kaiserslautern, Germany

Deformation Effects in Pressurized, Fiber-Reinforced and Preformed Hoses: From 3D Continuum Simulations to Experiments

Quirin Hoesch [1,2], Michael Roller [1], Fabio Schneider-Jung [1], Joachim Linn [1], Ralf Müller [2]

[1] Fraunhofer Institute for Industrial Mathematics ITWM, [quirin.hoesch, michael.roller, fabio.julian.schneider-jung, joachim.linn]@itwm.fraunhofer.de
[2] Technical University of Darmstadt, ralf.mueller@mechanik.tu-darmstadt.de

Keywords: Flexible hose, Experiments, Fiber orientation, Torus, Internal pressure

1. Introduction

Hoses are essential components in various industrial sectors, including automotive, heavy machinery, aerospace, and maritime applications. Unlike rigid pipes, hoses offer flexibility, allowing them to accommodate relative motion between connected components and to adapt fluctuating internal pressure conditions. For optimal space utilization, hoses are often preformed and contain curved sections, which can be geometrically regarded as segments of a torus, see Fig. 1a. They are mainly constructed of fiber-reinforced rubber, so they exhibit anisotropic material behavior. Given their functional importance, it is crucial to understand how geometry and fiber orientation influence the mechanical deformation of a preformed and pressurized hose.

In this work, we explore how pressure influences the hose deformation, highlighting key effects. One such effect is the Bourdon effect, where a curvature-dependent shear force acts outward [1]. In addition, the wrapping angle of the reinforcing fiber changes along the cross-section as a result of the double-curved surface of the torus [2]. Another effect investigated, is the toroidal neutral wrapping angle, which describes an isotensoidal load condition by balancing axial and circumferential stresses. This angle follows the same pattern as the geometrical wrapping angle but differs quantitatively. The extent to which these effects work individually and in combination will be shown. Particular attention is paid to the cross-sectional deformation of the torus, as the closed ring structure causes a complex geometric coupling between axial and radial deformation.

The reinforced hose is modeled with the help of suitable homogenization approaches and highly resolved 3D continuum elements, as these allow us to represent all pressure-dependent effects. Furthermore, a hose test rig was set up (Fig. 1b) to compare and validate our finite element simulation results with experiments, see Fig. 1c. Although the exact material parameters, fiber orientation, and fiber-matrix composition are unknown, we are able to fit them in such a way that they exhibit a deformation behavior equivalent to the experimental samples.

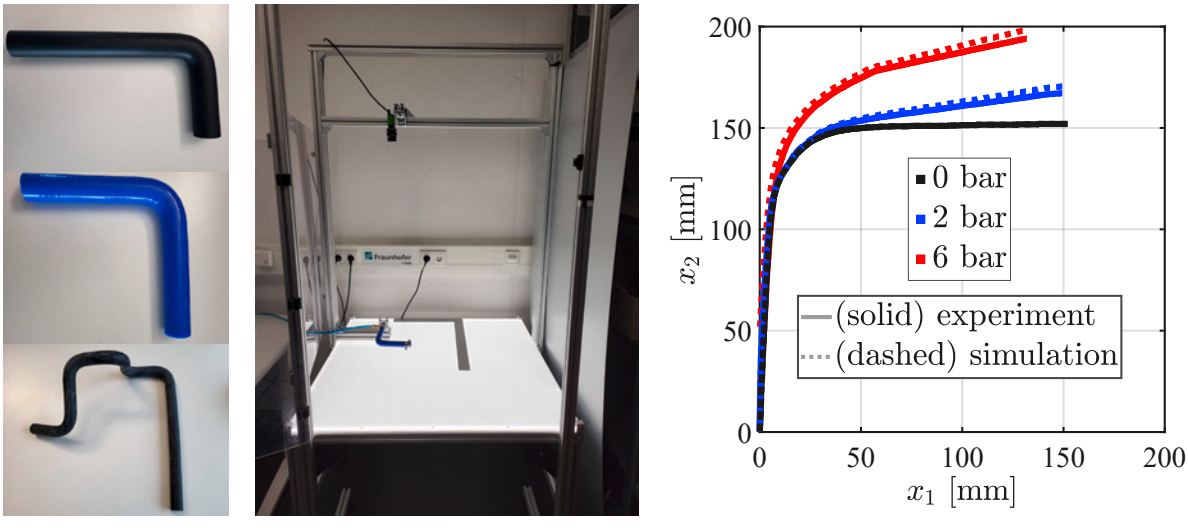

(a) (b) (c)

Figure 1: Preformed hose specimens in (a), experimental setup for detecting the deformed hose state in (b), and comparison between finite element results (dashed lines) and experimental results (solid lines) in (c).

2. Bourdon effect, geometrical and neutral toroidal wrapping angle

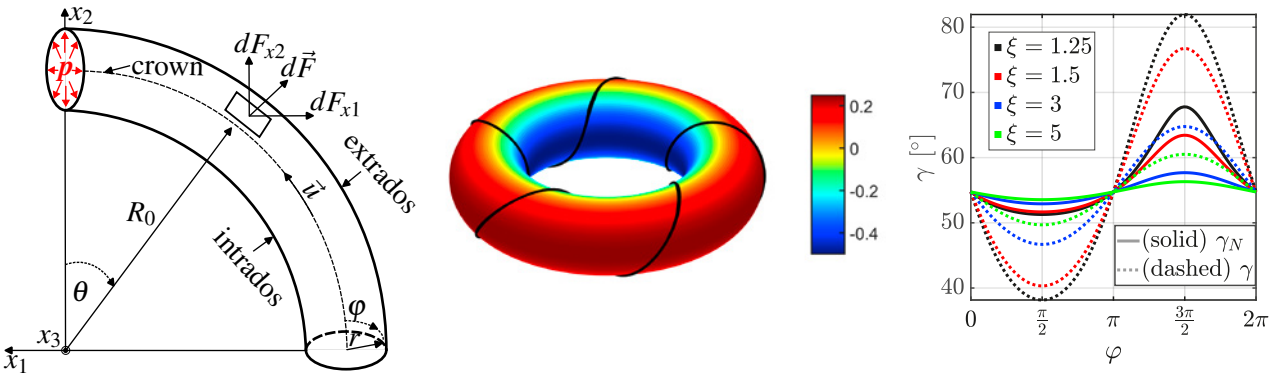

(a) (b) (c)

Figure 2: Outward force on an infinitesimal surface element dA of a pressurized curved hose, illustrating the Bourdon effect in (a), toroidal helix on a double-curved torus in (b), and comparison between the geometrical wrapping angle γ and the neutral wrapping angle γ_N of a torus for different aspect ratios $\xi = \frac{R_0}{r}$ in (c).

Integrating the pressure p over the torus surface element dA gives the Bourdon force components, see Fig. 2a:

$$dA = r(R_0 + r\sin\varphi)d\theta d\varphi, \quad F_{x1} = -\int_{\theta_1}^{\theta_2} p\pi r^2 \sin\theta \, d\theta, \quad F_{x2} = \int_{\theta_1}^{\theta_2} p\pi r^2 \cos\theta \, d\theta. \tag{1}$$

Figure 2b shows a helix on a torus with Gaussian curvature K in color. Due to curvature variation, the toroidal helix's wrapping angle changes along the cross-section φ and is determined by its tangent vector $\vec{t}$ and the torus's neutral fiber $\vec{u}$. The number of turns N characterizes how often the helix wraps around the torus:

$$\cos\gamma = \vec{t}\cdot\vec{u} \quad \rightarrow \quad \gamma = \cos^{-1}\left(\frac{R_0 + r\sin\varphi}{\sqrt{r^2N^2 + (R_0 + r\sin\varphi)^2}}\right). \tag{2}$$

The neutral wrapping angle γ_N of a torus ensures isotensoidal load distribution between the poloidal stress σ_φ and the toroidal stress σ_θ in the fiber. Figure 2c illustrates the distinction between γ and γ_N:

$$\frac{\sigma_\varphi}{\sigma_\theta} = \frac{2R_0 + r\sin\varphi}{R_0 + r\sin\varphi} = \frac{\sin^2(\gamma_N)}{\cos^2(\gamma_N)} = \tan^2(\gamma_N) \quad \rightarrow \quad \gamma_N = \tan^{-1}\left(\sqrt{\frac{2\xi + \sin\varphi}{\xi + \sin\varphi}}\right) \tag{3}$$

3. Experimental setup

The preformed hose specimens (Fig. 1a) are pressurized and tested in the rig (Fig. 1b) for various load steps. Images of the deformed structure are captured with a camera and converted into binary images. The centerline is extracted using skeletonization and interpolated into a spline and compared with the simulation results of the 3D continuum model (Fig. 1c). Furthermore, the radial expansion behavior of the cross-section is analyzed.

4. Conclusions

3D models enable the identification and experimental validation of key effects in preformed, pressurized, and fiber-reinforced hoses. By adjusting the constitutive behavior, fiber orientation, and fiber-matrix composition, these models can be fine-tuned to closely replicate the deformation behavior observed in the experiments.

References

[1] D. Abdulhameed, S. Adeeb, R. Cheng, M. Martens. *The Influence of the Bourdon Effect on Pipe Elbow*, 11th International Pipeline Conference, 2016.

[2] Q. Hoesch, M. Roller, F. Schneider-Jung, J. Linn, R. Müller. *Modeling of fiber-reinforced, pressurised and preformed hoses*, 9th ECCOMAS Congress, 2024.

ECCOMAS Thematic Conference and IACM Special Interest Conference
Highly Flexible Slender Structures (HFSS 2025)
22–26 September 2025, Kaiserslautern, Germany

Prandtl-Ishlinskii operators as inelastic constitutive model in the framework of Cosserat rods for cable simulation

Davide Manfredo [1], Vanessa Dörlich [2], Joachim Linn [2], Martin Arnold [3]

[1] fleXstructures GmbH, Carl-Euler-Str. 8, 67663, Kaiserslautern, Germany, davide.manfredo@flexstructures.de
[2] Fraunhofer ITWM, Fraunhofer-Platz 1, 67663, Kaiserslautern, Germany, [vanessa.doerlich, joachim.linn]@itwm.fraunhofer.de
[3] Institute of Mathematics, Martin Luther University Halle-Wittenberg, Theodor-Lieser-Str. 5, 06120 Halle (Saale), Germany, martin.arnold@mathematik.uni-halle.de

Keywords: Cosserat rods, Inelastic constitutive behaviour, Hysteresis operators, Plane bending experiments

1. Introduction

Electric cables are complex objects due to their multi-material composition and geometric properties. As a result, various internal interaction effects arise, leading to an observed effective inelastic deformation behavior. Cyclic bending experiments exhibit open hysteresis loops, with a noticeable difference between the first loading cycle and the subsequent ones. In this context, the mathematical theory of hysteresis provides an appropriate framework to model and describe such complex phenomena [1]. In this contribution, we present a procedure to incorporate an inelastic constitutive law–formulated in terms of a suitable hysteresis operator–into a 2D Cosserat rod model to perform quasi-static simulations.

2. The Prandtl-Ishlinskii (P-I) operator

As shown in [2], hysteresis operators are a well-studied subject with a wide range of applications. The P-I operator $\mathscr{P}$ plays a significant role in modeling the input-output relationship in systems exhibiting hysteretic behavior. It can be expressed as a superposition of elementary stop operators $\mathscr{S}_r$, weighted by a suitable function $\omega(r)$, which is assumed to vanish for large values of r. In this contribution, we assume the bending moment–curvature (M-K) relationship in terms of the P-I operator, as a discretized version of

$$M(t) = \mathscr{P}[K](t) = \int_0^{+\infty} \omega(r)\mathscr{S}_r[K](t)\mathrm{d}r. \tag{1}$$

The stop operator $\mathscr{S}_r$ can be defined recursively. For a detailed analysis, we refer the reader to [2]. By superimposing multiple elementary stop operators, one can model more complex hysteretic effects that account for the history of the process, as well as plasticity phenomena.

3. Continuous and discrete 2D Cosserat rod model

A 2D Cosserat rod of length L is described by its centerline $[x(s), y(s)]^{\mathrm{T}}$ and its rotation angle $\alpha(s)$, with $s \in [0, L]$. In the continuous case, the bending curvature $K(s)$ and the shear-extensional strain $\mathbf{\Gamma}(s)$ are given by

$$\mathbf{\Gamma}(s) = \mathsf{R}^{\mathrm{T}}(s) \cdot \begin{bmatrix} x'(s) \\ y'(s) \end{bmatrix} - \begin{bmatrix} 1 \\ 0 \end{bmatrix}, \quad K(s) = \alpha'(s), \quad \text{with } \mathsf{R}(s) = \begin{bmatrix} \cos(\alpha(s)) & -\sin(\alpha(s)) \\ \sin(\alpha(s)) & \cos(\alpha(s)) \end{bmatrix}.$$

We assume the bending moment be given by (1), and the two-dimensional forces to be given by a linear elastic constitutive relationship as $\mathbf{F}(s) = \mathbf{C}_{\mathbf{\Gamma}} \cdot \mathbf{\Gamma}(s)$ with $\mathbf{C}_{\mathbf{\Gamma}} = \mathrm{diag}([EA], [GA])$. The parameters $[EA], [GA]$ are respectively the effective tension and shear stiffness. A discrete 2D Cosserat rod model can be derived from the continuous one by considering a staggered grid made of vertices $[x_i, y_i]^{\mathrm{T}}$ for $i = 0, \ldots, N$ and edge-centered rotation matrices $\mathsf{R}(\alpha_{i+\frac{1}{2}})$ for $i = 0, \ldots, N-1$. For further details, see [3].

4. Plane bending simulations of a Cosserat rod with inelastic constitutive law

Simulations are performed by consecutive solutions of the discrete balance equations

$$\begin{cases} \mathbf{f}_{i+\frac{1}{2}} - \mathbf{f}_{i-\frac{1}{2}} = \mathbf{0}, & i = 1,\dots,N-1, \\ (M_i - M_{i-1}) + \left[(x_i - x_{i-1}) f^y_{i-\frac{1}{2}} - (y_i - y_{i-1}) f^x_{i-\frac{1}{2}} \right] = 0, & i = 1,\dots,N, \end{cases}$$

where $\mathbf{f}_{i-\frac{1}{2}} = \mathsf{R}(\alpha_{i-\frac{1}{2}}) \cdot \mathbf{F}_{i-\frac{1}{2}} = \left[f^x_{i-\frac{1}{2}}, f^y_{i-\frac{1}{2}} \right]^{\mathrm{T}}$, given suitable boundary conditions. Results for three different plane bending simulations are shown in Figure 1. In all cases, residual plastic curvature is observed when one of the two cable ends is released after the maximum load step. This deformation arises from the assumption that the bending moment is given by applying the P-I operator to the bending curvature, as expressed in Equation (1).

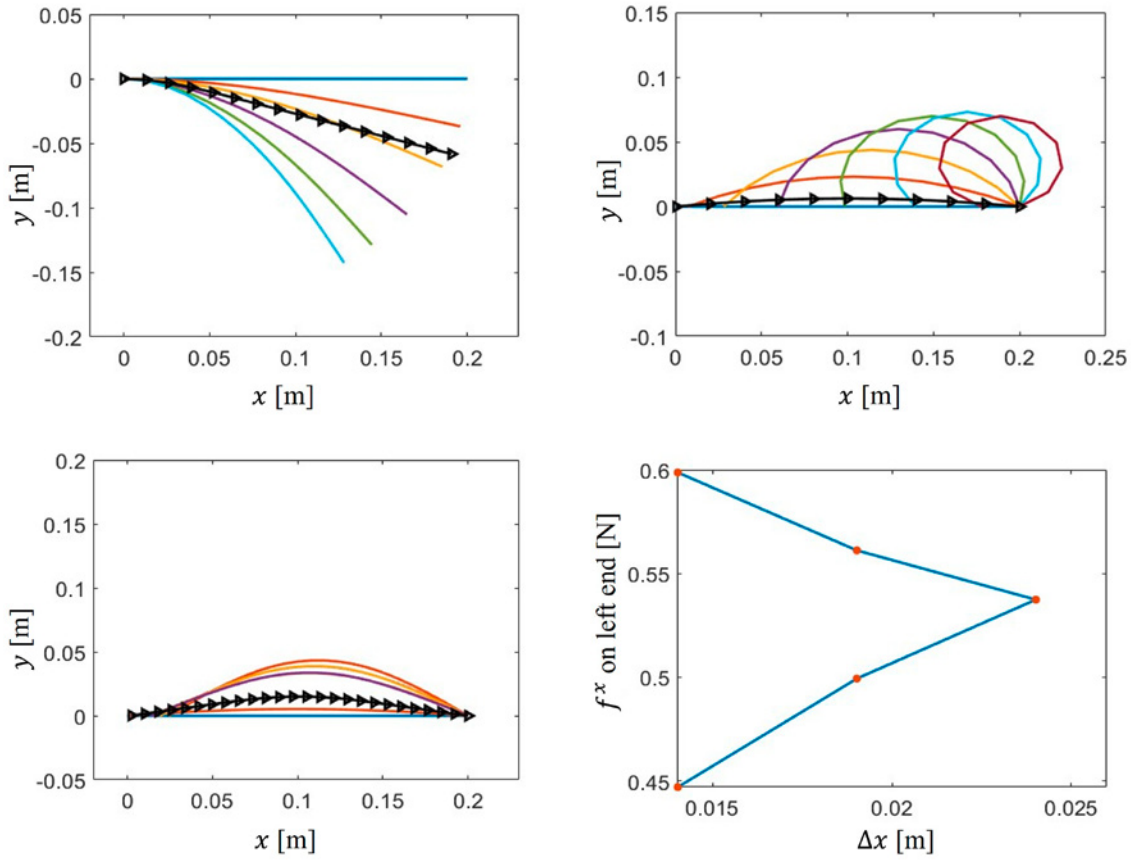

Figure 1: Benchmark simulations for cantilever bending (*top left*), pure bending (*top right*) and MeSOMICS bending [4] (*bottom left*). The black-triangle line shows the plastic deformation when a stress-free state is reached at the end of each benchmark simulation. *Bottom right*: horizontal component of the force for different displacement values of the left end during the MeSOMICS bending.

References

[1] D. Manfredo *et al.*, *Data based constitutive modelling of rate independent inelastic effects in composite cables using Preisach hysteresis operators*, Multibody System Dynamics 62:581-596. - 2024.

[2] M. Brokate, J. Sprekels, *Hysteresis and Phase Transition*, Springer-Verlag, New York, 1996.

[3] T. Zhao *et al.*, *Simulating Nonlinear Elastic Behaviour of Cables Using an Iterative Method*, ECCM, 2022.

[4] www.mesomics.eu

ECCOMAS Thematic Conference and IACM Special Interest Conference
Highly Flexible Slender Structures (HFSS 2025)
22–26 September 2025, Kaiserslautern, Germany

Physics-augmented neural network constitutive models for structural elements

Jasper O. Schommartz [1], Dominik K. Klein [1], Juan C. Alzate Cobo [1], Friedrich Gruttmann [2], Oliver Weeger [1]

[1] Institute Cyber-Physical Simulation, TU Darmstadt, schommartz@cps.tu-darmstadt.de
[2] Institute for Mechanics, TU Darmstadt, gruttmann@mechanik.tu-darmstadt.de

Keywords: Beam, Shell, Physics-augmented neural network, Thermodynamic consistency, FE2

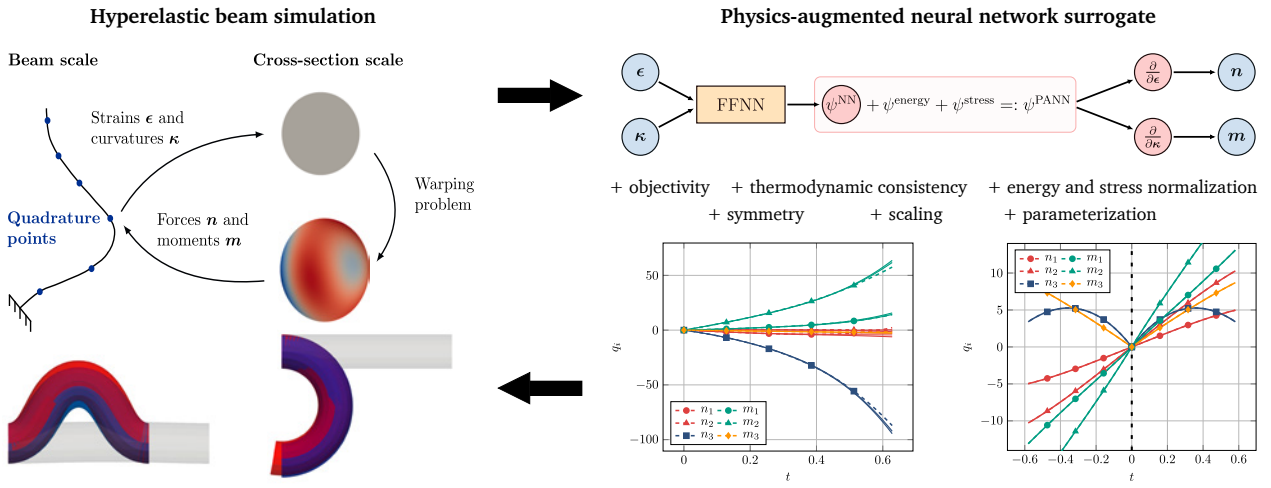

Figure 1: Sequential multiscale beam simulation using physics-augmented neural network constitutive models for geometrically exact Simo-Reissner beams as presented in [5].

1. Introduction

We present physics-augmented neural network (PANN) constitutive models for shear deformable beams and shells. They can be calibrated a priori on beam/shell cross-section data and serve as nonlinear surrogate constitutive models for multiscale structural element simulations.

Geometric and material nonlinearities in thin-walled beams and laminate shell structures necessitate the use of nonlinear constitutive models in terms of the effective strain measures and stress resultants [1, 2]. Analytical constitutive models usually only cover the linear elastic relations between strain measures and stress resultants. Hence, several authors have proposed multiscale or FE^2 models enabling the application of arbitrary 3D continuum constitutive models [2, 3, 4]. These FE^2 models rely on a separation of scales, where the strain measures obtained on the beam/shell scale serve as inputs to a mesoscale FE problem, representing a cross-section or representative volume element (RVE) of the structure. After evaluating the mesoscale FE problem, a homogenization is performed and the effective stress resultants and stiffnesses are passed back to the beam/shell scale for the next iteration. The process is visualized in the top left of Figure 1 for the example of a beam with a deformable hyperelastic cross-section [5].

Although these concurrent multiscale approaches demonstrate high accuracy compared to full-resolution 3D finite element analyses [2, 3], they cause significant costs, both numerically and in implementation. Increased numerical cost arises since every Newton iteration on the beam/shell scale requires at least one Newton iteration on the mesoscale for every quadrature point. This quickly results in drastically increased computational effort and memory usage, undermining the main benefit of using structural elements in the first place.

2. Physics-augmented neural network constitutive models

PANN constitutive models for beams and shells can help close the gap between efficiency and accuracy in multiscale structural element simulations, by moving from concurrent to sequential multiscale simulations. The

models proposed in this work fulfill important mechanical conditions by construction [5]. Strains and curvatures are used as inputs for feed-forward neural networks, which represent the hyperelastic beam potential. Forces, moments, and stiffnesses are received as the first and second gradients of the potential ensuring thermodynamic consistency. The potential is complemented with normalization terms guaranteeing stress and energy normalization. By modifying the inputs to the neural network, additional constraints such as symmetry and scaling are enforced [5]. Lastly, a geometric parameterization is introduced.

For beams, the PANN constitutive models are calibrated to data from circular and ring-shaped deformable hyperelastic cross-sections at varying dimensions. They demonstrate excellent accuracy and generalization. The straightforward applicability of the proposed models is further demonstrated in isogeometric beam simulations [5]. Analogously, the shell constitutive models are calibrated to data generated for hyperelastic laminates according to [2].

3. Conclusion

We presented PANN constitutive models for beams and shells to enable accurate and efficient sequential multiscale simulations for structural elements. Mechanical constraints strictly enforced in the architecture ensure the reliability of the models. Besides their use as surrogate models, the presented constitutive models may also be relevant for other applications, such as automated discovery of constitutive models for cables and effective constitutive modeling using experimental data.

Acknowledgments

The authors acknowledge the financial support by the Deutsche Forschungsgemeinschaft, Germany (DFG, German Research Foundation, project numbers 460684687 and 492770117), the Graduate School of Computational Engineering at TU Darmstadt, and Hessian.AI. Furthermore, D. K. Klein acknowledges support by a fellowship from the German Academic Exchange Service (DAAD).

References

[1] A. Arora, A. Kumar, P. Steinmann. *A computational approach to obtain nonlinearly elastic constitutive relations if special Cosserat rods*, Computer Methods in Applied Mechanics and Engineering, 350 (2019) 295-324

[2] F. Gruttmann, W. Wagner. *A FE2 shell model with periodic boundary conditions for thin and thick shells*, International Journal for Numerical Methods in Engineering, 125 (2024) e7433

[3] L. Herrnböck, A. Kumar, P. Steinmann. *Two-scale off-and online approaches to geometrically exact elastoplastic rods*, Computational Mechanics, 71 (2023) 1-24

[4] S. Klarmann, F. Gruttmann, S. Klinkel. *Homogenization for coupled multiscale analysis of structural elements: beam kinematics*, Computational Mechanics, 65 (2020) 635-661

[5] J. O. Schommartz, D. K. Klein, J. C. Alzate Cobo, O. Weeger. *Physics-augmented neural networks for constitutive modeling of hyperelastic geometrically exact beams*, Computer Methods in Applied Mechanics and Engineering, 435 (2025) 117592

ECCOMAS Thematic Conference and IACM Special Interest Conference
Highly Flexible Slender Structures (HFSS 2025)
22–26 September 2025, Kaiserslautern, Germany

Hybrid Analytical-Numerical Model for Accurate and Efficient Simulation of Adhesive Debonding in Beam-Like Specimens

Leo Škec [1], Damjan Jurković [2], Giulio Alfano [3]

[1] University of Rijeka, Faculty of Civil Engineering, Radmile Matejčić 3, 51000 Rijeka, Croatia, leo.skec@uniri.hr

[2] University of Rijeka, Faculty of Civil Engineering, Radmile Matejčić 3, 51000 Rijeka, Croatia, damjan.jurkovic@gradri.uniri.hr

[3] Department of Mechanical and Aerospace Engineering, Brunel University London, Kingston Lane, Uxbridge UB8 3PH, UK, giulio.alfano@brunel.ac.uk

Keywords: Adhesive Joints, Debonding, Delamination, Cohesive-Zone Model, Analytical Solution

1. Introduction

Adhesively bonded joints are widely used in automotive, aerospace and civil engineering due to their structural and manufacturing advantages. However, their design must account for potential failure by debonding, a critical mode in which the adhesive bond between components is lost. To characterise this behaviour, standard fracture mechanics tests are performed to extract material parameters for design and verification. With the growing reliance on bonded structures in demanding applications, there is a strong need for numerical models that can simulate debonding both accurately and efficiently. Such models support experimental interpretation, design optimisation and virtual testing. In particular, efficient modelling of the fracture process zone and crack growth is essential for reducing computational cost while maintaining predictive capability.

2. Hybrid analytical-numerical model

In this work, we propose a novel hybrid analytical–numerical model for the simulation of adhesive debonding in standard fracture mechanics tests, such as the Double Cantilever Beam (DCB), End-Notch Flexure (ENF) and Mixed-Mode Bending (MMB) configurations. The DCB test (Figure 1(a)) is designed to evaluate Mode I (opening mode) fracture resistance by applying symmetrical tensile loads at the ends of two bonded beams (arms), causing the crack to propagate in pure opening. The ENF test (Figure 1(b)) targets Mode II (sliding mode) failure by applying a three-point bending load to a specimen with a pre-crack located at the interface between the two bonded beams. The MMB test (Figure 1(c)) combines the DCB and ENF setups to produce a controlled mix of Mode I and Mode II loading by applying loads through a lever arm system, allowing investigation of mixed-mode fracture behaviour. In these tests, the region ahead of the crack tip is referred to as the damage process zone (DPZ), where the adhesive undergoes material softening prior to complete failure. The remainder of the specimen (including the fully separated arms and the bonded region that remains undamaged) exhibits linear-elastic behaviour.

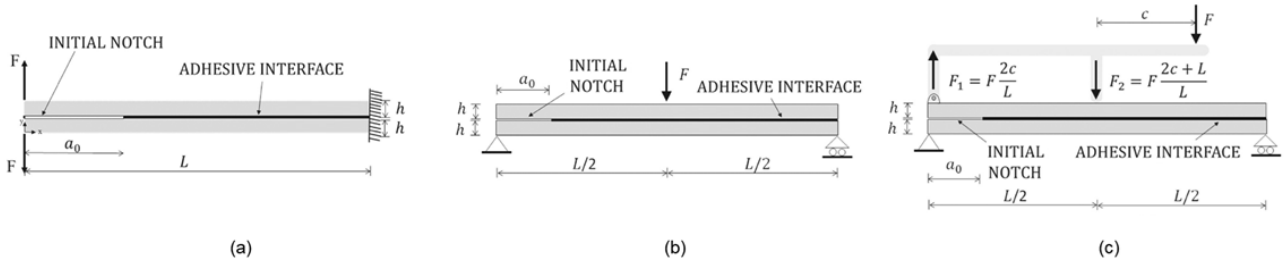

Figure 1: Standard fracture mechanics tests: (a) DCB, (b) ENF and (c) MMB.

The concept behind the hybrid model is to combine exact analytical solutions [1,2], applied to the fully separated and undamaged parts of the specimen, with finite element (FE) solutions in the damage process zone (DPZ) [3]. This approach enables a substantial reduction in the total number of degrees of freedom compared

to conventional fully-meshed FE models, resulting in significantly lower computational cost. The method is applicable not only to bilinear and trilinear (or trapezoidal) traction–separation laws (TSLs), but also to non-linear TSLs, such as exponential or power-law formulations, for which closed-form analytical solutions are not available. For each displacement or time increment, a stack of finite elements is placed in the DPZ and moves with it as the crack propagates, while the remainder of the specimen (whether it consists of an intact interface, a fully debonded interface or an initial crack) is represented analytically.

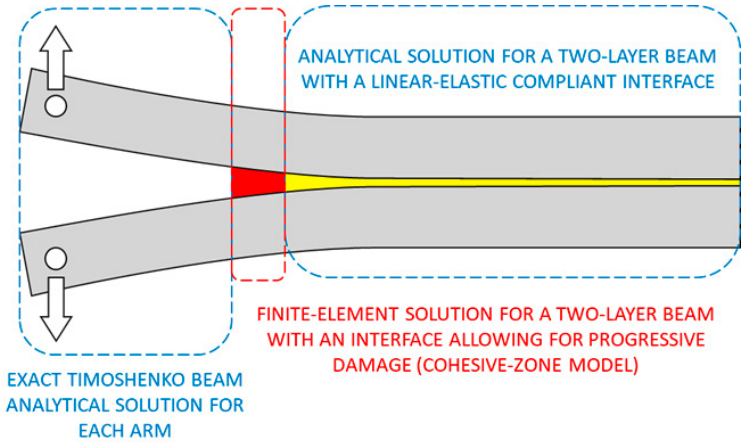

Figure 2: The concept of the hybrid analytical-numerical model.

This hybrid framework is particularly well suited for efficiently simulating the rate-dependent debonding of adhesive joints. In the rate-dependent cohesive zone model (CZM) [4], the adhesive response in compression (which governs most of the undamaged region) is considered rate-independent and can therefore be captured using analytical solutions. Consequently, the FE formulation developed in [4] can be restricted to the narrow zone ahead of the crack tip. The rate-dependent CZM is based on fractional viscoelasticity, which provides a compact yet accurate framework for modelling the rate sensitivity of polymers and elastomers across a broad range of strain rates, using far fewer parameters than classical models based on exponential kernels.

3. Conclusions

The proposed hybrid analytical–numerical model offers an efficient and accurate framework for simulating adhesive debonding in standard fracture mechanics tests. By coupling closed-form analytical solutions in the linear-elastic regions with finite element analysis confined to the damage process zone, the model significantly reduces computational cost while retaining fidelity in the prediction of crack propagation. The approach holds strong potential for integration into design and analysis tools aimed at characterising and optimising the performance of adhesively bonded structures.

References

[1] A.F. Siciliano, L. Škec, G. Jelenić *Closed-form solutions for modelling the rotational stiffness of continuous and discontinuous compliant interfaces in two-layer Timoshenko beams*, Acta Mechanica, 232 (2021), 2793–2824

[2] A.F. Siciliano, L. Škec, G. Jelenić *Closed-form solutions for two-layer Timoshenko beams with interlayer slip, uplift and rotation compliance*, Meccanica, 58 (2023) 893–918

[3] M. Ranjbar M, L Škec, G. Jelenić, D. Ribarić *Mixed-mode delamination of layered structures modeled as Timoshenko beams with linked interpolation*, International Journal for Numerical Methods in Engineering, 124(8) (2023) 1773–1797

[4] L. Škec, G. Alfano, *Experimental and numerical study of rate-dependent mode-I failure of a structural adhesive*, The Journal of Adhesion, 99(8) (2022), 1323–1355

ECCOMAS Thematic Conference and IACM Special Interest Conference
Highly Flexible Slender Structures (HFSS 2025)
22–26 September 2025, Kaiserslautern, Germany

Enhanced constitutive behaviour of cables under bending loads

Martina Stavole [1], Davide Manfredo [2], Tian Zhao [1], Fabio Schneider-Jung [1]

[1] Fraunhofer ITWM, Fraunhofer Platz 1, 67663, Kaiserslautern, Germany
martina.stavole, tian.zhao, fabio.julian.schneider-jung@itwm.fraunhofer.de
[2] fleXstructures GmbH, Carl-Euler-Straße 8, 67663 , Kaiserslauter, Germany
davide.manfredo@flexstructures.de

Keywords: Non-linear Inelastic Constitutive Law, Hysteresis operators, Cable Simulations, Cosserat Rods

1. Introduction

Flexible slender structures are characterised by a complex constitutive mechanical behaviour. Hence, a linear elastic constitutive law is sometimes insufficient to model and simulate complex loading phenomena. This work aims to enhance the constitutive model of 1-dimensional objects for faster and more realistic cable simulation tools relevant for industrial applications. In particular, two aspects are investigated for the simulation of geometrically non-linear rod models undergoing planar bending, i.e., the non-linear elasticity by means of a curvature-dependent bending stiffness and the inelastic effects prescribed by hysteresis operators.

2. Constitutive model for planar bending and simulation strategy

In [1], an algorithmic approach was presented for simulating the non-linear elastic bending behaviour of the 2-dimensional geometrically exact Cosserat rod model (see e.g. [2] for a more complete overview of the Cosserat rods). The simulation strategy consists of solving a linear elastic energy minimisation problem with locally constant algorithmic bending stiffness values until the equilibrium state converges. In this work, a similar energy minimisation problem is solved by taking into account at each iteration, not only the curvature-dependent bending stiffness, but also updates of the plastic curvature. Then, the enhanced bending moment can be defined as,

$$m_b(\kappa_i(\alpha), \kappa_i^H) = \int_{\mathscr{K}_p(\kappa_i(\alpha),\kappa_i^H)}^{\kappa_i(\alpha)} \mathscr{F}_{[EI]}(\xi)d\xi \tag{1}$$

where, $\kappa_i(\alpha)$ is the current curvature, κ_i^H is the curvature history, $\mathscr{K}_p(\kappa_i(\alpha), \kappa_i^H)$ is the plastic curvature, $\mathscr{F}_{[EI]}(\kappa)$ is the curvature-dependent bending stiffness and the index i indicates the spatial discretisation along the centreline of the rod for $i = 0, ..., N$. In [3, 4], hysteresis operators, such as Prandtl-Ishlinskii operators, of stop-type are used to develop an inelastic constitutive law for Cosserat rods. Similarly, $\mathscr{K}_p(\kappa_i(\alpha), \kappa_i^H)$ is a play-type operator, or a superposition of those, used to prescribe the plastic curvature. Such an operator is defined by a threshold r and a weight function $\omega(r)$.

3. Constitutive parameter identification

An inverse problem is formulated for the cable constitutive parameter identification, i.e., for the identification of the bending stiffness values characterising $\mathscr{F}_{[EI]}$ and the weight functions ω characterising $\mathscr{K}_p$. Experimental data can be collected from a bending test.
Figure 1 shows on the left the bending experiments performed with MeSOMICS, see [5], and, on the right, the results of a cyclic bending test in terms of boundary forces f_x measured at imposed displacements. Based on the measured forces, a data fitting problem is solved for a sequence of equilibrium states characterised by a constitutive law as in Equation (1).

4. Conclusions

In some industrial applications, the inelastic effects of cables cannot be neglected, and, consequently, the assumption of linear-elastic behaviour cannot describe the reality. We propose a new approach for identifying and modelling a non-linear inelastic constitutive law for cables by combining two methods available in the literature, i.e., the algorithmic approach for non-linearities and the hysteresis operators for inelasticity. Thanks to those tools, we aim at enabling enhanced cables simulations.

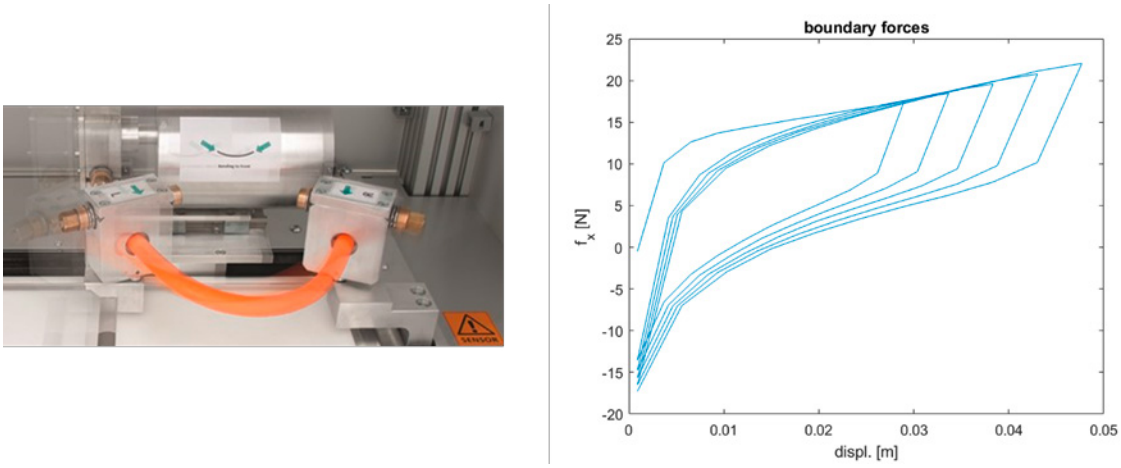

Figure 1: *Left:* Bending experiment performed in MeSOMICS (Measurement System for the Optically Monitored Identification of Cable Stiffnesses). *Right:* Results of a cyclic bending experiment performed in MeSOMICS.

References

[1] T. Zhao, F. Schneider-Jung, J. Linn, R. Müller. *Simulation and parameterization of nonlinear elastic behavior of cables*, Multibody System Dynamics, (2024) 1–20

[2] J. Linn, T. Hermansson, F. Andersson, F. Schneider. *Kinetic aspects of discrete cosserat rods based on the difference geometry of framed curves*, ECCOMAS Thematic Conference on Multibody Dynamics, (2017) 163–176

[3] D. Manfredo, V. Dörlich, J. Linn, M. Arnold. *Data based constitutive modelling of rate independent inelastic effects in composite cables using Preisach hysteresis operators*, Multibody System Dynamics, 62 (2023) 581–596

[4] D. Manfredo, M.A. Saadat, V. Dörlich, J. Linn, D. Durville, M. Arnold. *Modelling the inelastic constitutive behaviour of multi-layer spiral strands: comparison of hysteresis operator approach to rheological model*, Proceedings of Multibody Dynamics 2023 (ECCOMAS Thematic Conference), (2023)

[5] www.mesomics.eu

ECCOMAS Thematic Conference and IACM Special Interest Conference
Highly Flexible Slender Structures (HFSS 2025)
22–26 September 2025, Kaiserslautern, Germany

A Quasi-Static ALE-Frictional Formulation for Soft Robotics Applications

O. Devigne, O. Brüls

University of Liège, Belgium, (o.devigne, o.bruls)@uliege.be

Keywords: ALE, friction, soft robot, cable, augmented Lagrangian formulation

1. Introduction

Cable-driven actuation is widely used in fields such as soft robotics and deployable space structures. Typically, cables are pass through pulleys, sleeves or structural components, resulting in localized regions of permanent contact while the main portion of the cable span remains contact-free. Finite element modeling of these contact zones require a fine mesh, which is computationally inefficient if applied to the entire cable. To address this, an arbitrary Lagrangian-Eulerian (ALE) approach offers an effective alternative. This method is particularly advantageous in sliding contact scenarios, as it allows cable nodes within contact regions to remain stationary relative to the interacting surface while enabling material flow as commonly found in Eulerian formulations. Meanwhile, nodes outside the contact area follow a standard Lagrangian description of the motion. Previous studies have explored ALE-based formulations both in frictionless conditions [1] and with frictional interactions [2].

This work focuses on the quasi-static description of frictional contact between a cable and the inside cavities of soft robots, e.g., used for the manipulation of fragile objects. When the robot deforms, the main contact points will be the entry and exit points of the cable in the robot structure. Those points remain spatially fixed with respect to the robot, motivating the use of an ALE formulation for the cable. The friction description derives from an augmented Lagrangian formulation, avoiding both the need for a regularization of Coulomb's law, as usually done in compliant models, and the *ad hoc* implementation of the stick-slip transition depending on the considered example.

2. Methodology

First, the quasi-static ALE cable model presented in [3] is extended to incorporate a geometrically exact beam formulated on the Lie group $SE(3)$, thereby accounting for curvature and bending stiffness. The spatial configuration of each node is described by a frame $\mathbf{H}(s)$, while the material coordinate is represented by the centerline coordinate s. The ALE equilibrium equations for the beam are derived from the virtual work principle as

$$\delta\mathscr{W} = \delta_{\mathbf{H}}\mathscr{W} + \delta_s\mathscr{W} = 0 \tag{1}$$

where $\mathscr{W}$ denotes the total potential energy, $\delta_{\mathbf{H}}(\bullet)$ represents the variation with respect to the spatial coordinates holding the material coordinate fixed, and $\delta_s(\bullet)$ represents the variation with respect to the material coordinate holding the spatial coordinates fixed.

We assume that the interactions between the cable and the robot are limited to point-to-point contacts at fixed locations on the robot structure. Then, friction is modeled using Coulomb's law. As each contact remains closed, the frictional contact conditions are

$$|v_T| \geq 0, \quad |\lambda_T| \leq \mu\lambda_N, \quad |v_T|\,(|\lambda_T| - \mu\lambda_N) = 0 \tag{2}$$

with the slip rule $|v_T|\lambda_T = -|\lambda_T|v_T$, where v_T is the relative tangential slip between the cable and the other body, while λ_N and λ_T are the Lagrange multipliers associated with the normal and tangential contact forces, respectively. The friction coefficient is denoted by μ. In this model, frictional effects are only considered in the cable longitudinal direction, making v_T and λ_T scalar quantities. Within the ALE formulation, it is important to note that, unlike conventional friction models, both the relative slip v_T and the tangential contact force λ_T contribute to the material equilibrium equations (i.e., those involving the material coordinate s), since the relative spatial positions of the nodes in the contact patch remain fixed.

The final system of equations is solved using an augmented Lagrangian approach combined with an implicit Newton scheme.

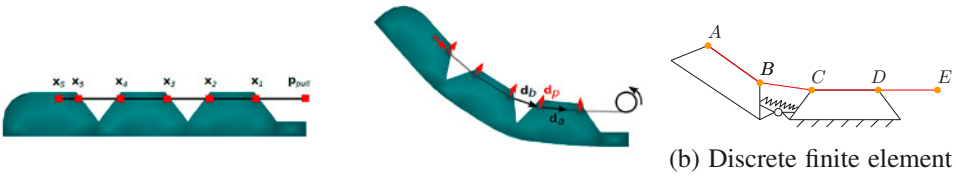

(a) Cable-actuated soft finger [4].

(b) Discrete finite element model.

Figure 1: Continuous and discretized models of the soft finger.

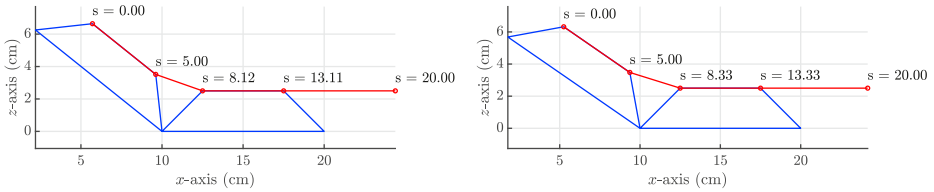

(a) Frictionless case ($\mu = 0$).

(b) With dry friction ($\mu = 0.3$).

Figure 2: Cable-actuated soft finger with and without friction.

3. Soft Finger Model

To illustrate the formulation, a model of a soft finger is proposed, inspired by [4] and studied in the frictionless case in [3], see Fig. 1a. The phalanges are modeled as rigid bodies linked by a flexible joint. The cable is attached to the end phalange at node A, goes through the robot structure, and is pulled from the end node E with a traction force, as shown in Fig. 1b. The first phalange is fixed. The cable is modeled as a beam and is sliding inside the phalange cavities and dry friction is considered at the entry and exit nodes B and C with a Coulomb friction coefficient $\mu = 0.3$. No friction occurs at node D as no normal force acts on the cable at this location.

Numerically, the cable is discretized using 4 beam finite elements and the loading is applied in 1 load step. No-flow boundary conditions are applied at node A and E. Nodes B, C and D are spatially fixed on the phalanges, while the flow of material is permitted through them.

In Fig. 2, the quasi-static solutions for both the frictionless case and the case with friction are shown. The red circles represent the nodes of the cable mesh. A flow of material is observed at nodes C and D, since the cable is pulled. It is shown that when friction is considered, the finger bends less for the same input force, which is of high interest for position control in the context of manipulation. Although not shown in this result, the formulation is also able to capture hysteresis phenomena under cycling loadings.

4. Conclusion

In this work, an ALE cable model with friction is proposed for the modeling of a cable-actuated soft finger. The approach is based on the virtual work principle and dry friction is modeled without any regularization using an augmented Lagrangian approach. This represents a first step for the development of a general framework enabling the frictional quasi-static simulation of general cable-actuated multibody systems.

References

[1] Han, S., Bauchau, O. A. (2023). Configurational forces in variable-length beams for flexible multibody dynamics. Multibody System Dynamics, 58(3), 275-298.

[2] Oborin, E., Vetyukov, Y., Steinbrecher, I. (2018). Eulerian description of non-stationary motion of an idealized belt-pulley system with dry friction. International Journal of Solids and Structures, 147, 40-51.

[3] Devigne, O., Cosimo, A., Brüls, O. (2024). A quasistatic ALE cable formulation for multibody systems applications. Multibody System Dynamics, 1-29.

[4] Coevoet, E., Morales-Bieze, T., Largilliere, F., Zhang, Z., Thieffry, M., Sanz-Lopez, M., ... & Duriez, C. (2017). Software toolkit for modeling, simulation, and control of soft robots. Advanced Robotics, 31(22), 1208-1224.

ECCOMAS Thematic Conference and IACM Special Interest Conference
Highly Flexible Slender Structures (HFSS 2025)
22–26 September 2025, Kaiserslautern, Germany

Simulation of the dynamics of two-motor elevator systems with the arbitrary Lagrangian-Eulerian finite element method considering guide contact

José L. Escalona

[1] Department of Mechanical and Manufacturing Eng. University of Seville, escalona@us.es

Keywords: ALE method, reeving systems, cable-pulley systems, wire ropes, elevator dynamics

1. Introduction

High velocity elevators installed in high buildings are nowadays designed using a twin set of drive motors. To keep symmetry in the power transmission system, that includes a double set of traction ropes, drive and deviation sheaves and traction and compensating wire ropes, besides an accurate velocity control system, the geometric and viscoelastic properties of the elevator must be in perfect balance. This research develops a 2D *arbitrary Lagrangian-Eulerian* (ALE) [1,2] finite element model of the two-motor reeving system to analyse the effect un-symmetries of the two transmission mechanisms on the elevator dynamics. It is shown that the normal contact forces between the shoes of the cabin and the counterweight and the steel guides play a fundamental role.

2. ALE model of the two-motor elevator system

Figure 1 shows two sketches of the model of the system. As it can be observed, the drive motors and drive ropes are at the top of the installation and a different set of wire ropes and deviation sheaves are installed in the lower part to compensate for the mass of the ropes that move from left to right when the cabin moves along the well. This compensation system is essential to keep the motors torque approximately constant in high buildings. To model non-symmetrical effects on the system, the dynamic model must be able to describe transverse displacements and rotation of the different rigid and deformable bodies. The sketch on the right shows an arbitrary position of the system. Although it looks that the cabin (*cab*) and counterweight (*cw*) can displace laterally and rotate freely, they are constrained by the contact forces with the guides, that in this work is modelled using a linear elastic penetration-based contact model.

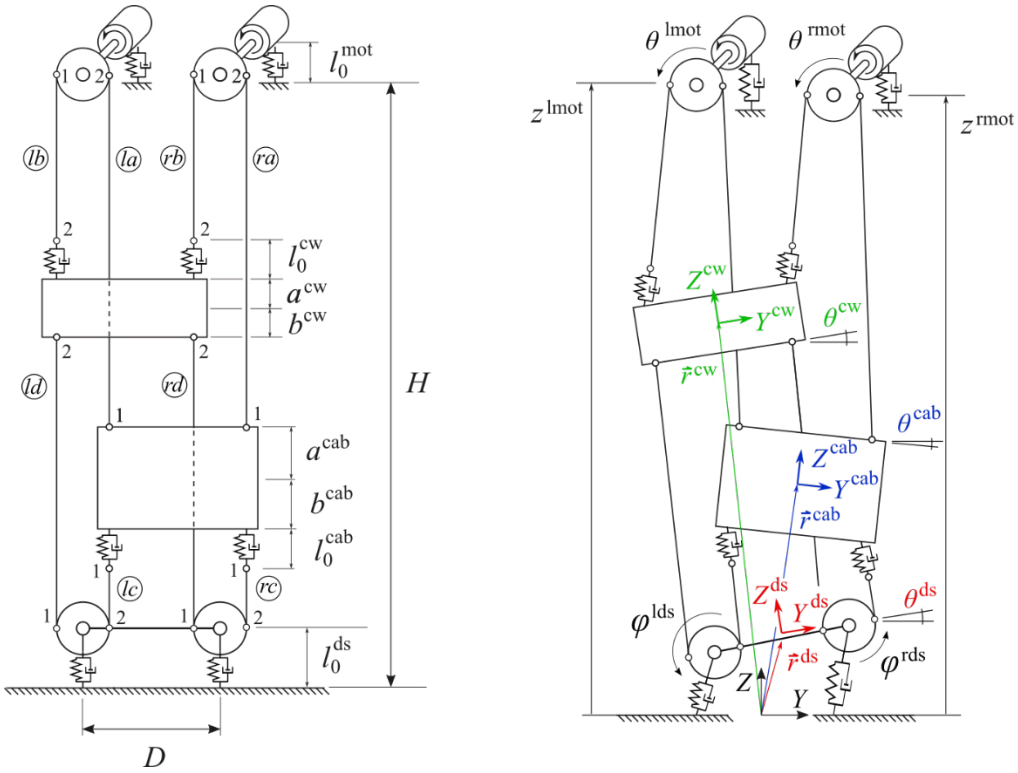

Figure 1. Model of the two-motor elevator system

The model uses a set of coordinates $\mathbf{p}$ that include rigid body coordinates $\mathbf{q}^{RB}$ and wire rope deformation coordinates $\mathbf{q}^{WR}$, as follows:

$$\mathbf{p} = \begin{bmatrix} \mathbf{q}^{RB} \\ \mathbf{q}^{WR} \end{bmatrix}, \quad \mathbf{q}^{RB} = \begin{bmatrix} \mathbf{q}^{cab} \\ \mathbf{q}^{cw} \\ \mathbf{q}^{ds} \\ \mathbf{q}^{lmot} \\ \mathbf{q}^{rmot} \end{bmatrix}, \quad \mathbf{q}^{WR} = \begin{bmatrix} \mathbf{q}^{la} \\ \mathbf{q}^{lb} \\ \mathbf{q}^{lc} \\ \mathbf{q}^{ld} \\ \mathbf{q}^{ra} \\ \mathbf{q}^{rb} \\ \mathbf{q}^{rc} \\ \mathbf{q}^{rd} \end{bmatrix} \tag{1}$$

where the superscripts show the elements that these sets of coordinates kinematically describe. They can be identified with the help of Figure 1. Each wire rope ALE finite element includes 8 nodal coordinates. The total number of generalized coordinates is $n = n_{rb} + n_{wr} = 15 + 64 = 79$. These coordinates are subjected to a set of $m = 56$ linear constraint equations. Therefore, the number of degrees of freedom of the model is $g = n\text{-}m = 23$. Because the constraints are linear, the equation of motion can be written in terms of 23 independent coordinates as a set of second order ordinary differential equations.

3. Results

Three different simulations are performed for a 200-m high elevator. In the first one the two traction systems are assumed as perfectly symmetric. In the second and third simulations it is assumed that the undeformed length of the traction ropes is slightly different, their stiffness is slightly different, and the radius of the two drive sheaves is slightly different. In the second simulation the normal contact forces with the guides are considered, while the third simulation assumes that the cabin and counterweight are free to displace laterally and to rotate. Results show important effect of these un-symmetries in the system dynamics only when the contact with the guides is modeled. Figure 1 shows the axial forces in the traction and compensating ropes on the left-hand side of the system. It can be concluded that the effect of the un-symmetries turns into a very uneven share of the traction force only when the contact forces with the guides are accounted for.

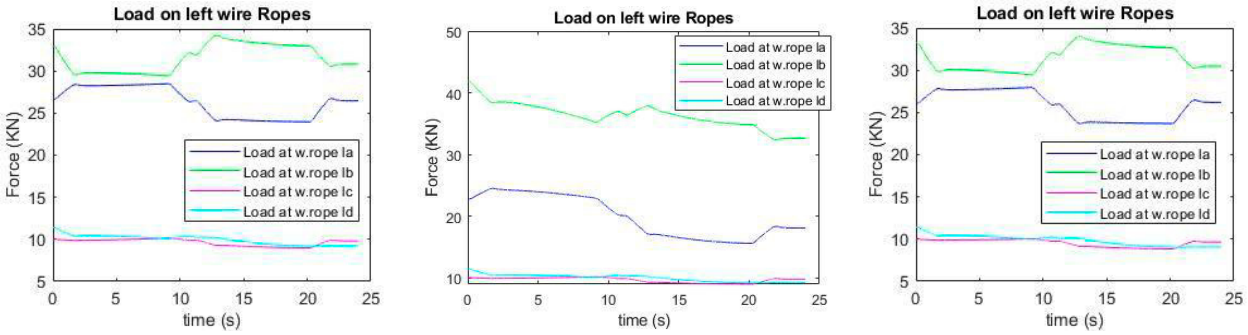

(a) (b) (c)

Figure 2. Axial forces on traction ropes: (a) symmetric system, (b) non-symmetric system with guide contact, (c) non-symmetric system without guide contact

References

[1] Escalona, J.L, Orzechowski, G, Mikkola, A, *Flexible multibody modeling of reeving systems including transverse vibrations*, Multibody System Dynamics, 44(2018) 107-133.

[2] Escalona, J.L, Mohammadi, N, *Advances in the modeling and dynamic simulation of reeving systems using the arbitrary Lagrangian-Eulerian modal method*, Nonlinear Dynamics, 108(2022), 3985-4003.

ECCOMAS Thematic Conference and IACM Special Interest Conference
Highly Flexible Slender Structures (HFSS 2025)
22–26 September 2025, Kaiserslautern, Germany

Beam-to-beam Frictional Contact Formulation with Small Sliding for Overhead Conductors Undergoing Large Rotations

P.-A. Guidault [1], K. Aït Ammar [1,2], P.-A. Boucard [1], J. Said [2], F. Hafid [2]

[1] Université Paris-Saclay, CentraleSupélec, ENS Paris-Saclay, CNRS,
LMPS - Laboratoire de Mécanique Paris-Saclay, 91190, Gif-sur-Yvette, France,
{karim.ait_ammar, pierre-alain.guidault, pierre-alain.boucard}@ens-paris-saclay.fr
[2] RTE, direction de la R&D, pôle Gestion des Actifs, 92073, Paris la Defense Cedex, France,
{julien.said, fikri.hafid}@rte-france.com

Keywords: Beam-to-Beam Contact, Friction, Small-Sliding, Finite Rotations, Spiral Strand Wire Ropes

1. Industrial context and challenges

Spiral strand wire ropes exhibit high tensile strength and flexibility making them essential in many applications such as mooring lines for offshore structures or overhead conductors. Simulation demand for these structures is high, particularly to evaluate their lifespan, the main source of damage usually coming from a combination of fretting between wires and fatigue. As such simulations require extensive calculations to account for multiple loading states [1], speed and accuracy of frictional contact models are crucial. Full 3D models obtain results close to experimental data but at high numerical costs [2]. Thus, a common way to reduce the CPU cost is to model each wire with beam finite elements [3] and use beam-to-beam contact formulations [4, 5, 6] allowing arbitrary large sliding. However, the need for a CPU-intensive contact search phase in each iteration makes them computationally expensive, and sometimes unnecessary, particularly when dealing with fretting interactions where the relative slip amplitudes are small. The proposed work is a continuation of [7] where a small-sliding beam-to-beam point-wise frictional contact element between non-collinear beams has been proposed and implemented as a user-element in Abaqus™. Due to their peculiar helical architecture, using the penalty method for normal contact as in [7] can lead to significant interpenetration induced by significant tension-bending coupling. To improve accuracy and robustness, normal contact is treated here using Lagrange multipliers. Similarly to [7], the tangential behavior is also handled with a regularized Coulomb's law. Moreover, the formulation in [7] is written for an updated Lagrangian framework well-adapted to Abaqus™. This formulation easily handles very large rotations by evicting singularities but does not perfectly respect frame objectivity and path independence principles. Considering that the target applications do not involve very large rotations, the Eulerian framework has been chosen to better respect those fundamental principles. The current contact element is implemented in a Matlab™ home-made beam finite element code in large rotations based on Eulerian formulation [8].

2. Beam-to-beam contact kinematics under small-sliding assumption

The small-sliding hypothesis consists of assuming that two beams in point-wise contact are locally straight in the contact area (Figure 1). Therefore, the tangent vectors of the beams at points $\hat{\boldsymbol{x}}_1$ and $\hat{\boldsymbol{x}}_2$, which minimize

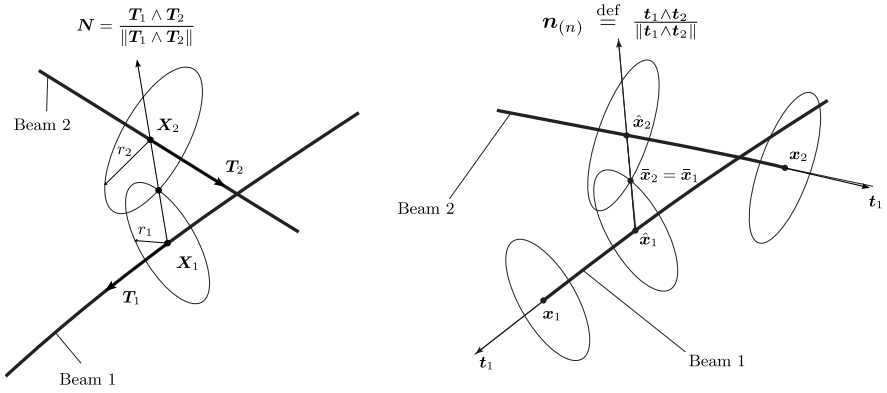

Figure 1: Beam-to-beam contact in initial configuration at $t = t_0$ (left) and configuration at $t = t_n$ (right)

the distance between the two beams in the deformed configuration, are considered equal to the tangent vectors

of the beams at points $\boldsymbol{x}_1$ and $\boldsymbol{x}_2$ - denoted $\boldsymbol{t}_1$ and $\boldsymbol{t}_2$ - which correspond to the current locations at $t = t_n$ of the initial contact points $\boldsymbol{X}_1$ and $\boldsymbol{X}_2$. Thus, the contact normal is defined by:

$$n \overset{def}{=} \frac{\boldsymbol{t}_1 \wedge \boldsymbol{t}_2}{\|\boldsymbol{t}_1 \wedge \boldsymbol{t}_2\|} \tag{1}$$

The current gap can then be decomposed into a normal gap g_N and a tangential part $\hat{\boldsymbol{g}}_T$ as follows:

$$\boldsymbol{g} = \boldsymbol{x}_2 - \boldsymbol{x}_1 - (r_1 + r_2)\,\boldsymbol{n} = g_N \boldsymbol{n} + \hat{\boldsymbol{g}}_T \quad \text{with} \quad \left\{ \begin{array}{rcl} g_N & = & (\boldsymbol{x}_2 - \boldsymbol{x}_1)\cdot\boldsymbol{n} - (r_1 + r_2) = (\bar{\boldsymbol{x}}_2 - \bar{\boldsymbol{x}}_1)\cdot\boldsymbol{n} \\ \hat{\boldsymbol{g}}_T & = & \Pi(\boldsymbol{x}_2 - \boldsymbol{x}_1) = \xi^1 \boldsymbol{t}_1 + \xi^2 \boldsymbol{t}_2 \end{array} \right. \tag{2}$$

where ξ^1 and ξ^2 are the contravariant components of $\hat{\boldsymbol{g}}_T$ in the basis $(\boldsymbol{t}_1, \boldsymbol{t}_2, \boldsymbol{n})$. Finally, the contact points $\hat{\boldsymbol{x}}_1$ and $\hat{\boldsymbol{x}}_2$ can be approximated as $\hat{\boldsymbol{x}}_1 \approx \boldsymbol{x}_1 + \xi^1 \boldsymbol{t}_1$ and $\hat{\boldsymbol{x}}_2 \approx \boldsymbol{x}_2 - \xi^2 \boldsymbol{t}_2$, thus effectively skipping the time-consuming contact search phase. The tangent vector $\boldsymbol{t}_i$ at node $\boldsymbol{x}_i$ in the deformed configuration is given by $\boldsymbol{t}_i = \boldsymbol{R}(\boldsymbol{\Phi}_i)\boldsymbol{T}_i$ where $\boldsymbol{R}$ is the rotation matrix. The rotation vector $\boldsymbol{\Phi}_i$ of the beam cross-section at node $\boldsymbol{x}_i$, neglecting shear effects, has been chosen among other existing possible rotation parameterizations. Besides, the contact normal (1) varies smoothly with the beams directors, and consequently nodal rotation vectors $\boldsymbol{\Phi}_i$, which allows for a better-performing Newton-Raphson resolution.

3. Numerical example

This presentation proposes a verification of the formulation on cable-like structures similar to the targeted application (Figure 2), featuring confrontation with analytical results, large sliding surface-to-surface contact reference, as well as a study of the sensitivity of the stick/slip transition to the regularization parameter.

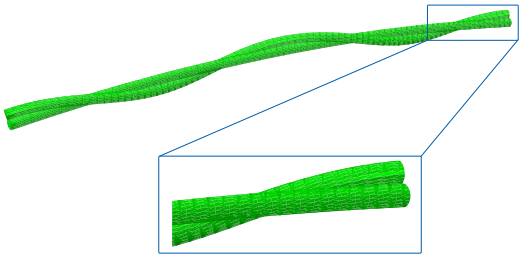

(a) 3D volume visualization of the two-wire cable benchmark modeled with beam finite elements (lay angle: 15°, wire radius: 2.40 *mm*, cable length: 22.51 *cm*)

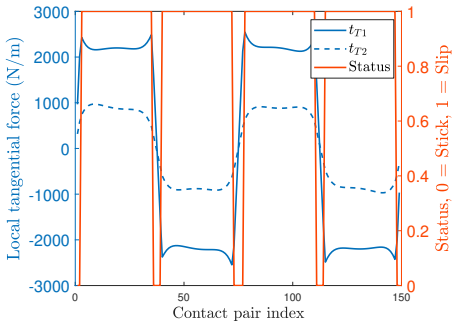

(b) Tangential frictional force components and contact status between the two wires at curvature $\kappa = 0.02\ m^{-1}(slip)$

Figure 2: Simple two-wire cable under tension and bending

References

[1] F. Bussolati, P.-A. Guidault, M.L.E Guiton, O. Allix, P. Wriggers. *Robust contact and friction model for the fatigue estimate of a wire rope in the mooring line of a floating offshore wind turbine*, Lect. Notes Appl. Comp. Mech., Virtual Design and Validation, Springer Int. Pub., (2020) 249–270

[2] J. Said, S. Fouvry, G. Cailletaud, S. Basseville, M. Coulangeon, J. Brocard, C. Yang, F. Hafid. *A global-local approach to predict the fretting-fatigue failure of clamped aluminium powerline conductors: From mono-contact crossed wires to full conductor vibrational tests*, Eng. Fail. Anal., 146, (2023) 107073

[3] S. Lalonde, R. Guilbault, F. Légeron. *Modeling multilayered wire strands, a strategy based on 3D finite element beam-to-beam contacts - Part I*, Int. J. Mech. Sc., 126 (2017) 281-296

[4] G. Zavarise, P. Wriggers. *On contact between three-dimensional beams undergoing large deflections*, Com. Num. Meth. Eng., 13(6) (1997) 429-438

[5] A.G. Neto, P.M. Pimenta, P. Wriggers. *A master-surface to master-surface formulation for beam to beam contact. Part II: Frictional interaction*, Comp. Meth. Appl. Mech. and Eng., 319 (2017) 146-174

[6] D. Durville. *Contact-friction modeling within elastic beam assemblies: an application to knot tightening*, Comp. Mech., 49(6) (2012) 687-707

[7] F. Busssolati. *Multi-scale modeling of the fatigue of mooring wire ropes for floating offshore wind turbines*, PhD thesis, Université Paris Saclay (COmUE), 2019.

[8] S. Ghosh, R. Roy. *A frame-invariant scheme for the geometrically exact beam using rotation vector parametrization*, Comp. Mech., 44(1) (2009) 103-118

ECCOMAS Thematic Conference and IACM Special Interest Conference
Highly Flexible Slender Structures (HFSS 2025)
22–26 September 2025, Kaiserslautern, Germany

Large Deformations of Rods deforming on Flexible Shells: an Arbitrary Lagrangian-Eulerian Framework

Sébastien J. Michel [1], Yury Vetyukov [1],

[1] Institute of Mechanics and Mecatronics, TU Wien, Getreidemarkt 9, 1060 Wien, Austria,
sebastien.michel@tuwien.ac.at, yury.vetyukov@tuwien.ac.at

Keywords: Arbitrary-Lagrange-Euler, Rod, Shell, Frictionless contact

1. Introduction

The computation of the joint response of assemblies of slender structural elements finds numerous applications in engineering and applied mechanics, ranging from the description of the packing of DNA filaments inside a cell, the investigation of drill-strings in the oil industry or the simulation of medical procedures. A crucial point for the simulations is the evaluation of the relative position of the structural members and the choice of an adequate meshing strategy for numerical solutions. Independently meshing the different members indeed leads to having to apply reaction forces and moments outside the nodes of the mesh, what is known to lead to numerical difficulties overcome by a costly remeshing. An idea embraced in the literature is that one can exploit the natural parametrization of one of the two members and give the other a Eulerian description. Although limited in applications due to the restrictions inherent to the Eulerian description, the strategy has been successfully applied to the investigation of the deformation of a rod on a rigid constraint [3, 5].

In this contribution, we investigate more specifically the computation of the equilibrium configuration of a flexible rod constrained to deform on a flexible shell under the assumption of perfect frictionless contact. For simplicity, we assume the rod to be unshearable, inextensible and have negligible torsional stiffness. Due to the non-conforming geometries of the two structural members, the initial configuration of the rod on the curved surface of the undeformed shell is a priori unknown and needs to be determined as part of the solution. We propose a framework based on arbitrary Lagrangian-Eulerian formalism allowing to compute the joint large deformations of the two elements. We introduce an initially unknown abstract auxiliary configuration, that we use as a common ground for parametrizing the deformed configurations of both the rod and the shell. This description is then exploited to provide a full reparametrization of the shell, what we achieve without introducing any further unknowns. Discretizing the problem over the auxiliary configuration allows to formulate the elasticity problem using the degrees of freedom associated with the shell deformation, and those associated with the reparametrization of the shell in a natural way.

2. The framework

We borrow the notation from [1]. We consider a shell in its reference configuration $\mathring{r}$ with associated differential operator on the tangent space $\mathring{\nabla}$. The deformed configuration of the shell and tangent operator are r, ∇. The transformation gradient relates the two configurations: $F^T = \mathring{\nabla} r$. The position of the rod on the deformable shell is a priori unknown, thus preventing the direct spatial discretization of the problem.

We introduce a yet undetermined auxiliary configuration $\tilde{r}, \tilde{\nabla}$ that we exploit to parametrize both the shell and the rod in a way reminiscent of [4]. On the auxiliary configuration, the rod can be parametrized using a single coordinate line of the shell, and we only have information about the motion of these points associated with the rod. Exploiting these degrees of freedom, we are able to extend this mapping to the whole shell. Postulating sufficient regularity and invertibility of the mapping allows the strain measures of the problem to be expressed from the variables of the auxiliary configuration. The problem is then formulated as the minimization of the total energy of the rod and of the shell expressed on the auxiliary configuration.

Rod and shell are then discretized following a finite element procedure. The rod discretization has four degrees of freedom per node characterizing the rod position on the shell reference configuration *i.e.* the transformation of a coordinate line between the reference and auxiliary configuration. By construction, the rod configuration in the deformed state can be expressed from a subset of the shell degrees of freedom. The shell element is chosen

to be the classical Bogner-Fox-Schmidt [2] with 12 degrees of freedom per node. The problem formulated over the auxiliary configuration can then solved numerically.

3. Results

Our formulation is first verified by keeping some degrees of freedom constrained. On the one hand, deactivating the rod degrees of freedom reduces the formulation to that of a shell with some additional stiffness at the position the rod is deemed to occupy. In this case, one retrieves the model of a shell with a rod of specified stiffnesses along a given line as a stiffener. On the other hand, deactivating the shell degrees of freedom lets us retrieve the formulation of a rod constrained to deform over a rigid surface as in figure 1. When the two sets of degrees of freedom are active together, we retrieve the joint deformation of the two structural members.

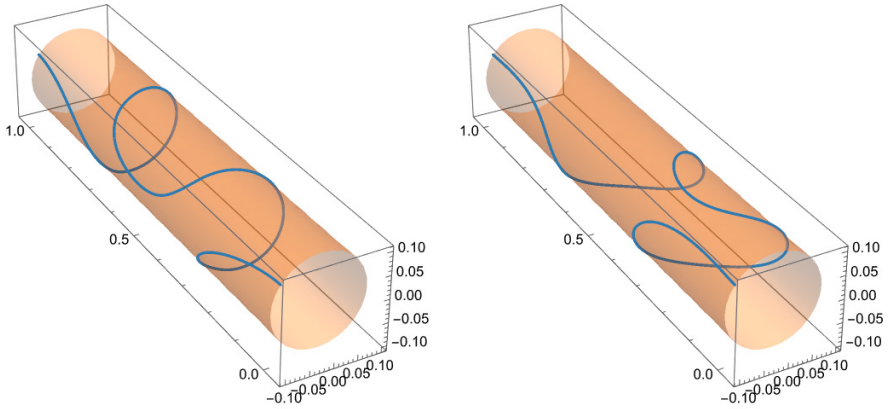

Figure 1: Loss of symmetry of a rod of increasing length constrained to lie on a cylinder under gravity.

Within the limits of the Eulerian description, the proposed framework allows for the investigation of the complex joint deformation of a flexible rod lying on a flexible shell. The inclusion of more complex rod mechanical models and of more realistic modes of contact should be possible.

References

[1] Vetyukov, Y. (2014). Nonlinear mechanics of thin-walled structures: asymptotics, direct approach and numerical analysis. Springer Science & Business Media.

[2] Vetyukov, Y. (2014). Finite element modeling of Kirchhoff-Love shells as smooth material surfaces. *ZAMM-Journal of Applied Mathematics and Mechanics/Zeitschrift für Angewandte Mathematik und Mechanik*, 94(1-2), 150-163.

[3] Huynen, A., Detournay, E., Denoël, V. (2016). Eulerian formulation of elastic rods. *Proceedings of the Royal Society A: Mathematical, Physical and Engineering Sciences*, 472(2190), 20150547.

[4] Vetyukov, Y., Gruber, P. G., Krommer, M. (2016). Nonlinear model of an axially moving plate in a mixed Eulerian-Lagrangian framework. *Acta Mechanica*, 227(10), 2831-2842.

[5] Shah, R., Van der Heijden, G. H. M. (2024). Buckling and lift-off of a heavy rod compressed into a cylinder. *Journal of the Mechanics and Physics of Solids*, 182, 105464.

ECCOMAS Thematic Conference and IACM Special Interest Conference
Highly Flexible Slender Structures (HFSS 2025)
22–26 September 2025, Kaiserslautern, Germany

Noether symmetries and conserved quantities for elastic rods with contact

Florence Bertails-Descoubes [1], Sébastien Neukirch [2]

[1] Univ. Grenoble-Alpes, INRIA, CNRS, Grenoble INP, LJK, France, florence.descoubes@inria.fr
[2] d'Alembert Institute for Mechanics, Sorbonne University, CNRS, Paris, France, neukirch@upmc.fr

Keywords: structural mechanics, dynamics, integral of motion

1. Introduction

The static-dynamic analogy discovered by G. Kirchhoff shows that the statics of an elastic beam are equivalent to the dynamics of a spinning top. In this analogy, time and angular velocity are, for example, equivalent to arc length and curvatures. This static-dynamic analogy allows us to use Noether's theorem and unravel several quantities that are invariant along the elastic rod at equilibrium. A spinning top having a Lagrangian independent of time will have its mechanical energy constant in time. In the same manner, an elastic rod with uniform elastic properties will have the sum of its curvature energy and its axial force uniform along the structure. The invariant property is known in simple cases, see e.g. [1,2], but the present approach generalizes it to more complex cases where extensibility, shear, gravity, and contact are involved.

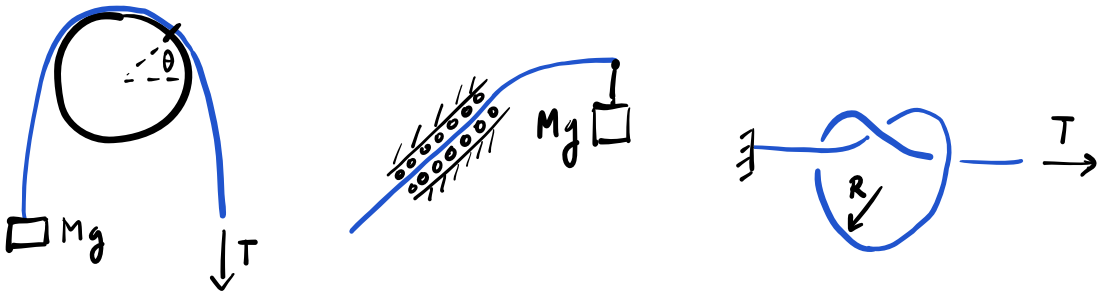

Figure 1. Three examples illustrate the use of the invariant in the statics of rods.

We will show how to compute this invariant and illustrate its usefulness in three examples. The first example is the capstan, where an elastic rod is wound around a disk. In this case, the use of the invariant easily leads to the computation of how the opening angle varies with the bending rigidity of the rod and the weight. The second example is the elastic arm scale [3], where the use of the invariant shows that the rod must have a horizontal tangent at the tip where the weight is attached. The third example is the open trefoil knot, where using the invariant leads to the relation between the applied axial force and the loop size.

Finally, we will discuss the generalization of the present approach to the dynamics of 3D twisted rods and its potential for the verification and comparison of numerical simulators for rods.

Acknowledgments

This project has received funding from CNRS and INRIA.

References

[1] J. H. Maddocks and D. J. Dichmann. *Conservation laws in the dynamics of rods*. Journal of elasticity, **34** (1994) 83-96

[2] S. Kehrbaum, J. H. Maddocks. *Elastic rods, rigid bodies, quaternions and the last quadrature.* Phil. Trans. Roy. Soc. A, **355** (1997) 2117-2136

[3] F. Bosi, D. Misseroni, F. Dal Corso, and D. Bigoni. *An elastica arm scale*. Proc. Roy. Soc. A, **470** (2014) 20140232.

ECCOMAS Thematic Conference and IACM Special Interest Conference
Highly Flexible Slender Structures (HFSS 2025)
22–26 September 2025, Kaiserslautern, Germany

Exact Computation of Contact Regions for Nonlinear Beams with Cubic Interpolation

Leon Radman [1], Robert Winkler [1], Michael Pieber [2], Johannes Gerstmayr [2]

[1] Dept. of Engineering & IT, Carinthia University of Applied Sciences, [l.radman, r.winkler]@fh-kaernten.at
[2] Dept. of Mechatronics, Leopold-Franzens-Universität Innsbruck, [micheal.pieber, johannes.gerstmayr]@uibk.ac.at

Keywords: Contact Detection, Contact Modeling, Cable-Pulley System

1. Introduction

In this work, a novel contact detection method applicable for modeling beam to sheave contact is presented. Interaction of this kind occurs in many mechanical systems, e.g., ropeway systems and elevators. First, we describe the contact detection method and the corresponding contact force model. Subsequently, the new formulation is tested via numerical example and validated by a comparison with a semi-analytical reference model.

2. Methods

The novelty of the present approach lies in the geometrically exact calculation of intersection points during beam to sheave contact. First, the beam is modeled using the improved version of two-dimensional ANCF beam element [1]. In the element formulation, $\mathbf{r}(\bar{x},t) = \begin{bmatrix} r_x & r_y \end{bmatrix}^T = \mathbf{S}(\bar{x})\mathbf{q}(t)$ is the position of a point at time t located on the beam axis with $\bar{x}$ being a local Lagrangian position coordinate. The interpolation of positions makes use of 3rd order polynomial shape functions, organised in the matrix $\mathbf{S}$, and the vector of coordinates $\mathbf{q} = \begin{bmatrix} \mathbf{r}_1^T & \mathbf{r}_1'^T & \mathbf{r}_2^T & \mathbf{r}_2'^T \end{bmatrix}^T$ containing the nodal positions $\mathbf{r}_1$, $\mathbf{r}_2$, as well as the slopes $\mathbf{r}_1'$ and $\mathbf{r}_2'$ [1].

The sheave, as shown in Figure 1(a), is considered given a rigid circle with center $\mathbf{p}_j = \begin{bmatrix} p_{j,x} & p_{j,y} \end{bmatrix}^T$ and radius R_j. Consequently, the position vector $\mathbf{r}$ of a point on the beam element intersecting the circle obeys the equation of the circle $[r_x(\bar{x}) - p_{j,x}]^2 + [r_y(\bar{x}) - p_{j,y}]^2 = R_j^2$, which is equivalent to a polynomial equation $p(\bar{x})$ of 6th order. This equation can then be solved by computing the corresponding companion matrix $\mathbf{C}(p)$ of $p(\bar{x})$ and determining the eigenvalues of $\mathbf{C}(p)$ [2]. The eigenvalues coincide with the roots of the polynomial, which represent the intersection points of the beam and the circle.

To determine the contact force, two reference coordinates s_0 and s_1 are introduced which define the start and end of the penetrating beam section, see Figure 1(a). The computation is then based on integrals over the interval $[s_0, s_1]$. The integration is performed numerically using a 3-points Lobatto integration rule. As illustrated in Figure 1(a), $\mathbf{d}_k$ is the vector pointing from the circle center to the position of integration point with number k. The normal contact force is computed using a linear contact model [3] as

$$f_{c,k} = k_c\, g_k + d_c\, v_{n,k} \tag{1}$$

with contact stiffness k_c, constant damping factor d_c, and the gap $g_k = L_k - r + \frac{h}{2}$, with $L_k = |\mathbf{d}_k|$, the circle radius r, and the height of the beam h. Further, $v_{n,k}$ is the velocity component in the contact force direction $\hat{\mathbf{d}}_k = \frac{1}{L_k}\mathbf{d}_k$. The resulting contact force vector corresponding to integration point k reads

$$\mathbf{f}_k = \frac{1}{2}(s_1 - s_0) w_k \cdot f_{c,k} \cdot \hat{\mathbf{d}}_k \tag{2}$$

3. Numerical Investigations

To validate the presented contact formulation, it is applied to the cable-pulley system illustrated in Figure 1(b). The system layout and most geometric and material parameters are adopted from [4] with the difference that axial flexibility of the cable is accounted for in the present work. Friction between cable and pulleys is not considered and gravity loads are disregarded for the cable. To obtain the initial configuration for the dynamic

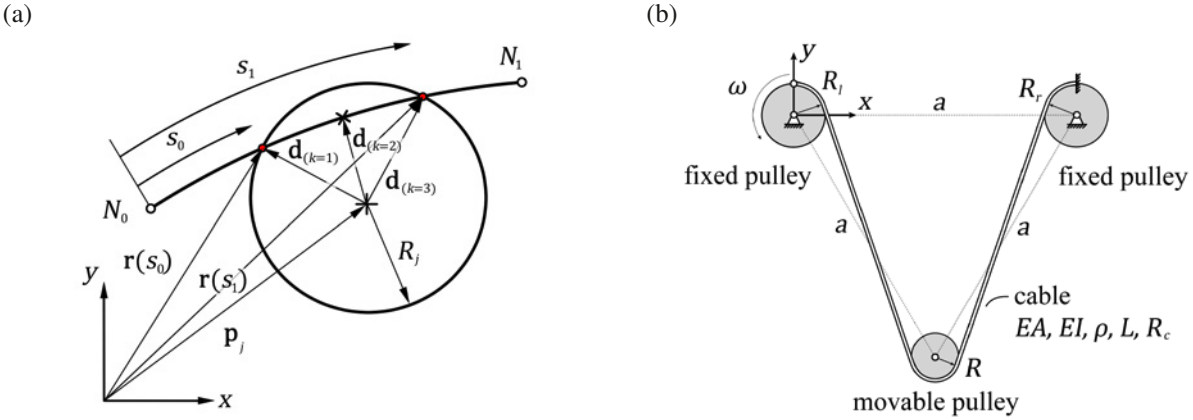

Figure 1: (a) Contact between an ANCF element and a circle. (b) Pulley system.

simulation, a static simulation step is carried out in advance. In the second step, the prescribed sinusoidal angular velocity ω acting on the driven pulley is activated and the dynamic simulation is executed. The simulation is performed repeatedly using the present contact model as well as the segment method introduced in [5]. In both cases, the number of elements n_e is varied. In case of the segment method, $n_{cs} = 2$ contact segments per element are used, as this results in almost identical computation times compared to the exact method, while higher segment numbers increase the computation time significantly. In Figure 2, the motion of the movable

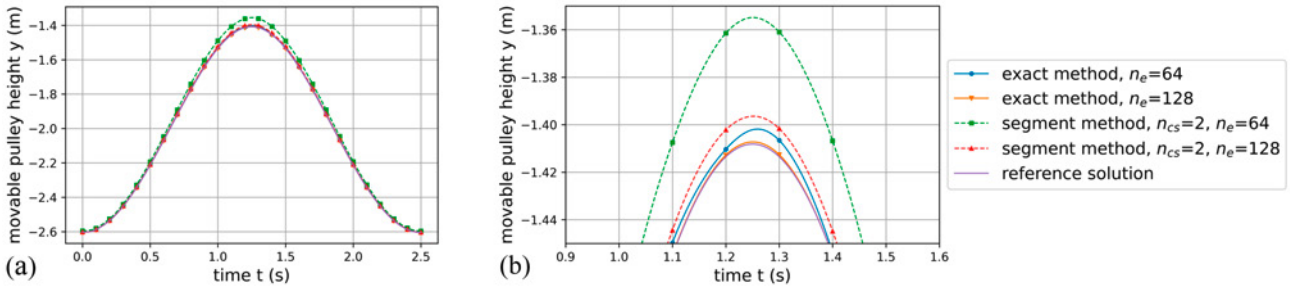

Figure 2: (a) Motion of the movable pulley center in y direction. (b) Detailed view of subplot a.

pulley's center in y direction is plotted over time for both models, and compared to a reference solution obtained from a semi-analytical pulley system model developed for this work. We observe, that the exact contact model exhibits significantly faster convergence.

Acknowledgments

This project has received funding from INTALES GmbH, Innsbruckerstraße 1, A-6161 Natters.

References

[1] J. Gerstmayr, H. Irschik. *On the correct representation of bending and axial deformation in the absolute nodal coordinate formulation with an elastic line approach*, J. Sound Vib., 318(3) (2008) 461-487

[2] R.A. Horn, C.R. Johnson. *Matrix Analysis*, Cambridge University Press, Cambridge, 1985.

[3] H.M. Lankarani, P.E. Nikravesh. *A contact force model with hysteresis damping for impact analysis of multibody systems*, J. of Mechanical Design, 112 (1990) 369-376

[4] J. Wang, Z. Qi, G. Wang. *Hybrid modeling for dynamic analysis of cable-pulley systems with time-varying length cable and its application*, J. Sound Vib, 406 (2017) 277-294

[5] K. Ntarladima, M. Pieber, J. Gerstmayr. *A model for contact and friction between beams under large deformation and sheaves*, Nonlinear Dyn., 111 (2023) 20643–20660

ECCOMAS Thematic Conference and IACM Special Interest Conference
Highly Flexible Slender Structures (HFSS 2025)
22–26 September 2025, Kaiserslautern, Germany

Three-Dimensional Configurations of an Elastic Whisker Touching a Plane Wall

Eugene L. Starostin [1,2], Victor G. A. Goss [1]

[1] School of Engineering, London South Bank University, 103 Borough Rd, London SE1 0AA, UK, staroste@lsbu.ac.uk; gossga@lsbu.ac.uk

[2] Department of Civil, Environmental and Geomatic Engineering, University College London, Gower St, London WC1E 6BT, UK, e.starostin@ucl.ac.uk

Keywords: Whisker, Contact, Thin Elastic Rod

1. Introduction

When a mammal's whisker makes contact with an object it bends and may also twist. The resultant forces and moments arising at the whisker base can be measured by mechanoreceptors inside the whisker follicle (Fig. 1A) [1]. The creature's brain processes that information, enabling it to explore its surroundings, even in the dark. To date, studies of whisker contact problems have focused on intrinsically straight whiskers in contact with flat walls, at either a single point or along an interval. However, whiskers are intrinsically curved. Moreover, contact with an object may arise at multiple points along the whisker shaft. Taking the research forwards, we consider a whisker with intrinsic curvature that touches a plane wall arbitrarily positioned and oriented in space (Fig. 1B).

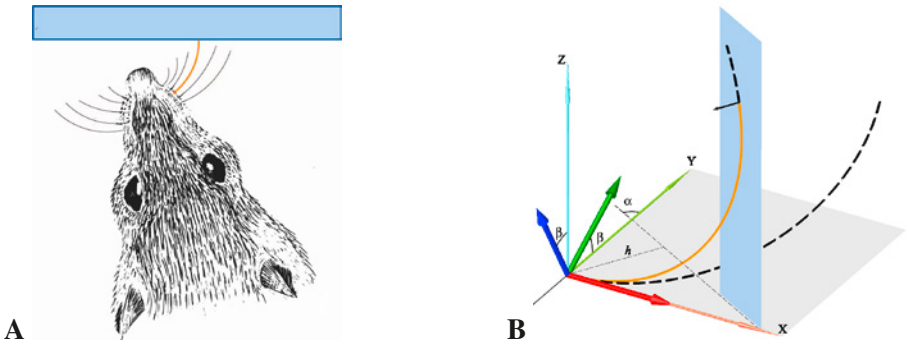

Figure 1: (**A**) A whisker (orange) approaches a wall. (**B**) A whisker touching a wall at a single point. The deformed part of the whisker is shown in orange, the free part after the tangential contact point dashed black. Thick red, green and blue arrows indicate the material frame at the base; the red and green vectors span the osculating plane of the intrinsic centreline (dashed black). The wall (blue) is located at distance h from the base. The rig frame is marked XYZ. The contact force is normal to the wall (the black arrow).

2. Theory

Our aim is to gain insight into the role of intrinsic curvature as a key parameter governing 3D equilibrium configurations of a whisker when it touches a plane frictionless wall. Consequently, we approach the problem from an analytical perspective. To that end, we consider a weightless, isotropic, homogeneous, Kirchhoff elastic rod [3], possessing intrinsic circular curvature, with length $L = 1$, spanning an angle κ_i. It has linear constitutive relations (B and C are the bending and torsional constant stiffness coefficients, resp).

Our analysis distinguishes four qualitatively different types of contact (Fig. 2): a single point contact at the tip or at an interior point, at two points (one being the tip), and a contact along an interval plus the tip point contact. Thus we formulate a boundary value problem (BVP) for each case, i.e. a system of ordinary differential equations (ODEs) governing the equilibria, plus boundary conditions (BCs). In each case we require continuity of the bending and twisting moments along the entire length of the rod. Single point contact problems are presented in [4]. For the case with two contact points we solve a three-point BVP with BCs specified at the base, at the first (tangential) contact point and the tip. For configurations with a finite contact interval plus tip contact we first derive the equations describing a twisted curved rod constrained to a plane (cf. [5]) and then specify a four-point BVP with conditions at the base, at both ends of the contact interval and at the tip. For a given κ_i, in each of the four aforementioned scenarios, three parameters characterise the set of solutions: the

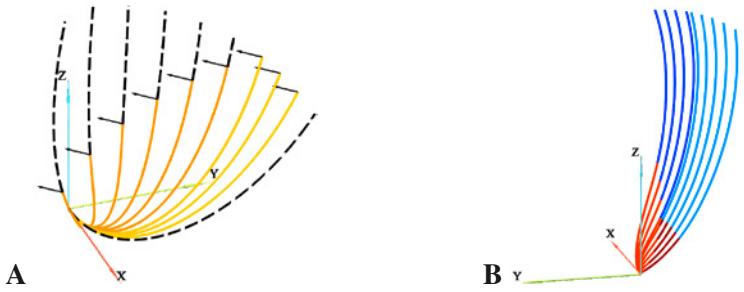

Figure 2: Whisker configurations for qualitatively different configurations corresponding to various wall distances $x = h$, with $\alpha = \beta = 45°$, $\kappa_i = 1.825$, $C = 0.75B$, $L = 1$. (**A**) Single point contact configurations: tip contact ($0.718 > h > 0.563$) or interior tangential contact ($0.563 > h > 0.137$). Dashed black = intrinsic shape/free parts of the whisker. Yellow/orange = bent whisker. Arrows = the normal to the wall plane at the contact point. (**B**) Tip contact plus either an interior point, $0.137 > h > 0.080$ or an interval (brown), $0.080 > h > 0$. Red = base to first contact point. Blue = final contact point to tip.

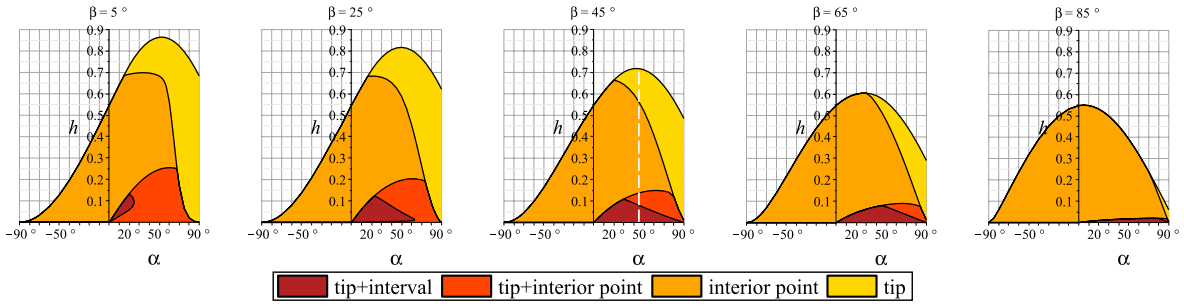

Figure 3: The coloured zones depict qualitatively different equilibrium solutions for orientations α and distances h, at a selection of fixed elevation angles β. In each case $\kappa_i = 1.825$, $C = 0.75B$, $L = 1$. Note, for the case $\beta = 45°$, the dashed white vertical line at $\alpha = 45°$ corresponds to solutions presented in Fig. 2.

distance h from the whisker base end to the wall and two angles: the orientation angle $\alpha \in (-90°, 90°]$ between the normal plane to the whisker at its base (the coordinate plane YZ) and the wall, and the elevation angle $\beta \in [0, 90°]$ between the horizontal plane XY and the intrinsic principal normal of the rod at the base (Fig. 1B). In each case, we compute numerical solutions to the BVPs by path continuation in h, with fixed angles, α, β.

3. Results and Discussion

Results are presented in terms of the geometric parameters h, α, β, see diagrams in Fig. 3. We have derived the conditions that specify the solutions at the boundaries between domains with different contact types. This enables us to compute the boundary curves, facilitating transitions between different BVPs when a boundary is crossed. Theoretical predictions are compared with data obtained from experiments on nitinol rods in contact with a rigid wall. These results may help our understanding of how mammal whiskers work, and guide the design of artificial whisker sensors.

References

[1] M. H. Evans et al. *Sensing the Environment with Whiskers.* Oxford Research Encyclopedia, Neuroscience (oxfordre.com/neuroscience), subject: Sensory Systems, 2019.

[2] T. Pipe and M. J. Pearson. *Whiskered Robots.* Scholarpedia of Touch, Scholarpedia, 2016.

[3] A. E. H. Love. *A Treatise on the Mathematical Theory of Elasticity.* Cambridge University Press, 1927.

[4] E. L. Starostin, V. G. A. Goss, G. H. M. van der Heijden. *Whisker sensing by force and moment measurements at the whisker base.* Soft Robotics, **10** (2023) 326–335.

[5] G. H. M. van der Heijden et al. *Spatially complex localisation in twisted elastic rods constrained to lie in the plane.* Journal of the Mechanics and Physics of Solids, **47** (1999) 59–79.

ECCOMAS Thematic Conference and IACM Special Interest Conference
Highly Flexible Slender Structures (HFSS 2025)
22–26 September 2025, Kaiserslautern, Germany

Contact Modelling of Shells for Roll Forming Simulations

Manuel Strondl [1], Jakob Scheidl [2], Yury Vetyukov [3]

[1] TU Wien, manuel.strondl@tuwien.ac.at
[2] TU Wien, jakob.scheidl@tuwien.ac.at
[3] TU Wien, yury.vetyukov@tuwien.ac.at

Keywords: Roll forming, Kirchhoff-Love shells, Penalty regularization method, Frictionless contact, Contact initiation

Roll forming is a bending-dominant process in which a metal sheet is fed through a number of roll stands. These consist of rollers that impose elasto-plastic deformations on the sheet to generate a desired profile. Conventional approaches to model this process utilize Lagrangian continuum finite elements, where nodal points coincide with material particles. This is problematic for the axially moving sheet due to the movement of the mesh at the contact zone, which may cause numerical oscillations [1]. Furthermore, the refinement of the mesh in the vicinity of the rollers becomes difficult.

We take advantage of the low thickness of the sheet and use the nonlinear Kirchhoff-Love shell theory with three translational and two rotational degrees of freedom per particle of the material surface [2]. A Mixed-Eulerian-Lagrangian (MEL) framework [3] is employed, which uses a Eulerian coordinate in axial direction and a conventional Lagrangian coordinate in transverse direction to parametrize the material surface. The nodal point deflection is thereby decoupled from the axial motion of the material particles. This allows for a mesh, which is fixed axially, but follows the deformation of the material in the transverse directions. As a result, an advection problem arises for the plastic variables in account for their downstream transport [4]. A stress resultant plasticity model for shell bending with isotropic hardening [5] is used. It is solved with a variant of the well established return-mapping scheme [6] and features the usual alternation of elastic predictor and plastic corrector. Additionally, a finite difference scheme is applied to carry the plastic variables downstream [4].

One focus of this talk lies in modeling the rollers, which we consider as rigid bodies. Contact with the sheet is imposed by a penalty regularization method, in which the contact potential per unit reference area

$$V = \frac{1}{2} P \gamma^2 \tag{1}$$

accounts for the penetration depth γ quadratically. It satisfies the impenetrability of the rollers exactly for $P \to \infty$. We evaluate the penetration depth γ by projecting the radial distance between the respective point and the contour curve $C(y_*)$ onto the normal direction $\boldsymbol{\nu}$ in the coordinate system $\{x_*, y_*, z_*\}$ fixed to the roller [4]. This can be described by the relation

$$\gamma = \max\left\{0, \frac{C(y_*) - d}{\sqrt{1 + C'(y_*)^2}}\right\} \quad \text{with} \quad d = (\boldsymbol{r} + \boldsymbol{h} - \boldsymbol{r}_0) \cdot \boldsymbol{k}_*, \tag{2}$$

which is sketched in fig. 1. The vectors $\boldsymbol{r}$ and $\boldsymbol{r}_0$ denote the position of the shell and the roller with respect to an inertial coordinate system. The thickness h of the shell, with normal vector $\boldsymbol{n}$, is accounted for by $\boldsymbol{h} = h/2\boldsymbol{n}$. The contour curve $C(y_*)$ and its first derivative with respect to the axial coordinate $C'(y_*)$ are constructed from CAD data of the rollers.

This talk is also concerned with the sequential simulation of the sheet and the construction of beneficial initial configurations. Since the model covers the entire forming line at all times due to the MEL formalism, merely a segment spanning over a few forming stages is considered. New pieces are added in downstream direction once the stationary solution has been established for the currently considered upstream part. The pre-strained initial configuration is constructed from the desired shape in the respective forming stages [7] and the upstream end, such that geometric compatibility is ensured. The (plastic) material quantities $\boldsymbol{p}$, which are transported with the velocity v in the longitudinal direction, are coupled smoothly by a regularized transport approach. The advective term $v\partial_x \boldsymbol{p}$ of the plastic rate $\dot{\boldsymbol{p}}$ is modified with $c \in [0, 1]$

$$\partial_t \boldsymbol{p} = \dot{\boldsymbol{p}} - cv\partial_x \boldsymbol{p}. \tag{3}$$

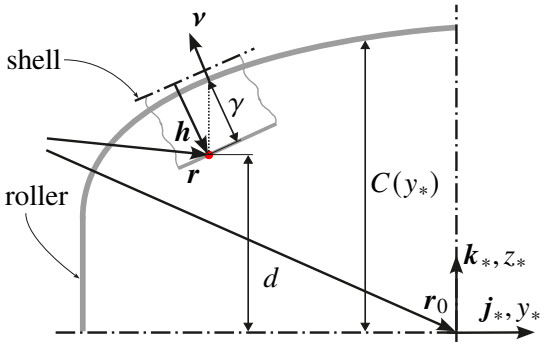

Figure 1: Sketch of the sheet penetrating the roller, which rotates about the y_*-axis (basis vector $\boldsymbol{j}_*$).

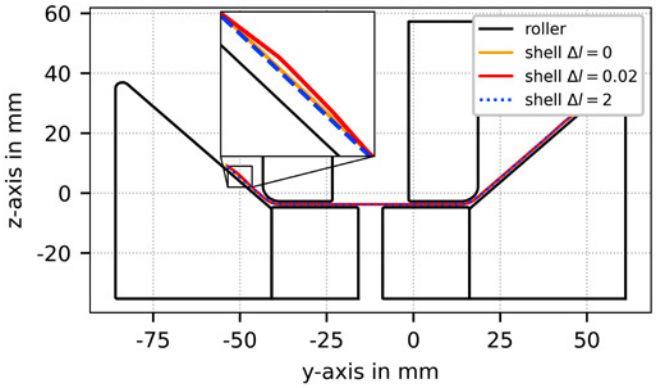

Figure 2: Rollers with sheet in forming gap, depicted at different phases of the simulation.

It is slowly increased at the interface between the new piece and the previously treated segment, and set to 1 elsewhere. As new pieces are added to the segment in downstream direction, the ones at the opposite end upstream can be removed and replaced by corresponding interface conditions. This allows to keep the size of the governing system small, which is very relevant for forming lines with a high number of forming stages.

The results at a forming stage of a simple model of length l are depicted in fig. 2. The initial configuration, i.e., no transport has yet occured in the length direction $\Delta l = 0$, fits in the rolling gap due to its geometric construction. As depicted for $\Delta l = 0.02$, transient effects occur since the previous state is just an approximation. Over time these phenomena decay as the solution converges towards its steady-state at $\Delta l = 2$.

Acknowledgments

The support by the Austrian Research Promotion Agency (FFG) is gratefully acknowledged; FFG project number: 914865.

References

[1] I. Steinbrecher, A. Humer, and L. Vu-Quoc. "On the numerical modeling of sliding beams: A comparison of different approaches". In: *Journal of Sound and Vibration* 408 (2017), pp. 270–290. DOI: 10.1016/j.jsv.2017.07.010.

[2] Y. Vetyukov. *Nonlinear mechanics of thin-walled structures : Asymptotics, direct approach and numerical analysis*. Foundations of engineering mechanics. Springer, 2014. DOI: 10.1007/978-3-7091-1777-4.

[3] Y. Vetyukov, P.G. Gruber, and M. Krommer. "Nonlinear model of an axially moving plate in a mixed Eulerian–Lagrangian framework". In: *Acta Mechanica* 227 (2016), pp. 2831–2842. DOI: 20.500.12708/126.

[4] E. Kocbay et al. "Mixed Eulerian–Lagrangian modeling of sheet metal roll forming". In: *Thin-walled structures* 186 (2023), p. 110662. DOI: 10.1016/j.tws.2023.110662.

[5] E. Kocbay et al. "An enhanced stress resultant plasticity model for shell structures with application in sheet metal roll forming". In: *The International Journal of Advanced Manufacturing Technology* 130.1-2 (2024), pp. 781–798. DOI: 10.1007/s00170-023-12544-1.

[6] J.C. Simo. *Numerical analysis and simulation of plasticity*. Vol. 6. Handbook of Numerical Analysis. Elsevier, 1998. DOI: 10.1016/S1570-8659(98)80009-4.

[7] R. Boman and J.P. Ponthot. "Continuous roll forming simulation using arbitrary Lagrangian Eulerian formalism". In: *Key Engineering Materials* 473 (2011), pp. 564–571. DOI: 10.4028/www.scientific.net/KEM.473.564.

ECCOMAS Thematic Conference and IACM Special Interest Conference
Highly Flexible Slender Structures (HFSS 2025)
22–26 September 2025, Kaiserslautern, Germany

Advanced Modeling of Nonsmooth Contact Dynamics between Rigid and Deformable Bodies

Katarina Tutić[1], Teo Mudrić[2], Nina Čeh[3], Martin Arnold[4]

[1] Faculty of Civil Engineering, University of Rijeka, katarina.tutic@gradri.uniri.hr.
[2] Faculty of Civil Engineering, University of Rijeka, teo.mudric2@gradri.uniri.hr
[3] Faculty of Civil Engineering, University of Rijeka, nina.ceh@gradri.uniri.hr
[4] Institut fur Mathematik, Martin-Luther-Universitat Halle-Wittenberg,
martin.arnold@mathematik.uni-halle.de

Keywords: Contact Dynamics, Finite Element Method, Rigid-Deformable Interaction, Unilateral Constraints

The dynamic interaction between a deformable body and a rigid body under unilateral contact constraints is a critical subject in engineering mechanics, particularly in the analysis of impact events and load-bearing scenarios. To address these challenges, specialized algorithms for nonsmooth dynamics are required. By combining numerical simulations with targeted experimental validations, the research aims to refine the modeling and predictive accuracy of contact interactions involving rigid and deformable bodies. This study models the deformable body as a prismatic beam governed by the classical Euler–Bernoulli theory, which considers bending as the primary deformation mode and neglects shear deformations and rotational inertia. To solve the resulting fourth-order partial differential equation numerically, we employ a finite element approach. Within each element, displacement and slope are approximated using shape functions that ensure sufficient continuity. The global system incorporates contact forces as additional nodal contributions whenever contact with a rigid body is detected. These forces are computed based on the instantaneous gap function and can exhibit high gradients over short time intervals. The problem is formulated using a system of differential equations coupled with complementarity conditions:

$$M(q(t))\,\dot{v}(t) = F(t,q(t),v(t)) + G(q(t))\,\lambda(t), \tag{1}$$

$$\dot{q}(t) = v(t), \tag{2}$$

$$g(t) = g(q(t)), \quad \dot{g}(t) = G^T(q(t))\,v(t), \tag{3}$$

$$0 \le g(t) \perp \lambda(t) \ge 0, \tag{4}$$

$$\dot{g}^+(t) = -e\,\dot{g}^-(t). \tag{5}$$

In this formulation, the generalized coordinates $q(t)$ describe the configuration of the system, and their time derivatives, $v(t) = \dot{q}(t)$, represent the velocities. The system dynamics are governed by an equation in which the mass matrix $M(q(t))$ encapsulates the inertial properties, and the force term $F(t,q(t),v(t))$ accounts for both external and internal forces. The term $G(q(t))\,\lambda(t)$ captures the influence of the Lagrange multipliers $\lambda(t)$ that enforce the unilateral contact constraints. Moreover, the gap function $g(q(t))$ quantifies the separation between the bodies, while its time derivative, expressed as $G^T(q(t))\,v(t)$, describes how this separation evolves over time. A complementarity condition ensures that a positive gap implies no contact force (i.e., $\lambda(t) = 0$), whereas a zero gap permits a nonzero contact force. Finally, the restitution law models the instantaneous change in the normal gap velocity during an impact, with the coefficient of restitution e relating the pre-impact velocity $\dot{g}^-(t)$ to the post-impact velocity $\dot{g}^+(t)$. A widely used approach to handling these nonsmooth events are the time-stepping methods. Rather than detecting and processing collisions as discrete events, these methods integrate the governing equations over fixed time intervals, thereby implicitly capturing velocity jumps and transitions in contact status. One of the most influential time-stepping schemes is the Moreau-Jean method [1], which has laid the groundwork for many subsequent approaches in nonsmooth dynamics. We build upon this foundation by aiming to improve contact algorithms, particularly in scenarios involving the interaction between a deformable beam and a rigid body.

In this work, we propose an innovative approach to contact force determination, grounded in momentum conservation and designed to refine existing algorithms. The core idea is to predict the beam's deformation shape

during impact, enabling precise velocity evaluation at every node in the system. Our scheme incorporates the entire beam, thus accounting for its complete deformation profile in the system's equations of motion. This broader perspective allows for a more accurate representation of dynamic effects and the resulting contact forces. By coupling predefined deformation assumptions with detailed velocity data, our algorithm preserves the inertia-driven phenomena often overlooked in previous studies. To validate the proposed numerical models, an extensive series of experimental tests will be performed. High-speed imaging was employed using a ZEISS Aramis 4M camera operating at 600 frames per second to capture the overall dynamics, building on previous studies that focused on the free rocking of a block on an elastic beam [2]. These high-fidelity measurements enabled a thorough analysis of rapid deceleration and other transient effects, thereby corroborating the effectiveness of the nonsmooth contact formulation in capturing instantaneous velocity changes. Digital image correlation (DIC) techniques were applied to reconstruct the three-dimensional motion and deformation profiles. The combined imaging methods will provide comprehensive insights into both the global dynamics and the localized contact events, thus substantiating the accuracy and robustness of the numerical models.

Figure 1 shows preliminary results obtained using the classical Moreau-Jean NSCD method. The left graph presents the vertical trajectories of the ball and the beam's mid-span node, highlighting the ball's rebound upon impact and the subsequent beam vibrations. The right graph compares numerical displacement of the beam's mid-span node against high-speed measurements. Although the existing algorithm captures the general trend and frequency, discrepancies remain in the initial oscillation peaks. These preliminary results serve as a baseline reference. We propose a new formulation designed to ensure momentum conservation, potentially enhance numerical accuracy, and accelerate convergence. Its performance will be compared with experimental data to evaluate the proposed improvements. Future research will seek to extend this methodology to address more complex impact scenarios such as rocking.

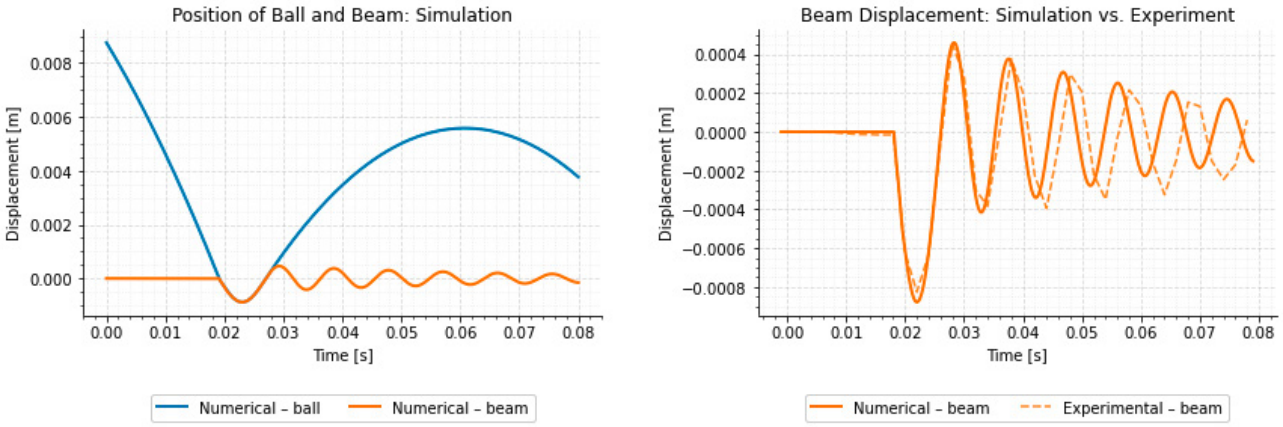

Figure 1: (*Left*) Numerical results for position (*Right*) Beam displacement: numerical simulation vs. experimental data.

Acknowledgments

MZO - DAAD 2024/2025 project titled "Fixed Time-Step Integration Schemes for non-smooth Dynamic Systems with Contact and Friction" funded by the Ministry of Science and Education of the Republic of Croatia.

References

[1] M. Jean, The non-smooth contact dynamics method, *Computer Methods in Applied Mechanics and Engineering*, 177(3–4):235–257, 1999.

[2] Mudrić, T., Čeh, N., Hante, S., & Arnold, M., Free Rocking of a Rigid Block on a Flexible Structure with Non-Smooth Contact Dynamics, *Applied Sciences*, 14(15):6483, 2024.

ECCOMAS Thematic Conference and IACM Special Interest Conference
Highly Flexible Slender Structures (HFSS 2025)
22–26 September 2025, Kaiserslautern, Germany

Automated Constitutive Modeling of Dielectric Elastomer Actuators (DEAs) – Towards Realistic Modeling of Artificial Muscles

Gamal Amer [1], Denisa Martonová [2], Sigrid Leyendecker [3]

[1] Institute of Applied Dynamics, Friedrich-Alexander-Universität Erlangen-Nürnberg, gamal.amer@fau.de
[2] Institute of Applied Mechanics, Friedrich-Alexander-Universität Erlangen-Nürnberg, denisa.martonova@fau.de
[3] Institute of Applied Dynamics, Friedrich-Alexander-Universität Erlangen-Nürnberg, sigrid.leyendecker@fau.de

Keywords: Constitutive Artificial Neural Networks, Automated Model Discovery, Constitutive Modeling, Electro-Mechanical Coupling, Machine Learning.

1. Introduction & Motivation

Electromechanically coupled (EMC) materials are a class of materials that exhibit a direct interplay between electrical and mechanical states, enabling them to convert electrical energy into mechanical energy and vice versa. They have broad range of applications in fields such as sensors, actuators, energy harvesting, biomedical devices, and biological tissues. In this research, dielectric elastomer actuators (DEAs) are considered as a prominent example of isotropic EMC material. They are soft, flexible materials that can undergo substantial deformation in response to an applied electric field [1]. These "artificial muscle'" materials are attractive for soft robotics and biomedical actuators due to their high energy density and fast response. However, accurately modeling their behavior is challenging since DEAs exhibit nonlinear coupled responses and pronounced inelastic effects. Traditional constitutive models often fail to accurately capture the full nonlinear behavior of DEAs [2]. This limitation motivates data-driven approaches that learn material behavior directly from experiments, while embedding known physics to ensure realism and generalizability of the developed constitutive law.

Recent advances in machine learning-based constitutive modeling show promise for automated model discovery in complex materials [3, 4]. In particular, Constitutive Artificial Neural Networks (CANNs) have been proposed as a physics-informed neural network framework for material laws. Instead of treating the material as a black-box function approximator, CANNs integrate fundamental principles of continuum mechanics (kinematics and thermodynamics) into the neural network architecture [3]. This assures the learned model to satisfy physical laws by design, for example, ensuring frame-indifference of the stress response, and obeying thermodynamic consistency during deformation [3, 4]. Building on these insights, this work develops a data-driven, physics-informed constitutive model for DEAs using CANNs, focusing on incorporating electromechanical coupling and inherent material physics into the network.

2. Methodology

CANNs architecture is employed in this work to represent the constitutive behavior of an elastomer under combined mechanical deformation and electric field. Its design encodes continuum mechanics principles like:

- **Thermodynamic consistency**: Network's output is designed to learn a free energy function $\psi(\mathbf{F}, \mathbf{E})$ in terms of the deformation gradient **F** and the electric field **E**. Then, stresses and electric displacements are derived via differentiation of ψ, automatically enforcing energy-conjugacy and the Clausius–Duhem inequality (non-negative dissipation) for any loading path and ensuring energy consistency. Additionally, **polyconvexity** requirements on ψ are satisfied.
- **Material Objectivity**: Network inputs are chosen as invariant measures of deformation and field, so that the predicted stress/response does not depend on arbitrary frame rotations [3]. For instance, the free energy function (ψ) for isotropic materials is mathematically formulated in [5] in terms of purely mechanical invariants I_1^m, I_3^m, purely electrical invariant I_4^e, and coupling invariant I_5^{em} to be:

$$\psi = \frac{1}{2} I_1^m - \mu \ln I_3^m + \lambda (\ln I_3^m)^2 + c_1 I_4^e + c_2 I_5^{em}$$

  where μ, λ, c_1, c_2 represent material parameters.
- **Energy dissipation**: inelastic effects can be modeled via internal-variable sub-networks, ensuring non-negative energy loss. This is done by building up on the work of [2].
- **Electromechanical coupling**: The network learns coupled response by training on data involving both electric and mechanical loading.

Training involves supervised learning on mechanical and electromechanical experimental datasets. Physical bounds (e.g., non-negative energy dissipation) are enforced either through architecture or regularization. The resulting model is compact, interpretable, and transferable to finite element environments.

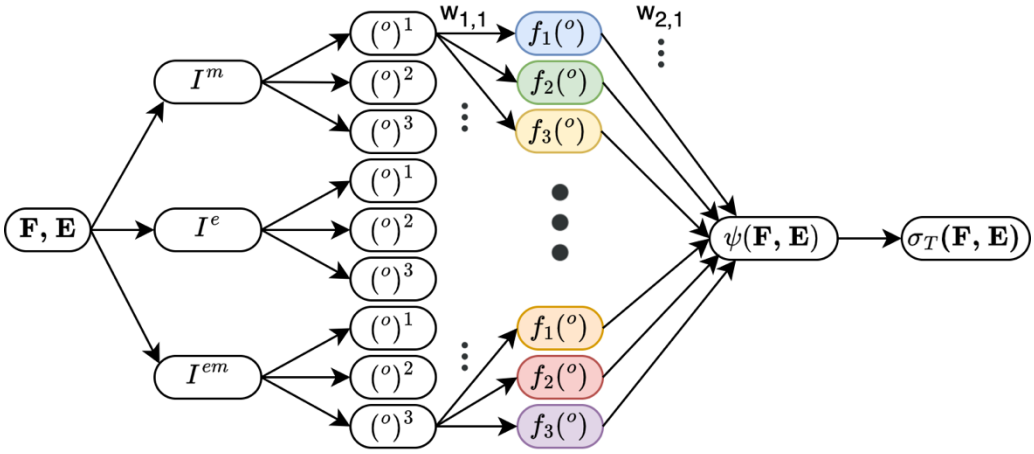

Figure 1. Schematic illustration for a general example of feed-forward CANN architecture of a compressible and elastic DEA based on assumptions in [6] where the total stress σ_T is a sum of the mechanical and electrical stresses. The first layer computes invariants of: purely mechanical (I^m), purely electrical (I^e), and electromechanically coupled (I^{em}) properties. The second layer generates invariants' powers, and the third applies custom-designed activation functions.

3. Main Findings

- Model discovery and accuracy: A data-driven, physics-informed constitutive model for DEAs using CANNs is developed. The model integrates the strengths of machine learning (flexibility to fit complex, high-dimensional data) with the rigor of continuum physics (thermodynamic consistency, etc.). The trained model fits experimental DEA data across multiple loading conditions with high accuracy (coefficient of determination R^2 and mean square error). The network identifies a compact and interpretable energy function, reflecting the material's response according to the data.
- Electromechanical coupling: The trained network successfully learns and describes the nonlinear coupling behavior between electric field and mechanical deformation in DEAs. The resulting constitutive model is generalizable and can be used in different electromechanical loading scenarios, not just the ones it was trained on.
- Comparison with traditional models: The developed CANN model represents a natural generalisation of existing classical models, like [5]. However, it avoids the need for predefined constitutive forms and it handles complex data consistently. Unlike classical material models, the CANN can generalize well to unseen configurations and modes [3, 4]. Once trained, it can be integrated efficiently in FEM solvers and supports robust design and control of DEA devices.

This represents a step toward autonomous model discovery in the field of smart materials, reducing the reliance on manual trial-and-error in constitutive law development. Future work can explore extending this framework to other coupled multiphysics phenomena such as thermo-electro-mechanical effects.

References

[1] E. Hajiesmaili and D. R. Clarke. *Dielectric elastomer actuators*. J. Appl. Phys. 129(15):151102(2021).

[2] H. Holthusen et al. *Theory and implementation of inelastic Constitutive Artificial Neural Networks*. Comput. Methods Appl. Mech. Eng. 428(1). (2024).

[3] K. Linka and E. Kuhl. *A new family of Constitutive Artificial Neural Networks towards automated model discovery*, Comput. Methods Appl. Mech. Engrg. 403:115731(2023).

[4] D. Martonová et al. *Automated model discovery for human cardiac tissue: Discovering the best model and parameters*, Comput. Methods Appl. Mech. Engrg. 428:117078 (2024).

[5] G. Possart et al. *Coupled Modeling and Simulation of Electro-Elastic Materials at Large Strains*. SPIE Smart Structures and Materials + Nondestructive Evaluation and Health Monitoring (2006).

[6] A. Dorfmann and R. W. Ogden. *Nonlinear Electroelasticity*. Acta Mechanica 174(3). (2005).

ECCOMAS Thematic Conference and IACM Special Interest Conference
Highly Flexible Slender Structures (HFSS 2025)
2226 September 2025, Kaiserslautern, Germany

Symplectic Model Order Reduction with Autoencoders and Transformers

Benedikt Brantner [1], Michael Kraus [2],

[1] Max–Planck–Institut für Plasmaphysik, benedikt.brantner@ipp.mpg.de
[2] Max–Planck–Institut für Plasmaphysik, michael.kraus@ipp.mpg.de

Keywords: Machine Learning, Neural Networks, Hamiltonian Systems, Structure Preservation, Manifold Optimization

1. Introduction

In this talk we give an overview over machine learning techniques that can be applied for model order reduction of Hamiltonian systems [4]. We thereby put an emphasis on using neural networks for this task.

In recent years machine learning has not only shown successes in fields such as natural language processing and image classification [6], but also in scientific computing [2]. Other than in natural language processing and image processing however, structure preservation has traditionally been an important factor in scientific computing [1, 7] and is now also increasingly recognized in machine learning [10, 8].

Data-driven reduced order modeling is a specific application of machine learning in which the aim is to construct a cheap representation of a full order model (FOM) with machine learning techniques, which are applied to data coming from the FOM. We also refer to such a cheaper representation as a *reduced order model* (ROM).

The talk will be presented in four parts. In the first part we sketch the idea behind Hamiltonian systems and structure preservation. In the second part we explain the concept of symplectic model order reduction to motivate the application of specific neural network architectures which we will introduce in parts three and four; those architectures are symplectic autoencoders and symplectic transformers.

2. Hamiltonian Systems and Structure Preservation

Hamiltonian systems are a special class of differential equations. The vector field describing an HODE is of the following form: $X_H(z) = \mathbb{J}\nabla_z H$, where $\mathbb{J} = \begin{bmatrix} \mathbb{O} & \mathbb{I}_n; & -\mathbb{I}_n & \mathbb{O} \end{bmatrix}$ is the Poisson tensor, $H : \mathbb{R}^{2n} \to \mathbb{R}$ is a differentiable function called the *Hamiltonian* and $\nabla_z H$ is the gradient of H at z. The form of the vector field X_H is a very restrictive one and this also implies very strong properties for the flow of the HODE $\varphi : \mathbb{R}^{2n} \to \mathbb{R}^{2n}$, most importantly symplecticity: $(\nabla_z \varphi)^T \mathbb{J} \nabla_z \varphi = \mathbb{J}$.

Symplecticity implies the conservation of all Poincaré invariants (there are in total n such invariants) [7] as well as Gromov's non-squeezing theorem [9]. In a two-dimensional Hamiltonian system these properties largely correspond to volume preservation, but they become stronger as n increases. For large n considering symplecticity in numerical schemes becomes almost inevitable for long-term stable simulations [10, 11].

3. Symplectic Model Order Reduction

In symplectic model order reduction the aim is to build a reduced model that shares the property of symplecticity with the full system. The ultimate goal is to construct a ROM that is much cheaper to solve than the FOM while preserving its Hamiltonian structure, i.e. a symplectic FOM should be reduced to a symplectic ROM.

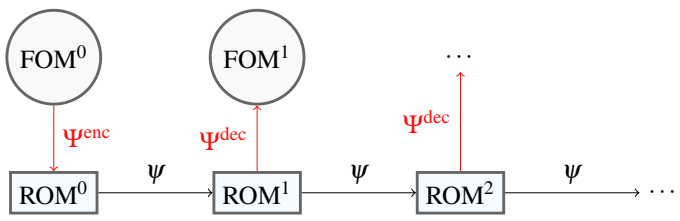

Figure 1: The splitting in *offline* and online phase. In the offline phase we construct a pair of an encoder Ψ^{enc} and a decoder Ψ^{dec}. In the online phase we solve the reduced dynamics with a map ψ.

The idea behind constructing and solving a reduced model is sketched in Figure 1. Here we divide the workflow into two phases: an offline phase and an online phase. In the offline phase we construct an encoder Ψ^{enc} and a decoder Ψ^{dec} whose purpose it is to communicate between the FOM and the ROM. In the online phase we solve the reduced system. For the offline phase we can use symplectic autoencoders (see Section 4.) and for the online phase we can use symplectic transformers (see Section 5.).

4. Symplectic Autoencoders

Symplectic autoencoders (SAEs) [3] offer a way of constructing neural networks that can map a symplectic FOM to a symplectic ROM. Here the pair $(\Psi^{\text{enc}}, \Psi^{\text{dec}})$ satisfies the following requirements:

$$(\nabla_z \Psi^{\text{enc}}) \mathbb{J}_{2N} (\nabla_z \Psi^{\text{enc}})^T = \mathbb{J}_{2n} \text{ and } (\nabla_{\tilde{z}} \Psi^{\text{dec}})^T \mathbb{J}_{2N} (\nabla_{\tilde{z}} \Psi^{\text{dec}}) = \mathbb{J}_{2n}, \tag{1}$$

for all $z \in \mathbb{R}^{2N}$ and $\tilde{z} \in \mathbb{R}^{2n}$. If the requirements in Equation (1) are satisfied, then we get via "symplectic manifold Galerkin projection" [4] an equation $f^{\text{ROM}}(z) = \mathbb{J}_{2n} \nabla_z (H \circ \Psi^{\text{dec}})$.

5. Symplectic Transformers

Symplectic transformers can be used in the online phase of reduced order modeling, i.e. they model ψ (see Figure 1). They are based on the popular transformer architecture [12]. The important advantage of transformers over standard neural networks is that they can resolve time series data and are very efficient for application on GPU. The first property is of advantage in reduced order modeling [5]. We derive the new symplectic transformer architecture similarly to how *generalized Hamiltonian neural networks* [8] are constructed.

References

[1] Douglas N Arnold, Richard S Falk, and Ragnar Winther. "Finite element exterior calculus, homological techniques, and applications". In: *Acta numerica* 15 (2006), pp. 1–155.

[2] Nathan Baker et al. *Workshop report on basic research needs for scientific machine learning: Core technologies for artificial intelligence*. Tech. rep. USDOE Office of Science (SC), Washington, DC (United States), 2019.

[3] Benedikt Brantner and Michael Kraus. "Symplectic autoencoders for Model Reduction of Hamiltonian Systems". In: *arXiv preprint arXiv:2312.10004* (2023).

[4] Patrick Buchfink, Silke Glas, and Bernard Haasdonk. "Symplectic model reduction of Hamiltonian systems on nonlinear manifolds and approximation with weakly symplectic autoencoder". In: *SIAM Journal on Scientific Computing* 45.2 (2023), A289–A311.

[5] Stefania Fresca, Luca Dede, and Andrea Manzoni. "A comprehensive deep learning-based approach to reduced order modeling of nonlinear time-dependent parametrized PDEs". In: *Journal of Scientific Computing* 87 (2021), pp. 1–36.

[6] Ian Goodfellow, Yoshua Bengio, and Aaron Courville. *Deep learning*. Cambridge, MA: MIT press, 2016.

[7] Ernst Hairer, Christian Lubich, and Gerhard Wanner. *Geometric Numerical integration: structure-preserving algorithms for ordinary differential equations*. Heidelberg: Springer, 2006.

[8] Philipp Horn et al. "A generalized framework of neural networks for Hamiltonian systems". In: *Journal of Computational Physics* 521 (2025), p. 113536.

[9] Dusa McDuff and Dietmar Salamon. *Introduction to symplectic topology*. Oxford University Press, 2017.

[10] Liqian Peng and Kamran Mohseni. "Symplectic model reduction of Hamiltonian systems". In: *SIAM Journal on Scientific Computing* 38.1 (2016), A1–A27.

[11] Tomasz M Tyranowski and Michael Kraus. "Symplectic model reduction methods for the Vlasov equation". In: *Contributions to Plasma Physics* 63.5-6 (2023), e202200046.

[12] Ashish Vaswani et al. "Attention is all you need". In: *Advances in neural information processing systems* 30 (2017).

ECCOMAS Thematic Conference and IACM Special Interest Conference
Highly Flexible Slender Structures (HFSS 2025)
22–26 September 2025, Kaiserslautern, Germany

Stability of Discretized Flows on Riemannian Manifolds

Marta Ghirardelli [1], Brynjulf Owren [2], Elena Celledoni [3]

[1] Norwegian University of Science and Technology, marta.ghirardelli@ntnu.no
[2] Norwegian University of Science and Technology, brynjulf.owren@ntnu.no
[3] Norwegian University of Science and Technology, elena.celledoni@ntnu.no

Keywords: Optimization, Riemannian manifolds, Geometric integrators

1. Introduction

Neural networks (NN) can be considered as discretizations of continuous dynamical systems. In this context, stability is an important consideration both for the architecture itself and for the gradient flow for optimizing the parameters. In both cases, stable discretization methods can be relevant e.g. for improving adversarial robustness [3]. To address issues such as exploding or vanishing gradients, it is common to model the feature and/or parameter spaces of NNs as Riemannian manifolds. As a result, architectures defined on Riemannian manifolds have gained popularity. Figure 1 illustrates an example of such a model on the 2-sphere S^2. The task is to classify points belonging to two intertwined spirals. A neural ODE, whose architecture is intrinsically defined on S^2, is trained to approximate the flow of a vector field that moves the points to facilitate their separation. Our goal is to provide a tool for controlling the time step in a neural ODE such that the input/output map is non-expansive (or 1-Lipschitz).

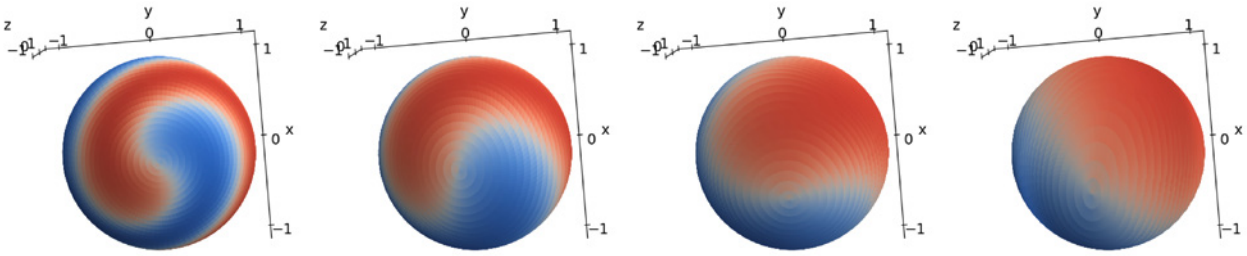

Figure 1: Evolution of two intertwined spirals on S^2.

We propose a framework for analyzing the stability of numerical integrators on Riemannian manifolds. Our approach establishes conditions on the ODE vector field and the step size that makes the numerical solution non-expansive whenever the exact solution is non-expansive over the same time step. We focus on a geodesic version of the explicit Euler method and derive precise stability bounds in the case of Riemannian manifolds with constant sectional curvature. The analysis is based on a cocoercivity property of the vector field adapted to manifolds from Euclidean space. Such formulation enables us to compare the new results to the corresponding well-known results in flat spaces, and in general we observe that a non-zero curvature will deteriorate the stability region of the geodesic Euler method. In [1] numerical experiments for spheres and hyperbolic 2-space are shown and confirm that the bounds are tight.

2. Stability analysis for nonlinear problems on Riemannian manifolds

Let (M, g) be a smooth Riemannian manifold, ∇ its associated Levi-Civita connection. The metric g induces an inner product $\langle \cdot, \cdot \rangle$ and a norm $\| \cdot \|$ on each tangent space T_pM, $p \in M$, and a distance d on M [5, 6].
The notion of stability of nonlinear problems is often related to contractivity with respect to a distance: given two initial points y_0 and z_0 in M and an ODE vector field X defined on M, a method is stable if

$$d(\Phi_{h,X}(y_0), \Phi_{h,X}(z_0)) \leq d(y_0, z_0) \quad \Rightarrow \quad d(y_1, z_1) \leq d(y_0, z_0),$$

for some step size h, where $\Phi_{h,X}(y_0)$ denotes the exact flow of X at time h departing from y_0, and y_1 its approximation given by the method. The above condition on X is closely related to its monotonicity

$$\langle \nabla_{v_p} X, v_p \rangle \leq -\nu \|v_p\|^2, \tag{1}$$

for some $\nu \in \mathbb{R}$, which implies

$$d(\Phi_{t,X}(y), \Phi_{t,X}(z)) \leq e^{-\nu t} d(y,z),$$

and guarantees that the flow of X is non-expansive whenever $\nu \geq 0$.
The monotonicity condition (1) is well-suited for highly stiff vector fields X [2], but limited in non-stiff scenarios, where explicit schemes may be favorable. Inspired by Dahlquist and Jeltsch [4], we replace (1) with the cocoercivity condition

$$\langle \nabla_{v_p} X, v_p \rangle \leq -\alpha \|\nabla_{v_p} X\|^2, \quad \alpha \geq 0. \tag{2}$$

Condition (2) also ensures non-expansivity of the flow of X.

3. Precise bounds for the Geodesic Explicit Euler method

One step of the Geodesic Explicit Euler (GEE) method is given by

$$y_{n+1} = \exp_{y_n}(hX|_{y_n}), \tag{3}$$

i.e. the point reached at time h by the geodesic emanating from y_n with initial velocity $X|_{y_n}$.
Let M have constant sectional curve equal to 1 and let X satisfy (2) for some $\alpha > 0$. Then the GEE method is non-expansive whenever h fulfills

$$h \leq 2\alpha - 2\mu F(h\|X\|)$$

where $\mu > 0$ depends on X and F is a non-negative increasing function. The size of h must hence be adjusted depending on the distance traveled over one step. The above bound reduces to $h \leq 2\alpha$ in flat spaces [4].
We refer to [1] for further details and results in any space with constant sectional curvature.

4. Conclusions

We have introduced a framework for analyzing the stability of numerical integrators on Riemannian manifolds, deriving precise bounds that guarantee the stability of the Geodesic Explicit Euler method in the case of constant sectional curvature. These bounds are more restrictive than in flat (zero-curvature) space. Nonetheless, they can be useful for designing non-expansive neural ODE architectures when such models are defined on Riemannian manifolds.

Acknowledgments

This project has received funding from the Horizon Europe, MSCA-SE project 101131557 (REMODEL).

References

[1] M. Ghirardelli and B. Owren and E. Celledoni. *Conditional Stability of the Euler Method on Riemannian Manifolds*, arXiv, 2025.

[2] M. Arnold and E. Celledoni and E. Çokaj and B. Owren and D. Tumiotto. *B-stability of numerical integrators on Riemannian manifolds*, Journal of Computational Dynamics, 11 (2024), 92-107.

[3] F. Sherry and E. Celledoni and M.J. Ehrhardt and D. Murari and B. Owren and C. Schönlieb. *Designing stable neural networks using convex analysis and ODEs*, Physica D. Nonlinear Phenomena, 463 (2024).

[4] G. Dahlquist and R. Jeltsch. *Generalized disks of contractivity for explicit and implicit Runge-Kutta methods*, Dept. of Numerical Analysis and Computer Science, The Royal Institute of Technology, Stockholm, (1979).

[5] J. M. Lee. *Introduction to Riemannian manifolds*, Springer, Cham, second edition, 2018.

[6] J. Jost. *Riemannian geometry and geometric analysis*, Springer, Cham, seventh edition, 2017.

ECCOMAS Thematic Conference and IACM Special Interest Conference
Highly Flexible Slender Structures (HFSS 2025)
22–26 September 2025, Kaiserslautern, Germany

AI-Based Methods for Accelerating the Simulation of Flexible Structures

Michael Burger [1], Jochen Fiedler [1], Vicky Holfeld [1], Joachim Linn [1],
Michael Roller [1] and Fabio Schneider-Jung [1]

[1] Fraunhofer ITWM, Division Mathematics for Vehicle Engineering, Fraunhofer-Platz 1, 67663 Kaiserslautern, Germany, [michael.burger,jochen.fiedler,vicky.holfeld]@itwm.fraunhofer.de, [michael.roller,joachim.linn, fabio.julian.schneider-jung]@itwm.fraunhofer.de

Keywords: structural mechanics, shell, machine learning methods, AI-based surrogate modelling, neural networks

1. Introduction

In industry, there is a high interest in assembly simulations involving flexible surface-like and flexible volumetric components. The overall goal is to make realistically behaving models of such deformable structures available for interactive handling in virtual or augmented, i.e. extended reality (XR). This could be achieved by physics-based simulation technology and mathematical methods for nonlinear model order reduction [1] in combination with data-based modelling and artificial intelligence (AI). Speeding up simulations by methods of this type is necessary, since the physics-based simulation models in focus belong to the class of geometrically nonlinear structural model are far too costly to achieve the performance necessary for simulations at interactive frame rates. In this contribution, we focus on a nonlinear quasi-static shell model [2] as mechanical system and investigate AI-based methods for this class of problems due to their real-time capability.

2. Problem Description

In the recent study, the system under consideration is a shell of fixed size, i.e. length, width and thickness, see Figure 1, which is clamped at the left. The right end is clamped to a rigid body, which is movable as prescribed. More formally, let the trajectory of rigid body positions be denoted by $q_r \in \mathbb{R}^{L\times n_r}$, $n_r = 3$, and the corresponding

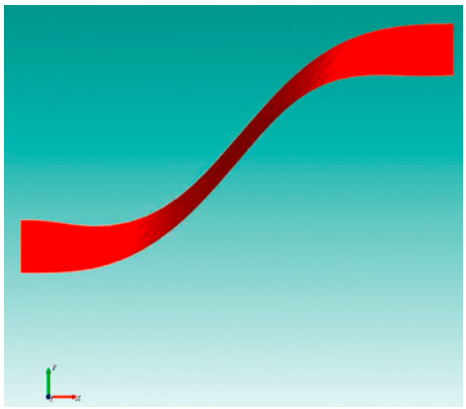

Figure 1: Deformation of a shell with clamped left end and moving right end.

trajectory of shell configurations by $q_s \in \mathbb{R}^{L\times n_s}$, $n_s = 744$, where L is the length in time, n_r the dimension of the rigid body position and n_s is the number of degrees of freedom of the shell. Then, our goal is to find a surrogate model f, being a map of the form

$$q_s = f(q_r), \tag{1}$$

that allows us to analyze and predict the resulting trajectories of shell deformations as the right end is displaced over time. Here, the output dimension n_s is explained as follows. For each node of the shell discretization, that are in total $N = 124$, we have 6 degrees of freedom being given by translation and rotation. That is, the modelling problem is of low-dimension in the input but high-dimensional in the output.
The deformation trajectories q_s are crucial as they serve as training data for our surrogate models. By systematically varying the displacement at the right end and capturing the corresponding deformations, we create a

comprehensive dataset (q_r, q_s) that encapsulates the nonlinear behavior of the shell under load. This simulated dataset is then used for training and validating our surrogate models, enabling them to accurately predict the shell's behavior in real-time applications.

3. AI-based Surrogate Modelling

To efficiently model the complex behavior of the shell, we particularly employ AI-based methods, specifically recurrent neural networks (RNNs) such as Long Short-Term Memory (LSTM) networks [3] and graph neural networks (GNNs) [4] as surrogates f. LSTMs are particularly suitable for this class of problems due to their ability to capture temporal dependencies in sequential data, making them effective for learning the dynamic changes in the shell's deformation over time. On the other hand, GNNs excel at modeling the interactions between different parts of the shell, considering its geometric properties and connectivity. The real-time capability of these models is a significant advantage, as they can provide rapid predictions of deformation states without the computational overhead associated with traditional physics-based simulations. Our initial results indicate promising accuracy in the predictions of shell deformations using the named networks, and we systematically analyze the errors made by the surrogate models. Furthermore, we test these models on new, unknown test data to validate their generalization capabilities. In our presentation, we will illustrate the general usability, the modelling approach and show first results.

References

[1] P. Benner, M. Ohlberger, A. Cohen and K. Willcox. *Model Reduction and Approximation*, Society for Industrial and Applied Mathematics, 2017.

[2] M. Roller, C. Cromvik and J. Linn. *Robust and Fast Simulation of Flexible Flat Cables*, Multibody Dynamics 2019: Proceedings of the 9th ECCOMAS Thematic Conference on Multibody Dynamics, 2022.

[3] B. Ghojogh, A. Ghodsi. *Recurrent Neural Networks and Long Short-Term Memory Networks: Tutorial and Survey*, 2023.

[4] T. N. Kipf, M. Welling. *Semi-Supervised Classification with Graph Convolutional Networks*, 5th International Conference on Learning Representations, 2017.

ECCOMAS Thematic Conference and IACM Special Interest Conference
Highly Flexible Slender Structures (HFSS 2025)
22–26 September 2025, Kaiserslautern, Germany

Learning dynamics and symmetry

David Martín de Diego [1], Miguel Vaquero [2]

[1] ICMAT, Spain (david.martin@icmat.es)
[2] IE University, Spain (mvaquero@faculty.ie.edu)

Keywords: Generating function, Lagrangian submanifold, learning, Hamiltonian function, symmetry

1. Introduction

Neural networks have proven to be effective in learning patterns from data in many different contexts. A remarkable and recent example is the use of neural networks to learn dynamical systems.

A recent trend in the machine learning community aims at combining the mentioned success of neural networks with other known structures, in order to improve the performance of the former. For instance, when the system under concern has an underlying structure (e.g. Lagrangian or Hamiltonian) one could identify the equations of motion directly, or alternatively, identify the Hamiltonian or the Lagrangian functions which define them. This simple idea led to the construction of Hamiltonian Neural Networks (HNN) [3] and Lagrangian Neural Networks (LNN), which have increased accuracy in prediction and improved the models. We propose to continue this development of more involved constructions that combine machine learning and geometric structures. In particular, one important aspect is the inclusion of symmetries and momentum mappings in the learning process [5, 1]. In classical mechanics the study of symmetries and momentum mappings has become one of the recurrent topics due to the importance in applications. Therefore, when learning geometric systems the next question is of pivotal importance: How can we design learning paradigms that learn the underlying symmetries and use them to improve the performance of the resulting models?

Additionally, exploitation of other geometric structures besides symplectic geometry. This is the case of Poisson and Dirac structures and dynamics described by Lagrangian submanifolds. Even in the current nascent state of the field, the inclusion of symplectic geometry has shown to be very relevant and of high impact on the machine learning community.

Acknowledgments

This project has received funding from Grants PID2022-137909-NB-C21, PCI2024-155047-2, TED2021-129455B-I00 and CEX2023-001347-S funded by MICIU/AEI/10.13039/501100011033.

References

[1] M. Barbero-Liñán, J.C. Marrero, D. Martín de Diego. *F*rom retraction maps to symplectic-momentum numerical integrators, IFAC-PapersOnLine, 58 (6), 155-159, 2024.

[2] M. Barbero Linán and David Martín de Diego and R. T. Sato: *A new perspective on symplectic integration of constrained mechanical systems via discretization maps*, https://arxiv.org/abs/2306.06786,

[3] S. S. Greydanus, M. Dzamba, J. Yosinski. *Hamiltonian Neural Networks*, Advances in neural in formation processing systems, 32 (2019).

[4] Vaquero, M; Cortés, J., Martín de Diego, D. *Symmetry preservation in Hamiltonian systems: simulation and learning*, J. Nonlinear Sci. 34 (2024), no. 6, 29 pp.

[5] Vaquero, M; Cortés, J., Martín de Diego, D. *Designing Poisson integrators through machine learning* IFAC-PapersOnLine 58 (6), 31-35, 2024

ECCOMAS Thematic Conference and IACM Special Interest Conference
Highly Flexible Slender Structures (HFSS 2025)
22–26 September 2025, Kaiserslautern, Germany

Error analysis of higher order integration schemes in the context of neural network based modelling

Felix Mest, Martin Arnold
Institute of Mathematics, Martin Luther University Halle-Wittenberg
{felix.mest, martin.arnold}@mathematik.uni-halle.de

Keywords: Approximation order, Numerical integration, Neural networks, Euler's elastica

1. Introduction

Classical modelling approaches for highly flexible slender structures result in variational problems and differential equations, which can be difficult to solve efficiently by standard solvers [2]. With the rise of neural network applications in science and computational mechanics [5], a natural idea is to use neural networks for such tasks. Two main trends in machine learning-based approximation for solving ordinary or partial differential equations have been identified: Training a neural network to produce a discrete solution and training a neural network to represent a continuous solution to the problem [2]. We focus on the latter. More specifically, we consider the case where the solution is obtained integrating the continuous function represented by the neural network and show how the neural network model and training process may affect the error of numerical integration schemes.

For numerical experiments, we follow Celledoni et al. [2] and consider a typical model of highly flexible slender structures: Euler's elastica. We investigate a neural network introduced by [2], which represents the continuous tangential angle function of a solution of Euler's elastica under certain boundary conditions. Numerical integration methods are applied to the respective tangential vectors for reconstructing Euler's elastica and method-specific errors are presented.

2. Test problem: Euler's elastica

Euler's elastica models the deformation of the centerline of an inextensible beam with constant cross-section, which is assumed to be perpendicular to the centerline [2]. Let $\mathbf{q} \in C^2([0,L],\mathbb{R}^2)$ be a planar centerline for simplicity. If s is the arc length parameter of $\mathbf{q}$, then $\|\mathbf{q}'(s)\| = 1$ and the length of the beam is given by L. Let $\kappa(s) = \|\mathbf{q}''(s)\|$ denote the curvature, then $F = EI \cdot \kappa$ (Hooke's law) and the potential energy is given by $U(s) = EI\kappa^2/2$, assuming constant bending stiffness EI. The goal is to minimize the action functional

$$S[\mathbf{q}] = \int_0^L U(s) + \Lambda(s)\phi(\mathbf{q}(s),\mathbf{q}'(s))ds$$

under boundary conditions $\mathbf{q}(0) = \mathbf{q}_0, \mathbf{q}'(0) = \mathbf{q}'_0, \mathbf{q}(L) = \mathbf{q}_L, \mathbf{q}'(L) = \mathbf{q}'_L \in \mathbb{R}^2$, where $\phi(\mathbf{q},\mathbf{q}') = \|\mathbf{q}'\|^2 - 1$ is the constraint function for arclength parameterization and Λ are Lagrange multipliers.

With data generated by classical methods [2], which may in practice be replaced by real-world data, a neural network is trained, such that it represents the tangential angle function θ of Euler's elastica under certain boundary conditions. Specifically, for input $(\theta_0, \theta_N, s_n)$ with θ_0 and θ_N being tangential angles at the boundary, a network is trained to have the output $\hat{\theta}(s_n) \approx \theta(s_n)$ on an equidistant partition $0 = s_0 < s_1 < \cdots < s_N = L$ with $N = 50$. During training, Euler's elastica is reconstructed via numerical integration of $\hat{\mathbf{q}}' = \mathbf{f}(\hat{\theta})$, $\hat{\mathbf{q}}(0) = \mathbf{q}_0$, $\mathbf{f}(\theta) = (\cos\theta, \sin\theta)^\top$. The mean squared error of $(\mathbf{q}_n, \mathbf{q}'_n)$, $n = 0,1,\ldots,N$, to the classical solutions is then minimized by stochastic gradient descent using the Adam optimizer [2].

Note that this is a pure quadrature problem, since $\mathbf{f}$ only depends on the output $\hat{\theta}(s)$ of the neural network. The mean squared error over the reconstructed test curves and their derivatives was $6.289 \cdot 10^{-6}$. The boundary condition at $s = L$ may be considered by a minor modification of $\hat{\theta}$ at both ends of the elastica [2].

3. Numerical results

As in [2], we investigate the composite 3-point Gaussian quadrature formula. For $g \in C^6[0,L]$, this formula has an error of $C_0 L h^p g^{(p)}(\xi)$ for some $\xi \in [0,L]$, $C_0 \approx 4.96 \times 10^{-7}$ and $p = 6$, see [3]. We calculate the average errors of 98 reconstructed curves for various numbers of nodes. The reference solution used $M = 83160$ nodes

and is also calculated by the composite 3-point Gaussian method. Numerical results show errors $\hat{C}h^{\hat{p}}$ with error constant $\hat{C} \approx 0.88$ and order $\hat{p} \approx 3.14$, which is a substantial loss of accuracy compared to the classical setting.

Fig. 1 shows the errors over $h = L/m$, where $L = 3.3$ and m is the number of subintervals in the composite rule. Furthermore, Fig. 1 displays the errors of the trapezoidal sum, the randomized trapezoidal sum and the composite Simpson's $1/3$ rule. The trapezoidal sum has $C_0 \approx 0.08,\ p = 2$ and $\hat{C} \approx 1.3,\ \hat{p} \approx 2.09$. Simpson's rule is characterized by $C_0 \approx 3.47 \times 10^{-4},\ p = 4$, while $\hat{C} \approx 1.63,\ \hat{p} \approx 2.96$. For the randomized trapezoidal sum, we observe $\hat{C} \approx 0.73,\ \hat{p} \approx 2.12$, which is below its optimal order $p = 2.5$ for $g^{(2)} \in \mathscr{L}^2[0,L]$. It shows only a slight improvement over the deterministic trapezoidal sum. Randomization could not compensate the missing smoothness of the neural network generated data $\hat{\theta}(s)$.

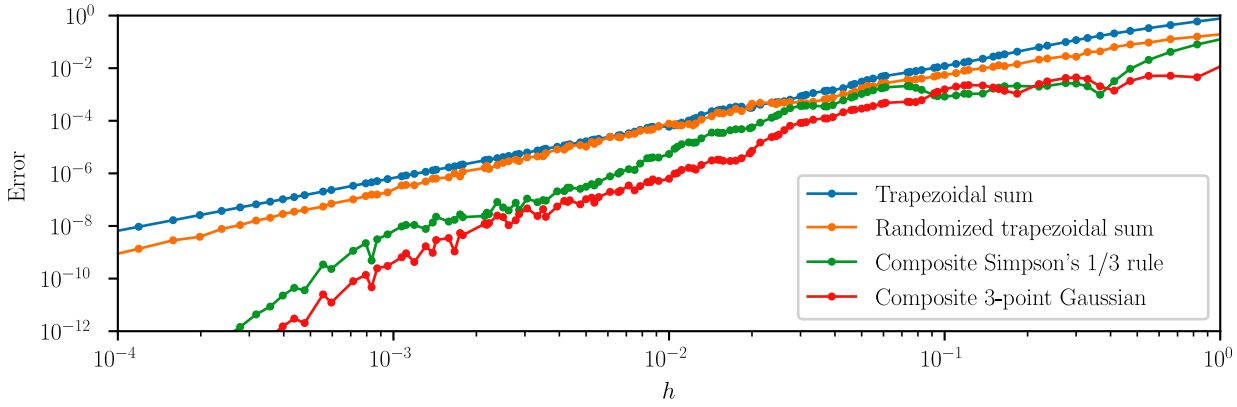

Figure 1: Errors of quadrature formulae

4. Conclusions

Numerical methods of higher order are tailored to mathematical problems that are "smooth" in the sense that they are sufficiently often differentiable and all derivatives are bounded by constants of moderate size. Standard neural network approximations do not meet these requirements. Numerical test results for a neural network approximation of Euler's elastica illustrate that high order Gaussian quadrature may loose much of its benefits in this context. On the other hand, the asymptotic behaviour on fine grids is clearly superior to lower order methods like trapezoidal rule and compares to Simpson's $1/3$ rule. Up to now, there is no strict theoretical justification for this favourable asymptotic behaviour. In future work, we plan to investigate locally defined smooth shadow problems that have been used successfully in the error analysis of higher order ODE time integration methods for models that contain data being approximated by linear or cubic spline functions [1].

Acknowledgement
The authors acknowledge gratefully the advice of Raphael Kruse (Halle) on randomized quadrature formulae.

References

[1] M. Arnold. Towards improved error estimates for higher order time integration of ODEs with non-smooth right hand side. In Per Grove Thomsen and Hans True, editors, *Non-smooth Problems in Vehicle Systems Dynamics*, pages 227–237, Berlin, Heidelberg, 2010. Springer Berlin Heidelberg.

[2] E. Celledoni, E. Çokaj, A. Leone, S. Leyendecker, D. Murari, B. Owren, R. T. Sato Martín de Almagro, and M. Stavole. Neural networks for the approximation of Euler's elastica. *Computer Methods in Applied Mechanics and Engineering*, 435:117584, 2025.

[3] P. Deuflhard and A. Hohmann. *Numerical Analysis*. De Gruyter, Berlin, Boston, 1995.

[4] S. Haber. A modified Monte-Carlo quadrature II. *Math. Comp. 21, 388–397*, 1967.

[5] L. Vu-Quoc, A. Humer. Deep learning applied to computational mechanics: A comprehensive review, state of the art, and the classics. *Computer Modeling in Engineering & Sciences*, 137(2):1069–1343, 2023.

ECCOMAS Thematic Conference and IACM Special Interest Conference
Highly Flexible Slender Structures (HFSS 2025)
22–26 September 2025, Kaiserslautern, Germany

Asymptotic expansion method for curved and variable beams

Mohammed-Khalil Ferradi [1]

[1] College of Computing, Mohammed VI Polytechnic University, khalil.ferradi@um6p.ma

Keywords: Enriched beam model, asymptotic expansion method, curved beam, variable cross-section.

1. Introduction

In a previous work in [1,2], the asymptotic expansion method was used to derive a 3D beam model, incorporating the local effects of external forces. The model is valid for straight beams with a constant cross-section, and can be seen as the projection of the beam's 3D displacement $\boldsymbol{u}$ onto a set of kinematic modes:

$$\boldsymbol{u}(\boldsymbol{x}) = \sum \boldsymbol{\psi}^i(x^1, x^2)\zeta^i(x^3) \ , \tag{1}$$

where (x^1, x^2) are the transverse coordinates of the section, x^3 is the longitudinal coordinate, $\boldsymbol{\psi}^i(x^1, x^2)$ is the ith mode of the beam, and $\zeta^i(x^3)$ its associated degree of freedom. The greater the number of modes used, the more accurate the 1D model becomes, approximating the 3D model with a very high accuracy. The goal of the asymptotic method is then to determine the most optimal set of modes representing the beam's response.

However, directly using the modes obtained for a straight beam to define the kinematics for a curved beam is not a viable solution for constructing the enriched beam model. Indeed, not only do these modes fail to capture effects specific to curvature, but they can also lead to erroneous results due to locking issues. It is therefore necessary to define an enrichment that accounts for the effect of the curvature and/or a variable cross-section of the beam in the computation of the modes.

2. The asymptotic method for curved and variable beams

In [3] and [4], the asymptotic method was respectively developed for the case of a beam with constant curvature, and for the case of a beam with a linearly varying cross-section.

For each case, the method can be summarized in the following steps:

- Choose an adequate parametrization of the beam's geometry.
- Write the 3D mechanical problem in the curvilinear coordinates associated to the natural base (covariant base) of the beam.
- Introduce the scaling factor η on the covariant and contravariant components of the stress, strain and displacement tensors $(\boldsymbol{\sigma}, \boldsymbol{\varepsilon}, \boldsymbol{u})$, to separate the transversal and the longitudinal variation.
- Express the different unknowns as power series of η, and derive a series of hierarchical problems to solve.
- Determine the kinematic modes $\boldsymbol{\psi}^i$ and stress modes $\boldsymbol{\Phi}^i$ from the solution of the hierarchal problems.

The accuracy of the obtained model was tested through several examples by comparing it with the results of a shell discretization. For example, in Fig.1, a box girder with a large curvature is considered. The results in Fig.2 show a good agreement between the beam model with the shell model.

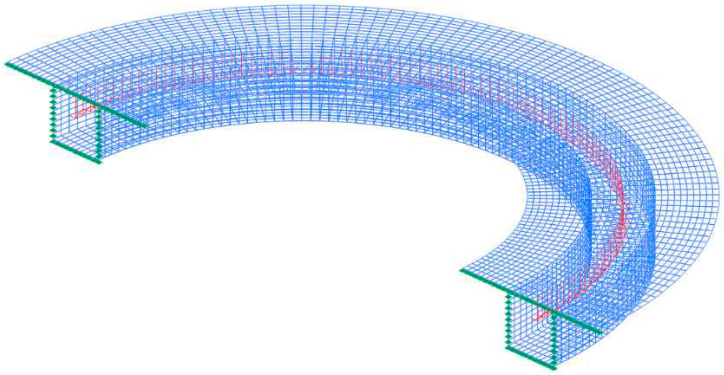

Figure 1. Semi-circular box girder. Clamped at both ends with a vertical linear force at its center.

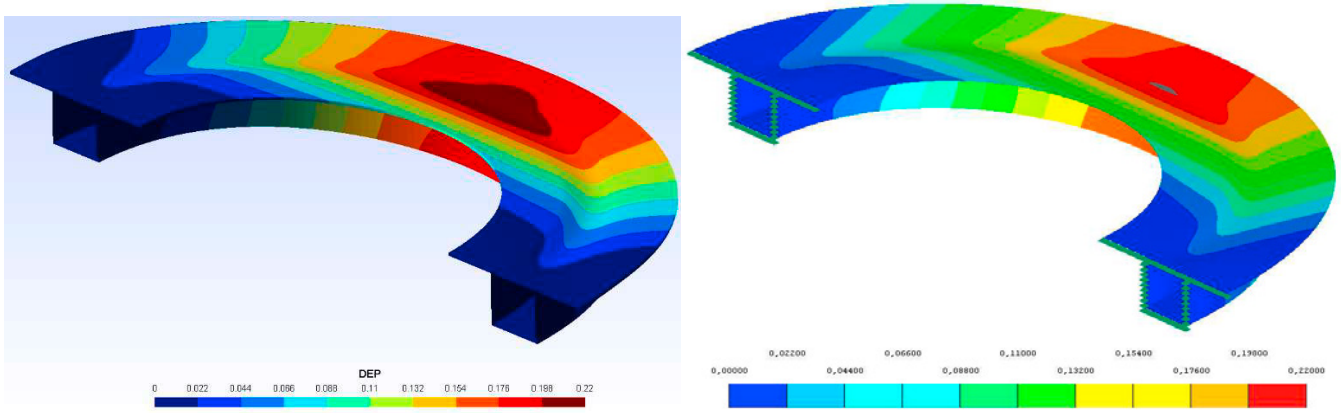

Figure 2. Iso-displacement lines. Beam model (right), shell model (left).

3. Conclusions

The results show that the effects of geometry and external forces are well captured by the kinematics derived from the asymptotic method, demonstrating that the beam model can serve as a suitable alternative to a more computationally expensive shell or 3D model. However, a general framework for arbitrarily varying beams has yet to be established.

References

[1] Ferradi, M. K., Lebée, A., Fliscounakis, A., Cespedes, X., & Sab, K. (2016). A model reduction technique for beam analysis with the asymptotic expansion method. *Computers & Structures*, *172*, 11-28.

[2] Corre, G., Lebée, A., Sab, K., Ferradi, M. K., & Cespedes, X. (2018). The asymptotic expansion load decomposition elastoplastic beam model. *International Journal for Numerical Methods in Engineering*, *116*(5), 308-331.

[3] Ferradi, M. K., & Cespedes, X. (2021). A curved beam model with the asymptotic expansion method. *Engineering Structures*, *241*, 112494.

[4] Ferradi, M. K. (2022). The Saint-Venant Solution of a 3D Tapered Beam. *Journal of Elasticity*, *148*(1), 1-25.

ECCOMAS Thematic Conference and IACM Special Interest Conference
Highly Flexible Slender Structures (HFSS 2025)
22–26 September 2025, Kaiserslautern, Germany

Twisting instabilities in elastic ribbons with inhomogeneous pre-stress

Michael Gomez [1,2], Pedro M. Reis [1], Basile Audoly [3]

[1] Flexible Structures Laboratory, Institute of Mechanical Engineering, École Polytechnique Fédérale de Lausanne (EPFL), 1015 Lausanne, Switzerland
[2] Department of Engineering, King's College London, Strand, London WC2R 2LS, United Kingdom
[3] Laboratoire de Mécanique des Solides, CNRS, Institut Polytechnique de Paris, 91120 Palaiseau, France

Keywords: Ribbon, pre-stress, torsional buckling, phase separation, dimension reduction

1. Introduction

In many physical and biological settings, slender elastic filaments (rods or ribbons) possess internal structure: the material or geometric properties of the filament vary significantly over its cross-section, or non-uniform residual stresses arise due to active processes such as thermal expansion, swelling, or growth. Just as one curls a ribbon of cloth by irreversibly stretching its outer layer over a sharp blade, such filaments can exhibit dramatic shape changes that may be central to their function — a canonical example being the bimetallic strip studied by Timoshenko [1]. In general, predicting global behaviour from internal structure is a complex task, except in some special cases. For example, for a slender elastic filament subject to small pre-stress, it is well known that the filament can be modelled as an Euler-Bernoulli rod with effective natural curvature and twist. An ongoing challenge is to formulate effective models in situations where the kinematic assumptions underlying classical rod models do not apply; this may be because the pre-stress is large or varies non-affinely in the cross-section, so that elastic instabilities occur on the scale of the cross-section dimensions.

2. Pre-stressed elastic ribbons

Here, we study an elastic ribbon subject to large, uniaxial pre-stress confined to a central region within the cross-section. In practice, this pre-stress can be created by a stretch-and-bond procedure (Fig. 1a–d): a uniaxially pre-stretched strip (red) is glued along its outer, lateral edges to two identical strips (green) that are initially unstressed. This system is a symmetric version of the bi-strip studied previously by Refs. [2, 3]. We demonstrate that the ribbon can buckle spontaneously to form helicoidal-like shapes, featuring regions of alternating chirality that are separated by so-called perversions (phase boundaries). This instability cannot be described by classical rod theory, which predicts zero spontaneous curvature and twist due to the mirror symmetry of the pre-stress. Thus, the ribbon serves as a model system to develop and test novel reduced-dimension theories.

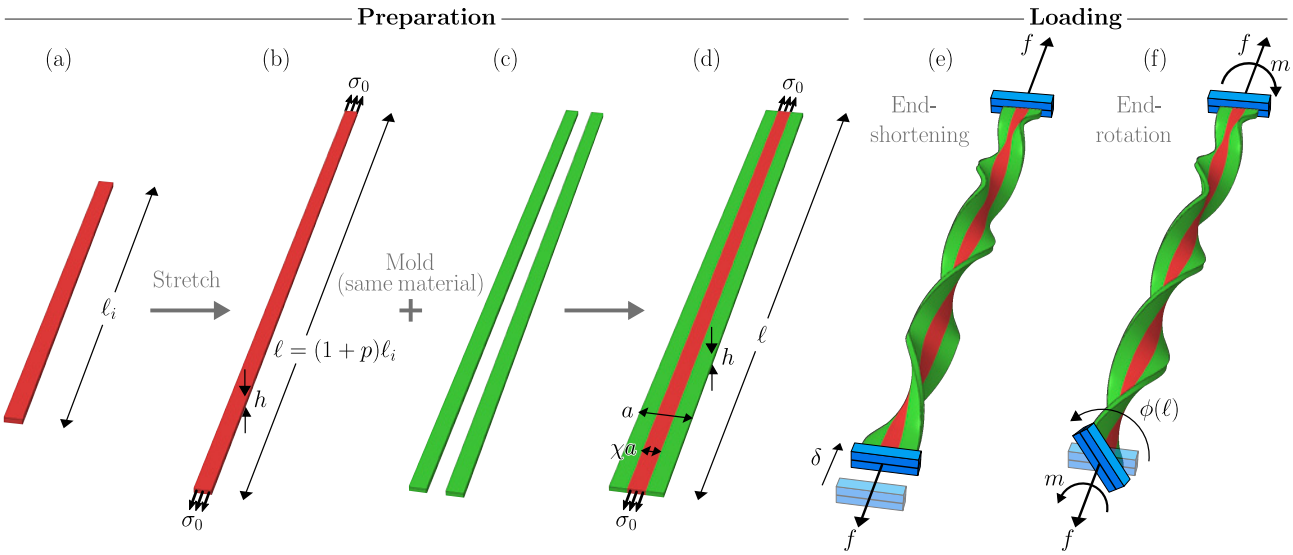

Figure 1: (a)–(d) Preparation of an elastic ribbon with inhomogeneous, uniaxial pre-stress. The pre-stretched strip (red) and 'outer' strips (green) are composed of the same material. (e)–(f) Loading scenarios.

As shown in Fig. 1e–f, we explore the mechanical behaviour of the ribbon under two loading scenarios: (i) end-shortening (Fig. 1e), which effectively controls the average axial strain in the ribbon; and (ii) end-rotation (Fig. 1f), which controls the average twist rate. We derive a one-dimensional (1D) model for the ribbon that carefully accounts for inhomogeneous, uniaxial pre-stress, by extending the extensible ribbon model developed by Ref. [4]. Starting from a geometrically-nonlinear plate theory, we use an energy relaxation method to obtain a 1D 'rod-like' model in which the strain energy is expressed solely in terms of 'macroscopic' strains attached to the ribbon centreline; see Fig. 2. Our model is asymptotically valid in the slenderness limit characteristic of ribbons (*i.e.*, thickness $h \ll$ width $a \ll$ length ℓ) and accounts for extensibility of the ribbon mid-surface and finite rotations of its cross-section; though we limit ourselves to the case of steady deformations and a straight centreline (zero bending strains), and we neglect higher-order gradient terms in the strain energy.

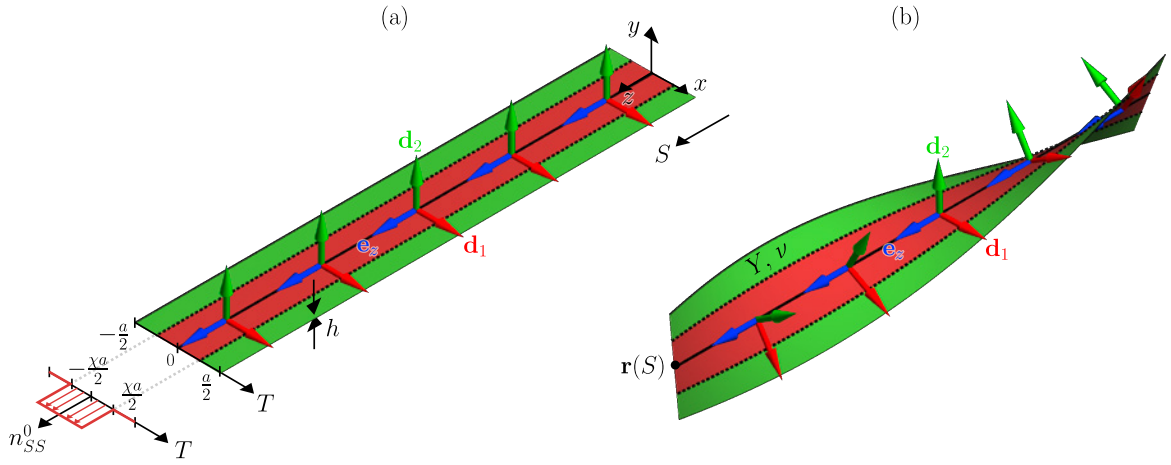

Figure 2: Centreline-based kinematic description used in the ribbon model. (a) Reference configuration showing the discontinuous distribution of pre-stress (fabrication procedure in Fig. 1a–d). (b) Deformed configuration.

By comparing with numerical (finite-element) simulations and experiments on elastomeric samples, we demonstrate that the ribbon model successfully captures the qualitative features of torsional buckling under end-shortening and end-rotation. While the twist has a single preferred value in classical theories, the pre-stress triggers an instability associated with two competing values, which govern an effective nonlinear macroscopic behaviour (as quantified by the applied axial force, f, and moment, m; see Fig. 1e–f). Furthermore, we show how this system provides a desktop-scale elastic analogue of thermodynamic phase separation — for example, of a real gas into its liquid and vapour phases — in which the regions of alternating chirality (Fig. 1e–f) can be regarded as distinct thermodynamic phases. More broadly, our system yields insight into torsional instabilities observed in elastic ribbons [5, 6] and other prismatic solids [7] featuring similar distributions of residual stress.

References

[1] S. Timoshenko. *Analysis of bi-metal thermostats*, J. Opt. Soc. Amer., 11 (1925) 233–255.

[2] J. Huang, J. Liu, B. Kroll, K. Bertoldi, D. R. Clarke. *Spontaneous and deterministic three-dimensional curling of pre-strained elastomeric bi-strips*, Soft Matter, 8 (2012) 6291–6300.

[3] C. Lestringant, B. Audoly. *Elastic rods with incompatible strain: Macroscopic versus microscopic buckling*, J. Mech. Phys. Solids, 103 (2017) 40–71.

[4] B. Audoly, S. Neukirch. *A one-dimensional model for elastic ribbons: A little stretching makes a big difference*, J. Mech. Phys. Solids, 153 (2021) 104457.

[5] M. A. R. Koehl, W. K. Silk, H. Liang, L. Mahadevan. *How kelp produce blade shapes suited to different flow regimes: a new wrinkle*, Integr. Comp. Biol., 48 (2008) 834–851.

[6] E. Siéfert, E. Reyssat, J. Bico, B. Roman. *Programming stiff inflatable shells from planar patterned fabrics*, Soft Matter, 163 (2020) 7898–7903.

[7] S. Turcaud, L. Guiducci, P. Fratzl, Y. J. M. Bréchet, J. W. C. Dunlop. *An excursion into the design space of biomimetic architectured biphasic actuators*, Int. J. Mat. Res., 102 (2011) 607–612.

ECCOMAS Thematic Conference and IACM Special Interest Conference
Highly Flexible Slender Structures (HFSS 2025)
22–26 September 2025, Kaiserslautern, Germany

Pure 2D bending of a hyperelastic strip – first integral of equilibrium and integrability conditions

Gordan Jelenić,

University of Rijeka, Faculty of Civil Engineering, Rijeka, gordan.jelenic@uniri.hr

Keywords: Pure bending, 2D hyperelasticity, Integrability conditions

1. Introduction and motivation

Large-deformation pure cylindrical bending of a straight homogeneous hyperelastic strip of finite thickness is analysed with a view of establishing integrability conditions enabling a solution procedure depending on the character of the relationship between the longitudinal and the transversal stretch. There appear in the literature a number of approaches to the problem for diverse material constitutions including semi-linear and Hencky material, as well as a general class of Seth–Hill materials, but here we analyse for what wider class of hyperelastic materials may those approaches be generalised to provide an integrable solution. The earliest attempt at providing a 2D pure-bending solution including the evolution of through-the-thickness stress component appears to be Seth's [1], followed by Rivlin [2]. Ogden [3] formulated the problem for the class of John's harmonic materials [4], while Lurie [5] provided the solution for the simplest amongst them – the so-called semilinear material. Carroll and Horgan [6] derived a solution for Blatz and Ko's material [7], while Bruhns et al. did the same for Hencky's material [8]. Xiao et al. [9] realised that the approach may be generalised to encompass the whole set of Seth-Hill materials. The question we pose here is may this be generalised even further, to a wider class of hyperelastic materials?

2. Lurie's solution

A rather simple solution to the problem is provided by Lurie for the so-called semilinear material whereby the longitudinal and transversal strains are defined as Biot's: $\varepsilon_B^{11} = \frac{r}{\rho} - 1$ and $\varepsilon_B^{22} = -(1 + r')$, with ρ as the radius of curvature of the unstrained fibre, r as the radial co-ordinate of a deformed fibre and the dash (') as the derivative with respect to the through-the-thickness co-ordinate X. For the constitutive relationship

$$\begin{Bmatrix} B^{11} \\ B^{22} \end{Bmatrix} = \frac{E}{(1+n)(1-2n)} \begin{bmatrix} 1-n & n \\ n & 1-n \end{bmatrix} \begin{Bmatrix} \varepsilon_B^{11} \\ \varepsilon_B^{22}, \end{Bmatrix},$$

with E as Young's modulus, n as Poisson's ratio and B^{11}, B^{22} as Biot's stress components in the longitudinal and transversal directions, respectively. Principal differential equation of the problem has been derived as $r'' - \frac{1}{\rho^2} r = -\frac{1}{(1-n)\rho}$, providing the simple solution $\frac{r}{\rho} = \frac{1}{1-n} - \frac{a\cosh\frac{X}{\rho} + \sinh\frac{X}{\rho}}{\cosh\frac{h}{2\rho}}$ with h as the specimen's thickness.

3. Seth-Hill family of linear materials and a first integral of equilibrium

In the same family with the semilinear material in Lurie's solution characterised by the linear relationship between the Biot strain tensor and the energy-conjugate Biot stress tensor, there exist other popular hyperelastic material models using the same constitutive matrix, such as e.g. Saint Venant–Kirchhoff's material or Hencky's material. The strain tensors used in all of them belong to Seth-Hill's family and may be expressed as $\boldsymbol{\varepsilon}_c = \frac{1}{c}(\mathbf{U}^c - \mathbf{I})$, where c is a material-describing parameter (1 – semilinear, 2 – Saint Venant–Kirchhoff's, 0 – Hencky's, but otherwise arbitrary) and $\mathbf{U}$ is the right stretch tensor. As shown by Xiao et al. [9], the resulting eqilibrium may be expressed as

$$\left\{ \frac{1}{2}\left[\left(\varepsilon_c^{11}\right)^2 - \left(\varepsilon_c^{22}\right)^2 \right] + \left[(1-c)\varepsilon_c^{22} - 1 \right] \left(\frac{n}{1-n}\varepsilon_c^{11} + \varepsilon_c^{22} \right) \right\}' = 0,$$

clearly indicating the existence of a first integral of the solution providing a quadratic relationship between the two strains. Since they depend on the deformed radial position and its change over the cross-section, respectively, this results in a first-order differential equation for the radial position, highly non-linear, but integrable.

4. First integral of equilibrium for a general class of hyperelastic materials

In hyperelastic materials there exists a strain-energy density ϕ and the equilibrium may be then stated as

$$\frac{1}{\rho}\frac{\partial \phi}{\partial \lambda_1} + \frac{d}{dX}\frac{\partial \phi}{\partial \lambda_2} = 0$$

with λ_1 and λ_2 as the longitudinal and the transversal stretch. This may be expressed as $\frac{d}{dr}\left(\phi - \lambda_2 \frac{\partial \phi}{\partial \lambda_2}\right) = 0$, i.e. it also provides a first integral of the problem equilibrium, now in the more general form of $\phi - \lambda_2 \frac{\partial \phi}{\partial \lambda_2} = \phi\big|_{\mp \frac{h}{2}}$.

5. Constitutive restrictions necessary for problem integrability

Since strain-energy density ϕ is a function of $\lambda_1 = \frac{r}{\rho}$ and $\lambda_2 = -\frac{dr}{dX}$, the first integral of equilibrium turns out to be an (implicit) first-order differential equation relating r to r'. The problem becomes integrable for a *reduced class of hyper-elastic materials* for which r' is an explicit function of r. Hence, all strain-energy densities for which the first integral of equilibrium is a polynomial of order not larger than four provide an integrable solution. For example, Ogden's materials may be generally expressed as

$$\phi = \sum_{p,q,r=0}^{\infty} a_{pqr}\left\{\left[\lambda_1^p\left(1+\lambda_2^q\right) + \lambda_2^p\left(1+\lambda_1^q\right) + \lambda_1^q + \lambda_2^q\right]\left(\lambda_1\lambda_2\lambda_3\right)^r - 6\right\},$$

therefore for the upper limit in the sum set to $p+r=4$ and $q+r=4$ the first integral becomes a quartic enabling a solution for a very elaborate material.

6. Conclusions

In large-strain 2D pure bending of hyperelastic materials there exists a first integral of equilibrium. It relates the two strain components – longitudinal and transversal – possibly in a highly non-linear manner. If the first integral is a polynomial in r' of order not larger than four, the problem becomes integrable.

Acknowledgments

This project has received funding through the Research Project ANEMIC PM (HRZZ-IP-2024-05-9904) financially supported by the Croatian Science Foundation

References

[1] B.R. Seth. *Finite strain in elastic problems*, Philosophical Transactions of the Royal Society London A, 234 (1935) 231-–264

[2] R.S. Rivlin. *Large elastic deformations of isotropic materials. V. The problem of flexture*, Proceedings of the Royal Society London A, 195 (1949) 463-–473

[3] R.W. Ogden. *Non-Linear Elastic Deformations*, Dover Publications, Inc., New York, 1984.

[4] F. John. *Plane strain problems for a perfectly elastic material of harmonic type*, Communications on Pure and Applied Mathematics, 13 (1960) 239—296

[5] A. Lurie. *Nonlinear Theory of Elasticity*, North-Holland ,Amsterdam, 1990.

[6] M.M. Carroll, O. Horgan. *Finite strain solutions for compressible elastic solid*, Quarterly of Applied Mathematics, 48 (1990) 767–780

[7] P.J. Blatz, W.L. Ko. *Application of finite elasticity to the deformation of rubbery materials*, Transactions of the Society of Rheology, 6 (1962) 223—251

[8] O.T. Bruhns, H. Xiao, A. Meyers. *Finite bending of a rectangular block of an elastic Hencky material*, Journal of Elasticity, 66 (2002) 237-–256

[9] H. Xiao, Z.F. Yue, L.H. He. *Hill's class of compressible elastic materials and finite bending problems: Exact solutions in unified form*, International Journal of Solids and Structures, 48 (2011) 1340-1348

ECCOMAS Thematic Conference and IACM Special Interest Conference
Highly Flexible Slender Structures (HFSS 2025)
22–26 September 2025, Kaiserslautern, Germany

Morphorods: A modelling framework for active slender structures

Derek E Moulton [1], Alain Goriely [1], Hadrien Oliveri [2], Bartek Kaczmarski [3], Ellen Kuhl [3]

[1] Mathematical Institute, University of Oxford, moulton@maths.ox.ac.uk
[2] Max Planck Institute for Plant Breeding Research
[3] School of Engineering, Stanford University

Keywords: active structure, morphoelasticity, soft robotics, plant tropism

Elastic filamentary structures are ubiquitous in nature, and can be found at all scales, from microscopic chains of molecules to hairs, vines, umbilical cords, and elephant trunks. Our interest in this talk is active slender elastic structures, which are capable of changing their properties in response to their environment and/or to accomplish a task. For biological structures, this may be achieved through some combination of growth, remodelling, or muscle activity. For instance, a vine searching for a pole to climb actively generates a helical shape through a directed change in growth hormone, while an elephant modulates the shape of its trunk by contraction of muscle groups. Active filamentary structures also have strong relevance in engineering applications, with great potential in biomedical devices and in the expanding field of soft robotics.

Due to their inherent slenderness, the mechanical behaviour of growing filaments is well-characterised by a one-dimensional continuum representation. The challenge is how to incorporate active processes within a 1D elastic rods setting. In this talk I will outline our modelling framework for describing the mechanical behaviour of active slender elastic structures, which we term morphoelastic rods, or simply morphorods. The theory begins with a characterisation of a thin elastic structure as a full, three-dimensional object, such that the active change of properties is described by a heterogeneous and anisotopic growth tensor. By framing the mechanics in an energy setting and performing an asymptotic analysis that utilises the small aspect ratio inherent in slender structures, we conduct a dimensional reduction that allows to describe the object via an equivalent elastic rod, whose properties (intrinsic curvature, stiffness, length) emerge as functions of the imposed growth tensor[1, 3].

After outlining the theoretical approach, I will demonstrate its utility through application to the tropic movement of plants [2] and mechanical mimicry of the remarkable dexterity of the elephant's trunk [4].

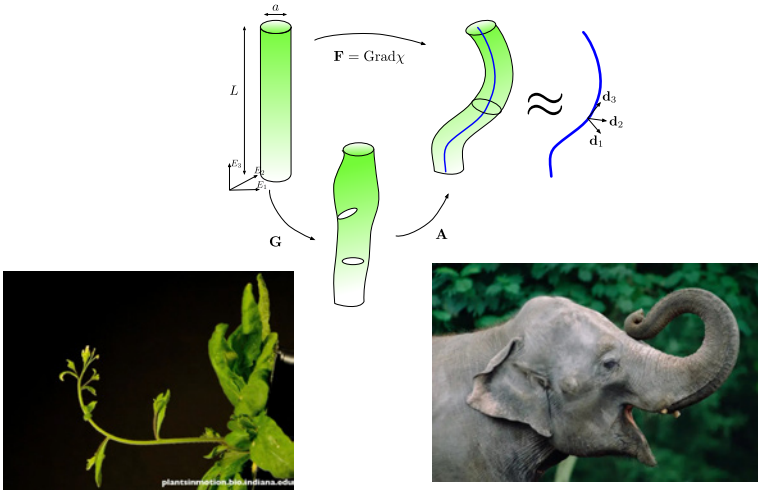

Figure 1: Our conceptual approach consists in dimensional reduction of an active slender 3D elastic object to a 1D rods representation. The resulting framework may be adapted to diverse applications such as the bending of a stem away from gravity to the remarkable dexterity of an elephant's trunk.

References

[1] Moulton, Derek E., Thomas Lessinnes, and Alain Goriely. *Morphoelastic rods III: Differential growth and curvature generation in elastic filaments*, Journal of the Mechanics and Physics of Solids, 142 (2020): 104022.

[2] Moulton, Derek E., Hadrien Oliveri, and Alain Goriely. *Multiscale integration of environmental stimuli in plant tropism produces complex behaviors*, Proceedings of the National Academy of Sciences 117.51 (2020): 32226-32237.

[3] Kaczmarski, B., Moulton, D. E., Kuhl, E., and Goriely, A. *Active filaments I: Curvature and torsion generation*, Journal of the Mechanics and Physics of Solids, 164, (2022) 104918.

[4] Goriely, A., Moulton, D., Kaczmarski, B., Leanza, S., Zhao, R., and Kuhl, E. *Minimal design of the elephant trunk as an active filament*, Physical Review Letters, 132 (2024)

ECCOMAS Thematic Conference and IACM Special Interest Conference
Highly Flexible Slender Structures (HFSS 2025)
22–26 September 2025, Kaiserslautern, Germany

A 1D Kinematically Enriched Ribbon Model for Simulation of REBCO Tapes

Mohammad Ali Saadat [1], Alexandre Torre [2], Damien Durville [1]

[1] CentraleSupélec, ENS Paris-Saclay, CNRS, Université Paris-Saclay, LMPS - Laboratoire de Mécanique Paris-Saclay, 3 rue Joliot-Curie, Gif-sur-Yvette, 91190,
{mohammad-ali.saadat,damien.durville}@centralesupelec.fr
[2] CEA, IRFM, F-13108 Saint-Paul-lez-Durance, France , Alexandre.TORRE@cea.fr

Keywords: 1D Ribbon Model, Kinematically Enriched, REBCO, CORC, Superconductor

1. Introduction

CORC (Conductor on Round Core) superconductors have gained importance due to their enhanced current-carrying capabilities and improved mechanical performance. These superconductors are constructed by winding REBCO (Rare-earth Barium Copper Oxide) tapes around a round core in several layers, forming a multi-layer assembly that combine flexibility with high performance. The design of CORC superconductors allows for better handling of mechanical stresses and leads to superior operation in demanding power applications.

This work introduces a one-dimensional (1D) ribbon model aimed at capturing the fundamental mechanical response of REBCO tapes used in CORC conductors. Using a simplified 1D approach, we provide a systematic analysis of the tape's deformation characteristics, emphasizing the impact of different kinematic interpolation techniques on the predicted deflection profile.

2. Expected deformations in the ribbon

This section focuses on the range of deformations that the REBCO tape is expected to exhibit. In the simplest case, where the tape is free from any axial or contact forces, the cross-section of a bent tape can undergo several deformation modes, as shown in Figure 1(a). The ability of the model to capture these free deformation modes is crucial as it establishes a baseline for more complex scenarios.

When the tape is wrapped around a round core, the situation becomes more intricate. The presence of axial forces and the curvature of the core introduce additional contact phenomena. Depending on the magnitude of the force and the diameter of the core, the tape can exhibit different contact patterns. These may include a single line contact at the center, two distinct line contacts, or even continuous contact along the central region, as shown in Figures 1 (b)-(d). In cases with multiple or continuous contacts, the deformation of the tape cross section can become discontinuous. Therefore, the model should be capable to accurately capture both smooth and abrupt changes in the tape's geometry, ensuring that all expected deformation modes are well represented.

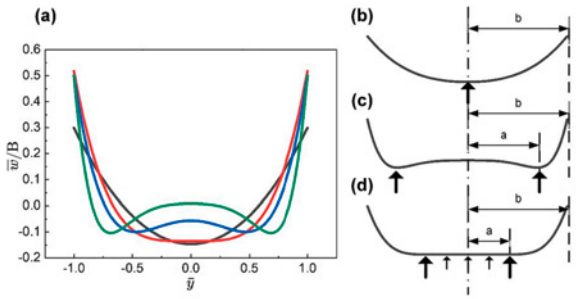

Figure 1: (a) Deflection modes of a tape under zero tension; (b)–(d) Deflection and contact modes when the tape is wrapped [1].

3. 1D ribbon kinematics

The kinematic formulation describes the position of any material point in the REBCO tape by combining the centroidal trajectory with the in-section deformation. The overall position vector is expressed as

$$\mathbf{x} = r(\xi_3) + g(\xi_1, \xi_2, \xi_3), \tag{1}$$

where $r(\xi_3)$ is the centroidal position of the tape's cross-section, with ξ_3 representing the parameter along the tape's length, and $g(\xi_1, \xi_2, \xi_3)$ defines the position of a material point within the cross-section, with ξ_1 and ξ_2 as the local coordinates in the cross-sectional plane.

To accurately capture the various deformation modes, different representations for the function g have been explored, such as the Taylor expansion, the Taylor expansion enriched by hyperbolic functions, the Fourier expansion and the 2D B-spline function. The 2D B-spline formulation offers more flexibility in representing both smooth variations and discontinuous deformations, which is needed, particularly under complex contact conditions, when the tape is wrapped around a core.

4. Results and discussion

The application of the model to simulate both free and wrapped configurations of the REBCO tape has produced encouraging results. In the free deformation case, the model effectively reproduces the expected complex deformation patterns of the tape's cross-section, as can be seen in Figure 2.

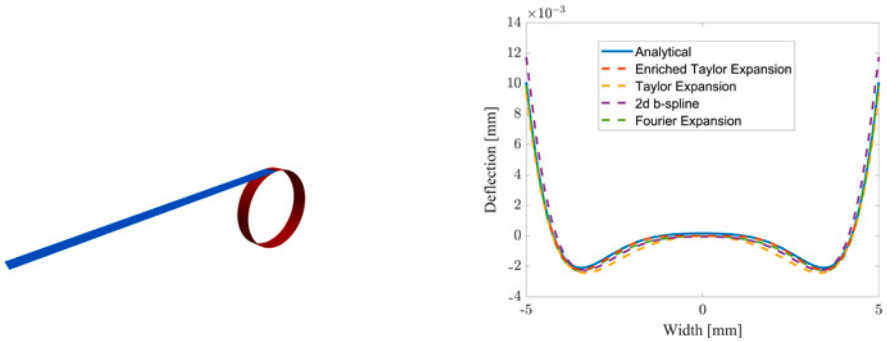

(a) (b)

Figure 2: (a) Comparison of the initial geometry (in blue) and the deflected geometry (in red) of a ribbon, (b) Comparison of the deflected shape of the centerline of the cross section of the bent ribbon using different methods.

The results of the wrapping simulations are encouraging. Our preliminary analysis indicates that the model successfully captures the key behaviors of the tape during the wrapping process. In particular, the predictions for the interaction between the tape and the core show promising trends that align with our theoretical expectations. However, while these initial outcomes support the validity of our approach, further exploration and additional refinements are needed to fully establish the model's robustness under various wrapping conditions.

5. Conclusions

A one-dimensional ribbon model for the mechanical response of REBCO tapes in CORC superconductors has been developed. Promising first results have been obtained, indicating that the essential deformation behaviors of the tape are captured both in free conditions and during the wrapping process. A solid framework for understanding the tape's mechanical performance has been established, demonstrating the potential of this approach for broader applications in the design and analysis of superconducting devices.

Acknowledgments

This project has received funding from

References

[1] Y. Li, N. Mu, S. Tang, Z. Zhang, J. Zhou, H. Yong, and X. Zhang. *Deformation and crack prediction of CORC cable induced by Poisson effect: Theoretical modeling and experimental validation*, Engineering Fracture Mechanics, 292 (2023) 109625.

ECCOMAS Thematic Conference and IACM Special Interest Conference
Highly Flexible Slender Structures (HFSS 2025)
22–26 September 2025, Kaiserslautern, Germany

Geometric Mechanics of Curve-fold Origami with vertices

Zhixuan Wen [1], Fan Feng [1], Huiling Duan [1]
[1] College of Engineering, Peking University, Beijing, 100087, China

Keywords: Instructions, Curve-fold Origami, Slender Structures, Developable Shells

1. Introduction

Curve-fold origami is a new type of origami whose folds are spatial curves. In the past decades, abundant theoretical works have studied the geometry and mechanics of curve-fold origami. Geometrically, the flanks are modeled as developable surfaces with isometric deformation [1], and the deformation is determined by the geometry, i.e., the curvature and torsion distributions of the folds. Mechanically, the flanks are thus modeled as nonstretchable shells and the folds are modeled as elastic torsional springs. Minimizing the bending and folding energy yields the equilibrium geometry of the deformed crease as well as the configuration of the entire origami [2].

While previous works mainly focus on single-curve-fold origami with narrow flanks, the geometric mechanics of multi-curve-fold origami, especially for curved origami with vertices, is poorly understood. In this work, we will show how vertices affect the configuration space of folds and derive the geometric mechanics theory to predict the deformation of multi-curve-fold with vertices. The theory is validated by finite element analysis with good agreement.

2. Theory

While vertices introduce additional geometric constraints that strongly limit the configuration space of the folds, the deformation of curved origami with vertices no longer follows the Euler-Lagrange equations derived via energy minimization[3]. Three types of geometric constraints exist in single-vertex multi-curve-fold origami, which are listed below.

Constraints between neighboring folds Due to developability, geometric correlations exist between neighboring curved folds. Specifically, the geometry of one fold determines the geometry of parts of the neighboring folds, expressed as

$$\begin{aligned}\kappa_{i\pm1}(\theta_{i\pm1}) &= \kappa_{i\pm1}(\kappa_i(\theta_i),\kappa_i'(\theta_i),\kappa_i''(\theta_i),\tau_i(\theta_i),\tau_i'(\theta_i);\theta_i),\\ \tau_{i\pm1}(\theta_{i\pm1}) &= \tau_{i\pm1}(\kappa_i(\theta_i),\kappa_i'(\theta_i),\kappa_i''(\theta_i),\kappa_i'''(\theta_i),\tau_i(\theta_i),\tau_i'(\theta_i),\tau_i''(\theta_i);\theta_i),\end{aligned} \tag{1}$$

where κ,τ are the curvature and torsion of the folds and θ_i is the polar coordinate of fold i, as shown in Figure 1(a).

Folding angle constraints at the vertex As shown in Figure 1(b), at the vertex the tangent vectors of the folds satisfy the same geometric constraints as straight-fold origami, which is expressed as

$$[(\sin\frac{\phi_1(0)}{2}\sin\frac{\phi_2(0)}{2})^{-1}-\cot\frac{\phi_1(0)}{2}\cot\frac{\phi_2(0)}{2}]\cos\alpha=1, \tag{2}$$

Periodic constraints Due to symmetry, the curvature and torsion distribution of the i th fold is the same as the $i+2$ th fold, i.e., $\kappa_{i+2}(S)=\kappa_i(S),\tau_{i+2}(S)=\tau_i(S)$.

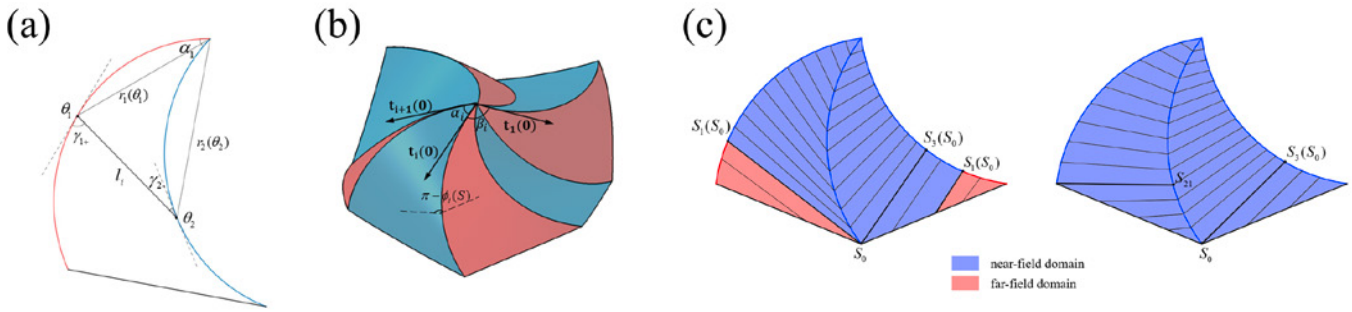

Figure 1: Illustrations of (a) geometric correlations between folds, (b) folding angle constraints at the vertex, (c) near-field domain distributions.

The folding angle constraints constrain the initial values of the curvature, and the periodic constraints constrain the geometry of the whole structure. While Eqs, (1) cannot be solved explicitly under periodic constraints, we prove a strikingly easy theorem to handle the problem: *The near-field deformation of a single-vertex curve-fold origami only depends on the curvature at the vertex.*, which also applies to dynamical cases. The near-field domains are painted in Figure 1(c). The deformation of far-field domains is solved via energy minimization.

3. Numerical Simulations and Conclusions

To validate the theorem, we simulate the deformation of single-vertex multi-curve-fold origami structures in Abaqus, and calculate the discrete curvature and torsion to compare with the theoretical results. As shown in Figure 2(a), (b), the FEM results qualitatively meet the experiments, and the theoretical results shows good agreement with FEM results, indicating that the deformation of most regions are irrelevant with stiffness and geodesic curvatures. Furthermore, to explain the disagreement at the end of the folds, we anticipate that the disagreement is triggered by symmetry breaking, causing discontinuities in κ' and τ. The modified theoretical results capture the deformation at the end of the folds well(Figure 2(c)).

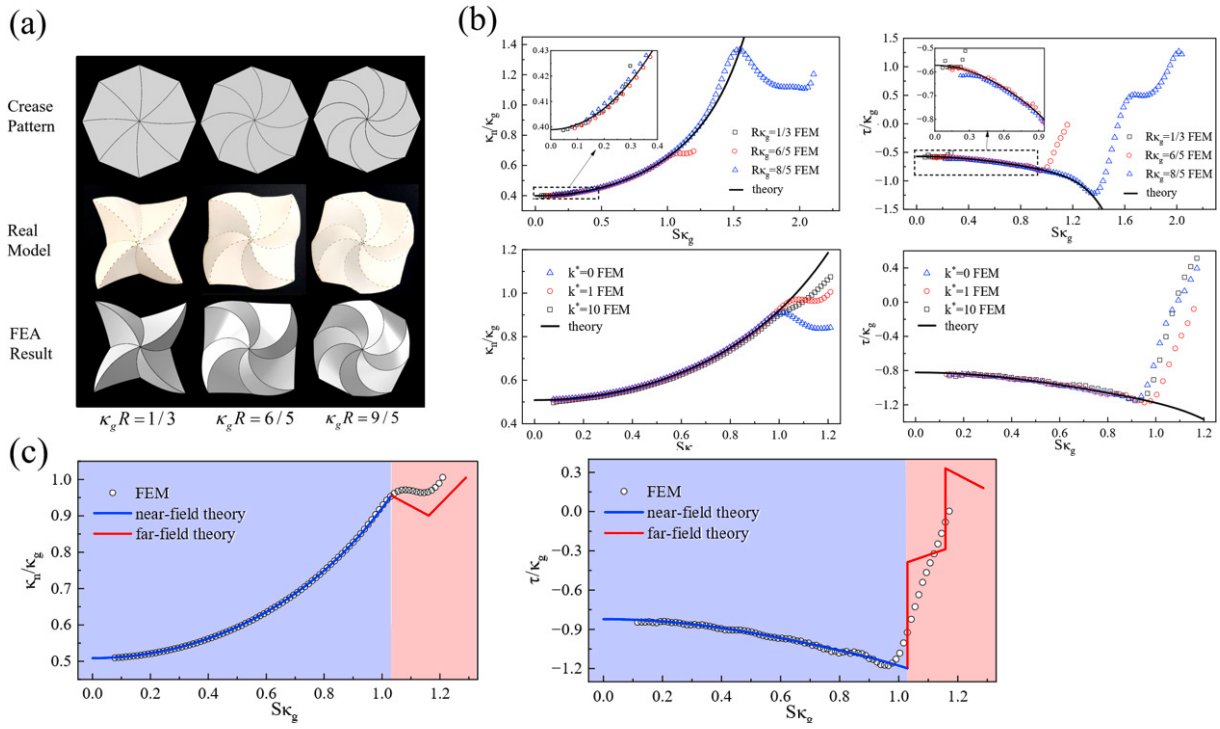

Figure 2: (a) FEA results and real models of curved origami with different geodesic curvatures. (b) Comparisons between FEA results and theoretical results. (c) Comparisons between FEA results and modified theoretical results.

Acknowledgments

This project has received funding from the National Natural Science Foundation of China (grant nos. 11988102) and the National Key Research and Development Program of China (grant no. 2020YFE0204200).

References

[1] Huffman. Curvature and creases: A primer on paper. *IEEE Transactions on Computers*, C-25(10):1010–1019, 1976.

[2] Marcelo A Dias, Levi H Dudte, L Mahadevan, and Christian D Santangelo. Geometric mechanics of curved crease origami. *Physical review letters*, 109(11):114301, 2012.

[3] Zhixuan Wen, Pengyu Lv, Fan Feng, and Huiling Duan. A generalized geometric mechanics theory for multi-curve-fold origami: Vertex constrained universal configurations. *Journal of the Mechanics and Physics of Solids*, 192:105829, 2024.

ECCOMAS Thematic Conference and IACM Special Interest Conference
Highly Flexible Slender Structures (HFSS 2025)
22–26 September 2025, Kaiserslautern, Germany

Non-material Poincaré equations for the sliding of geometrically exact rods with illustrative examples

F. Boyer [1], S. Zhang [2], V. Lebastard [1]

[1] IMT Atlantique, LS2N, UMR CNRS 6004, F-44307 Nantes, France, frederic.boyer@imt-atlantique.fr
[2] Northwestern Polytechnical University, 710072, Xi'an, China, zscm@mail.nwpu.edu.cn

Keywords: Dynamics, Cosserat rods, sliding rods

1. Introduction

The counterpart of Lagrange's equations on a non-commutative Lie group G of configurations is called Poincaré's equations [1]. These equations are deduced from Hamilton's principle of least action on G. The approach allows to reformulate Lagrange mechanics in terms of transformations $g \in G$ instead of the usual generalized coordinates $q \in \mathbb{R}^n$. This considerably simplify the formulation by removing the artificial geometric nonlinearities that are then deported to some reconstruction equations, for which there exist efficient numerical integration schemes. Although Poincaré's approach is familiar to the geometrical mechanics community when applied to the spinning top, we will see how it can be naturally extended to the rigid body, to the (geometrically exact) theory of Cosserat rods, and finally to sliding one-dimensional Cosserat media, with a numerical illustration on fish swimming.

2. Poincaré's equations

For a system with a finite number of degrees of freedom, whose configuration space is a Lie group G, Poincaré's equations take the form:

$$\frac{d}{dt}\left(\frac{\partial l}{\partial \eta}\right) - ad_{\eta}^{T}\left(\frac{\partial l}{\partial \eta}\right) - X_g(l) = F_{\text{ext}} \ , \ \dot{g} = g\hat{\eta}. \tag{1}$$

From left to right, the first equations govern the time-evolution of velocities η, while the second is a reconstruction equation of the trajectory $t \mapsto g(t)$ on G.

2.1. Application to the rigid body

When applied to the Lagrangian of the heavy top on the configuration Lie group $G = SO(3)$, they give the famous Euler's equations in the body frame:

$$J\dot{\Omega} + \Omega \times J\Omega + C_{\text{g}}(R) = 0 \ , \ \dot{R} = R\hat{\Omega}, \tag{2}$$

while, when applied to the Lagrangian of the rigid body expressed on the Lie group $SE(3)$ of its rigid displacements, they give the well-known Newton-Euler dynamic model of the rigid body in the body frame:

$$\begin{pmatrix} J & m\hat{S} \\ m\hat{S}^T & m1 \end{pmatrix}\begin{pmatrix} \dot{\Omega} \\ \dot{V} \end{pmatrix} + \begin{pmatrix} (mS\times\Omega)\times V + \Omega \times J\Omega \\ (mS\times\Omega)\times\Omega + \Omega \times mV \end{pmatrix} = \begin{pmatrix} C_{\text{g}} \\ N_{\text{g}} \end{pmatrix} \ , \ \dot{R} = R\hat{\Omega} \ , \ \dot{r} = RV \ . \tag{3}$$

which is used in many applications of vehicle dynamics and rigid robotics.

3. Poincaré-Cosserat equations

In recent years, Poincaré's approach has been applied to a Cosserat medium, i.e. a continuous set of rigid microstructures "glued" together, whose configurations are described by a field of poses on $SE(3)$. In this case, the classical ordinary Poincaré differential equations are transformed into a set of partial differential equations on $SE(3)$, which we call Poincaré-Cosserat partial differential equations [2]. They take the form:

$$\frac{\partial}{\partial t}\left(\frac{\partial \mathfrak{L}}{\partial \eta}\right) - ad_{\eta}^{T}\left(\frac{\partial \mathfrak{L}}{\partial \eta}\right) + \frac{\partial}{\partial X}\left(\frac{\partial \mathfrak{L}}{\partial \xi}\right) - ad_{\xi}^{T}\left(\frac{\partial \mathfrak{L}}{\partial \xi}\right) - X_g(\mathfrak{L}) = \bar{F}_{\text{ext}}, \tag{4}$$

These equations are supplemented with boundary conditions (provided by the least action principle), reconstruction equations both in time t and space X, and a model of internal elastic energy contained in the Lagrangian density $\mathfrak{L}$ (constitutive law).

3.1. Application to Cosserat rods

When applied to a Cosserat rod, i.e. a continuous staking of rigid cross-sections along a single material dimension, these equations provide J.C. Simo's dynamic model of Geometrically-Exact rods [3]. A model that is now widely used in continuous and soft robotics to capture the dynamics of elongated robots whose finite deformations are controlled.

4. Non-material Poincaré-Cosserat equations

After having briefly recalled the Poincaré equations of the rigid body and Cosserat rods and the variational calculus that leads to them from the principle of least action stated on a non-commutative Lie group. We will then turn to sliding elongated structures [4], for which we recently proposed an extension of the Poincaré-Cosserat framework [5]. In this case, the cross-sectional pose field in $SE(3)$ is no longer a function of a material (Lagrangian) variable X, but of a non-material (Eulerian) variable s. We'll see how this extension can be achieved in order to get a new set of Poincaré equations, named non-material Poincaré-Cosserat equations, that formally read:

$$\frac{D}{Dt}\left(\frac{\partial \mathfrak{L}}{\partial \eta_{D}}\right) - ad_{\eta_{D}}^{T}\left(\frac{\partial \mathfrak{L}}{\partial \eta_{D}}\right) + \frac{\partial}{\partial s}\left(\frac{\partial \mathfrak{L}}{\partial \xi}\right) - ad_{\xi}^{T}\left(\frac{\partial \mathfrak{L}}{\partial \xi}\right) = \bar{F}_{\text{ext}}. \tag{5}$$

with boundary conditions given by the least action principle, a constitutive law, and space-time reconstruction equations. Note that compared to (4), in (5) the partial time-derivation is replaced by the material (particular) derivative $D./Dt$ of fluid mechanics.

4.1. Conclusions

We will conclude our presentation, by illustrating the approach with simulations of the large amplitude elongated theory of [6], which has been used to model and control the swimming of robotic fish [7].

References

[1] H. Poincaré. Sur une forme nouvelle des equations de la mecanique. *Compte Rendu de l'Academie des Sciences de Paris*, 132:369 – 371, 1901.

[2] F. Boyer and F. Renda. Poincare's equations for cosserat media: Application to shells. *Journal of Nonlinear Science*, 2016.

[3] J.C. Simo and L. Vu-Quoc. On the dynamics in space of rods undergoing large motions - a geometrically exact approach. *Computer Methods in Applied Mechanics and Engineering*, 66(2):125 – 161, 1988.

[4] Yury Vetyukov, Alexander Humer, and Alois Steindl. Nonlinear dynamics of a flexible rod partially sliding in a rigid sleeve under the action of gravity and configurational force. *Journal of the Mechanics and Physics of Solids*, 193:105–54, 2024.

[5] F. Boyer, V. Lebastard, F. Candelier, and F. Renda. Extended hamilton's principle applied to geometrically exact kirchhoff sliding rods. *J. Sound Vibr.*, 516:116511, jan 2022.

[6] M. J. Lighthill. Large-amplitude elongated-body theory of fish locomotion. *Proceedings of the Royal Society of London. Series B, Biological Sciences*, 179(1055):125–138, 1971.

[7] F. Boyer, M. Porez, and A. Leroyer. Poincare - cosserat equations for the lighthill three-dimensional large amplitude elongated body theory: Application to robotics. *Journal of Nonlinear Science*, 20(1):47 – 79, 2010.

ECCOMAS Thematic Conference and IACM Special Interest Conference
Highly Flexible Slender Structures (HFSS 2025)
22–26 September 2025, Kaiserslautern, Germany

A multiscale approach to simulate the interaction between air jets and hairy yarns

Axel Bral [1], Lode Daelemans [2], Joris Degroote [1,3]

[1] Department of Electromechanical, Systems and Metal Engineering, Ghent University; Axel.Bral@UGent.be
[2] Department of Materials, Textiles and Chemical Engineering (MaTCh), Ghent University
[3] Flanders Make @ UGent - Core lab MIRO, Belgium

Keywords: Actuator Line Method (ALM), Air-jet weaving, Fluid-Structure Interaction (FSI), Multiscale analysis, Yarn

1. Introduction

Air-jet weaving is a textile manufacturing process in which a weft yarn is transported through the shed of the loom by a high-speed airflow. This technology allows for high insertion rates, in the order of 2000 insertions per minute, but at the cost of a high energy use, in the order of 5 kW/kg of woven fabric [1]. Attempts to reduce the energy use are often limited by the weaving stability. Therefore, it is crucial to understand the interactions between the air jets and the weft yarn. While significant progress has been made in modelling the insertion dynamics of smooth monofilament yarns [2], the behaviour of hairy staple-fiber yarns remains largely unexplored due to their complex microstructure. This work introduces a fully three-dimensional, two-way coupled Fluid-Structure Interaction (FSI) framework tailored for simulating staple-fiber yarns in an air-jet weaving environment. By employing an adapted version of the Actuator Line Method (ALM) for the flow field coupled to beam elements for the structural representation of the yarn, the framework enables the prediction of yarn trajectory, velocity, and tension. This approach provides an essential tool for optimizing weaving machine design, particularly for applications involving complex, flexible yarns.

2. Methodology

The FSI framework developed in this study couples an ALM-based aerodynamic force computation with a structural beam model for yarn dynamics [3]. Unlike conventional approaches, the yarn is not explicitly resolved in the flow field. Instead, its centerline is discretized into segments bounded by actuator points where aerodynamic forces are computed using precomputed force coefficients [4]. These coefficients, obtained from high-fidelity microscale Computational Fluid Dynamics (CFD) simulations [5], account for the influence of fibrous and irregular surface structure on drag and lift forces.

On the structural side, the yarn is modelled as a series of interconnected beam elements with material properties derived from microscale fiber simulations [6]. This approach ensures that the macroscale tensile and bending stiffness reflect the yarn's inherent mechanical behaviour. The coupling between the fluid and structural submodels occurs along the yarn centerline, where displacements from the structural solver are mapped to the actuator points in the flow solver, and aerodynamic forces from the flow solver are applied to the load points of the beam elements. This communication loop is performed once per time step, leading to an explicit coupling scheme.

3. Results

The framework is applied to simulate the launch of a wool staple-fiber yarn from the main nozzle of an air-jet weaving loom [3]. Under a supply (total) pressure of 4.7 bar gauge, the yarn reaches a peak velocity of approximately 70 m/s. Additionally, the yarn centerline position throughout the launch is shown in Figure 1. Its wrinkled appearance is attributed to the low bending stiffness of $1.908 \cdot 10^{-9}$ Nm^2.

The analysis of the yarn tension reveals a maximum at the air inlet region with, after 10 ms of simulated time, a value of 0.21 N, corresponding to a strain of 0.76%. This low axial force value is balanced only by the aerodynamic and inertial forces. If additional components, such as the prewinder, stopper and balloon breaker, were included in the (structural) submodel, the peak tension would likely reach significantly higher values for a short time.

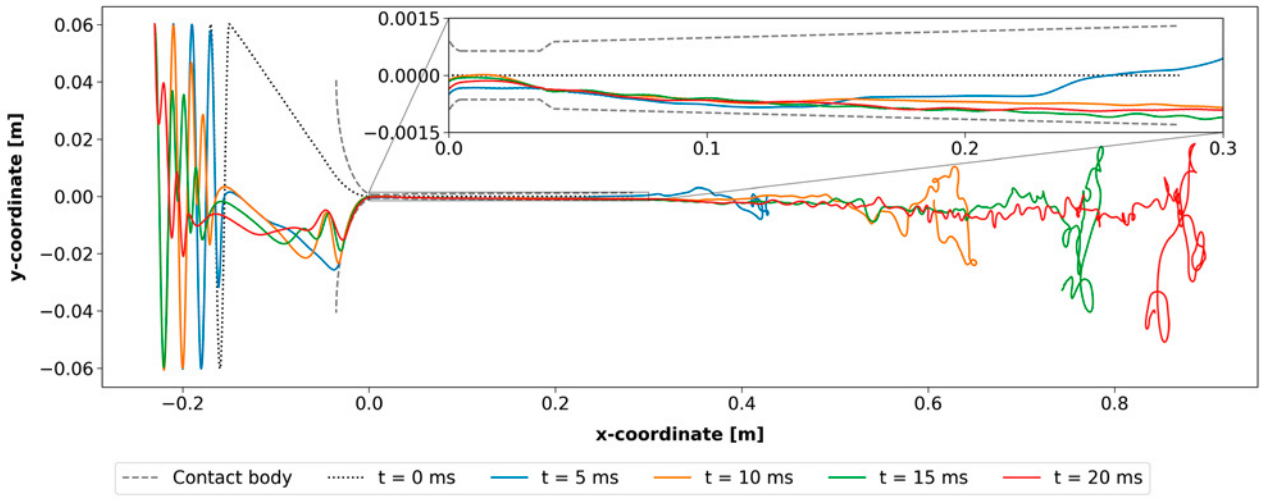

Figure 1: Position of the yarn centerline projected on the xy-plane at different time instants. The contact body represents the inner wall of the nozzle and serves as contact boundary in the structural submodel of the yarn.

4. Conclusions

The presented FSI framework provides a novel approach to modelling the insertion of wool staple-fiber yarns in air-jet weaving. By leveraging microscale force coefficients and structural properties, the model allows to predict the yarn velocity, deformation, and tension without the need for empirical parameter tuning. This study lays the foundation for future investigations into the complete weaving process, including interactions with prewinders, reeds, and relay nozzles, ultimately contributing to the design of more efficient air-jet weaving systems for staple-fiber yarns.

Acknowledgments

This project has received funding from the Research Foundation Flanders (FWO) with project number 1S30824N.

References

[1] C. Grassi, A. Schröter, Y.-S. Gloy, T. Gries *Increasing the energy efficiency of air jet weaving based on a novel method to exploit energy savings potentials in production processes of the textile industry*, Journal of Environmental Science and Engineering B, 5 (2016), 26-34.

[2] L. Delcour, L. Van Langenhove, J. Degroote *Towards numerical simulation of yarn insertion on air-jet weaving looms*, Aachen-Dresden-Denkendorf International Textile conference, pp. 10, 2019.

[3] A. Bral, L. Daelemans, J. Degroote. *Modelling the fluid-structure interactions of a hairy yarn in air-jet weaving*, Under review at International Journal for Numerical Methods in Engineering, (2025).

[4] A. Bral, J. Peeters, L. Daelemans, J. Degroote. *Development and validation of an actuator line method for fuzzy yarns in high-speed air flow*, Under review at International Journal for Numerical Methods in Engineering, (2025).

[5] A. Bral, L. Daelemans, J. Degroote. *A method to determine local aerodynamic force coefficients from fiber-resolved 3D flow simulations around a staple fiber yarn*, Multibody System Dynamics, (2024), pp. 25.

[6] A. Bral, L. Daelemans, J. Degroote. *A novel technique to simulate and characterize yarn mechanical behavior based on a geometrical fiber model extracted from microcomputed tomography imaging*, Textile Research Journal, 93 (2023), 2042-2062.

ECCOMAS Thematic Conference and IACM Special Interest Conference
Highly Flexible Slender Structures (HFSS 2025)
22–26 September 2025, Kaiserslautern, Germany

Nonlinear Dynamics of Anchoring Elements for Submerged Floating Tunnels subject to Hydrodynamic Loads

Stefano Corazza [1], Francesco Foti [1], Luca Martinelli [1], Vincent Denoël [2]

[1] Department of Civil and Environmental Engineering, Politecnico di Milano
stefano.corazza@polimi.it, francesco.foti@polimi.it, luca.martinelli@polimi.it
[2] Structural and Stochastic Dynamics Division, University of Liège, Belgium, v.denoel@uliege.be

---

Keywords: Submerged Floating Tunnels, Coupled system, Multiple Time Scales, Cable dynamics

1. Introduction

Seabed-anchored Submerged Floating Tunnels (SFTs) are interesting modular structures which are deemed to be a valuable option for crossing deep and long waterways, such as sea straits, fjords, bays and alpine lakes. Due to their inherent flexibility, SFTs are prone to the effect of dynamic loadings, such as earthquakes, waves, currents and traffic. Among all of them, hydrodynamic loadings are deemed to be the most critical for serviceability and fatigue life assessments of the whole SFT, because of their persistent and cyclic nature. While the global hydrodynamic response of the SFT can be studied by resorting to several modeling strategies, the local dynamic response of the anchoring elements is inherently hard to capture with standard finite element models, because their natural frequencies are well-separated from those of the global vibration modes.
The present work briefly reviews the main findings of the research activity recently carried out by the authors on this topic [1, 2]. A reduced-order cross-sectional model of the SFT is formulated and the coupled system of equations governing its dynamic response is derived. Different hydrodynamic loading conditions are then identified as critical and studied one at a time. The multiple time-scales perturbation method is applied to derive approximate closed-form solutions of the steady-state vibration amplitude of the anchoring elements. As an application example, a parametric analysis in the drag coefficient of the anchor is carried out, providing useful considerations aimed at supporting the conceptual design phase of SFTs.

2. Cross-sectional model of the SFT

The cross-section of the tube is modeled as a two-dofs oscillator, possessing mass and stiffness which are representative of the same modal quantities describing the SFT global vibration mode of interest. Vertical and horizontal dimensionless displacements of the tube are respectively denoted by the symbols w_T and v_T, while its torsional behavior is disregarded. The anchoring elements are modeled according to the small-sag cable theory, accounting for geometrical nonlinearities, supports motion, added mass and damping effects to the presence of the water. By adopting a standard Galerkin discretization procedure, each anchoring element is then described as a single-dof system, denoting with z its dimensionless time-varying modal coordinate. Numerical inspection of the dimensionless coefficients of the equation of motion performed with reference to hollow-core circular cross-section tethers reveal that (1) the dynamic coupling is one-way only. i.e. the bare tunnel has an influence on the dynamics of the mooring system and not vice-versa, and that (2) the in-plane and out-of plane response of the SFT are almost decoupled. Exploiting the cross-section's symmetry, coupled in-plane vibrations are controlled by the following system of dimensionlesss equations of motion:

$$\begin{cases} \ddot{w}_T + 2\xi_T \omega_T \dot{w}_T + \omega_T^2 w_T = F_T(\tau) + T(\tau)\sin\theta \\ \ddot{z} + 2\xi\,\omega\,\dot{z} + \omega^2 z + \nu z^3 + 3\beta z^2 + 3\tilde{\beta} z^2 w_T \sin\theta - \eta^* w_T z + \ddot{w}_T(\zeta^* + \alpha^*) = F(\tau) \end{cases} \tag{1}$$

where τ is the dimensionless time variable, T is the dimensionless dynamic tension of the anchor, ω (ω_T), ξ (ξ_T), and F (F_T) are the dimensionless natural circular frequency, damping coefficient and generalized external force of the anchoring element (tube cross-section), respectively. Moreover, θ is the inclination angle of the tether, while β, $\tilde{\beta}$, ν are coefficients governing geometrical nonlinearities, η^* is related to the parametric excitation term, while α^* and ζ^* are related to the inertial support motions induced by the coupling with the tube. Three different Loading Conditions (LCs) have been identified as critical. The first two consider an hydrodynamic force acting on the tunnel which is expressed as an harmonic function depending upon a detuning

parameter δ, and whose frequency content is Quasi-Simple-Resonant (LC1) or Quasi-Parametric-Resonant (LC2) with the anchor. The generalized external force acting on the tunnel read $F_T(\tau) = f \sin[\omega(1+\delta\varepsilon)\tau]$ for LC1 and $F_T(\tau) = f \sin[\omega(2+\delta\varepsilon)\tau]$ for LC2, where ε is a small dimensionless ordering variable. Finally, the Loading Condition 3 (LC3) considers an hydrodynamic force acting on the anchor, Quasi-Resonant with the anchor itself, i.e. $F(\tau) = \tilde{f} \sin[\omega(1+\delta\varepsilon)\tau]$. For each loading condition, the equations of motion of the system have been attacked according to an application of the Multiple Times-scales perturbation method, and closed-form expressions for the steady-state vibration amplitude a of the anchoring elements have been derived.

3. Parametric analyses

After a numerical validation of the closed-form expressions has been performed, extensive parametric analyses in the space of technically relevant parameters of the mooring system have been carried out.
As an application example, the influence of the drag coefficient C_d of the tether on its dimensionless vibration amplitude a is depicted in Fig. 1, for Loading Conditions 1 (LC1) and 2 (LC2).

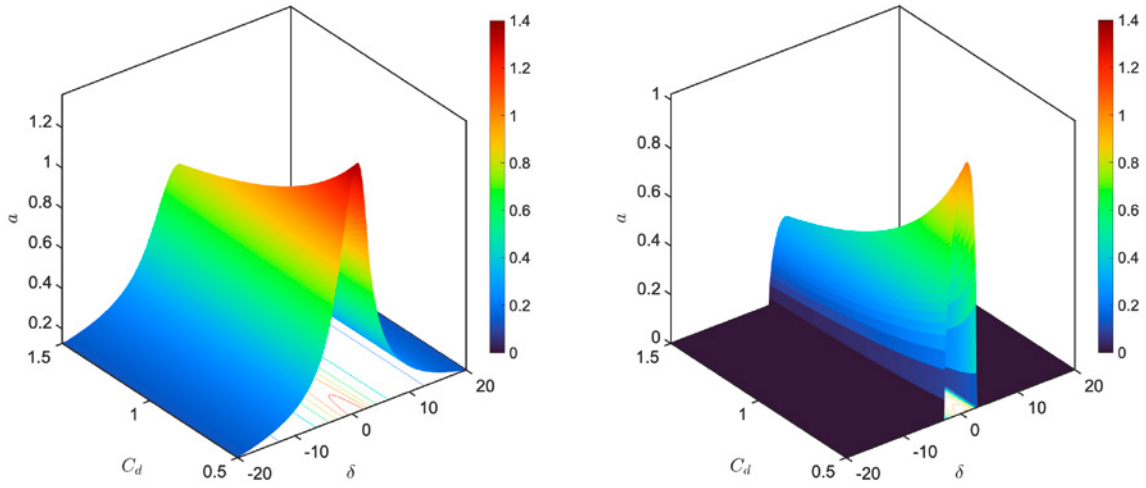

Figure 1: Dimensionless steady-state vibration amplitudes a of the anchor predicted by the perturbation solutions, as a function of the detuning parameter δ and of the drag coefficient C_d, for LC1 (left) and LC2 (right).

Fig. 1 clearly shows that the dynamic response of the anchor, subject to loading scenario 1 can be assimilated to that of a Duffing oscillator with hardening behavior. On the contrary, loading scenario 2 delivers a Mathieu-Duffing type response, with hardening behavior as well. The drag coefficient negatively correlates with the amplitude of oscillations. In particular, the nonlinear increase of vibration amplitude observed passing for high values to low values of C_d is faster for LC2, compared to LC1. This highlights the sensitivity of the Mathieu-Duffing equation to the damping of the system.

4. Conclusions

This work dealt with the complete characterization of the nonlinear dynamic response of anchoring elements for Submerged Floating Tunnels (SFTs) considering the coupling with the tube and hydrodynamic loading conditions. The derived approximate closed-form solutions allowed for an extreme reduction of the computational burden encountered with standard time-domain numerical simulations, serving as a fundamental tool in the optimization of the mooring system's parameters for the conceptual design phase of seabed-anchored SFTs.

References

[1] S. Corazza, F. Foti, L. Martinelli, and V. Denoël. Submerged floating tunnels: nonlinear dynamics of anchoring elements subject to hydrodynamic loads. Submitted to Journal of Sound and Vibration, 2025.

[2] S. Corazza, F. Foti, and L. Martinelli. Dynamic substructuring technique for submerged floating tunnels. In J.S. Jensen, D.M. Frangopol, and J.W. Schmidt, editors, *Bridge Maintenance, Safety, Management, Digitalization and Sustainability*, pages 1029–1036. CRC Press/Balkema, 2024.

ECCOMAS Thematic Conference and IACM Special Interest Conference
Highly Flexible Slender Structures (HFSS 2025)
22–26 September 2025, Kaiserslautern, Germany

Closed Catenary Loops: Lariat Chain, String Shooter, and Heavy Elastica

A. R. Dehadrai [1], J. A. Hanna [2]

[1] Amrita Vishwa Vidyapeetham, Bengaluru, d_abhinav@blr.amrita.edu
[2] University of Nevada, Reno, jhanna@unr.edu

Keywords: string, elastica, catenary, axially moving

The problem at hand is to determine the equilibrium configurations of a closed loop of axially-moving string subject to a uniform body force and one external point force. This is an idealized model of a thin, flexible body, in the presence of gravity, driven by a small wheel or pair of wheels [1]. Allowance is made for a jump in angle (kink) at the launching point.

We will review the history of this and closely related problems, going back to the 19th century. We will provide a general perspective, alongside a selection of solutions using both previously published and new results, while addressing several errors and misconceptions in the literature.

Solutions for a perfectly-flexible string can be obtained analytically [2], described by the shifted tension $\sigma - v^2$ and tangential angle θ of a planar curve,

$$d_s\theta = \frac{C\cos^2\theta}{(\sec\theta+\tan\theta)^D}\,, \tag{1}$$

$$\sigma - v^2 = \frac{(\sec\theta+\tan\theta)^D}{C\cos\theta}\,, \tag{2}$$

where the parameter D is the ratio of drag forces to weight, and an integration constant C relates the total length and subtended angle of a segment of curve. These equations will generate either upper or lower portions of the eventual closed loop, formed by stitching these together. As the drag parameter D varies, there are two bifurcations, separating three regimes, as follows:

- At low drag ($D < 1$), no closed loop solution can exist. The solutions are akin to the classical stationary catenary, approaching vertical orientation and vanishing curvature asymptotically as the arc length and shifted tension diverge. Finite-length upper and lower branches can only be stitched together if a second point force is provided at a second kink.

- At intermediate drag ($1 < D < 2$), it is possible to stitch finite-length upper and lower curves with vanishing shifted tension and curvature at the vertical. These are of identical lengths, a curious result due to Gregory [3].

- At high drag ($2 < D$), the curvature diverges at finite arc length at the vertical. The curves are still rectifiable, and can be stitched. The shapes are noticeably different than those at intermediate drag.

Figure 1 shows an example of each type of solution. The low-drag solution is not physically admissible, as there is no second point force present.

To construct physically admissible low-drag solutions, we add a small amount of bending stiffness, connecting the problem with that of a hanging loop elastica. This is an atypical regularization, in that bending stiffness does not smooth out a sharp feature such as a curvature singularity or a kink, but rather provides an additional derivative of curvature term that allows for the structure to pass through a vertical orientation — forbidden for the catenary because of an unbalanced nonzero product of shifted tension and curvature. For highly flexible rods, this is a numerically stiff problem. There are significant differences in shape from the perfectly flexible case.

We will also discuss the global balances of linear, angular, and pseudo-momentum; the latter is further related to energy losses through drag.

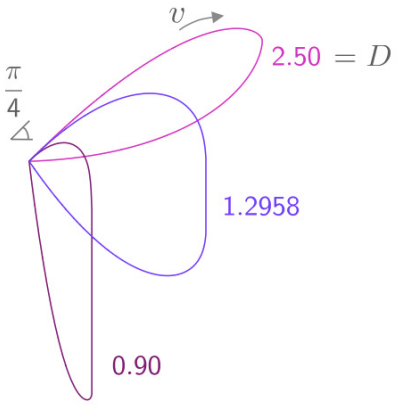

Figure 1: Three types of solution with the same launch angle: low, intermediate, and high nondimensional drag D. A force is supplied at the launching point on the left, and the axial velocity v of the shapes is clockwise. The low-drag solution requires an additional point force on the right, and is thus inadmissible as a physical solution.

References

[1] B. Yeany. *String shooter-String launcher- physics of toys*, `https://www.youtube.com/watch?v=rffAjZPmkuU`

[2] B. Chakrabarti and J. A. Hanna. *Catenaries in viscous fluid*, Journal of Fluids and Structures, 66 (2016) 490-516

[3] C. C. L. Gregory. *Theory of a loop revolving in air, with observations on the skin-friction*, The Quarterly Journal of Mechanics and Applied Mathematics, II (1949) 30-39

ECCOMAS Thematic Conference and IACM Special Interest Conference
Highly Flexible Slender Structures (HFSS 2025)
22–26 September 2025, Kaiserslautern, Germany

Dynamics of a Total Lagrangian Mixed Petrov–Galerkin Cosserat Rod

Marco Herrmann[1], Simon R. Eugster[1]

[1] Dynamics and Control, Department of Mechanical Engineering,
Eindhoven University of Technology, The Netherlands,
[m.herrmann, s.r.eugster]@tue.nl

Keywords: Rod Finite Elements, Objectivity, Locking-free, Quaternion Interpolation, Petrov–Galerkin

1. Introduction

The computational complexity of multibody systems increases dramatically with the inclusion of flexible components. The complexity arises not only from the highly nonlinear and coupled interpolation of the position and orientation fields, as discussed in [1], but also from the nonlinear calculation of strains and stresses based on the previous quantities. Additional challenges are posed by numerical effects leading to membrane or shear locking and the general need for an objective interpolation. To overcome these challenges, the quaternion interpolation proposed by [2] combined with a mixed Petrov–Galerkin approach is used. This work presents therefore an objective, locking-free and computationally efficient Cosserat rod finite element formulation, that can be seamlessly integrated into existing standard multibody frameworks without the need for specialized Lie-group solvers.

2. Continuous Rod Description

Let $\xi \in \mathscr{I} = [0,1] \subset \mathbb{R}$ denote the centerline parameter, the motion of the Cosserat rod is described by the centerline point ${}_I\mathbf{r}_{OP}(\xi,t) \in \mathbb{R}^3$ with respect to an inertial basis I. The respective cross-section orientation for time t is captured by the transformation matrix $\mathbf{A}_{IB}(\xi,t) \in SO(3)$. Using the derivatives w.r.t. the centerline parameter ξ (indicated by $(\bullet)_{,\xi}$), the deformation can be characterized by ${}_B\bar{\boldsymbol{\gamma}} = \mathbf{A}_{IB}^{\mathrm{T}}\,{}_I\mathbf{r}_{OP,\xi}$ and ${}_B\tilde{\bar{\boldsymbol{\kappa}}}_{IB} = \mathbf{A}_{IB}^{\mathrm{T}}\mathbf{A}_{IB,\xi}$. The reference centerline ${}_I\mathbf{r}_{OP}^0(\xi)$ and the reference transformation matrix $\mathbf{A}_{IB}^0(\xi)$ allow a similar characterization of the reference deformation through ${}_B\bar{\boldsymbol{\gamma}}^0$ and ${}_B\bar{\boldsymbol{\kappa}}_{IB}^0$. This allows to introduce the objective strain measures as $\boldsymbol{\varepsilon}_{\boldsymbol{\gamma}} = ({}_B\bar{\boldsymbol{\gamma}} - {}_B\bar{\boldsymbol{\gamma}}^0)/J$ and $\boldsymbol{\varepsilon}_{\boldsymbol{\kappa}} = ({}_B\bar{\boldsymbol{\kappa}}_{IB} - {}_B\bar{\boldsymbol{\kappa}}_{IB}^0)/J$, where $J = \|{}_I\mathbf{r}_{OP,\xi}^0\|$ is the reference arc length. Herein, $\boldsymbol{\varepsilon}_{\boldsymbol{\gamma}}$ measures the dilatation and shear strains, and $\boldsymbol{\varepsilon}_{\boldsymbol{\kappa}}$ measures torsion and bending strains.

The resultant contact forces ${}_B\mathbf{n}(\xi,t)$ and moments ${}_B\mathbf{m}(\xi,t)$ can be derived by the partial derivatives of the strain energy density function $W(\boldsymbol{\varepsilon}_{\boldsymbol{\gamma}}, \boldsymbol{\varepsilon}_{\boldsymbol{\kappa}})$. Alternatively, the resultant contact force and moment can be interpreted as independent fields and related to the objective strain measures by the Hellinger–Reissner principle. The internal virtual work is then expressed as

$$\delta W^{\mathrm{int,HR}} = -\int_{\mathscr{I}} \Big\{ \delta({}_B\bar{\boldsymbol{\gamma}})^{\mathrm{T}}\,{}_B\mathbf{n} + \delta({}_B\bar{\boldsymbol{\kappa}})^{\mathrm{T}}\,{}_B\mathbf{m} \Big\} J \mathrm{d}\xi - \int_{\mathscr{I}} \Big\{ \delta({}_B\mathbf{n})^{\mathrm{T}} \Big[\boldsymbol{\varepsilon}_{\boldsymbol{\gamma}} - \frac{\partial W^\star}{\partial\,{}_B\mathbf{n}} \Big] + \delta({}_B\mathbf{m})^{\mathrm{T}} \Big[\boldsymbol{\varepsilon}_{\boldsymbol{\kappa}} - \frac{\partial W^\star}{\partial\,{}_B\mathbf{m}} \Big] \Big\} J \mathrm{d}\xi\,, \quad (1)$$

where $W^\star({}_B\mathbf{n}, {}_B\mathbf{m})$ is the complementary strain energy density function, which satisfies Fenchel's equation $W(\boldsymbol{\varepsilon}_{\boldsymbol{\gamma}}, \boldsymbol{\varepsilon}_{\boldsymbol{\kappa}}) + W^\star({}_B\mathbf{n}, {}_B\mathbf{m}) = \boldsymbol{\varepsilon}_{\boldsymbol{\gamma}B}^{\mathrm{T}}\mathbf{n} + \boldsymbol{\varepsilon}_{\boldsymbol{\kappa}B}^{\mathrm{T}}\mathbf{m}$. Note that the complementary strain energy density function $W^\star$ is only available, if the strain energy density function W is convex. In the quadratic case, the strain energy density function and the complementary strain energy density function are given by

$$W = \frac{1}{2}\boldsymbol{\varepsilon}_{\boldsymbol{\gamma}}^{\mathrm{T}}\mathbf{C}_{\boldsymbol{\gamma}}\boldsymbol{\varepsilon}_{\boldsymbol{\gamma}} + \frac{1}{2}\boldsymbol{\varepsilon}_{\boldsymbol{\kappa}}^{\mathrm{T}}\mathbf{C}_{\boldsymbol{\kappa}}\boldsymbol{\varepsilon}_{\boldsymbol{\kappa}}\,, \quad W^\star = \frac{1}{2}{}_B\mathbf{n}^{\mathrm{T}}\,\mathbf{C}_{\boldsymbol{\gamma}}^{-1}\,{}_B\mathbf{n} + \frac{1}{2}{}_B\mathbf{m}^{\mathrm{T}}\,\mathbf{C}_{\boldsymbol{\kappa}}^{-1}\,{}_B\mathbf{m}\,, \quad (2)$$

with $\mathbf{C}_{\boldsymbol{\gamma}} = \mathrm{diag}(k_{\mathrm{e}}, k_{\mathrm{s_y}}, k_{\mathrm{s_z}})$ and $\mathbf{C}_{\boldsymbol{\kappa}} = \mathrm{diag}(k_{\mathrm{t}}, k_{\mathrm{b_y}}, k_{\mathrm{b_z}})$, where the diagonal elements are the stiffness coefficients for dilatation, shear, torsion and bending, respectively. In the limit case of infinite stiffness, when e.g., inextensibility or shear-rigidty is modelled, the inverse of these parameters approaches zero. The mixed approach allows to represent these constraints without any additional effort.

3. Discretization

For a quaternion $\mathbf{P} = (p_0, \mathbf{p}) \in \mathbb{R}^4$ of arbitrary length with the scalar part $p_0 \in \mathbb{R}$ and the vectorial part $\mathbf{p} \in \mathbb{R}^3$, the quaternion formula $\mathbf{A}(\mathbf{P}) = 1 + 2(p_0\tilde{\mathbf{p}} + \tilde{\mathbf{p}}\tilde{\mathbf{p}})/\|\mathbf{P}\|^2$ returns always a proper transformation matrix $\mathbf{A} \in$

$SO(3)$. Using $p+1$ nodes per element with Lagrangian polynomials of p-th order, in accordance with [2], an objective interpolation is obtained by interpolating nodal centerline points ${}_I\mathbf{r}_{OP_i^e}$ and nodal quaternions $\mathbf{P}_{IB_i^e}$. The interpolated quaternion is then used in the previously mentioned quaternion formula to obtain $\mathbf{A}_{IB}$. All nodal centerline points ${}_I\mathbf{r}_{OP_i^e} \in \mathbb{R}^3$ and nodal quaternions $\mathbf{P}_{IB_i^e} \in \mathbb{R}^4$ are collected in the vector of generalized coordinates $\mathbf{q}$. In analogy to [3], the virtual displacements and virtual rotations are interpolated using the same $p+1$ nodes per element with the same Lagrangian polynomials. All nodal variations, i.e., the nodal virtual displacements ${}_I\delta\mathbf{r}_{P_i^e} \in \mathbb{R}^3$ and nodal virtual rotations ${}_B\delta\boldsymbol{\phi}_{IB_i^e} \in \mathbb{R}^3$ are collected in $\delta\mathbf{s}$. In order to obtain a constant and symmetric mass matrix, the velocities are considered as independent fields and are interpolated similarly. The stresses, i.e., the resultant contact forces and moments are interpolated with p nodes per element, resulting in one polynomial degree less than the interpolation of the placement and orientation. All nodal contact forces ${}_B\mathbf{n}_i^e \in \mathbb{R}^3$ and moments ${}_B\mathbf{m}_i^e \in \mathbb{R}^3$ are collected in $\boldsymbol{\lambda}_c$. The variation of the resultant contact forces and moments is consistent with their interpolation. While the functions ${}_I\mathbf{r}_{OP}$, $\mathbf{A}_{IB}$, ${}_I\delta\mathbf{r}_P$ and ${}_B\delta\boldsymbol{\phi}_{IB}$ are (C^0-) continuous, the contact forces and moments ${}_B\mathbf{n}$ and ${}_B\mathbf{m}$ are discontinuous at internal element boundaries.

4. Equations of Motion

The equations of motion of the discretized rod directly are obtained by substituting all approximations into the principle of virtual work of the continuous Cosserat rod. This results in a set of first order differential equations in the form

$$\dot{\mathbf{q}} = \mathbf{B}(\mathbf{q})\mathbf{u}\,, \quad \mathbf{M}(\mathbf{q})\dot{\mathbf{u}} = \mathbf{f}^{\mathrm{gyr}}(\mathbf{u}) + \mathbf{f}^{\mathrm{ext}}(\mathbf{q}) + \mathbf{W}_c(\mathbf{q})\boldsymbol{\lambda}_c\,, \qquad \mathbf{K}_c^{-1}\boldsymbol{\lambda}_c + \mathbf{l}_c(\mathbf{q}) = \mathbf{0}\,, \quad \mathbf{g}_S(\mathbf{q}) = \mathbf{0}\,. \tag{3}$$

The first equation is also known as kinematics differential equation, connecting the generalized velocities $\mathbf{u}$, which contains the nodal linear velocities ${}_I\mathbf{v}_{P_i^e}$ and angular velocities ${}_B\boldsymbol{\omega}_{IB_i^e}$, with the time derivative of the generalized coordinates $\dot{\mathbf{q}}$. The second equation is the differential equation containing generalized forces and the time derivative of the generalized velocities. The third equation is the algebraic constitutive equation in compliance form. The last equation is the algebraic equation for the quaternion constraint, which arises through requiring for each quaternion $\mathbf{P}_{IB_i^e}$ to be a unit quaternion.

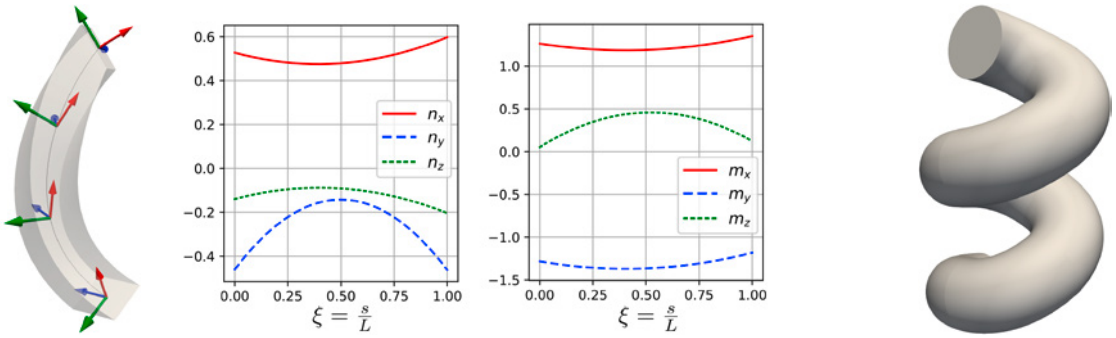

Figure 1: The four-node element has cubic interpolation of the kinematics and quadratic interpolation of the resultant contact stresses. In a static analysis, an initially straight rod is bent to a helix with two coils. The proposed mixed formulation only requires one increment of the applied moment, while displacement based formulations require more than 100 load increments.

References

[1] J. Harsch, S. Sailer, and S. R. Eugster. A total Lagrangian, objective and intrinsically locking-free Petrov-Galerkin SE(3) Cosserat rod finite element formulation, International Journal for Numerical Methods in Engineering, Vol. 124(13), pp. 2931-3111, 2023.

[2] I. Romero. The interpolation of rotations and its application to finite element models of geometrically exact rods. Computational Mechanics, 34(2):121-133, 2004.

[3] S. R. Eugster, J. Harsch. A family of total Lagrangian Petrov–Galerkin Cosserat rod finite element formulations. GAMM-Mitteilungen, 46(2023), e202300008.

ECCOMAS Thematic Conference and IACM Special Interest Conference
Highly Flexible Slender Structures (HFSS 2025)
22–26 September 2025, Kaiserslautern, Germany

Mixed Modal Planar Oscillations of a Cantilevered Pipe with an End Mass

K. Katsura [1], Y. Kuroyanagi [2], K. Yamashita [3]

[1] Fukui University of Technology, kosuke.katsura@gmail.com
[2] Fukui University of Technology, mm24002yk@edu.fukui-ut.ac.jp
[3] Fukui University of Technology, yamashita@fukui-ut.ac.jp

Keywords: Pipe Conveying Fluid, Experiment, Self-Excited Oscillation, Modal Interaction

1. Introduction

Post-critical nonlinear motions of a cantilevered pipe conveying fluid have been studied as an essential problem on dynamically unstable oscillations of continuous systems. From visual inspections in experiments, Copeland and Moon [1] clarified that an attached end mass is a key parameter to generate complex non-planar motions. Païdoussis and his research group extensively have conducted numerical calculations on post-critical non-planar pipe motions based on Galerkin's discretization method. Their theoretical results also revealed that attached end mass enriches the dynamical features of this system. In order to clarify the complex modal interactions in the post-critical pipe motions, analytical methods based on modal techniques are useful. In addition to that, multi-points non-contacting measurements are needed to extract hidden nonlinear modal interactions in experiments. In this study, we consider planar lateral pipe vibration. We focus on the modal interactions which caused periodic doubling bifurcation in single-mode flutter. In particular, detailed experiments were conducted to capture the complex modal interactions.

2. Analytical model and basic equations

As shown in Fig. 1(a), we consider planar vibrations of a pipe which is hung vertically and has an attached mass at the lower free end. The pipe is sufficiently long that the effects of gravitational force cannot be neglected. s is the curvilinear coordinate along the pipe axis and $w(s,t)$ is the lateral displacement of pipe axis. Following governing equation and boundary conditions can be derived by using the usual assumptions.

$$\ddot{w}+\delta\dot{w}''''+2\sqrt{\beta}V\dot{w}'+V^2w''-\gamma\{(\alpha+1-s)w'\}'+w''''=n(w) \tag{1}$$

$$s=0:\ \ w=0,\ \ w'=0,\ \ s=1:\ \ w''+\delta\dot{w}''=0,\ \ w'''+\delta\dot{w}'''-\alpha\gamma w'-\alpha\ddot{w}=b(w) \tag{2}$$

where $\dot{(\ )}$ and $'$ denote the derivative with time t and curvilinear coordinate s. $n(w)$ and $b(w)$ represent third order nonlinear terms of w. There are five dimensionless parameters involved in Eqs. (1) and (2). α means dimensionless attached mass, β means fluid mass ratio, γ means the ratio of gravitational force to elastic force, δ is dimensionless internal damping coefficient, and V is dimensionless flow velocity.

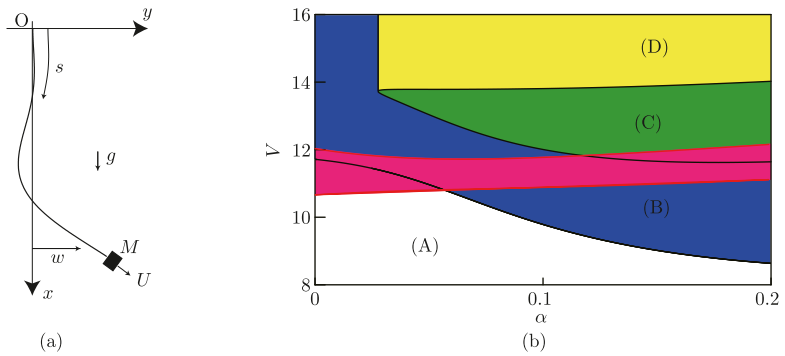

Figure 1: (a) lateral vibration of a pipe with an end mass, (b) linear unstable regions in $\alpha-V$ parameter plane ($\beta=0.25$, $\gamma=128$, $\delta=0.4\times10^{-3}$) (A) stable, (B) flutter (third mode), (C) flutter (third and fourth modes), (D) flutter (fourth mode), red region indicates that first mode natural frequency is zero.

3. Theoretical analyses

We conducted detailed linear stability analyses to determine dynamically unstable regions. Figure 1(b) shows the linear stability boundaries in $\alpha - V$ plane. In region (C), both third and fourth modes reveal dynamic instability. Natural frequency of the first mode is zero in the red region. In this region, natural frequency of fourth mode ω_{4r} is almost twice the natural frequency of third mode ω_{3r} ($\omega_{4r} = 2\omega_{3r} + \sigma$), where σ is the detuning parameter. In the vicinity of region (C) in Fig.1(b), lateral displacement w can be written as $w = A_1\Phi_1 + A_3\Phi_3 + A_4\Phi_4 + y + c.c.$, where A_n and Φ_n represent the amplitude and eigen-function of nth mode, respectively. Φ_3 and Φ_4 are complex function while Φ_1 is real function. y is the complementary subspace of $A_1\Phi_1 + A_3\Phi_3 + A_4\Phi_4$. By using the adjoint function of the system, evolutional equations of amplitudes A_1, A_3 and A_4 can be derived. From the amplitude equations, periodic doubling bifurcation in single mode flutter of the fourth mode can be produced.

4. Experiments

Experiments were conducted with the silicone rubber pipe conveying water ($D_o = 12.5$mm, $D_i = 6.7$mm, ℓ = 565mm). Three dimensional movements of the pipe could be captured by image processing system. Figure 2 shows the time histories of w and features of pipe vibration obtained from multi-points measurement. In Fig. 2(a), the lateral pipe vibration has two dominant frequencies. The dominant frequency 4.33 Hz corresponds to self-excited vibration in the fourth mode. Another dominant frequency 2.16 Hz is half the frequency of 4.33 Hz. Figure 2(b) shows the typical features of the mixed modal self-excited pipe vibration.

5. Conclusions

In this study, as a first step to clarify the complex modal interactions in post-critical pipe motions, we consider the periodic doubling oscillations which are caused by two dynamically unstable modes and the first mode with zero natural frequency. In particular, we experimentally confirmed this type oscillation from the multi-points measurements.

Acknowledgements

This work was supported by JSPS KAKENHI Grant Number JP23K03753.

References

[1] G.S. Copeland, F.C. Moon. *Chaotic flow-induced vibration of a flexible tube with end mass*, Journal of fluids and structures, 6 (1992) 705-718.

[2] Y. Modarres-Sadeghi, C. Semler, M. Wadham-Gagnon, M.P. Païdoussis. *Dynamics of cantilevered pipes conveying fluid. Part 3: Three-dimensional dynamics in the presence of an end-mass*, Journal of fluids and structures, 23 (2007) 589-603.

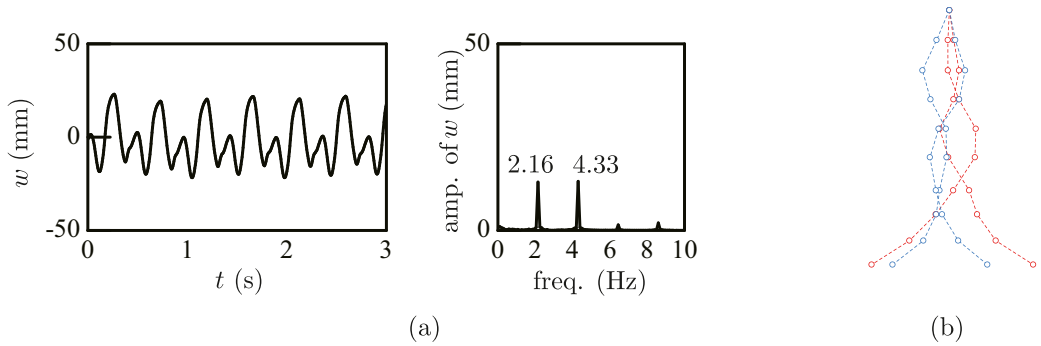

Figure 2: Periodic doubling pipe vibration (a) time history of w and its spectrum analysis, (b) typical features of pipe motion.

ECCOMAS Thematic Conference and IACM Special Interest Conference
Highly Flexible Slender Structures (HFSS 2025)
2226 September 2025, Kaiserslautern, Germany

Nonlinear Vibrations of an Elastica at its Post-buckled Configurations

Hasnaa Kibach [1], Alireza Ture Savadkoohi [2]

[1] Univ Lyon, ENTPE, Ecole Centrale de Lyon, CNRS, LTDS, UMR5513, Vaulx-en-Velin, France, hasnaa.kibach@entpe.fr

[2] Univ Lyon, ENTPE, Ecole Centrale de Lyon, CNRS, LTDS, UMR5513, Vaulx-en-Velin, France, alireza.turesavadkoohi@entpe.fr

Keywords: Elastica, Post-buckling, Nonlinear dynamics, Multiple Scales Method

1. Introduction

In contrast to classical materials, where built-in micro-scale properties determine the macro-scale responses, artificially architected materials are designed so that their micro-scale behaviors are programmed to control the system behaviors at macro-scales. To this end, as an example from mechanics, compliant mechanisms have been exploited [1], enabling the fabrication of structures that exhibit extraordinary responses such as energy trapping [2], shock absorption [3], and vibration isolation [4]. Their highly flexible components allow them to exhibit instabilities and to go beyond the domain of linear elasticity, such as large deformations occuring both at the element and system scales.

This study focuses on the nonlinear post-buckling responses of an elastica under external harmonic excitation.This considered system can be supposed as a single element of an architected material.

2. The system under consideration

We consider the model of a prestressed, forced elastica with clamped-guided boundary conditions, as depicted in Figure 1. The straight beam is initially inclined at an angle of θ_0 with respect to the horizontal axis. The external loading P is first applied gradually, along the beams initial axis, until it reaches a target critical buckling load, namely F_S. Then, a harmonic excitation of the form $\varepsilon F_D \cos(\Omega t)$, where ε ($\varepsilon << 1$), a small book-keeping parameter, is added to F_s. The system is analyzed analytically, via the multiple scales method, around one of its equilibrium configurations and also around one of its vibration mode shapes.

This study provides some insights for tuning physical and mechanical properties of the element in order to create desired responses.

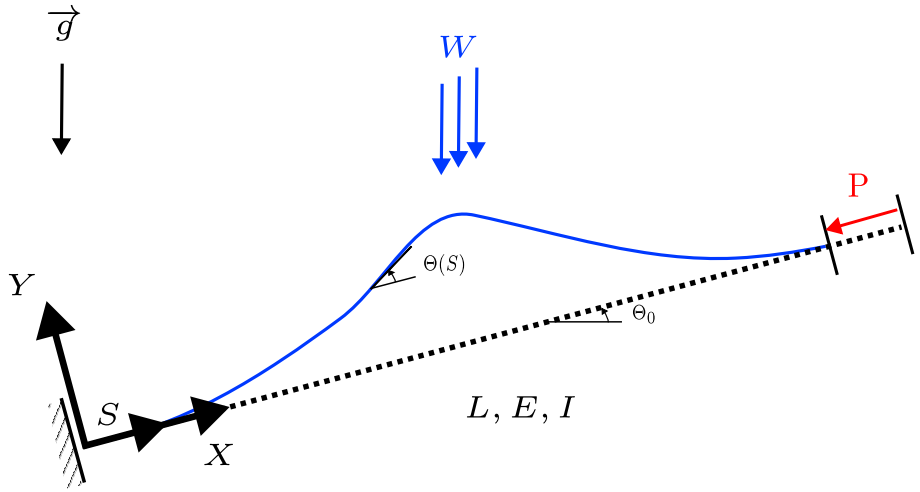

Figure 1: System under consideration - a clamped-guided elastica under excitation P.

3. Main results

Backbone curves of the system around different vibration and buckling modes are detected showing hardening and softening behaviors, depending on the selected modes. Then, the time history of some prints of the element in its post-buckled configuration under dynamic excitation are presented and commented.

4. Conclusion and Outlook

For a given post-buckled configuration, variations of the nonlinear frequency of the system can present different nonlinear dynamic behaviors, as articulated in this study. The outlook of this work is to study and to describe the dynamic behaviors of multiple cells composed of such studied elements.

Acknowledgments

The authors would like to thank the following organizations for supporting this research : (i) The "Ministère de la Transition écologique et de la Cohésion des territoires" and (ii) LABEX CELYA (ANR-10-LABX-0060) of the "Université de Lyon" within the program "Investissement d'Avenir" (ANR-11-IDEX-0007) operated by the French National Research Agency (ANR).

References

[1] Fowler, Robert M., Larry L. Howell, and Spencer P. Magleby. "Compliant space mechanisms: a new frontier for compliant mechanisms." Mechanical Sciences 2.2 (2011): 205-215.

[2] Shan, S., Kang, S. H., Raney, J. R., Wang, P., Fang, L., Candido, F.,& Bertoldi, K. (2015). Multistable architected materials for trapping elastic strain energy. Adv. Mater, 27(29), 4296-4301.

[3] Bertoldi, K., Vitelli, V., Christensen, J., & Van Hecke, M. (2017). "Flexible mechanical metamaterials." Nature Reviews Materials 2.11, 1-11.

[4] Virgin, L. N., S. T. Santillan, and R. H. Plaut. "Vibration isolation using extreme geometric nonlinearity." Journal of Sound and Vibration 315.3 (2008): 721-731.

ECCOMAS Thematic Conference and IACM Special Interest Conference
Highly Flexible Slender Structures (HFSS 2025)
22–26 September 2025, Kaiserslautern, Germany

Experimental and Numerical Investigation of Flexible Wing Flutter

F. Maetz [1], B. Chouvion [2], F. Renaud [1], A. Leroy [2], J.-L. Dion [1], O. Montagnier [2]

[1] Laboratoire Quartz (EA-7393), ISAE-Supméca, florian.maetz@isae-supmeca.fr
[2] CREA, École de l'Air et de l'Espace

Keywords: Highly Flexible Wing, Non Linear Dynamic, Nonlinear beam, Camera Acquisition

1. Main Motivation

Flutter has always been a critical concern in aircraft design and operation, as it poses significant risks to structural integrity and flight safety. High-aspect-ratio wings enhance aerodynamic efficiency but also increase flexibility, making aircraft more susceptible to flutter and lowering the flutter onset speed. Understanding and mitigating this phenomenon is essential to ensuring the safe and optimal performance of modern aircraft. This study investigates the flutter behavior of high-aspect-ratio wings, providing insights into their dynamic response.

2. Methodological Features

This study is part of a larger project focused on reconstructing the aerodynamic forces acting on a wing using video recordings. The first step in this process is accurately measuring the wing's displacement from the videos. This approach eliminates the need for physical sensors, which can alter flutter dynamics by adding stiffness and mass. Additionally, camera-based methods enable full-field measurement techniques, offering a more comprehensive analysis of the wing's motion.

2.1. Wind Tunnel Experiments

A scaled-down wing model was placed in a wind tunnel to study the flutter phenomenon. Figure 1 shows the initially straight wing undergoing large deflection due to gravity and wind in the tunnel. Modal analysis is conducted from zero wind speed up to flutter onset with release test experiments. Thanks to these experiments, we can track the evolution of mode frequencies and shapes as a function of wind speed. The wing's full 3D motion is estimated using a Kalman filter, following the approach in [1]. This requires a kinematic model of wing displacement to assimilate tracking data into the system's state. Moving forward, particular attention will be given to the model's reliability in capturing nonlinear structural stiffness.

2.2. Model Comparisons

In order to optimize the wing during the design phase, it is desirable to obtain fast approximations of results for given geometric and material parameters. This highlights the need for reduced models, as the goal is not extreme accuracy, but rather rapid computation. The primary model of interest in this study is HiFleW [2], a one-dimensional beam model for wings based on Hodges' work [3]. Its kinematic description is illustrated in Figure 2, where the fields (u, v, w, ϕ) characterizing beam motion are discretized using power series polynomials. The new generalized coordinates $(\mathbf{q_u}, \mathbf{q_v}, \mathbf{q_w}, \mathbf{q}_\phi)$ and their associated shape functions approximate these values. The model relies on the following key assumptions:

- Small strains, an elastic isotropic material, large displacements, and large rotations.
- An asymptotic expansion of the exact highly nonlinear equations, truncated at third order, assuming different orders of magnitude $(1 \gg v, w, \phi \gg u)$.
- Rayleigh-Ritz discretization of the fields (u, v, w, ϕ) for computational resolution. Truncated power series expansions are chosen as the subspace for different fields. This provides an accurate representation of low-order modes for large deflections with a minimal number of unknowns. The resulting discretion of a field λ, where λ is a placeholder for (u, v, w, ϕ), is : $\lambda(x,t) = \sum_i^{N_\lambda} q\lambda_i (\frac{x}{L})^i$.

Figure 1: Picture of the deformed beam under aerodynamic forces in the wind tunnel

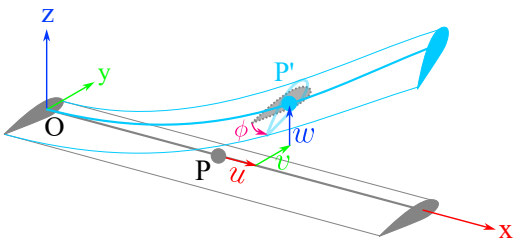

Figure 2: HiFleW kinematic description with its discretization

This formulation results in structural stiffness depending on the current position. To verify structural accuracy, static comparisons were performed against other models: a Finite Element Method (FEM) beam model, used as a reference, and a multibody model where the beam is discretized into rigid sections with compliance provided by torsion springs between them.

These comparisons simulated various loading scenarios with different amplitudes to mimic aerodynamic forces. By neglecting aerodynamic effects, the structural accuracy of the model could be assessed in isolation.

3. Results and Conclusion

Tracking algorithms enable the analysis of the evolution of linear modes as a function of wind speed, provided the system undergoes small vibrations. However, these algorithms reach their limits when confronted with the large amplitudes and high velocities associated with flutter-induced limit cycle oscillations.

Using power series expansions to represent the deformed beam configuration introduces negligible kinematic error, as they effectively capture beam deformation and the first few linear modes. The static study showed that the HiFleW model performs well under low loading levels; however, as the amplitude increases, static error becomes more significant due to the approximation of nonlinear stiffness effects.

To conclude, the kinematic description in HiFleW is well-suited for estimation purposes, but improvements may still be required to enhance its ability to capture the structural dynamics of the beam more accurately. This would allow for better prediction in the Extended Kalman Filter, which will be useful in improving the tracking algorithm's predictive capabilities.

Acknowledgments

This project has received funding from the French Armed Forces Ministry and Defense Innovation Agency (AID), and the French National Research Agency (ANR-24-CE51-7440).

References

[1] Franck Renaud, Stefania Lo Feudo, Jean-Luc Dion, and Adrien Goeller. 3D vibrations reconstruction with only one camera. *Mechanical Systems and Signal Processing*, 162:108032, 2022.

[2] Roberto Alcorta, Benjamin Chouvion, Guilhem Michon, and Olivier Montagnier. On the use of frictional dampers for flutter mitigation of a highly flexible wing. *International Journal of Non-Linear Mechanics*, 156:104515, 2023.

[3] Dewey H Hodges and Earl H Dowell. Nonlinear equations of motion for the elastic bending and torsion of twisted nonuniform rotor blades. Technical report, 1974.

ECCOMAS Thematic Conference and IACM Special Interest Conference
Highly Flexible Slender Structures (HFSS 2025)
22–26 September 2025, Kaiserslautern, Germany

Simulation Models for Large Vibrations of an Axially Moving Suspension Cable of Variable Length in a Vertical Transport System

Jakob Scheidl[1], Yury Vetyukov[1]

TU Wien, Institute of Mechanics and Mechatronics
jakob.scheidl@tuwien.ac.at

Keywords: vertical transport systems, moving rods, ALE kinematics, FEM, perturbation methods

1. Introduction

Vertical transport systems in high buildings or deep mining shafts feature very long suspension cables of hundreds of metres length. The eigenmodes and frequencies of the suspension system change as its free length varies during operation. The frequency range of such systems is large, which poses a significant risk of resonance due to external vibration sources such as building sway or earthquakes [1, 2]. Furthermore, travelling suspension cables, like axially moving structures of variable length in general, are susceptible to different kinds of parametric resonance and self-excited vibrations [3]. Simulation models that allow for an accurate estimation of the system dynamics are helpful in the design of vibration mitigation measures and provide the necessary foundation to thoroughly investigate the different dynamic phenomena.

Presently, different finite element implementations to capture the transient dynamics of axially moving cables in vertical transport systems are considered. Various simplified models, including second order beam and reduced modal models, are compared against a high fidelity geometrically nonlinear reference model. The passing through a resonance due to an external harmonic excitation is considered as a test case to demonstrate the capabilities of the individual strategies. Perturbation techniques are applied to deduce parametrisable reduced order systems based on the modal analysis of the initial system, which also provides an opportunity to introduce a consistent form of modal damping in the original finite element problem.

2. Transient dynamics of a simple vertical transport system

We consider the simple planar model of a vertical transport system depicted in Figure 1. It features a point mass

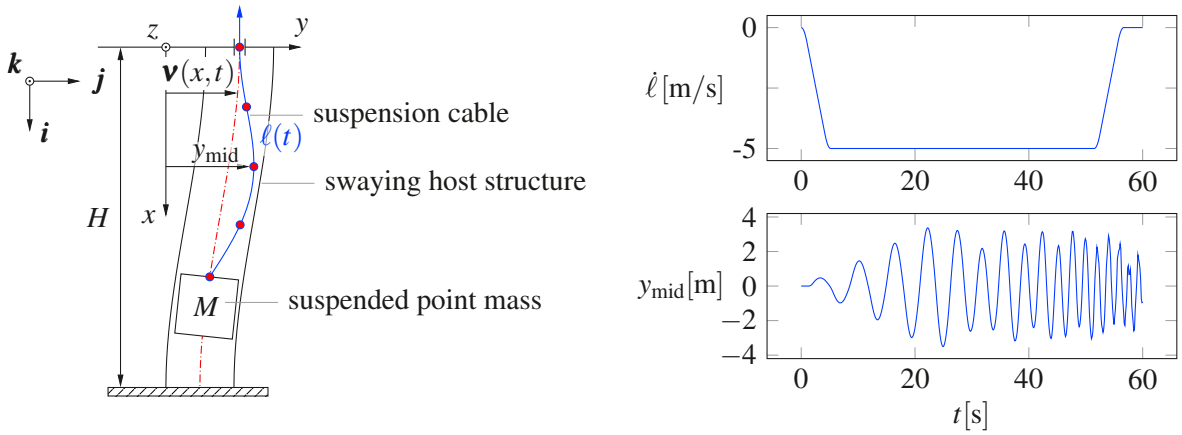

Figure 1: Model of a simple vertical transport system with a point mass hanging on a single moving suspension cable in a tall host structure that is subjected to a harmonic building sway (left). As the system follows a prescribed hoisting profile $\dot{\ell}$, the mid-point of the cable exhibits large transverse deflections y_{mid}.

M that is suspended by a single cable. A harmonic sway of the host structure $v(x,t)$ induces vibrations of the transport system, as it moves upwards or downwards according to a given hoisting profile. The moving structure is modelled as an extensible, but unshearable Kirchhoff rod. Its current material length in the control volume changes as material particles move across the spatially fixed boundary $x = 0$. A mixed kinematic parametrisation

of the primary variables is employed to account for the variable length $\ell(t)$ of the structure, which facilitates the development of efficient finite element models [4] in contrast to standard Lagrangian formulations [5].

Based on this switch of variables, a second order beam and a geometrically nonlinear rod finite element model are developed. The second order model is augmented with an additional single degree of freedom, denoted by $u_{\mathrm{M}}(t)$, to account for the vertical vibrations of the suspended mass [6]. The linearised dynamic system with respect to the straight undisturbed reference motion in the generalised degrees of freedom $\boldsymbol{q}(t)$ has the matrix form:

$$\mathbf{M}\cdot\ddot{\boldsymbol{q}}+(\mathbf{C}+\mathbf{G})\cdot\dot{\boldsymbol{q}}+(\mathbf{K}+\mathbf{N})\cdot\boldsymbol{q}=0, \tag{1}$$

with mass $\mathbf{M}$, damping $\mathbf{C}$, gyroscopic $\mathbf{G}$, stiffness $\mathbf{K}$ and circulatoric $\mathbf{N}$ matrices. Reduced approximate, but fully parametrisable models can be deduced by means of modal perturbation methods [7]. Comparative numerical analyses of the transient motion are carried out with different simulation strategies. For example, Figure 1 depicts the passing of the resonance with the harmonic sway at two different hoisting velocities as obtained with the geometrically nonlinear model. It demonstrates the coupling of transverse (y_{mid}) and axial (u_{M}) vibrations as well as the dependence of vibration amplitudes on the hoisting-speed $\dot{\ell}_{\max}$.

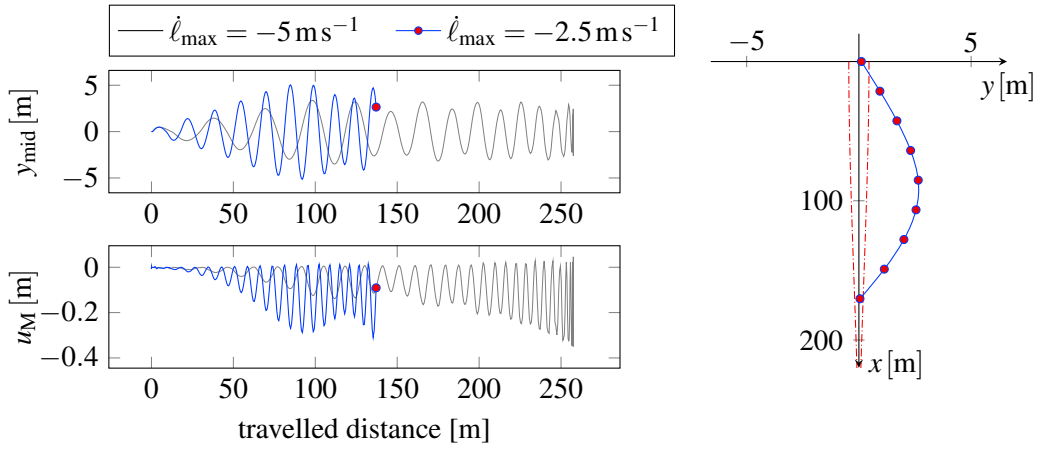

Figure 2: Passing of the resonance with the harmonic building sway at different hoisting speeds, depicting: time-evolutions of the transverse midpoint deflection y_{mid} and the vertical cabin deflection u_{M} as well as a snapshot of the deformed structure.

References

[1] Nick V. Gaiko and Wim T. van Horssen. Resonances and vibrations in an elevator cable system due to boundary sway. *Journal of Sound and Vibration*, 424:272–292, 2018.

[2] Jing Wang and Wim T. van Horssen. On resonances and transverse and longitudinal oscillations in a hoisting system due to boundary excitations. *Nonlinear Dynamics*, 111(6):5079–5106, Mar 2023.

[3] Stefan Kaczmarczyk. The dynamic interactions and control of long slender continua and discrete inertial components in vertical transportation systems. In Andrei K. Abramian, Igor V. Andrianov, and Valery A. Gaiko, editors, *Nonlinear Dynamics of Discrete and Continuous Systems*, pages 117–128. Springer International Publishing, Cham, 2021.

[4] Jakob Scheidl and Yury Vetyukov. Review and perspectives in applied mechanics of axially moving flexible structures. *Acta Mechanica*, 234(4):1331–1364, Apr 2023.

[5] Ivo Steinbrecher, Alexander Humer, and Loc Vu-Quoc. On the numerical modeling of sliding beams: A comparison of different approaches. *Journal of Sound and Vibration*, 408:270–290, 2017.

[6] Hanna Weber, Stefan Kaczmarczyk, and Radosław Iwankiewicz. Non-linear stochastic dynamics of a cable-mass system with finite bending stiffness via an equivalent linearization technique. *Journal of Theoretical and Applied Mechanics*, 58(2):483–497, 2020.

[7] L. Meirovitch and G. Ryland. A perturbation technique for gyroscopic systems with small internal and external damping. *Journal of Sound and Vibration*, 100(3):393–408, 1985.

ECCOMAS Thematic Conference and IACM Special Interest Conference
Highly Flexible Slender Structures (HFSS 2025)
22–26 September 2025, Kaiserslautern, Germany

Contact problems in elastic rods

Harmeet Singh [1], Krishnan Suryanarayanan [2], Anup K. Pathak [3], Parthkumar A. Patel [4]

[1] Indian Institute of Technology Gandhinagar, harmeet.singh@iitgn.ac.in
[2] Indian Institute of Technology Gandhinagar, krishnan.s@iitgn.ac.in
[3] Indian Institute of Technology Gandhinagar, anup.pathak@iitgn.ac.in
[4] Indian Institute of Technology Gandhinagar, parthkumar.patel@iitgn.ac.in

Keywords: Capstan, local and global contact, Hamiltonian, Elastic rods, conservation laws

1. Introduction

Contact problems involving elastic rods may be identified and classified into various categories. We will concern ourselves with three such problems. The first is an elastic rod in frictionless contact with an external rigid body (Fig. 1a). The second is the contact of a terminally loaded elastic rod with itself (Fig. 1b) [1]. We refer to such a contact as *global contact*, where two material points on a rod that are distant in the arc-length coordinate come close enough in the ambient space to establish contact. Finally, the third kind of contact is what we call *local contact*, where sufficiently high local curvatures in an elastic rod of finite thickness may cause the material to approach local self-penetration (Fig. 1c).

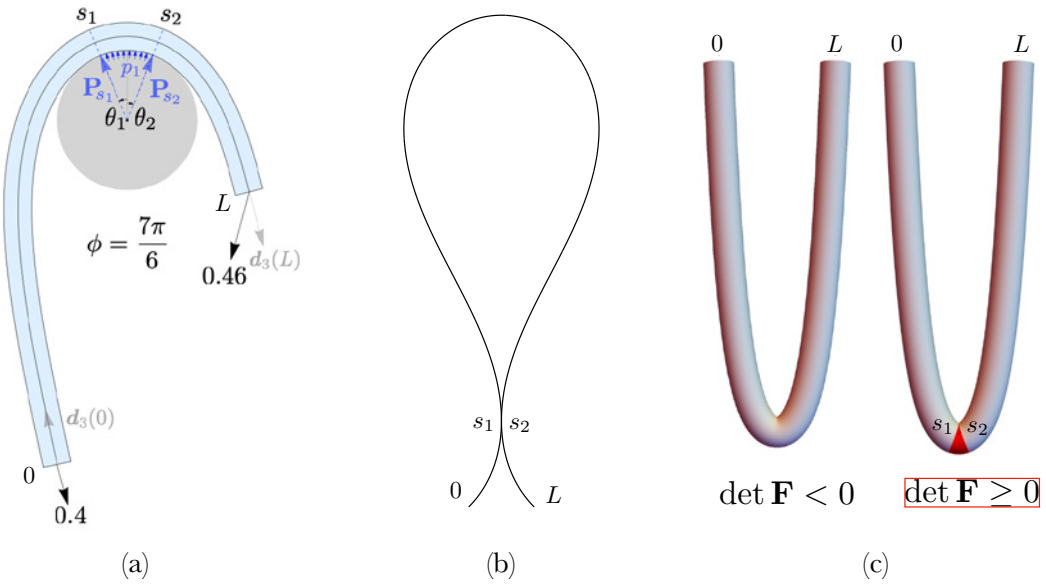

Figure 1: (a) An elastic rod of finite thickness wrapped around a frictionless rigid circular capstan [1] (b) An elastic rod in contact with itself. (c) Two configurations of an ideal tube, with no bending elasticity, and of finite thickness, hanging under gravity. Here $\mathbf{F}$ is the deformation gradient of the deformed configuration.

In this presentation, we will discuss mathematical formulations of the three kinds of contact problems as multi-point boundary value problems. Our main emphasis will be on the use of conservation laws (i.e. functions that are constants along the arc-length coordinate) in the construction of such boundary value problems. While the three problems remain qualitatively different, a key feature common across them is that the region of contact, or the point of contact (as the case may be), is typically an unknown of the problem. We will discuss the utility of a conserved quantity called the *Hamiltonian*, and its continuity across points of contact, in solving such problems.

2. Contact Problems and the *Hamiltonian* Function

In Kirchhoff rod theory, any configuration of a slender body is represented by the set $\{\mathbf{r}(s), \mathbf{d}_1(s), \mathbf{d}_2(s)\}$, where $\mathbf{r}(s) \in \mathbb{R}^3$ is the position vector of a material point identified with a parameter s, often chosen to be the arc-

length coordinate in some reference configuration [2]. Vectors $\mathbf{d}_1(s)$ and $\mathbf{d}_2(s)$ form an orthonormal triad of directors with $\mathbf{d}_3(s) := \mathbf{d}_1(s) \times \mathbf{d}_2(s)$ such that $\mathbf{d}_3(s)$ coincides with the tangent at the point s, i.e. $\mathbf{r}'(s) = \mathbf{d}_3(s)$. The orthonormality of the directors requires that $\mathbf{d}_i'(s) = \mathbf{u}(s) \times \mathbf{d}_i(s)$, where $\mathbf{u}(s)$ is the Darboux vector whose components in the director basis, i.e. $u_i(s) := \mathbf{u}(s) \cdot \mathbf{d}_i(s)$, represent the bending strains of the rod. Furthermore, in Kirchhoff rod theory, the elastic energy density $W(\mathbf{u})$ associated with the rod is taken to be a quadratic function of $\mathbf{u}$.

We define below a function that we refer to as the *Hamiltonian*,

$$H(s) := \mathbf{n}(s) \cdot \mathbf{r}'(s) + \mathbf{m}(s) \cdot \mathbf{u}(s) - W(\mathbf{u}), \tag{1}$$

and state without derivation two properties of this function.

$$H'(s) = 0, \quad s \in [0, L]/\{s_1, s_2\}, \tag{2a}$$

$$[\![H]\!] = 0, \qquad s \in \{s_1, s_2\}. \tag{2b}$$

The first conservation law is a result of the homogeneity of the reference configuration of the elastic rod, whereas the second condition ensures that the free boundaries s_1 and s_2 are located so that a certain virtual work statement holds under infinitesimal variations in the free boundaries s_1 and s_2.

A direct consequence of relations (2) is that the conservation of the Hamiltonian function persists throughout the configurations of all the three aforementioned kinds of contacts.

In the first case, (2) enables us to determine the extent of contact between a circular capstan and an elastic rod wrapped around it. At the same time, it gives simple and direct explanation of how two unequal loads could be balanced at the two terminal ends without the presence of friction between the capstan and the elastic rod: an impossibility in the absence of bending elasticity.

In the second case, where an elastic rod comes into contact with itself, (2) allows us to: 1.) compute post contact configurations of the elastica (Fig. 1b), and 2.) classify the self-contacting solutions of a planar elastica as comprising sections of non-contacting solutions.

In the third case, we have an ideal tube with no bending elasticity and finite thickness hanging under gravity, with its two ends separated by a certain horizontal distance. Since the volume occupied by the tube is of material character, the deformation gradient of any configuration admitted by such a tube must satisfy $\det \mathbf{F} > 0$, where $\mathbf{F}$ is the deformation gradient that linearly maps the tangent space of the reference configuration to that of the deformed configuration. This condition translates into an upper bound on the curvature that any point on the tube can attain. Bringing the two ends of the tube sufficiently close violates the upper bound on the curvature at the lowest point on the tube. In such situations, a region of constant curvature nucleates at the lowest point of the rod, and continues to grow as the two ends are brought closer and closer. Condition (2b) allows us to compute the boundaries of this region of local contact, and consequently the full configuration.

Finally, we will relate condition (2b) with "configurational forces" posited by Bigoni et al. [3] in the context of sleeve problems, and argue that the results of Bigoni et al. are due to the absence, and not presence, of configurational forces.

Acknowledgments

Part of this work (the local and global contact problems) is supported by the Science and Engineering Research Board, grant SRG/2023/000079 awarded to H.S..

References

[1] H. Singh. *Planar Equilibria of an Elastic Rod Wrapped Around a Circular Capstan*, Journal of Elasticity, 151 (2022) 321-346.

[2] S. S. Antman. *Nonlinear Problems of Elasticity*, Springer New York, NY, 2005.

[3] D. Bigoni, F. Dal Corso, F. Bosi, D. Misseroni. *Eshelby-like forces acting on elastic structures: Theoretical and experimental proof*, Mechanics of Materials, 80 (2015) 368-374.

ECCOMAS Thematic Conference and IACM Special Interest Conference
Highly Flexible Slender Structures (HFSS 2025)
22–26 September 2025, Kaiserslautern, Germany

About the Soft Impact of a Rod-like Missile on a Robust Target

András A. Sipos[1,2], György Károlyi[3]

[1] Dept. Morphology and Geometric Modeling, Budapest University of Technology and Economics (BME)
[2] HUN-REN-BME Morphodynamics Research Group, BME, siposa@eik.bme.hu
[3] Institute of Nuclear Techniques, BME, karolyi@reak.bme.hu

Keywords: soft impact, wave equation, conformal mapping, damage potential

1. Introduction

Aircraft impacts are rare; hence, they are not included among the external actions in the design of engineering structures. However, the risk of an event is the product of its probability with the severity of its consequences. This means that if the consequences of an event are devastating, like in the case of an aircraft impact on a nuclear power plant or a valley closure dam, the event is included in the design basis despite its rarity [1]. Contrary to hard impacts, where the missile has no considerable deformations during the impact, the case of soft impacts [2] includes a missile that disintegrates. At the same time, its momentum is transferred to the target whose global displacements need to be investigated. A full-scale numerical model is often implemented when the consequences of a soft impact on an aircraft fuselage are considered. However, they are less valuable when one intends to gain insight into the parameter dependence of the outcome because of the large number of parameters. Simplified models are applied to gain more insight into the essential parameters. Specifically, we investigate an elastic-plastic rod colliding and crushing on a robust elastic target such that local effects are neglected. The model is a natural generalization of the Riera model [3], widely used in the nuclear industry.

2. Model Development

In the design of the target, the time-dependent reaction force is essential. Our model assumes a rigid-plastic missile modeled as a straight, slender rod. Following the lead of Figure 1, we derive a set of nondimensional partial differential equations on a time-dependent domain. In the simplest case of a homogeneous, cylindrical aircraft fuselage impacting a rigid target, the initial value problem is solved analytically using conformal mapping [4], which maps the original wave equation to an invariant domain.

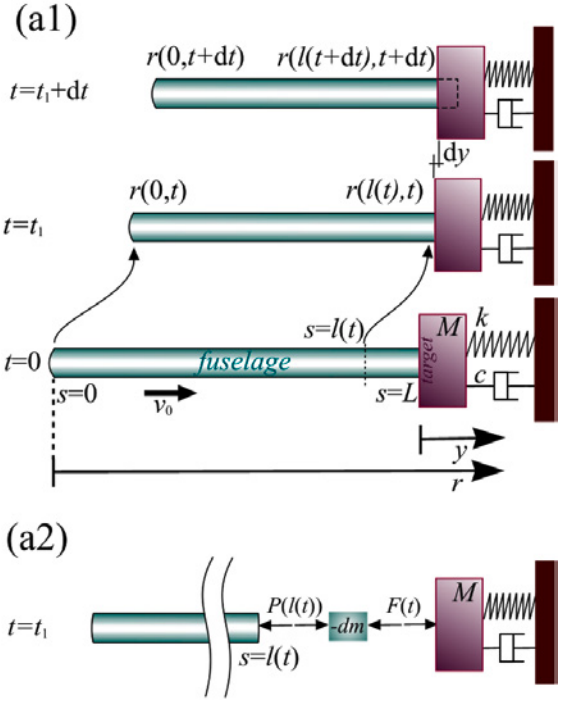

Figure 1. Aircraft fuselage impacting an elastic target. (a1) Constraints enforce the contact between the crushing aircraft and the target. The initial fuselage length L shrinks, and the length at time t reads $l(t)$. (a2) Free body diagram during the impact showing the crush force $P(l(t))$ and the reaction force $F(t)$ loading the target.

The case of an elastic target is solved numerically, and we find that among the parameters present in our dimensionless formalism, the damage potential, defined as

$$D := \frac{\frac{1}{2}m_0 v_0^2}{P_0 L} \tag{1}$$

has a significant role in the reaction force acting on the target. Here, m_0, v_0, and L are the mass, the velocity, and the initial length of the rod, respectively, and P_0 stands for the crushing force. Other parameters in the problem have an ignorable effect on the nondimensional reaction force $f(t)$.

3. Results

We find that the maximum reaction force during the impact is higher than its initial value by up to 20% in the investigated parameter range for specific parameter values. We identify the reason for this counter-intuitive outcome as a resonance-like effect due to vibrations both in the missile and the target. We introduce an approximate formula that predicts at which parameter values the reaction force is amplified the most, and we demonstrate that the formula is recovered in numerical experiments (see Figure 2).

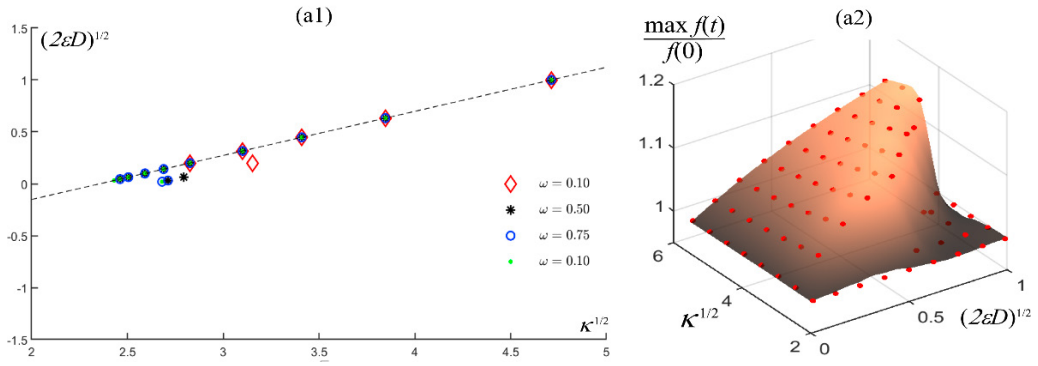

Figure 2. Parameter combinations yielding the highest maxima of the nondimensional reaction force $f(t)$ during the impact (a1) and a best-fit surface to the numerically computed maximal crushing force (a2).

4. Conclusions

As an extension of the Riera model [3], we account for the elasticity of both the missile and the target during the soft impact of missiles into robust engineering structures. While the original Riera model leads to ODEs, our approach results in a system of PDEs because of the presence of elastic waves. The analytical and numerical approaches reveal the parameter dependence of the solution and also yield the parameter settings with the highest maximum impact force. We find that the widely adopted assumption that the initial impact force is the peak force during an impact is not conservative during the design of engineering structures.

Acknowledgments

Support of grants TKP2021-NVA BME by NRDI and K128584 by NKFIH are kindly acknowledged.

References

[1] D.K. Thai, S.E. Kim. *Safety assessment of a nuclear power plant building subjected to an aircraft crash*. Nucl Eng Des;293 (2015) 38–52.

[2] J. Baroth, Y. Malecot, Z. Boukria, M. Briffaut, L. Daudeville. *Prediction of the perforation of targets impacted by deformable projectiles*. Int J Impact Eng 80 (2015) 36–44.

[3] J. Riera J. *On the stress analysis of structures subjected to aircraft impact forces*. Nucl Eng Des;8 (1968) 415–26.

[4] L. Gaffour. *Analytical method for solving the one-dimensional wave equation with moving boundary*. Prog Electromagn Res PIER 20 (1998) 63–73.

ECCOMAS Thematic Conference and IACM Special Interest Conference
Highly Flexible Slender Structures (HFSS 2025)
22–26 September 2025, Kaiserslautern, Germany

A Space-Time Finite Element Formulation for Geometrically Exact Shear Deformable Beams

Ivo Steinbrecher[1], Alexander Humer[2]

[1] Institute for Mathematics and Computer-Based Simulation (IMCS),
Universität der Bundeswehr München Neubiberg, Germany
[2] Institute of Technical Mechanics (TMech),
Johannes Kepler University Linz, Austria

Keywords: Space-time finite elements, geometrically exact beam formulation, Simo-Reissner beam theory

1. Introduction

The dynamic simulation of slender structures, i.e., beams, is crucial in various technical applications, including, e.g., aerospace structures, flexible robotics, or biomechanical systems. The state-of-the-art solution approach of such systems typically involves spatial discretization using the finite element method (FEM) combined with a time-stepping scheme, such as the Newmark algorithm, for integration in time.

In contrast to this classical methodology, space-time finite element formulations apply FEM simultaneously in both space and time. This leads to the solution of a single, coupled nonlinear system that captures the full dynamics of the simulation. While this approach generally results in larger system sizes, this is not the focus of the present work and can be addressed using specialized linear solvers and preconditioning strategies. Key advantages of the space-time approach include flexible time discretization (particularly beneficial for adaptive finite element methods), the potential for parallel-in-time computation, and the straight forward handling of changing material domains.

2. Space-time finite element formulations for geometrically exact beams

Recent works have demonstrated the effectiveness of space-time formulations in solid mechanics, including nonlinear elasticity [1], elasticity with the virtual element method [2], and rigid body dynamics [3]. These studies show the versatility and applicability of space-time finite element formulations in capturing complex mechanical behavior.

In the present work, we extend this concept by developing a fully nonlinear space-time formulation for a three-dimensional geometrically exact Simo–Reissner beam. Our formulation builds upon the same space-time formulation as employed in the aforementioned references. Specifically, we adopt a two-field approach, independently discretizing displacements and velocities. This separation enables straightforward imposition of initial and boundary conditions at the velocity level, offering additional flexibility in the required finite element interpolation spaces. To enhance numerical stability and robustness, we incorporate a residual-based stabilization technique, as utilized in [1, 2].

Since the considered beams are modeled as Cosserat continua, both position and rotation along the beam centerline must be treated as independent fields – unlike classical Boltzmann continua, which account only for translational degrees of freedom. Consistent and objective handling of finite rotations is a well-known challenge in geometrically exact beam formulations. While [3] employs a director-based representation of rigid bodies, defining orientation via three directors in addition to a position vector, we opt for a different strategy. In our approach, beam elements are discretized using nodal positions and rotational (pseudo)-vectors. The resulting interpolation of rotations closely follows the schemes proposed in [4, 5]. Our formulation yields 12 degrees of freedom per node: 3 translational displacements, 3 rotational vector components, 3 translational velocities, and 3 material angular velocities. Inserting the finite element approximation into the weak form of the space-time problem yields an efficient and accurate space-time finite element method capable of capturing the full dynamics of three-dimensional beam problems. To illustrate this, we consider the example of a free-floating L-shaped beam subjected to a line load along the vertical part of the beam. The corresponding results are presented in Figure 1, which shows snapshots of the space-time solution at selected time instances. It is

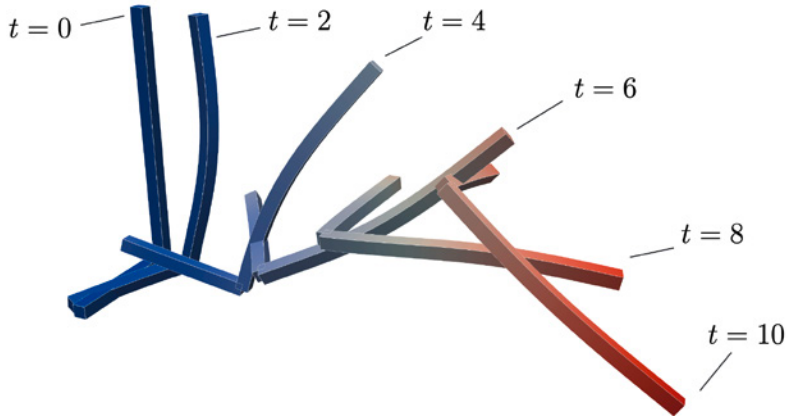

Figure 1: Free-floating L-shaped beam example: Snapshots of the space-time solution at various time instances.

important to note that the entire simulation is conducted using a single space-time grid.

3. Conclusions

Among the main topics addressed in this talk are the development of a fully nonlinear space-time finite element formulation for geometrically exact beams, as well as a discussion of the formulation's key features, such as the consistent treatment of finite rotations. Selected qualitative and quantitative examples are presented to highlight the accuracy and objectivity of the method, underlining its potential for real-world applications in structural dynamics. Furthermore, the advantages of the space-time approach in the context of changing material domains are demonstrated.

References

[1] S. Schuß, S. Glas, C. Hesch. *Non-linear space-time elasticity*, International Journal for Numerical Methods in Engineering, (2023)

[2] B.-B. Xu, P. Junker, P. Wriggers. *Space-time virtual element method for elastodynamics: Theory, applications, and code development*, Computer Methods in Applied Mechanics and Engineering, 435 (2025) 117683.

[3] C. Hesch, S. Glas, S. Schuß. *Space-time rigid multibody dynamics*, Multibody System Dynamics, 59 (2023) 293–316.

[4] M. A. Crisfield, G. Jelenić. *Objectivity of strain measures in the geometrically exact three-dimensional beam theory and its finite-element implementation*, Proceedings of the Royal Society of London A, 455 (1999) 1125–1147.

[5] G. Jelenić, M. A. Crisfield. *Geometrically exact 3D beam theory: implementation of a strain-invariant finite element for statics and dynamics*, Computer Methods in Applied Mechanics and Engineering, 171 (1999) 141–171.

ECCOMAS Thematic Conference and IACM Special Interest Conference
Highly Flexible Slender Structures (HFSS 2025)
22–26 September 2025, Kaiserslautern, Germany

Dynamic Shape Morphing of Slender Structures by Modulation of Intrinsic Curvature

Andrés F. Guerra Riaño[1], Péter L. Várkonyi[2]

[1] Budapest University of Technology and Economics, guerra.andres@edu.bme.hu
[2] Budapest University of Technology and Economics, varkonyi.peter@epk.bme.hu

Keywords: adaptive structures, feedback control, geometric nonlinearity, funicular structures

1. Motivation

Slender and soft plant organs react to various environmental effects by slowly changing their shape. For example, plant shoots turn towards light and against gravitational forces, whereas the tendrils of climbing plants attach to supports by developing curvature in response to contact [1]. Robots also solve various tasks ranging from locomotion to grasping and object manipulation by changing their shapes. In this case the shape evolution is often dynamic, i.e. it happens on a time scale comparable to that of the internal vibrations of the structure. For large-scale engineering structures, active vibration suppression is often used for earthquake protection as well as to improve serviceability under dynamic loads [2]. Other forms of shape control or morphing are barely used. The main motivation of this research is the hypothesis that shape control using appropriate principles can significantly improve the efficiency of structures, while the critical issues of reliability and safety can also be addressed.

2. A discrete model

We investigate the shape dynamics of slender rod structures with intrinsic curvatures evolving in time. A finite degree-of-freedom model proposed in our prior work [3], consisting of a chain of rigid bars, and rotary actuators at its joints is considered (Fig. 1). Masses and loads are concentrated in joints. The dynamic action of those actuators is dictated by feedback controllers using proportional-integral-derivative *(PID)* control with an appropriately chosen error function that depends on the actual shape of the structure, and dynamically changing internal state variables of the controller.

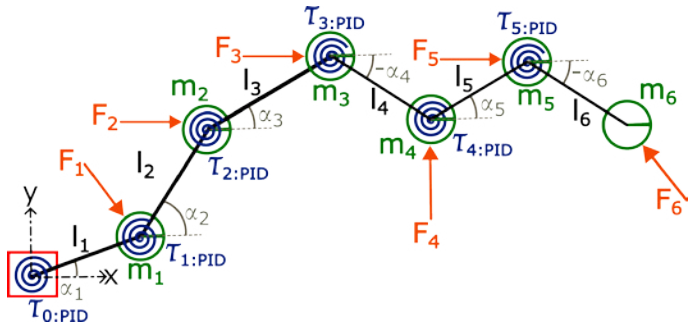

Figure 1: A discrete model representation of a morphing rod with state variables α_i, external loads F_i, actuation torques τ_i and lumped masses m_i.

3. The goal of shape control

A natural goal of shape control is to achieve a prescribed structural shape, where the main challenge is to cope with the unpredictability of external loads and the difficulty of direct load measurements. It is well known that the *I* components of the *PID* controllers are able to eliminate residual errors by automatically compensating for disturbances, such as unknown load values. At the same time, *I* control may also trigger various forms of dynamic instability ranging from monotonic divergence to self-excited oscillations. We go beyond the state of the art by investigating more advanced tasks where the target shape depends on the unknown load values, i.e. it cannot be prescribed explicitly. The task of eliminating load-induced bending moments from the structure (i.e. funicular shape control) is used as an example.

4. Classification and reliability of shape control strategies

The framework introduced above allows fundamentally different strategies of shape control, where the key properties are the number of actuators (underactuated or fully actuated), the type of sensory feedback (local or non-local), and the speed of actuation (dynamic or quasi-static). It is demonstrated that some shape control strategies qualify as *semi-active*, which means that they enjoy the beneficial properties of active control strategies, however a partial functionality is preserved if the active components fail due to power shortage or a breakdown event.

5. Results concerning stability

It is demonstrated through several examples that unstable states of the uncontrolled system can be stabilized by *PID* control, and that the control parameters determine the stability as well as the response time of the controller (Fig. 2). Finally we present an analytical proof for the existence of stable controllers for a wide class of problems.

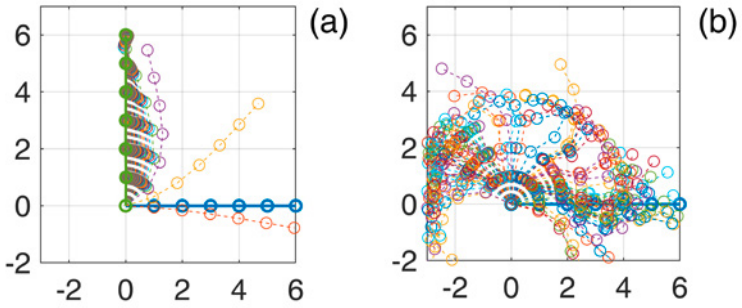

Figure 2: Snapshots of the shape dynamics, in the case of a stable (a) and an unstable (b) controller. The structure is subject to vertical load, which is unknown to the controller. The corresponding target shape is a straight, vertical line segment.

6. Open questions

The presented work focuses on the synthesis of powerful control laws. Several idealizations are used in the analysis. Most importantly, time delay is neglected even though delay is known to have large effect on stability in many control task. In addition, actuators are assumed to be ideal, i.e. the limitations of physical actuators are not taken into account by our models. These factors need further investigation.

Acknowledgments

This work has been supported by the National Research, Development and Innovation Fund of the Ministry of Culture and Innovation of Hungary under project K143175.

References

[1] R. Chelakkot, L. Mahadevan. *On the growth and form of shoots*, Journal of The Royal Society Interface 14 (2017) 20170001.

[2] F. Casciati, J. Rodellar, U. Yildirim. *Active and semi-active control of structures–theory and applications: A review of recent advances*, Journal of Intelligent Material Systems and Structures 23 (2012) 1181-1195.

[3] A. F. Guerra Riano, P. L. Varkonyi, *Shape control of adaptive funicular structures*, Eccomas Proceedia SMART (2023) 679-690. DOI: 10.7712/150123.9822.444919

ECCOMAS Thematic Conference and IACM Special Interest Conference
Highly Flexible Slender Structures (HFSS 2025)
22–26 September 2025, Kaiserslautern, Germany

Stick-slip Dynamics of a Flexible Rod Sliding in a Rigid Sleeve with Friction

Yury Vetyukov [1]

[1] TU Wien, Institute of Mechanics and Mechatronics, Getreidemarkt 9, 1060 Vienna, Austria
yury.vetyukov@tuwien.ac.at

Keywords: Flexible rod, Rod-sleeve contact, Configurational force, Nonlinear dynamics, Stick-slip

1. Introduction

Modern deployable structures often employ relative sliding of slender elastic elements as part of their functionality. A simple model example featuring an elastic rod, partially inserted in a straight rigid sleeve has frequently been the topic of investigation in the recent years, see [1, 2, 3, 4, 5, 6]. The complicated contact interaction is mostly simplified to an idealized setting with an ideal contact between the rod and the sleeve in the overlapping region. The notion of energy release rate helps efficiently describing the important configurational force, which repels the rod from the sleeve and promotes ejection [2, 6]. At the same time, the inevitable friction could only be taken into account in a very simplified manner up to date [1]. It is the aim of this contribution to propose a more realistic model for the frictional interaction and to investigate its influence on the dynamics of the axial-flexural motion of the rod.

2. Friction Model

Consider an elastic rod with bending stiffness a, partially inserted in a sleeve of thickness h, Fig. 1 (we neglect the small own thickness of the rod). A bending moment M_0 at the free end of the rod is balanced by a pair of contact forces F with the lever arm Δ, which is the length of the deformed segment of the rod within the sleeve. The contact force at the exit from the sleeve must act orthogonally to the axis of the rod $w(x)$, which gives rise to the axial configurational force $N = Fw'(\Delta)$. According to the analysis first presented in [2], the following relations hold:

$$\Delta = \sqrt{\frac{6ah}{M_0}}, \quad F = \sqrt{\frac{M_0^3}{6ah}}, \quad N = \frac{M_0^2}{2a}. \tag{1}$$

The result that N equals to the complementary strain energy density at the transition point is supported by the analysis of energy release rate at varying length of the free segment η.

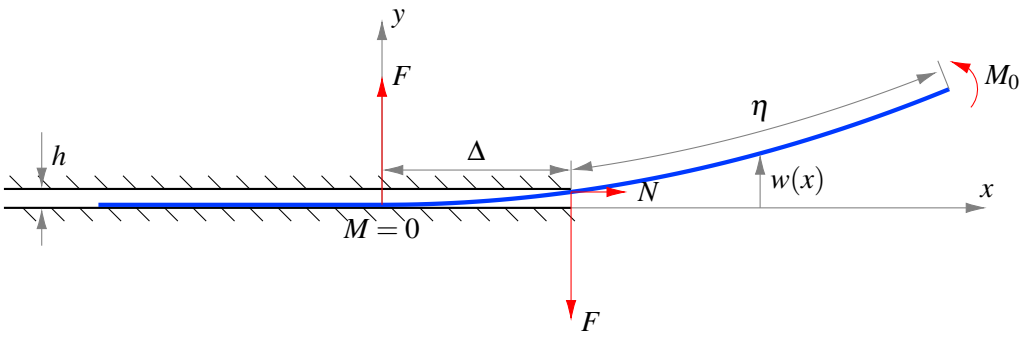

Figure 1: Flexible rod in a rigid sleeve: contact with transverse reaction forces F and axial one N

At axial motion $\eta(t)$, friction is to be expected at the locations of the reaction forces F, which allows to estimate the sliding friction force as

$$T = 2\mu F \operatorname{sign} \dot{\eta} \tag{2}$$

with μ being friction coefficient. The direction of T is determined by the direction of axial motion. The same value of T determines the maximum static friction force when there is stick in the contact pair.

3. Stick and Quasi-static Ejection

What is the value of the load M_0, at which the rods begins to slide ejecting from the sleeve? The motion starts when the frictional resistance is overcome, i.e.

$$N = |T| \quad \Rightarrow \quad \frac{M_0^2}{2a} = 2\mu\sqrt{\frac{M_0^3}{6ah}}. \tag{3}$$

Solving for M_0 and computing the curvature of the free segment $\kappa = M_0/a$, we find it to

$$\kappa = \frac{8\mu^2}{3h}. \tag{4}$$

In the critical state, the curvature radius κ^{-1} exceeds the thickness of the sleeve by the factor $3/(8\mu^2) = 9.375$ if we assume $\mu = 0.2$. The effect of jamming is strongly pronounced when the sleeve is thin.

4. Stick-slip Dynamics

In dynamics, sliding would take place at less severe deformations. Considering the set-up in Fig. 1 rotated counter-clockwise by 90° (such that the x-axis is pointing upwards) in the field of gravity, we model the coupled bending and axial dynamics using a simple model with two degrees of freedom, namely $\eta(t)$ representing the axial motion and $\gamma(t)$ being the coefficient in the Ritz approximation of bending of the free segment with the first vibration mode as shape function. Adopting the linearized kinematics of deformation and accounting for nonlinear dynamic coupling between the fast transverse vibrations and slow axial dynamics because of the varying length of the free segment, we follow the procedure outlined in [6] and arrive at the equations of motion

$$\begin{aligned} &4\rho\gamma\eta^3(40\dot{\gamma}\dot{\eta} + 13\eta\ddot{\gamma}) + 405\eta^4(\rho\ell(g+\ddot{\eta}) - T) - 8\gamma^2(243a + 5\rho\eta^2(\dot{\eta}^2 - 2\eta\ddot{\eta})) = 0, \\ &26\rho\eta^3(\dot{\gamma}\dot{\eta} + \eta\ddot{\gamma}) + \gamma(324a + \rho\eta^2(13\eta\ddot{\eta} - 20\dot{\eta}^2)) = 0. \end{aligned} \tag{5}$$

Here ℓ is the total length of the rod, ρ its mass per length, g the free fall acceleration and T is determined by Eq. (2). At vanishing friction $T = 0$ the systems becomes conservative and exhibits quasi-periodic vertical motion with varying frequency and amplitude of transverse vibrations $\gamma(t)$, see the detailed analytical study using the method of adiabatic invariants presented in [6]. With friction, we compute the dynamic trajectories by integrating Eq. (5) over time until the sliding velocity of the rod vanishes with $\dot{\eta} = 0$. The reached state is then used as initial condition for integrating the equation Eq. $(5)_2$ for $\gamma(t)$ keeping $\eta = \text{const}$ during the stage of stick. We switch the time integration back to the sliding regime when the static friction force exceeds the limit Eq. (2). Numerical experiments demonstrate various kinds of dynamic behavior, ranging from slow regular motion downwards with short sliding stages within a vibration period and increasing vibration frequency to complicated patterns of axial motion when the friction coefficient is low.

References

[1] C. Armanini, F. Dal Corso, D. Misseroni, D. Bigoni. *Configurational forces and nonlinear structural dynamics* Journal of the Mechanics and Physics of Solids 130 (2019) 82–100

[2] D. Bigoni, F. Dal Corso, F. Bosi, D. Misseroni. *Eshelby-like forces acting on elastic structures: theoretical and experimental proof* Mechanics of Materials 80 (2015) 368–374

[3] S. Han, O.A. Bauchau. *Configurational forces in variable-length beams for flexible multibody dynamics*, Multibody System Dynamics 58 (2023) 275–298

[4] A. Humer, I. Steinbrecher, L. Vu-Quoc. *General sliding-beam formulation: A non-material description for analysis of sliding structures and axially moving beams* Journal of Sound and Vibration 480 (2020) 115341

[5] P. Koutsogiannakis, D. Misseroni, D. Bigoni, F. Dal Corso. *Stabilization against gravity and self-tuning of an elastic variable-length rod through an oscillating sliding sleeve* Journal of the Mechanics and Physics of Solids 181 (2023) 105452

[6] Y. Vetyukov, A. Humer, A. Steindl. *Nonlinear dynamics of a flexible rod partially sliding in a rigid sleeve under the action of gravity and configurational force*, Journal of the Mechanics and Physics of Solids, 193 (2004) 105854

ECCOMAS Thematic Conference and IACM Special Interest Conference
Highly Flexible Slender Structures (HFSS 2025)
22–26 September 2025, Kaiserslautern, Germany

Dynamic analysis of a moving particle on a non-linear three-dimensional beam

Eva Zupan [1], Dejan Zupan [2]

[1] HSE and Faculty of Civil and Geodetic Engineering, University of Ljubljana, eva.zupan.lj@gmail.com
[2] Faculty of Civil and Geodetic Engineering, University of Ljubljana, dejan.zupan@fgg.uni-lj.si

Keywords: Structural Dynamics, Moving Mass, Three-Dimensional Beams, Velocity-Based Approach

1. Introduction

Analysing a deformable three-dimensional structure subjected to a moving body is a very complex and challenging problem. Due to its complexity, numerous simplified and partial models can be found in the literature in which different aspects of this strongly coupled problem are analysed in isolation. The main objective of this work is to introduce a geometrically nonlinear three-dimensional beam formulation that takes into account the effects of a moving mass. The finite element approach used has been specifically developed to allow a numerically efficient coupling between the beam formulation and the equations for the moving body. Particular attention is paid to the robustness of the numerical calculations, especially for large-scale simulations.

2. Cosserat beam dynamics

The Cosserat beam is determined at an arbitrary time $t \geq 0$ by the line of centroids and the family of rigid cross-sections. We take $x \in [0, L]$ to be the arc-length parameter of the initial line of centroids. The orientation of the cross-sections is represented here by rotational quaternions. The equations of the dynamic equilibrium of a three-dimensional Cosserat beam are then as follows

$$\mathbf{n}' + \tilde{\mathbf{n}} - \frac{d}{dt}\left(\rho A \mathbf{v}\right) = \mathbf{0} \tag{1}$$

$$\mathbf{m}' + \mathbf{r}' \times \mathbf{n} + \tilde{\mathbf{m}} - \frac{d}{dt}\left(\widehat{\mathbf{q}} \circ \left(\mathbf{J}_\rho \boldsymbol{\Omega}\right) \circ \widehat{\mathbf{q}}^*\right) = \widehat{\mathbf{0}}, \tag{2}$$

where $\mathbf{v}$ is the linear velocity and $\boldsymbol{\Omega}$ is the angular velocity, $\mathbf{r}$ is the position vector of the centroidal axis and $\mathbf{q}$ is the rotational quaternion. $\mathbf{n}$ and $\mathbf{m}$ represent stress-resultant force and moment vectors of the cross-section; $\tilde{\mathbf{n}}$ and $\tilde{\mathbf{m}}$ are vectors of applied distributed force and moment; ρ is the mass per unit of the initial volume; A is the area of the cross-section; $\mathbf{J}_\rho$ is the centroidal mass-inertia matrix of the cross-section.

Following the midpoint rule, equations (1) and (2) are replaced by the following time-discrete scheme:

$$\rho A \mathbf{v}^{[n+1]} - \rho A \mathbf{v}^{[n]} = h\left(\mathbf{n}'^{[n+1/2]} + \tilde{\mathbf{n}}^{[n+1/2]}\right) \tag{3}$$

$$\begin{aligned}\mathbf{J}_\rho\left(\boldsymbol{\Omega}^{[n+1]} - \boldsymbol{\Omega}^{[n]}\right) = h\Big[&\mathbf{M}'^{[n+1/2]} + \mathbf{K}^{[n+1/2]} \times \mathbf{M}^{[n+1/2]} - \boldsymbol{\Omega}^{[n+1/2]} \times \mathbf{J}_\rho \boldsymbol{\Omega}^{[n+1/2]} \\ &+ \left(\boldsymbol{\Gamma}^{[n+1/2]} - \boldsymbol{\Gamma}_0\right) \times \widehat{\mathbf{q}}^{*[n+1/2]} \circ \mathbf{n}^{[n+1/2]} \circ \widehat{\mathbf{q}}^{[n+1/2]} + \widehat{\mathbf{q}}^{*[n+1/2]} \circ \tilde{\mathbf{m}}^{[n+1/2]} \circ \widehat{\mathbf{q}}^{[n+1/2]}\Big].\end{aligned} \tag{4}$$

The superscript denotes the time at which a certain variable is evaluated, $h = t_{n+1} - t_n$ is the time step, and time $t_{n+1/2} = t_n + h/2$ denotes the mid-time between t_n and t_{n+1}.

The spatial discretization is based on the interpolation of velocities and angular velocities, where the unknown functions $\mathbf{v}(x,t)$ and $\boldsymbol{\Omega}(x,t)$ are approximated at each time t by N discrete values $\mathbf{v}^p(t)$ and $\boldsymbol{\Omega}^p(t)$ and interpolated in space

$$\mathbf{v}(x,t) = \sum_{p=1}^{N} I_p(x)\,\mathbf{v}^p(t), \qquad \boldsymbol{\Omega}(x,t) = \sum_{p=1}^{N} I_p(x)\,\boldsymbol{\Omega}^p(t), \tag{5}$$

where $I_p(x)$ denotes the selected interpolation functions. This approach leads to a relatively simple yet robust numerical method that is characterized by long-term stability. In addition, it guarantees either energy conservation or controlled energy dissipation [1] if the parameters are chosen appropriately.

3. Moving particle

We assume that a body moving along the beam can be modelled as a particle of constant mass moving along the centroidal axis of the beam. The initial position, $s_P^{[0]}$, and the initial velocity, $v_P^{[0]}$, are assumed to be known. The movement of the particle is uniquely described by the path parameter $s(t)$. To describe the motion, we take a standard Frenet frame $\mathscr{B}_P(s(t),t) = \{\mathbf{e}_t(s(t),t), \mathbf{e}_n(s(t),t), \mathbf{e}_b(s(t),t)\}$, where the parameter $s(t)$ and the position vector $\mathbf{r}^P = \mathbf{r}(s(t),t)$ define the location of the particle at a specific time t.

The influence of the moving particle on the beam is accounted for by expressing the contact forces $\mathbf{t}^P$, $\mathbf{n}^P$ and $\mathbf{b}^P$ in the Frenet frame of reference and incorporating their discrete contribution following the theory of distributions. A point force applied along the beam axis leads to a discontinuous jump in the internal forces at $x = s(t)$. The Dirac delta function (distribution) is employed to effectively account for local effects on an otherwise continuous beam element, ensuring a consistent formulation.

The equations of motion of a moving particle, expressed in a Frenet frame, can be reduced to a single scalar equation describing the position of a moving particle. A straightforward derivation gives

$$-\dot{s}\mu\left\|\frac{\dot{s}^2}{\rho_P}\mathbf{e}_n - g(\mathbf{e}_g\cdot\mathbf{e}_n)\mathbf{e}_n - g(\mathbf{e}_g\cdot\mathbf{e}_b)\mathbf{e}_b\right\| + g(\mathbf{e}_g\cdot\mathbf{e}_t) - \ddot{s} = 0, \tag{6}$$

where μ denotes the coefficient of friction, ρ_P is the radius of curvature, and g is gravitational constant. The base vectors in the above equation are expressed directly from the current configuration of the beam at $x = s(t)$:

$$\mathbf{e}_t = \mathbf{r}', \quad \mathbf{e}_n = \frac{\mathbf{r}''}{\|\mathbf{r}''\|} = \rho_P\mathbf{e}_t', \quad \mathbf{e}_b = \frac{\mathbf{r}'\times\mathbf{r}''}{\|\mathbf{r}'\times\mathbf{r}''\|}. \tag{7}$$

Equation (6) needs to be solved simultaneously with the dynamic equations of a beam. The additional unknowns introduced are the position of the particle $s(t)$ and its velocity $v_P = \dot{s}(t)$. The discretization of this equation follows the midpoint rule, in analogy with the beam discretization:

$$\begin{aligned} v_P^{[n+1]} - v_P^{[n]} = -hv_P^{[n+1/2]}\mu\left\|\frac{v_P^{2[n+1/2]}}{\rho_P}\mathbf{e}_n^{[n+1/2]} - g\left(\mathbf{e}_g\cdot\mathbf{e}_n^{[n+1/2]}\right)\mathbf{e}_n^{[n+1/2]} - g\left(\mathbf{e}_g\cdot\mathbf{e}_b^{[n+1/2]}\right)\mathbf{e}_b^{[n+1/2]}\right\| \\ + g\left(\mathbf{e}_g\cdot\mathbf{e}_t^{[n+1/2]}\right), \end{aligned} \tag{8}$$

with the midtime mass particle velocity being defined as

$$v_P^{[n+1/2]} = \overline{v_P} = \frac{1}{2}\left(v_P^{[n]} + v_P^{[n+1]}\right). \tag{9}$$

Equation (8) is added to the discrete beam equations and forms a coupled system. Due to the implicit nature of temporal discretization, the final set of discretized equations leads to a nonlinear problem at each time step. This nonlinear system is solved using Newton's iteration. It should be emphasised that both the linearization and the updating procedure are considerably simplified due to the chosen set of primary variables. As a result, the proposed approach ensures numerical efficiency and robustness.

Acknowledgments

This work was supported by the Slovenian Research and Innovation Agency through the research programme P2-0260. The support is gratefully acknowledged.

References

[1] E. Zupan and D. Zupan. On conservation of energy and kinematic compatibility in dynamics of nonlinear velocity-based three-dimensional beams. *Nonlinear Dynamics*, 95:1379–1394, 2019.

ECCOMAS Thematic Conference and IACM Special Interest Conference
Highly Flexible Slender Structures (HFSS 2025)
22–26 September 2025, Kaiserslautern, Germany

A Finite Swelling 3D Beam Model with Axial and Radial Diffusion

Juan C. Alzate Cobo [1], Xiang-Long Peng [2], Bai-Xiang Xu [2], Oliver Weeger [1]

[1] Cyber-Physical Simulation, Department of Mechanical Engineering,
Technical University of Darmstadt, alzate@cps.tu-darmstadt.de
[2] Mechanics of Functional Materials, Institute of Materials Science,
Technical University of Darmstadt

Keywords: Cosserat rod, Swelling, Diffusion, Isogeometric Analysis, Collocation

1. Introduction

We present a geometrically exact 3D beam model that incorporates axial and radial swelling strains, both small and large, resulting from a rotationally symmetric, thermal or chemical diffusion [1]. Isogeometric collocation is employed to discretize both the mechanical momentum balances and the axis-symmetric, steady-state 2D diffusion equation along the beam. The resulting coupled nonlinear problem for displacements, rotations, and temperatures or concentrations is solved using a staggered scheme. This novel finite swelling beam model can present the starting point for the efficient modelling of lattice structures under diffusion conditions, such as microstructured Li-ion electrodes [2] or thermoelectric semiconductors [3].

2. Coupled beam with finite swelling

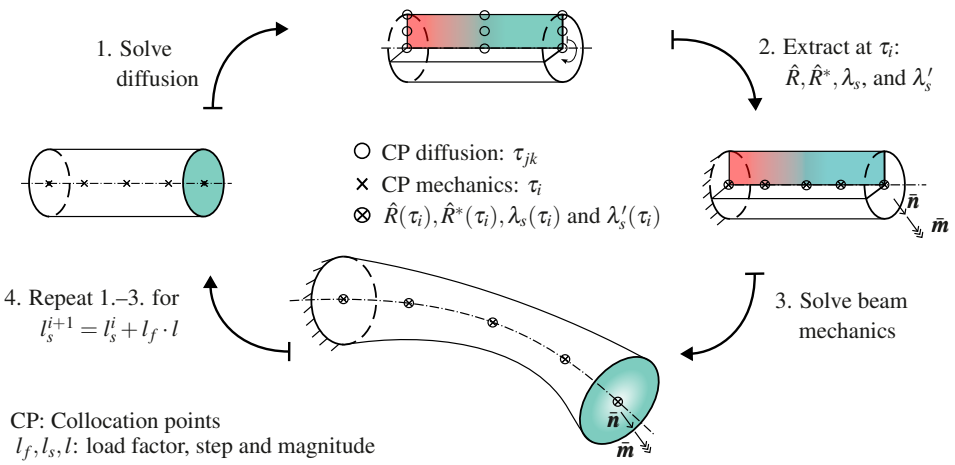

Figure 1: Schematic illustration of the staggered solution scheme.

The multiphysics problem, that includes diffusion and mechanics, is formulated in such a way that the solution of the diffusion equation implies a change in the initial length L and initial radius R of the beam. Due to finite swelling strains, material coordinates (r,s) and spatial coordinates $(\hat{r},\hat{s})$ can differ drastically. Consequently, and as usually done in continuum mechanics, a mapping between the initial and deformed configuration is necessary. In this work, this is achieved for the centerline through its stretch $\lambda_s(s)$ and its material arc-length derivative $\lambda_s(s)'$. For the radius it is achieved through computation of the swollen radius $\hat{\mathrm{R}}(s)$ and its spatial arc-length derivative $\hat{\mathrm{R}}^*(s)$.

To solve the aforementioned multiphysics problem, the staggered solution scheme illustrated in Figure (1) is applied. It can be explained as follows:

1. The diffusion problem is solved using IGA-C for a defined set of boundary conditions.

2. The coupling quantities λ_s, λ_s', $\hat{\mathrm{R}}$ and $\hat{\mathrm{R}}^*$, are obtained in a post-processing step from the diffusion problem. The coupling quantities are further evaluated at the collocation points τ_i of the mechanics problem.

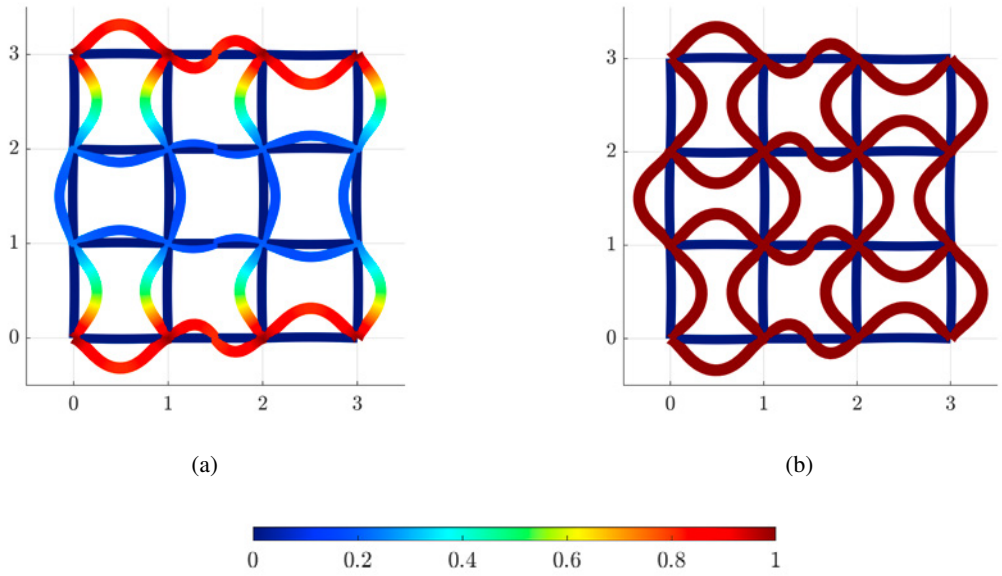

Figure 2: Collective type I and II buckling of tetragonal lattices under diffusion and swelling-induced expansion. (a) Deformation due to radial and axial diffusion. Joints at the top and bottom are subject to a constant concentration, whereas the rest of the beam surfaces interact via radial dissipation with the environment. (b) Buckling patterns due to 200 % constant volumetric expansion.

3. The coupling quantities are passed to the balance equation for beam mechanics, which is solved iteratively for a load step until convergeance is achieved.

4. The load step is updated and steps 1.–4. are repeated until the problem is solved at the last load step.

3. Swelling induced buckling

Architected lattice structures have the potential to improve the performance Li-ion batteries. It has been further shown that tetragonal lattices with inbuilt imperfections lead to controllable buckling patterns [2]. Figure (2) demonstrates the capability of the presented model to replicate such behavior.

4. Conclusion

We have presented a geometrically nonlinear beam formulation capable of accommodating radial and axial diffusion and radially symmetric finite swelling strains. For future contributions, we plan to expand the current formulation and include pre-curved beams. Additionally, we plan in future work to achieve a formulation of the two-way coupled problem between mechanics and diffusion.

Acknowledgments

The authors acknowledge the financial support provided by the Deutsche Forschungsgemeinschaft (DFG, German Research Foundation, project number 460684687).

References

[1] Juan C. Alzate Cobo, Xiang-Long Peng, Bai-Xiang Xu, Oliver Weeger. *A finite swelling 3D beam model with axial and radial diffusion*. In: *SSRN* 5139774 [Preprint] (2025).

[2] X. Xia, A. Afshar, H. Yang, C. M. Portela, D. M. Kochmann, C. V. Di Leo, and J. R. Greer. *Electrochemically reconfigurable architected materials*. In: *Nature* 573.7773 (2019), pp. 205–213.

[3] V. Karthikeyan, J. U. Surjadi, X. Li, R. Fan, V. C. Theja, W. J. Li, Y. Lu, and V. A. Roy. *Three dimensional architected thermoelectric devices with high toughness and power conversion efficiency*. In: *Nature Communications* 14.1 (2023).

ECCOMAS Thematic Conference and IACM Special Interest Conference
Highly Flexible Slender Structures (HFSS 2025)
22–26 September 2025, Kaiserslautern, Germany

Magnetoelastic modeling of planar ferromagnetic rods and ribbons

G. R. Krishna Chand Avatar [1], Vivekanand Dabade [2]

[1] Indian Institute of Science, krishnaagr@iisc.ac.in
[2] Indian Institute of Science, dabade@iisc.ac.in

Keywords: Magnetoelastic slender structures, Micromagnetics, Ribbons, Elastica, Kirchhoff's kinetic analogy

1. Introduction

Magnetoelastic slender structures exhibit complex coupling between magnetism and elasticity, allowing them to achieve significant displacements with minimal external magnetic fields. These structures have applications in soft robotics, MEMS devices, etc. In this work, we investigate the influence of magnetism on the planar deformation of rods and ribbons by developing a total energy functional that incorporates both elastic and magnetic energies. Two approaches are adopted to explore their equilibrium solutions under various combinations of magnetic fields and mechanical loads. In the first approach, Kirchhoff's kinetic analogy is applied to obtain symmetric deformed solutions of planar soft ferromagnetic rods subjected to various magnetic fields. In the second approach, an arclength-based continuation method is employed to capture a broader range of deformations, including both symmetric and asymmetric configurations.

2. Energy formulation for planar ferromagnetic elastic rod and ribbon

Rods are defined by two distinct length scales: length l and diameter d ($d \ll l$) while ribbons introduce a third dimension with length l, width a, and thickness t ($t \ll a \ll l$), see Fig. 1. Both structures are assumed to be uniform, inextensible, and unshearable, and their centerlines remain planar and untwisted in their deformed states (Fig. 1). The magnetic behavior of these ferromagnetic structures is governed by the magnetization vector $\boldsymbol{m}(s)$ and the externally applied magnetic field $\boldsymbol{h}_e$. Here, $|\boldsymbol{m}(s)| = 1$ and is supported locally on the structure.

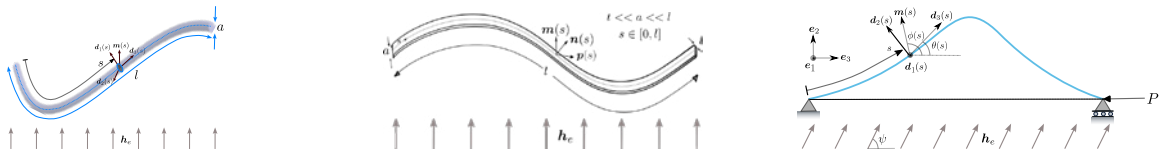

Figure 1: (left) Ferromagnetic rod, (center) Ferromagnetic ribbon, (right) Schematic of planar setup.

The total energy functional of the structure comprises of mechanical energy and magnetic energy:

$$\mathscr{E}_{\text{total}} = \mathscr{E}_{\text{mech}} + \mathscr{E}_{\text{magnetic}}. \tag{1}$$

The mechanical energy $\mathscr{E}_{\text{mech}}$ is the sum of the bending energy and the loading device energy as:

$$\mathscr{E}_{\text{mech}} = \frac{1}{2}\int_0^l EI(\theta'(s))^2 ds + P\left(l - \int_0^l \cos\theta(s) ds\right) \quad \text{subject to: } y(l) = \int_0^l \sin\theta(s)\, ds = 0, \tag{2}$$

where $\theta'(s)$ = bending curvature, E = Young's modulus, I = area moment of inertia, P = horizontal load.

The leading-order terms of the micromagnetic energy functional for planar ferromagnetic structures [2] are:

$$\mathscr{E}_{\text{magnetic}} = \mathscr{E}_{\text{demag.}} + \mathscr{E}_{\text{Zeeman}} = K_d \int_0^l (\boldsymbol{m}(s)\cdot\boldsymbol{d}_2(s))^2 d\boldsymbol{x} - 2K_d \int_0^l \boldsymbol{h}_e \cdot \boldsymbol{m}(s) d\boldsymbol{x}, \tag{3}$$

where, $\mathscr{E}_{\text{demag.}}$ is the magnetostatic or demag. energy, $\mathscr{E}_{\text{Zeeman}}$ is the Zeeman energy, and K_d is the magnetostatic constant. The total energy functional, along with the constraint, is non-dimensionalised as follows:

$$\bar{\mathscr{E}}_{\text{total}}(\theta, \boldsymbol{m}) = \int_0^1 \left[\frac{1}{2}\left(\theta'(\bar{s})\right)^2 + \bar{K}_d(\boldsymbol{m}(\bar{s})\cdot\boldsymbol{d}_2(\bar{s}))^2 - 2\bar{K}_d \boldsymbol{h}_e \cdot \boldsymbol{m}(\bar{s}) - \bar{P}\cos\theta(\bar{s}) - \bar{R}\sin\theta(\bar{s})\right] d\bar{s}. \tag{4}$$

3. Kirchhoff's kinetic analogy for planar ferromagnetic structures

Kirchhoff's kinetic analogy establishes a correspondence between the static deformation of an elastic rod or ribbon to the dynamic motion of a pendulum [1]. It maps the rod's arc length coordinate to the temporal evolution of a pendulum. To utilize this analogy, we construct the Hamiltonian of the total energy functional.

The energy functional for planar ferromagnetic structures is expressed as: $\mathscr{J}(f) = \int_0^1 f(\theta(\bar{s}), \theta'(\bar{s}))d\bar{s}$, where f denotes the Lagrangian. The Hamiltonian $\mathscr{H}$ of f takes the form: $\mathscr{H}(\theta(\bar{s}), \theta'(\bar{s})) = C$, where C is a constant. We construct the phase portrait of constant-$\mathscr{H}$ trajectories in (θ, θ')-space, with trajectories parametrized by the arc length parameter $\bar{s}$ (see Fig. 2). For a soft ferromagnetic rod subjected to a transverse $\boldsymbol{h}_e$, the Hamiltonian phase portraits reveal that the critical points undergo a subcritical pitchfork bifurcation as $\bar{P}$ varies. In the phase portrait corresponding to $\bar{P} = \pi^2/3$ and $\bar{K}_d = 100$, integrating along trajectories yields novel free-standing deformations and localised shapes. This approach yields symmetric deformation modes with zero vertical reaction ($\bar{R} = 0$) force at the loading device. To address this limitation and capture general planar deformations in ferromagnetic structures, an arc-length continuation method is employed, as detailed in the following section.

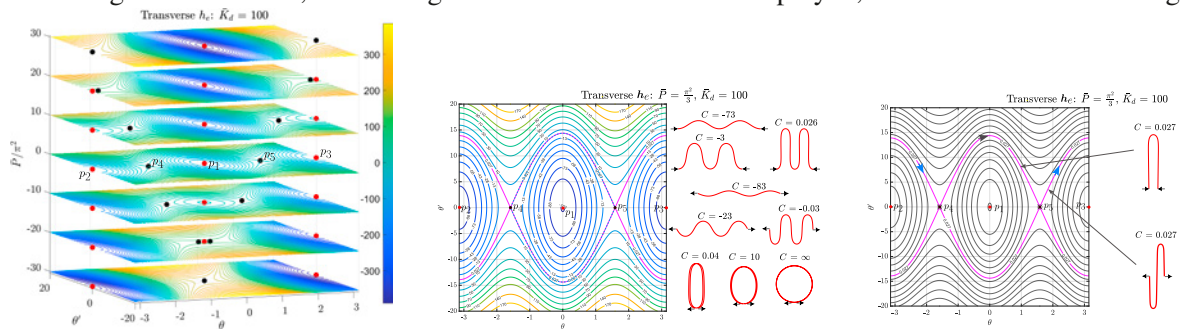

Figure 2: (left) Phase portrait snapshots as $\bar{P}$ is varied; $\bar{P} > 0$ (compression) and $\bar{P} < 0$ (tension), (center) Phase portrait with separatrices highlighted in magenta, and free-standing deformed shapes. (right) Localized shapes.

4. Deformation of planar ferromagnetic structures using continuation method

We derived the Euler-Lagrange equations for the total energy functional of the structures and obtained equilibrium solutions using an arclength-based continuation method [2] for various loading scenarios and boundary conditions. A stability analysis of these solutions was conducted using the Sturm-Liouville formulation. In Fig. 3, we compare the load-displacement curves of a ferromagnetic ribbon, composed of both soft and hard magnetic materials with fixed-fixed boundary conditions under transverse $\boldsymbol{h}_e$, to classical Euler's elastica. Our results highlight the significant influence of magnetism ($\mathscr{E}_{\text{demag.}}$ and $\mathscr{E}_{\text{Zeeman}}$) on the deformation behavior of ferromagnetic structures.

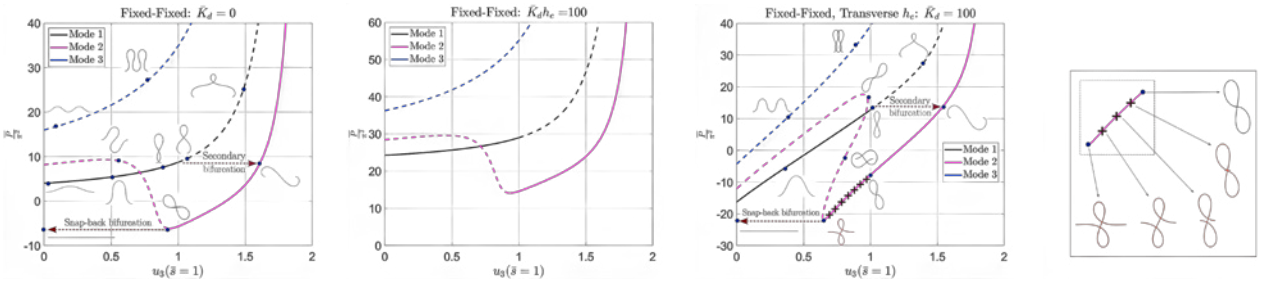

(a) (b) (c) (d)

Figure 3: Stability diagram for (a) Euler's elastica, (b) hard, and (c) soft ferromagnetic ribbon. (d) Segment of mode-2 branch showing novel stable deformed configurations.

5. Conclusions

Our model predicts novel stable deformed configurations for soft ferromagnetic rods and ribbons under transverse $\boldsymbol{h}_e$. The critical buckling load is tensile for soft ferromagnetic structures and increases for hard ferromagnetic materials subjected to transverse $\boldsymbol{h}_e$. Hamiltonian phase portraits of the rods reveal pitchfork bifurcations in the presence of $\boldsymbol{h}_e$, and novel localized deformed shapes are obtained along specific trajectories. In future work, we aim to experimentally validate these findings and perform a full three-dimensional stability analysis.

References

[1] G. R. Krishna Chand Avatar and Vivekanand Dabade. *Kirchhoff's analogy for a planar ferromagnetic rod*, Journal of Applied Mechanics, (2025).

[2] G. R. Krishna Chand Avatar and Vivekanand Dabade. *Deformation of a planar ferromagnetic elastic ribbon*, Journal of Elasticity, vol. 157 (2025).

ECCOMAS Thematic Conference and IACM Special Interest Conference
Highly Flexible Slender Structures (HFSS 2025)
22–26 September 2025, Kaiserslautern, Germany

Hydraulically Actuated Asymmetric Flexible Hinge: A Bio-Inspired Design Principle

Eugene L. Starostin [1,2], Victor G. A. Goss [1]

[1] School of Engineering, London South Bank University, 103 Borough Rd, London SE1 0AA, UK, staroste@lsbu.ac.uk; gossga@lsbu.ac.uk

[2] Department of Civil, Environmental and Geomatic Engineering, University College London, Gower St, London WC1E 6BT, UK, e.starostin@ucl.ac.uk

Keywords: Flexible Hinge, Elastica Hypoarealis

1. Introduction

One can think of an insect wing membrane as a set of flexible 'panels' connected by elastic rods (veins) [8]. Many species of insect can fold, unfurl, and adjust the shape of their wings during flight. Although insect wings lack internal musculature, they are spanned by a network of veins, which contain haemolymph ('insect blood'), a fluid circulated by thoracic 'wing hearts' [1]. Hydraulic pressure has been shown to be involved in the extension/unfolding of the hindwings of beetles and other insects [5, 6]. Asymmetric cross-sections of veins resemble the flexion-line section recently modelled as a one-way hinge in a beetle hindwing [4], whose operation depends on the buckling of one side. We propose a novel mechanism for active wing shape control: hydraulic distortion of vein cross-sections, which exerts leverage on adjacent cross-veins and membrane.

2. Methods

Insect veins exhibit a wide range of cross-sectional shapes and wall thicknesses. However, they are essentially elastic structures, making the entire wing an interconnected elastic continuum. Our mechanical model stems from the observation that insect wings are composed of double-layered highly flexible elastic membranes [1, 8]. Veins form where these layers separate, often creating campanulate cross-sections (Fig. 1,*left*). Hydraulic distortion of such vein cross-sections must correlate with relative orientation of adjacent membrane panels.

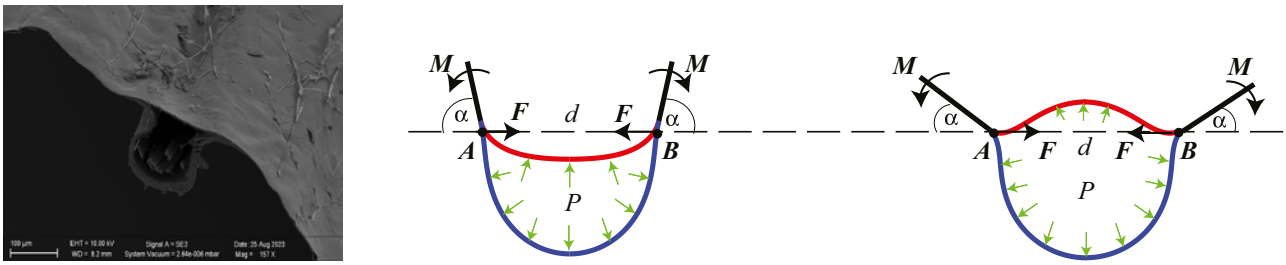

Figure 1: *Left:* A cut through a sun beetle (*Pachnoda marginata*) wing showing vein cross-sections (courtesy of Sepehr H. Eraghi). *Right:* A schematic showing variation in shape of a vein cross-section due to change of haemolymph pressure P, the boundaries are represented by two elastic curves (blue and red).

An assumption of translational invariance along the vein length allows us to simplify the analysis and consider the deformation of the vein cross-section. We model the vein cross-section as a cavity bounded by two elastic curves (elasticae) of different lengths (a difference that captures the asymmetry of the vein cross-section) (Fig. 1,*left*). Haemolymph pressure is approximated as a differential normal pressure P acting on the boundary. Our model may be considered a generalisation of the *'elastica hypoarealis'* [2] though note that in our case it is not differentiable in points A, B (Fig. 1,*right*), where the two membrane layers separate.

The force and moment balance equations (expressed as a system of nonlinear ODEs) describe how the vein cross-section quasi-statically deforms due to differential pressure P and the forces $\boldsymbol{F}$ and torques $\boldsymbol{M}$ exerted by adjacent wing membrane panels. We formulate and numerically solve a corresponding boundary value problem to obtain the equilibrium configurations of the vein wall.

3. Results

The pressure, and the force and moment acting on the end points A and B influence the deformation of the vein cross-section and the subsequent deflection of adjacent wing panels, i.e. opening and closing motions linked to unfurling and folding of a wing. This deflection is characterised by a relative orientation angle α and relative displacement d (Fig. 1,*right*).

We examined a range of solutions by adjusting the relevant parameters. For various values of the parameters specifying the vein cross-sectional intrinsic shape, wall stiffness and its mechanical properties, we explore how the variation of haemolymph pressure causes deformation of the vein cross-section. Our analysis shows that, depending on the parameter values, the wing panels can deflect (open or close) either smoothly or abruptly.

We treat the haemolymph pressure P and the external force $\boldsymbol{F}$ as the control parameters and the angle α as a behavioural variable. We then compute the solution surface, which exhibits a cusp singularity. This indicates that a continuous increase in pressure beyond a critical threshold would result in a discontinuous change in the angle, i.e. a quick opening of the hinge whereby the system jumps from one stable branch of solutions to another. Conversely, continuously lowering the pressure below a second, lower critical threshold would cause an abrupt closure. The system returns to the initial stable solution branch. Such a behaviour results in a hysteresis loop. This system property can be utilised for rapid change of the orientation of the adjacent wing panels. Notably, the pressure in either state (opened or closed) need not be high, which aligns with experimental data [6]. We formulate design criteria for triggering wing folding/unfolding. Graphical representations of key parameter relationships provide a benchmark for experimental studies and biomimetic design.

4. Discussion

We emphasise here that in recent years insect wings have become the subject of research from the perspective of deployable structures and actively controlled 'structural origami' [3]. Our research offers the possibility of smart fold lines forming a hydraulic circuit that facilitates distributed shape control of the whole structure. It is conceivable that the rigidity of the veins can be actively controlled by variations in pressure, either in phase with the wing-strokes or more plausibly maintained over a succession of wing beats. Our model can be used as a guidance for experimental and design work. The proposed mechanism holds significant technical potential, with applications in deployable structures and micro aerial vehicle wing design [7].

Acknowledgments

This work was supported by the Leverhulme Trust Research Project Grant RPG-2024-150.

References

[1] J. W. Arnold. *Blood circulation in insect wings.* Memoirs of the Entomological Society of Canada, **96** (1964) 5–60.

[2] G. Arreaga et al. *Area-constrained planar elastica.* Physical Review E, **65** (2002) 031801.

[3] S. A. Combes. *Materials, structure, and dynamics of insect wings as bioinspiration for MAVs.* In: Encyclopedia of Aerospace Engineering (eds R. Blockley and W. Shyy), 2010.

[4] H. Rajabi et al. *An insect-inspired asymmetric hinge in a double-layer membrane.* Proceedings of the National Academy of Sciences of the USA, **119** (2022) e2211861119.

[5] M. K. Salcedo et al. *Transient use of hemolymph for hydraulic wing expansion in cicadas.* Scientific Reports, **13** (2023) 6298.

[6] J. Sun et al. *The hydraulic mechanism of the unfolding of hind wings in Dorcus titanus platymelus (order: Coleoptera).* International Journal of Molecular Sciences, **15** (2014) 6009–6018.

[7] L. Wang et al. *Review on ultra-lightweight flapping-wing nano air vehicles: Artificial muscles, flight control mechanism, and biomimetic wings.* Chinese Journal of Aeronautics, **36** (2023) 63–91.

[8] R. J. Wootton. *The geometry and mechanics of insect wing deformations in flight: A modelling approach.* Insects, **11** (2020) 446.

ECCOMAS Thematic Conference and IACM Special Interest Conference
Highly Flexible Slender Structures (HFSS 2025)
22–26 September 2025, Kaiserslautern, Germany

A Flexoelectric Special Cosserat Rod under the Follower Load

Prakhar Gupta[1*], Pushkar Mishra[1]
[1]SUCSHM Lab, Department of Mechanical and Aerospace Engineering, IIT Hyderabad, India,
prakharg@mae.iith.ac.in, me22resch11007@iith.ac.in

Keywords: Follower load, Large Deformation, Direct and Converse Flexoelectricity, Special Cosserat rod

1. Introduction

All dielectrics, when subjected to a nonhomogenous deformation *such as bending*, lead to the development of net non-zero polarization, known as flexoelectricity. Unlike piezoelectricity, which has the limitation of being observed in noncentrosymmetric materials, only flexoelectricity is also observable in centrosymmetric materials. The coupling between non-homogeneous deformation (*i.e., strain gradients*) and polarization is achieved via a fourth-order tensor known as the flexoelectric tensor. The present work discusses the large deformation of such slender structures incorporating strain gradients and flexoelectricity.

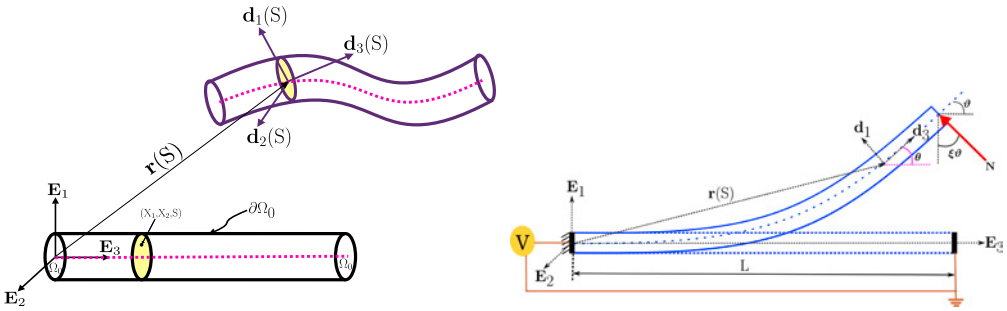

Figure 1: (a) A typical deformed flexoelectric strain-gradient special Cosserat rod from the undeformed straight configuration. (b) A schematic of a flexoelectric rod subjected to the follower load (for $\zeta = 1$).

2. Equilibrium equations for a three-dimensional dielectric solid

The three-dimensional equilibrium equations that incorporate direct and converse flexoelectric effects are derived using the principles of variational calculus. To do so, the first variation of the enthalpy density functional for a three-dimensional body [1] is equated to zero and the following equilibrium equations corresponding mechanical and electrical counterparts, respectively, are found:

$$\boldsymbol{\nabla}\cdot(\mathbf{P}-\boldsymbol{\nabla}\cdot\widetilde{\mathbf{P}})+\mathbf{b}=\mathbf{0},\quad \boldsymbol{\nabla}\cdot(\mathbf{D}-\boldsymbol{\nabla}\cdot\widetilde{\mathbf{D}})=\rho_{\mathrm{f}}, \tag{1}$$

where $\mathbf{b}$ and ρ_f denote body force and charge density per-unit undeformed volume, respectively. Also, the following quantities represent first Piola-Kirchhoff stress, higher-order stress, electric displacement, and higher-order electric displacement, respectively:

$$\mathbf{P}=\frac{\partial \mathrm{W}}{\partial \mathbf{F}},\qquad \widetilde{\mathbf{P}}=\frac{\partial \mathrm{W}}{\partial(\boldsymbol{\nabla}\mathbf{F})},\qquad \mathbf{D}=-\frac{\partial \mathrm{W}}{\partial \mathbf{E}},\qquad \widetilde{\mathbf{D}}=-\frac{\partial \mathrm{W}}{\partial(\boldsymbol{\nabla}\mathbf{E})}, \tag{2}$$

where 'W' is the strain energy density of the flexoelectric strain gradient special Cosserat rod, $\mathbf{F}$ and $\mathbf{E}$ is the deformation gradient and electric field, respectively. We also note that the symbol $\boldsymbol{\nabla}$ describes the derivative with respect to the undeformed configuration.

3. Equilibrium equations for a flexoelectric special Cosserat rod

The equilibrium equations for the flexoelectric strain gradient special Cosserat rod [1, 2] can be obtained by carrying out dimensionality reduction of equilibrium equations obtained in Eq. (1) and are given below

$$\mathbf{n}'-\widetilde{\mathbf{n}}''+\widehat{\mathbf{n}}=\mathbf{0},\quad (\mathbf{m}'-\widetilde{\mathbf{m}}'')+\mathbf{r}'\times(\mathbf{n}-\widetilde{\mathbf{n}}')+\widehat{\mathbf{m}}=\mathbf{0}, \tag{3a}$$

$$\begin{gathered}\frac{\partial\Phi}{\partial\phi_1}-\left(\frac{\partial\Phi}{\partial\phi_1'}\right)'+\left(\frac{\partial\Phi}{\partial\phi_1''}\right)''+\hat{w}_1=0,\quad \frac{\partial\Phi}{\partial\phi_2}-\left(\frac{\partial\Phi}{\partial\phi_2'}\right)'+\left(\frac{\partial\Phi}{\partial\phi_2''}\right)''+\hat{w}_2=0,\\ -\left(\frac{\partial\Phi}{\partial\phi_0'}\right)'+\left(\frac{\partial\Phi}{\partial\phi_0''}\right)''+\hat{w}_0=0,\end{gathered} \tag{3b}$$

where $(\cdot)'$ denotes derivative with respect to the undeformed arclength 'S'. The equations (3a) and (3b) represent the mechanical and electrical counterparts for a flexoelectric special Cosserat rod, respectively. Here, $\mathbf{n}$ and $\mathbf{m}$ are classical internal forces and moments [3], whereas $\widetilde{\mathbf{n}}$ and $\widetilde{\mathbf{m}}$ denote higher-order internal forces and moments respectively. A point on the deformed centerline is given as $\mathbf{r}$, which was previously at $\mathbf{SE}_3$ in the straight undeformed configuration (see Fig. 1(a)). A point in the local cross-section is defined using the directors $\mathbf{d}_1$, $\mathbf{d}_2$, and $\mathbf{d}_3$. The terms ϕ_0, ϕ_1, and ϕ_2 correspond to the unknowns in the Taylor series expansion of the electric potential [1]. For boundary conditions and constitutive relations, readers may refer to [1,2].

4. Validation and Conclusion

The nonlinear analytical solution for a flexoelectric Cosserat rod is obtained under the assumption that the rod is unshearable and inextensible [1]. The following equilibrium equation is obtained based on Fig.1(b)

$$\theta'' + \beta^2 \cos(\xi\vartheta - \theta) = 0, \quad \text{where,} \quad \beta^2 = \frac{\mathrm{N}}{\mathrm{EI}_{\mathrm{eff}}}, \quad \mathrm{I}_{\mathrm{eff}} = \mathrm{I} + \frac{\mathrm{A}\mu_T^{d\,2}}{\mathrm{E}\varepsilon}, \tag{4}$$

μ_T^d is the direct transverse flexoelectric coefficient, ε is permittivity, and N is the applied follower load. A

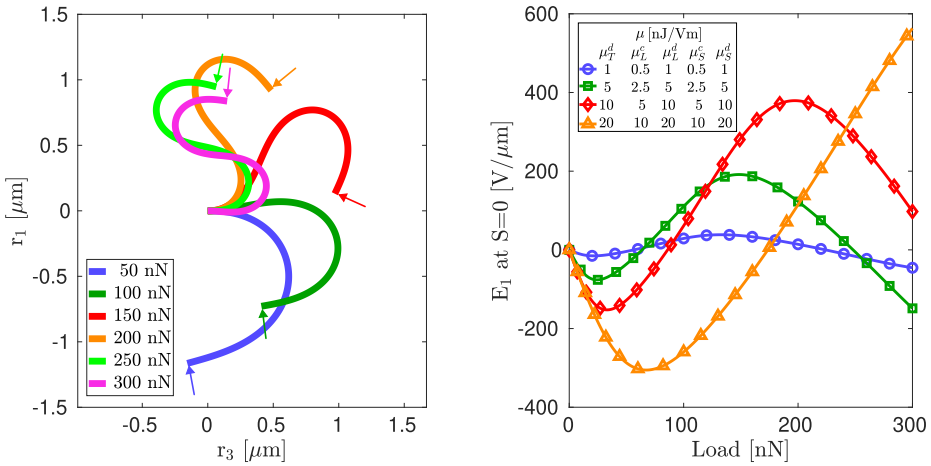

Figure 2: (a) Deformed shapes of a flexoelectric strain gradient special Cosserat rod when acted upon by a follower load. (b) Effect of various direct and converse flexoelectric coefficients on electric field E_1 at $\ell_e = 100$nm and $\ell_m = 20$nm.

close match was observed between the nonlinear analytical and numerical solution for a flexoelectric special Cosserat rod. Moreover, a sign-switching phenomenon was observed in the electric field, which could lead to the development of smart sensors and energy harvesters.

Acknowledgements

Prakhar Gupta acknowledges the financial support provided by the National Technical Textiles Mission (NTTM), Ministry of Textiles (MoT), under Project Order No. 1/9/2024-9th MSG/16. Pushkar Mishra acknowledges financial support from the PMRF fellowship.

References

[1] Pushkar Mishra and Prakhar Gupta. Modeling direct and converse flexoelectricity in soft dielectric rods with application to the follower load. *Journal of the Mechanics and Physics of Solids*, 195:105956, 2025.

[2] Vipin Kumar Yadav and Prakhar Gupta. A strain-gradient elastic theory for special cosserat rods. *International Journal of Solids and Structures*, 291:112696, 2024.

[3] Juan C Simo. A finite strain beam formulation. the three-dimensional dynamic problem. part i. *Computer methods in applied mechanics and engineering*, 49(1):55–70, 1985.

ECCOMAS Thematic Conference and IACM Special Interest Conference
Highly Flexible Slender Structures (HFSS 2025)
22–26 September 2025, Kaiserslautern, Germany

Finite element modeling of flexoelectric special Cosserat rods

Pushkar Mishra[1], Prakhar Gupta[1*]
[1]SUCSHM Lab, Department of Mechanical and Aerospace Engineering, IIT Hyderabad, India,
me22resch11007@iith.ac.in, prakharg@mae.iith.ac.in

Keywords: Large Deformation, Flexoelectricity, Finite Element Methods, Special Cosserat rod, Bending

1. Introduction

Flexoelectricity in dielectrics offers a potential alternative to piezoelectricity for centrosymmetric materials. Unlike piezoelectricity, which occurs only in noncentrosymmetric materials, flexoelectricity is present in all dielectrics. Its behaviour under large deformations [1, 2] provides insights relevant to the development of smart sensors and energy harvesters. Existing finite element (FE) formulations incorporating flexoelectricity [3] treat

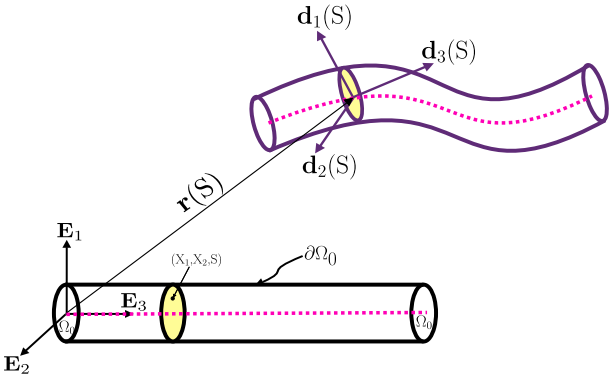

Figure 1: A schematic of a special Cosserat rod.

one-dimensional rod as a 3D finite element problem, leading to high computational costs. To address this, we propose an FE strategy for solving the boundary value problem of a flexoelectric special Cosserat rod under various loading conditions. Using C^0 shape functions to interpolate primary variables in bending-dominated flexoelectric [1] special Cosserat rod also reduces its computational complexity.

2. Equilibrium Equations for Flexoelectric Special Cosserat Rod

The equilibrium equations for the flexoelectric special Cosserat rod can be obtained by equating the first variation of the enthalpy density function for the rod to zero [1]. The obtained equilibrium equations are[1]

$$\mathbf{n}' + \widehat{\mathbf{n}} = \mathbf{0}, \quad \mathbf{m}' + \mathbf{r}' \times \mathbf{n} + \widehat{\mathbf{m}} = \mathbf{0}, \tag{1a}$$

$$-\left(\frac{\partial \Phi}{\partial \phi_0'}\right)' + \widehat{w}_0 = 0, \quad \frac{\partial \Phi}{\partial \phi_1} - \left(\frac{\partial \Phi}{\partial \phi_1'}\right)' + \widehat{w}_1 = 0, \quad \frac{\partial \Phi}{\partial \phi_2} - \left(\frac{\partial \Phi}{\partial \phi_2'}\right)' + \widehat{w}_2 = 0. \tag{1b}$$

The equations (1a) and (1b) represent the mechanical and electrical counterparts, respectively. Here, $\mathbf{n}$ and $\mathbf{m}$ denote the internal forces and moments, while $\mathbf{r}$ represents the deformed point on the centerline at S$\mathbf{E}_3$ (see Fig. 1). A point in the local cross-section is defined using the directors $\mathbf{d}_1$, $\mathbf{d}_2$, and $\mathbf{d}_3$. The terms ϕ_0, ϕ_1, and ϕ_2 correspond to the unknowns in the Taylor series expansion of the electric potential [1]. The weak form of these differential equations is obtained by applying the principle of virtual work and thereby perturbing the strong form [1, 4].

2.1. Linearization of Weak form and Discretization

The perturbed weak form of the equilibrium equations remains nonlinear in the unknowns and is linearized to obtain incremental equations solved iteratively via the Newton-Raphson method. The matrix-vector form of

[1] $(\cdot)'$ denotes derivative with respect to undeformed arclength 'S'

the linearized weak form is given as

$$\begin{bmatrix} \mathbf{K}_{uu} & \mathbf{K}_{u\phi} \\ \mathbf{K}_{\phi u} & \mathbf{K}_{\phi\phi} \end{bmatrix} \begin{Bmatrix} \Delta\mathbf{u} \\ \Delta\boldsymbol{\phi} \end{Bmatrix} = -\{\mathscr{R}\}, \tag{2}$$

where $\Delta\mathbf{u}$ corresponds to increment in mechanical unknowns i.e. $\mathbf{r}$ and $\boldsymbol{\theta}$, whereas $\Delta\boldsymbol{\phi}$ has unknowns from the assumed form of electric potential (namely ϕ_0, ϕ_1 and ϕ_2), also $\mathscr{R}$ denotes assembled residual vector. To discretize the linearized weak form, two noded linear Lagrange shape functions were utilized having C^0 continuity.

3. Validation

The finite element flexoelectric special Cosserat model was validated against existing nonlinear analytical solutions [1, 3], showing close agreement with numerical results (see Fig. 2).

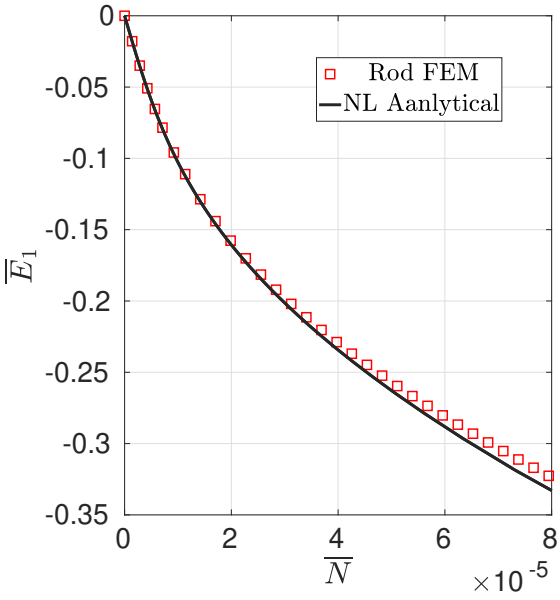

Figure 2: Comparison of FEM vs NL Analytical solution showing behaviour of normalized electric field $\overline{E}_1$ vs normalized load $\overline{N}$.

4. Conclusions

The proposed FE scheme significantly simplifies the analysis of flexoelectric structures. It enables the study of slender flexoelectric structures undergoing large deformations under various loads. Coupled with optimization techniques, this approach facilitates the development of sensors and energy harvesters with enhanced flexoelectric response.

References

[1] Pushkar Mishra and Prakhar Gupta. Modeling direct and converse flexoelectricity in soft dielectric rods with application to the follower load. *Journal of the Mechanics and Physics of Solids*, 195:105956, 2025.

[2] Juan C Simo and Loc Vu-Quoc. A three-dimensional finite-strain rod model. part ii: Computational aspects. *Computer methods in applied mechanics and engineering*, 58(1):79–116, 1986.

[3] David Codony, Prakhar Gupta, Onofre Marco, and Irene Arias. Modeling flexoelectricity in soft dielectrics at finite deformation. *Journal of the Mechanics and Physics of Solids*, 146:104182, 2021.

[4] Vipin Kumar Yadav and Prakhar Gupta. A strain-gradient elastic theory for special cosserat rods. *International Journal of Solids and Structures*, 291:112696, 2024.

ECCOMAS Thematic Conference and IACM Special Interest Conference
Highly Flexible Slender Structures (HFSS 2025)
22–26 September 2025, Kaiserslautern, Germany

Mathematical modeling of chemo-elastic special Cosserat rod

Asutosh Parida*[1], Prakhar Gupta*[2],

*SUCHSM Lab, Department of Mechanical and Aerospace Engineering, IIT Hyderabad, India,
[1]me22m24p100001@iith.ac.in, [2]prakharg@mae.iith.ac.in

Keywords: Chemo-mechanics, Cosserat rod, Energy minimization

1. Introduction

Chemo-mechanical interactions play a crucial role in various natural and engineered systems, particularly in soft materials, biological tissues, and energy storage devices. Previous studies on chemo-elastic modeling [1, 2] have primarily developed three-dimensional models, where the governing equations naturally take the form of partial differential equations (PDEs). While three-dimensional modeling frameworks are available, their complexity is non-essential in the context of rod-like structures, where lateral field variations can be neglected. In the current, we develop a mathematical framework for modeling a chemo-elastic special Cosserat rod, capturing both macroscopic mechanical responses and microscopic force interactions arising from concentration variations [1].

We formulated the constitutive behavior of the rod and derived the governing differential equations as a system of ODEs by minimizing the total free energy. Using this framework, we investigate how different loading conditions influence the distribution of chemical concentration along the rod, providing insights into the coupled chemo-mechanical behavior of slender structures.

2. Methodology

The rod's kinematics were defined using the special Cosserat rod theory, and a multiplicative decomposition of the deformation gradient was employed, which includes an eigen transformation due to chemical diffusion [2] followed by an elastic deformation (as shown in Fig.1).

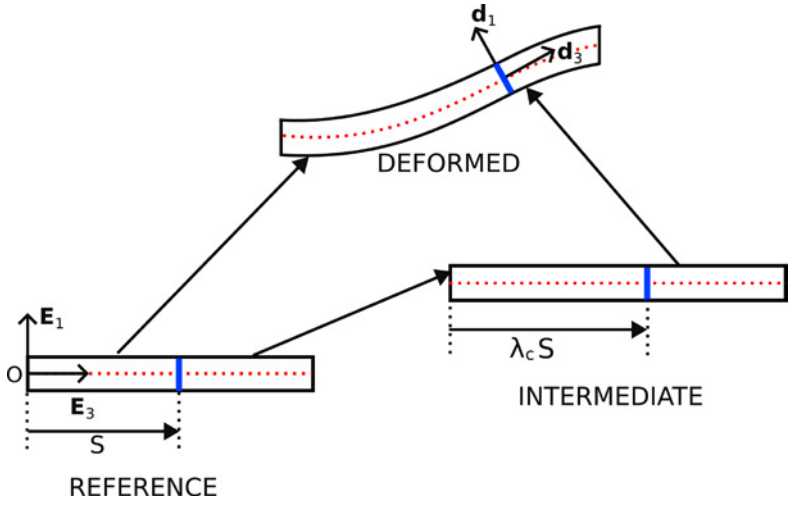

Figure 1: Kinematics of a chemo-elastic special Cosserat rod.

The strain measures defined w.r.t. the reference configuration as below:

$$\mathbf{v}^e = \frac{\mathbf{v}}{\lambda_c(C)}, \quad \text{and} \quad \mathbf{k}^e = \frac{\mathbf{k}}{\lambda_c(C)}, \tag{1}$$

where $\mathbf{v}^e$ and $\mathbf{k}^e$ are the strain measures, and C(S) represents the concentration of the diffusing species defined in moles per unit reference volume. Here, λ_c defines the axial stretch of the intermediate configuration w.r.t. the reference configuration because of the eigen transformation. Upon doing the minimization of the total free

energy, we obtain the following governing differential equations:

$$\mathbf{n}' + \hat{\mathbf{b}} = \mathbf{0}, \qquad \mathbf{m}' + \mathbf{r}' \times \mathbf{n} + \hat{\mathbf{m}} = \mathbf{0}, \tag{2}$$

$$\Gamma_c - \frac{\Lambda}{\lambda_c}\left[\mathbf{n}\cdot\mathbf{R}^{\mathrm{T}}\mathbf{v} + \mathbf{m}\cdot\mathbf{R}^{\mathrm{T}}\mathbf{k}\right] - \Gamma'_{cg} = 0, \quad \text{where } \Lambda = \frac{\mathrm{d}\lambda_c}{\mathrm{d}C}, \tag{3}$$

here $\mathbf{n}$ and $\mathbf{m}$ define the stress resultant and spatial stress couple respectively [3], Γ_c is the scalar micro force due to the concentration of the diffusing species, and Γ_{cg} is the scalar micro force which is generated due to the concentration gradient, $\hat{\mathbf{b}}$ and $\hat{\mathbf{m}}$ define the body force and body couple per unit undeformed length, respectively.

3. Result and Conclusion

To show the effect of mechanical loading on the variation of the concentration field, we present here a simple case of stretching (as illustrated in Fig. 2). For this, we assume that the axial stiffness (EA) is a linear function of normalized concentration $\overline{C} = C/C_{max}$ [4], which is expressed as $EA = (EA)_0 + \beta_1\overline{C}$, where β_1 is a constant and $(EA)_0$ defines the axial stiffness when $\overline{C} = 0$. C_{max} defines the maximum concentration that the material of the system can hold. We also assume $\lambda_c = 1 + \widetilde{\Lambda}\,\overline{C}$. After numerically solving Equations (2) and (3), we present the results in Fig. 2. The plot shows that as the applied force increases, the local concentration ($\overline{C}$) within the rod also increases, satisfying the boundary condition of the concentration.

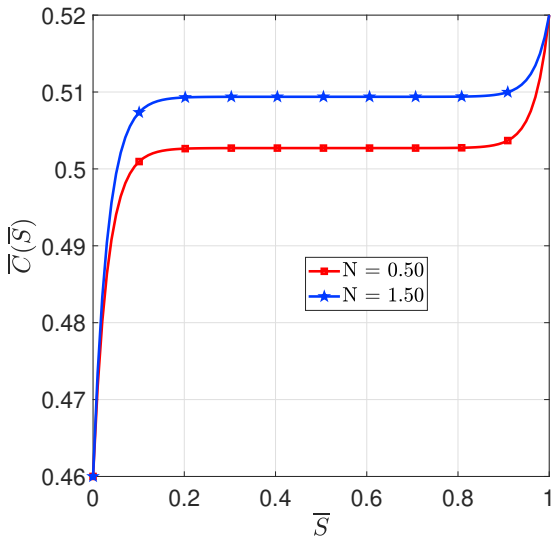

Figure 2: Plot illustrating the variation in concentration ($\overline{C}$) with respect to the applied contact force (N) at $\overline{S} = 1$, considering the parameters: $(EA)_0 = 25$, $\beta_1 = -10$, $\widetilde{\Lambda} = 0.05$, and $\mathcal{D}$ (coefficient of the energy term associated with the chemical gradient) = 0.02, all expressed in SI units.

References

[1] Lallit Anand. A cahn–hilliard-type theory for species diffusion coupled with large elastic–plastic deformations. *Journal of the Mechanics and Physics of Solids*, 60(12):1983–2002, 2012.

[2] Zhiwei Cui, Feng Gao, and Jianmin Qu. A finite deformation stress-dependent chemical potential and its applications to lithium ion batteries. *Journal of the Mechanics and Physics of Solids*, 60(7):1280–1295, 2012.

[3] Juan C Simo and Loc Vu-Quoc. A three-dimensional finite-strain rod model. part ii: Computational aspects. *Computer methods in applied mechanics and engineering*, 58(1):79–116, 1986.

[4] Minh-Quy Le, Huu-Tu Nguyen, and Thanh-Lam Bui. A computational comparative study of the lithium diffusion in amorphous silicon spheres, rods, and circular disks. *Journal of Electrochemical Energy Conversion and Storage*, 18(1):011010, 2021.

ECCOMAS Thematic Conference and IACM Special Interest Conference
Highly Flexible Slender Structures (HFSS 2025)
22–26 September 2025, Kaiserslautern, Germany

Theoretical and Experimental Studies of a Flexoelectric Actuator

Koneti Saiprasad*[1], Ranjith Ramadurai*[2], Prakhar Gupta*[3]
*Centre for Interdisciplinary Programs, IIT Hyderabad, India
[1]id23m24p100001@iith.ac.in, [2]ranjith@msme.iith.ac.in, [3]prakharg@mae.iith.ac.in

Keywords: PVDF, Cosserat rod, Flexoelectricity, Actuator

1. Introduction

Flexoelectricity is a universal phenomenon that is present in all dielectric materials. In this phenomenon, the electric field is generated due to strain gradients, unlike piezoelectricity, where uniform strains are responsible for the electric field generation. For a non-piezoelectric material, the flexoelectric effect in a cantilevered rod under voltage actuation has been studied [1]. However, for the piezoelectric material, we would anticipate a coupled effect of both piezoelectricity and flexoelectricity. The present work focuses on both these effects under large deformations of a slender cantilever rod under the application of voltages.

2. Theoretical Modeling

The piezoelectric and flexoelectric effects under large deformations can be modelled by defining the internal energy per unit reference volume. This internal energy density(ψ^{Int}) is expressed similarly to the formulation presented in [1]:

$$\psi^{Int}(\mathfrak{E},\tilde{\mathfrak{E}},\mathbf{P}) = \psi^{Mech}(\mathfrak{E},\tilde{\mathfrak{E}}) + \psi^{Diele}(\mathbf{P}) + \psi^{Piezo}(\mathfrak{E},\mathbf{P}) + \psi^{Flexo}(\tilde{\mathfrak{E}},\mathbf{P}). \tag{1}$$

Here, ψ^{Mech}, ψ^{Diele}, ψ^{Piezo}, and ψ^{Flexo} represent the mechanical, dielectric, piezoelectric, and flexoelectric energy densities, respectively. The Green-Lagrangian strain tensor is denoted by $\mathfrak{E}$, while $\tilde{\mathfrak{E}}$ refers to its gradient. In addition, the electric field is represented by $\mathbf{E}$, and the electric polarization is denoted by $\mathbf{P}$. In this formulation, the piezoelectric contribution is defined as follows:

$$\psi^{Piezo}(\mathfrak{E},\mathbf{P}) = -P_I h_{IJK} \mathfrak{E}_{JK},$$

where $\mathbf{h}$ is the piezoelectric coefficient of the material. The enthalpy of the system, $\psi^{Enth} = \psi^{Int} - \psi^{Elec}$, where $\psi^{Elec}(\mathfrak{E},\mathbf{E})$ is the electrostatic energy density. For self-consistency, the electromechanical(ψ^{Int}) and electrostatic(ψ^{Elec}) energy densities must be expressed in terms of the same variables. Hence, we expressed both energies in terms of the electric field using the partial Legendre transformation. Since we are interested in slender structures, using the above three-dimensional energy densities would be computationally expensive. Therefore, we will use the special Cosserat rod theory to model large displacements and rotations of the cross-section of these one-dimensional structures. To this rod-like structure, an electric potential (V) is applied at the top surface, while the bottom surface is grounded (see Fig. 1). In this setup, neglecting the localized boundary

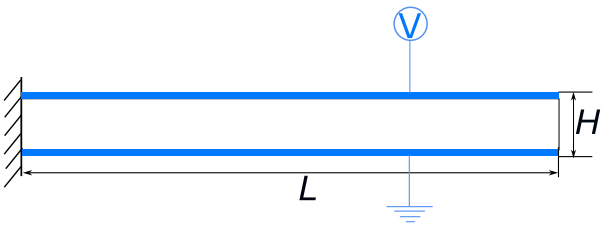

Figure 1: A schematic of a cantilevered rod under the application of voltages through electrodes at the top and bottom of the rod.

effects at the ends of the rod, the electric field components are $E_1 = -\dfrac{V}{H}$, $E_2 = 0$, and $E_3 = 0$, where H is the lateral dimension of the rod. Further, by using variational principles, we derived the Euler-Lagrange equation that describes the electromechanical behavior of the rod, given by:

$$\left[\tilde{Y}\tilde{I}\theta' - \mu_T \frac{V}{H}\tilde{A}\right]' = 0, \tag{2}$$

where

$$\tilde{Y} = \bar{Y} + \frac{\varepsilon V^2}{2H^2} + (\varepsilon - \varepsilon_0)\left[2h_{133}\frac{V}{H} - (h_{133}^2 + h_{233}^2 + h_{333}^2)\right], \bar{Y} = \frac{Y(1-\nu)}{(1+\nu)(1-2\nu)},$$
$$\tilde{I} = I - \left(\frac{\mu_T^2 A V^2}{2H^2\tilde{Y}}\right)\frac{\left[2H(\varepsilon-\varepsilon_0)(3h_{133}V - H(h_{133}^2+h_{233}^2+h_{333}^2)) + 2H^2\tilde{Y} - \varepsilon V^2\right]}{\left[(\varepsilon-\varepsilon_0)(2h_{133}V - H(h_{133}^2+h_{233}^2+h_{333}^2)) + H\tilde{Y}\right]^2},$$
$$\tilde{A} = A\left(1 + \frac{\varepsilon V^2 - 2HVh_{133}(\varepsilon-\varepsilon_0)}{2\tilde{Y}H^2 + 2H(\varepsilon-\varepsilon_0)(2Vh_{133} - H(h_{133}^2+h_{233}^2+h_{333}^2))}\right).$$

In the above equations, θ indicates the rotation of the cross section, $(\cdot)'$ represents the derivative with respect to the arc length parameter of the rod, and μ_T denotes the transverse flexoelectric coefficient. The symbols ε and ε_0 represent the permittivity of the material and the permittivity of the vacuum, respectively. Furthermore, I denotes the area moment of inertia of the cross section, and A means the cross-sectional area of the rod. Lastly, Y represents the Young's modulus of the material, and ν indicates the Poisson's ratio of the material. The equation (2) shows that the piezoelectric properties of the material do not independently contribute to

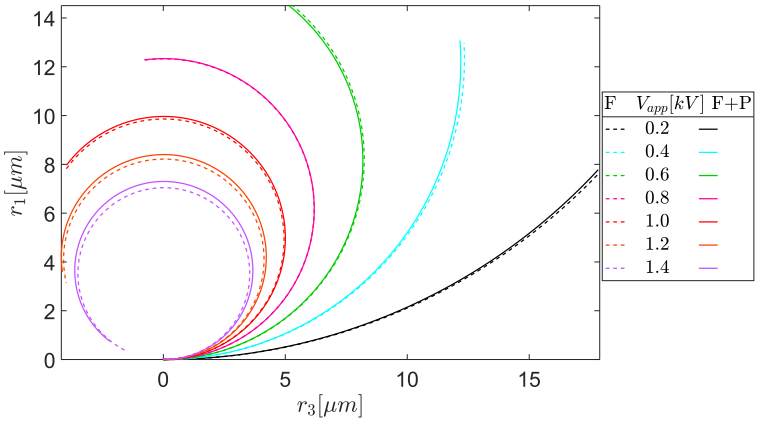

Figure 2: Deformed shape of the rod(F: Flexoelectric rod and F+P: Flexoelectric and piezoelectric rod) for various applied voltages($V_{app}[kV]$)

the bending of the rod. Instead, they modify the effective stiffness, influencing the rod's deformation behavior compared to one that exhibits only flexoelectricity (see Fig. 2).

3. Experimental Approach

In this work, polyvinylidene difluoride (PVDF) and its co-polymer-based cantilever sheets of varying dimensions will be fabricated using the conventional doctor-blade method, and the respective electrode patterning will be carried out using printing techniques. The preliminary studies suggest us that the PVDF films are sensitive to process conditions [2] and the optimized conditions for a dominant planar domain configuration will be utilized. The studies performed on PVDF cantilever sheets of (2cm x 1.5cm x 10μm) show that the deflections are of the order of a few micro-meter and also sensitive to the frequency of the electrical signal that is applied. However, in this study, the dimensions provided by the theory will be fabricated, and these cantilevers will be subjected to varying voltages, and the respective deflections will be measured. The study is expected to enhance the research on the flexoelectricity-driven piezoelectricity of PVDF-like materials.

References

[1] D. Codony, P. Gupta, O. Marco, I. Arias. *Modeling flexoelectricity in soft dielectrics at finite deformation*, Journal of the Mechanics and Physics of Solids.

[2] R. Ganguly, S. Bandyopadhyay, K. Miriyala, V. Gunasekaran, S. Bhattacharya, A. Acharyya, and R. Ramadurai. *Tunable polarization components and electric field induced crystallization in polyvinylidenefluoride: A piezo polymer*, Polymer Crystallization.

ECCOMAS Thematic Conference and IACM Special Interest Conference
Highly Flexible Slender Structures (HFSS 2025)
22–26 September 2025, Kaiserslautern, Germany

Modelling coupled fluid and mooring line interactions in floating body simulations

Amirhossein Taran [1*], Seevani Bali [1], Željko Tuković [2], Vikram Pakrashi [1], Philip Cardiff [1]

[1] School of Mechanical and Materials Engineering, University College Dublin, Ireland
[2] Faculty of Mechanical Engineering and Naval Architecture, University of Zagreb, Croatia
* amirhossein.taran@ucdconnect.ie

Keywords: Mooring lines, finite volume, Fluid-solid interaction, OpenFOAM

1. Introduction

This study presents a two-way coupled mooring line model based on the finite volume method for simulating moored floating structures. The model is developed using a finite volume formulation of the geometrically exact Simo-Reissner beam theory [3, 4], which allows for the representation of bending, tensile, and torsional loads. It captures the interaction between a floating rigid body and its mooring lines, offering an alternative to existing methods such as lumped-mass models with massless springs [1] and finite element techniques [2]. Furthermore, most coupled CFD-mooring models interact by exchanging position data and mooring forces at the mooring line attachment points, resulting in the mooring lines being unresolved in the CFD domain. This work introduces a two-way coupling between the mooring lines and the CFD model, where the fluid forces acting on the mooring lines are obtained by directly sampling the surrounding flow field. This approach allows the model to account for the local fluid motion around the mooring lines rather than assuming a quiescent fluid. This non-quiescent fluid approach enhances the accuracy of drag and inertia force predictions in both the mooring and CFD models. The coupled model is fully integrated within a unified finite volume framework and implemented using the OpenFOAM C++ toolbox for computational fluid dynamics, making it particularly effective for simulating extreme sea conditions, where it is challenging to assume that the surrounding fluid remains still.

2. Results

To assess the capabilities of the model, we propose two test cases:

2.1. Mooring line test case

The capabilities of the two-way finite-volume coupling are illustrated through a benchmark study that exposes the key challenges of fluid–structure–mooring interaction. The experimental arrangement places a 0.20 m × 0.20 m × 0.132 m rigid box in a 30 m × 1 m × 1.2 m flume. Each mooring line is an iron chain 1.455 m long, 3.7 mm in diameter, and 5.8 × 10^3 kg·m^{-3} in density. With an axial stiffness of 1.82 MPa, the lines are sufficiently compliant to form shallow catenary curves under load. Figure 1 shows the mooring line tension, comparing the present results with experimental data and with the output from the quasi-static model MoorDyn [1].

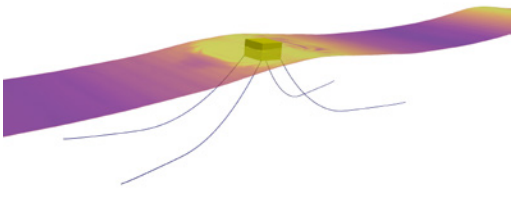

(a)

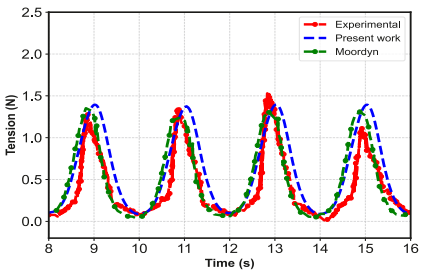

(b)

Figure 1. Mooring line test case results showing (a) instantaneous velocity field near the mooring line and (b) time series of tension at the anchor.

2.2. Flexible stem test case

To investigate the influence of wave-induced flow on deformable structures, a single flexible stem is placed in regular waves within a laboratory flume [4]. The test spans a wide range of non-dimensional parameters, including Cauchy and Keulegan–Carpenter numbers, capturing transitions from quasi-static to inertia-dominated behaviour. High-resolution displacement tracking along the stem provides insight into force distribution, internal shear, and dynamic response, serving as a stringent validation scenario for beam–fluid coupling models. Figure 2 shows the motion of the flexible stem as it interacts with incoming waves, and also presents the time history of tip displacement compared with experimental results [4].

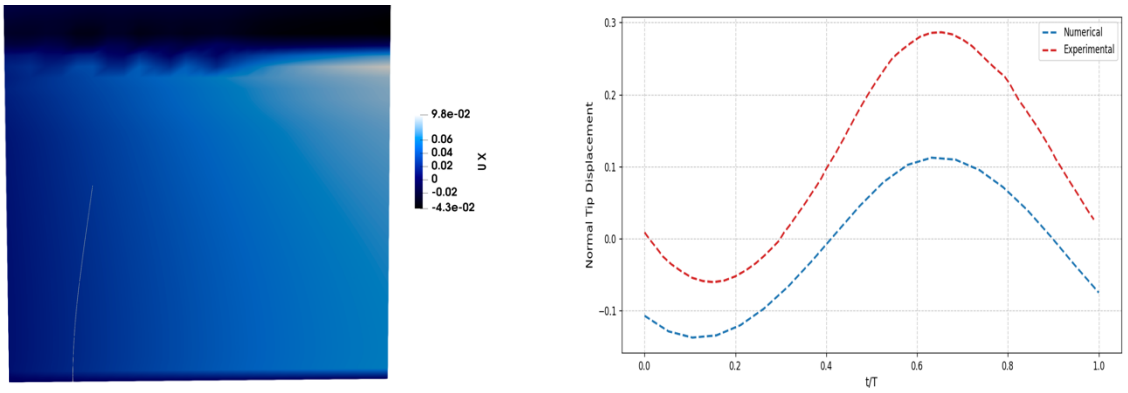

(a) (b)

Figure 2. Results from the flexible stem test case: (a) instantaneous stem deformation under wave forcing; (b) time history of tip displacement.

Acknowledgements

The authors would like to acknowledge Research Ireland, NexSys project 21/SPP/3756 for funding. Vikram Pakrashi would like to acknowledge SEAI RDD/966 FlowDyn and Research Ireland MaREI RC2302-2 projects. Philip Cardiff gratefully acknowledges financial support from the Irish Research Council (IRC) through the Laureate programme, grant number IRCLA/ 2017/45 and the European Research Council (ERC) under the European Union's Horizon 2020 research and innovation programme (Grant Agreement No. 101088740).

Additionally, the authors wish to acknowledge the Irish Centre for High-End Computing (ICHEC) for the provision of computational facilities and support (www.ichec.ie), and part of this work has been carried out using the UCD ResearchIT Sonic cluster which was funded by UCD IT Services and the UCD Research Office.

References

[1] Chen, H., & Hall, M. (2022). CFD simulation of floating body motion with mooring dynamics: Coupling MoorDyn with OpenFOAM, Applied Ocean Research, 124, 103210. https://doi.org/10.1016/j.apor.2022.103210

[2] J. Palm, C. Eskilsson, and L. Bergdahl, "An hp-adaptive discontinuous Galerkin method for modelling snap loads in mooring cables," Ocean Engineering, vol. 144, pp. 266–276, 2017.

[3] Bali S, Tuković Ž, Cardiff P, Ivanković A, Pakrashi V. A cell-centered finite volume formulation of geometrically exact Simo–Reissner beams with arbitrary initial curvatures. Int J Numer Methods Eng. 2022; 123(17): 3950–3973. doi:10.1002/nme.6994

[4] Jacobsen, N. G., Bakker, W., Uijttewaal, W. S., & Uittenbogaard, R. (2019). Experimental investigation of the wave-induced motion of and force distribution along a flexible stem. *Journal of Fluid Mechanics*, *880*, 1036-1069.

ECCOMAS Thematic Conference and IACM Special Interest Conference
Highly Flexible Slender Structures (HFSS 2025)
22–26 September 2025, Kaiserslautern, Germany

A Soft Robotic Gripper with Flexoelectric Effects

Vipin Kumar Yadav*, Prakhar Gupta*

*SUCSHM Lab, Department of Mechanical and Aerospace Engineering, Indian Institute of Technology Hyderabad, Kandi, Sangareddy, Telangana, India Pin: 502285

Keywords: Soft robotics gripper, Flexoelectricity, Special Cosserat rod.

1. Introduction

Soft robotic grippers offer a versatile and safe solution for handling delicate and fragile objects with greater flexibility than conventional rigid manipulators. Its natural compliance allows it to grasp the object securely; however, achieving precise control over deformation and force is still challenging and requires innovative solutions. One promising approach is the integration of the flexoelectric effect, which occurs when strain gradients generate electrical polarization in dielectric materials. Unlike piezoelectricity, which is confined to a certain class of materials, flexoelectricity is present in all dielectric materials and becomes especially important at large deformation, making it highly suitable for soft robotics. This phenomenon facilitates the self-sensing capabilities of the soft robotic grippers, thereby enhancing both efficiency and adaptability. This work develops a mathematical model based on the theory of intrinsically curved nonlinear rods to analyze a soft robotic gripper utilizing the flexoelectric effect and determines the necessary gripping force while accounting for frictional constraints and exploring stability under varying pre-flexural strains and control parameters. The ultimate goal is to optimize gripping performance by understanding how the pre-flexural strains and flexoelectric effect influence structural deformation and stability. Integrating this mechanism into soft robotics has the potential to revolutionize precision manipulation across biomedical, industrial, and space applications, offering a more efficient and adaptive alternative to conventional robotic systems.

2. Methodology

We model the gripper as a slender rod that undergoes large deformations and significant cross-sectional rotations while maintaining small strains. In this context, we utilize the intrinsically curved nonlinear flexoelectric special Cosserat rod theory [1, 2]. The curved flexoelectric rod is fixed at one end and grounded at another, experiencing normal and frictional forces, as shown in Fig. 1. The rod is considered inextensible and unshearable, with the

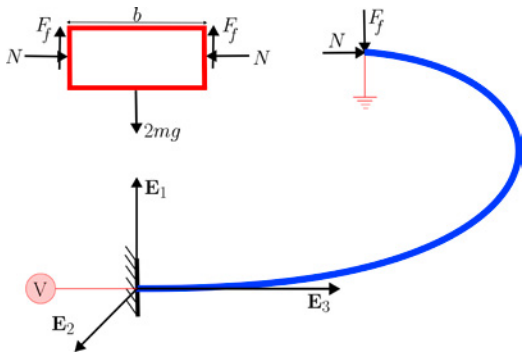

Figure 1: Free body diagram of the gripper

kinematics given below:

$$\mathbf{r}' = N\cos\theta\ \mathbf{E}_3 - F_f \sin\theta\ \mathbf{E}_1, \tag{1}$$

where $\mathbf{r}$ represents the deformed centerline mapping, N denotes the normal pinching force, and F_f is the frictional force required to grip the object. Additionally, the total potential energy of the gripper is written and minimized using the principle of variations and the governing equation is derived along with the boundary conditions with an additional constraint shown below:

$$EI_{eff}\left(\theta'' - \kappa_0'\right) - N\sin\theta \; - \; F_f\cos\theta = 0, \quad \text{where} \quad I_{eff} = I + \frac{\mu_T^{d^2} A}{E\varepsilon_0}, \tag{2a}$$

$$\theta(0) = 0, \quad \theta'(L) = \kappa_0, \quad \text{and} \quad \int_0^L \cos\theta = \frac{b}{2}. \tag{2b}$$

Here, E represents the Young's modulus, I_{eff} denotes the effective area moment of inertia, and θ indicates the rotation of the cross-section. Additionally, ε_0 signifies the material's permittivity, while μ_T^d refers to the transverse flexoelectric coefficient. The symbols A and I represent the cross-sectional area of the rod and the area moment of inertia, respectively. Lastly, κ_0 denotes the pre-flexural strain and $\overline{\kappa}_0$ represents the normalized preflexural strain with length.

3. Results

We solve the boundary value problem outlined in Equation (2a) to determine the gripping force and the electric field. The calculated normal forces correspond to different pre-flexural strains at various values of μ_T^d, as illustrated in Figure (2). An increase in the pre-flexural strain results in the enhancement of the normal force, and at a certain pre-flexural strain level, the normal force exceeds the required frictional force F_f, indicating that pre-flexural strains beyond this point are safe for designing the gripper to hold the object securely. In contrast, for any fixed pre-flexural strain, increasing the values of μ_T^d increases the normal force. Specifically, with a higher μ_T^d value, the normal force increases and enhances the weight-carrying capacity of the gripper.

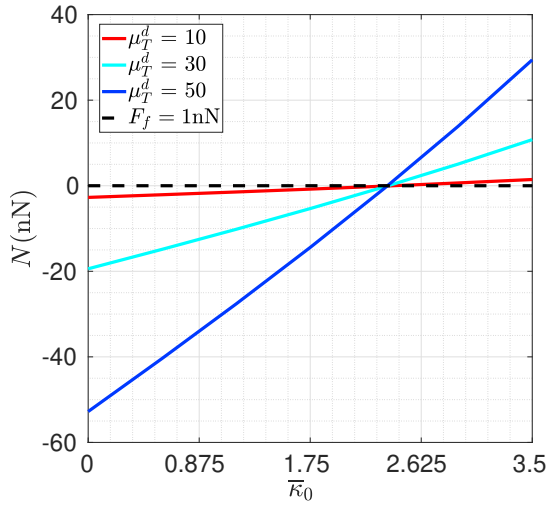

Figure 2: Variation of the normal force with the normalized pre-flexural strain for different value of μ_T^d(nJ/Vm).

4. Conclusions

This analysis shows that increasing the pre-flexural strain and the flexoelectric coefficient μ_T^d enhances the gripping force and improves the gripper's weight-carrying capacity. A sufficiently high pre-flexural strain ensures a secure hold on objects by exceeding the necessary frictional force. Furthermore, a higher μ_T^d value expands the range of normal force, resulting in greater electric field generation. These findings offer valuable insights for optimizing flexoelectric-based soft grippers to achieve efficient and adaptable grasping.

References

[1] Xuance Zhou, Carmel Majidi, and Oliver M O'Reilly. Soft hands: An analysis of some gripping mechanisms in soft robot design. *International Journal of Solids and Structures*, 64:155–165, 2015.

[2] Pushkar Mishra and Prakhar Gupta. Modeling direct and converse flexoelectricity in soft dielectric rods with application to the follower load. *Journal of the Mechanics and Physics of Solids*, 195:105956, 2025.

ECCOMAS Thematic Conference and IACM Special Interest Conference
Highly Flexible Slender Structures (HFSS 2025)
22–26 September 2025, Kaiserslautern, Germany

Compression of textile cords in an elastomer matrix: highlighting the helical buckling mechanism

Gianluca Auteri [1,2], Jan Neggers [1], Sophie Charpin[2], Kablan Guy-Delphin Agniman[1,2], Damien Durville [1]

[1] Université Paris-Saclay, CentraleSupélec, ENS Paris-Saclay, CNRS, LMPS - Laboratoire de Mécanique Paris-Saclay, 3 rue Joliot-Curie, Gif-sur-Yvette 91190, France.

[2] Michelin, Ladoux Research Center, 23 Place des Carmes Déchaux, Clermont-Ferrand, 63040, France

{gianluca.auteri, jan.neggers, kablan-guy-delphin.agniman, damien.durville} @centralesupelec.fr

sophie.charpin@michelin.com

Keywords: elastomer composites, textile reinforcement, helical buckling, Finite Element Modeling, numerical-experimental comparison

1. Introduction

Textile cords are slender structures with a complex filament assembly, often used to reinforce elastomeric matrices (Figure 1.a). The mechanical behavior of textile cords, both alone and within a matrix, has been extensively studied under common loading conditions such as tension and bending but remains unexplored for axial compression, which may appear in certain industrial applications. In particular, the response at the filament scale under compression is non-trivial, as local deformations vary significantly depending on the local filament arrangement. Moreover, beyond a critical compression threshold, buckling phenomena emerge, further complicating the overall mechanical response. The behavior of textile cords composites can be compared to any beam-like structure embedded in a surrounding medium. It has been documented experimentally that a single elastic fiber rod, when embedded in an elastomer matrix, exhibits a specific type of buckling in a helical shape [3]. In this work, the study of helical buckling is extended to textile cords, slender structures with a complex entanglement.

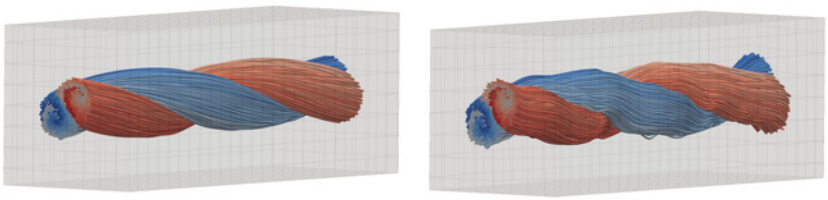

(a) Initial state.

(b) Compression and onset of helical buckling.

Figure 1: Textile cord-elastomer composite.

2. Methodology

The problem is addressed through filament scale finite element simulations, using the in-house finite element code Multifil [1]. Each filament is represented by 1D beams with enriched kinematics, undergoing contact-friction interactions and large deformations. An implicit solver is used to solve the global nonlinear problem, under quasi-static assumptions. A 3D overlapping non-conforming mesh of linear hexahedral elements represents the matrix. The coupling between the filaments and the matrix is enforced, by means of bonding elements uniformly distributed at the interface, through penalization of the relative displacement between a particle at the surface of the filaments and the corresponding overlapping matrix particle.

A distinctive feature of textile cords is that the filament arrangement is not known beforehand. This in fact highly depends on the manufacturing process. The migration phenomenon makes the paths of the filaments complex and difficult to describe analytically with accuracy [2]. Hence, the strategy chosen here is to reproduce the textile cord assembly procedure numerically. This is subdivided in the yarn twisting, consisting of applying a twist to a bundle of disordered straight filaments. Then, the second step of the assembly process consists of twisting two yarns together with a twist equal but opposite to the one applied during the single yarn twisting. Finally, to create the composite model, the cord is coupled with the matrix.

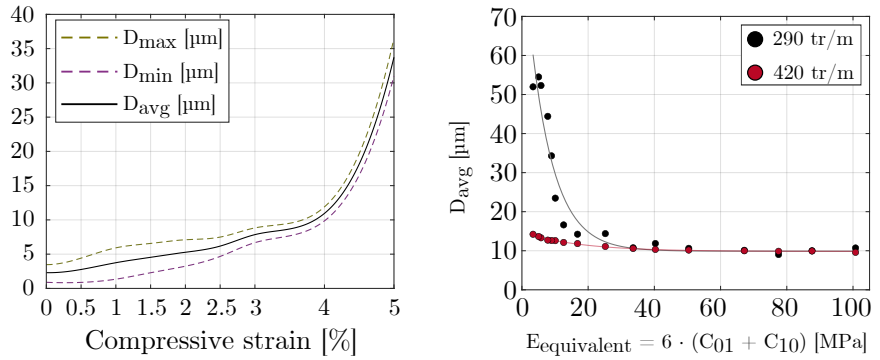

(a) Evolution of helical buckling diameter with compressive strain.

(b) Helical buckling diameter as a function of matrix rigidity for two different twist levels.

Figure 2: Dependence of helical buckling amplitude.

3. Results

When applying uniaxial compression to a textile cord-elastomer composite, multiple mechanisms activate to react to the loading. The most evident ones are the opening between the yarns, Euler buckling, and 3D helical buckling. The latter consists of the cord center-line trajectory adopting a three-dimensional helical shape. A compressed textile cord, after the onset of helical buckling, is shown in Figure 1.b. The buckling amplitude increases as a function of the global compressive strain (Figure 2.a). The curve is characterized by a stable phase, followed by a rapid growth after 4% strain. The three-dimensional buckling is actually originated from the superposition of two orthogonal planar buckling modes activated simultaneously [3]; the growth of these two perpendicular modes can be followed in Figure 2 in the dashed lines. The amplitude of the helical buckling depends mainly on two parameters of the composite: the rigidity of the matrix and the twist of the textile structure. Figure 2.b shows a decrease of the buckling amplitude as a function of the rigidity of the matrix. Still in Figure 2.b, it can be observed that increasing the twist reduces the 3D buckling response of the cord. These results are compared with experimental results, obtained using x-ray tomography. A good correspondence is found between numerical and experimental results. Furthermore, it has been highlighted that helical buckling has some consequences on the distribution of the local strains between filaments. The cord presents some fluctuations along the longitudinal direction for the filament's local strain level. Also, the appearance of buckling seems to distribute the deformation between filaments, reducing the peaks of local strains.

4. Conclusion

The helical buckling phenomenon has been described and characterized for the first time in textile cords-elastomer composite. Considering this mechanism, along with others, contributes to a comprehensive understanding of the behavior of this class of composites under compressive loading. Moreover, this study also provides a valuable validation opportunity for the presented finite element tool, demonstrating its ability to replicate complex instability mechanisms involving different scales.

References

[1] Durville, D. (2012). Contact-friction modeling within elastic beam assemblies: An application to knot tightening. Computational Mechanics, 49(6), 687–707. Springer.

[2] Sibellas, A., Adrien, J., Durville, D., Maire, E. (2020). Experimental study of the fiber orientations in single and multi-ply continuous filament yarns. The Journal of The Textile Institute, 111(5), 646–659. Taylor & Francis.

[3] Su, T., Liu, J., Terwagne, D., Reis, P. M., Bertoldi, K. (2014). Buckling of an elastic rod embedded in an elastomeric matrix: Planar vs. non-planar configurations. Soft Matter, 10(33), 6294–6302. Royal Society of Chemistry.

ECCOMAS Thematic Conference and IACM Special Interest Conference
Highly Flexible Slender Structures (HFSS 2025)
22–26 September 2025, Kaiserslautern, Germany

Asymptotic analysis of composite plates with stiff inclusions

Amartya Chakrabortty [1], Georges Griso [2], Julia Orlik [3]

[1] Fraunhofer ITWM, amartya.chakrabortty@itwm.fraunhofer.de
[2] Sorbonne Université, CNRS, LJLL, georges.griso@gmail.com
[3] Fraunhofer ITWM, julia.orlik@itwm.fraunhofer.de

Keywords: Homogenization, Dimension reduction, Non-linear elasticity, Plate theory, Pre-stress

1. Introduction

The use of 3D printing technology enables the deployment of pre-stretched membranes into desired shapes, presenting a challenge in determining the optimal pre-strain necessary for shaping a homogenized composite shell. This process involves extending the membrane in specific directions and printing a pattern on it, with a focus on effectively transferring pre-strain from the soft membrane to the stiffer composite shell. The study reveals that a soft membrane alone may not adequately transfer stress to the stiff shell, which is crucial for folding, especially when the printed pattern features thick beams. The findings suggest that incorporating pre-strain in the soft membrane can achieve the desired effects in practical applications. In this work, we derive asymptotically reduced models as approximations from real 3D slender plates subjected to non-linear elasticity.

2. Asymptotics on high-contrast slender plates

We discuss two cases one with a connected stiff part (see [1]) and another with a disconnected stiff or rigid part (see [2]) reinforced within the soft matrix part.

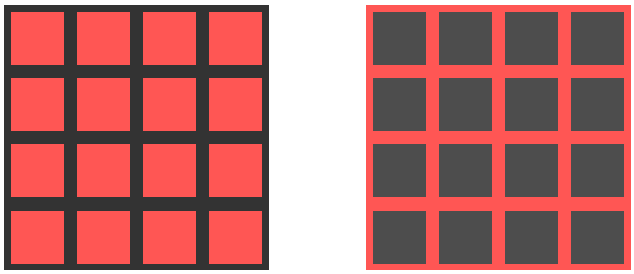

(a) Connected stiff part (b) Disconnected stiff part

Figure 1: 2D view of a toy domain

2.1. Stiff part connected

We focus on the simultaneous homogenization and dimension reduction of high contrast periodic composite plates within the framework of non-linear elasticity when the period ε and the thickness δ are of the same order, i.e. $\lim_{(\varepsilon,\delta)\to(0,0)} \frac{\delta}{\varepsilon} \in (0,1)$. The composite plate in its reference configuration consists of a connected periodic perforated plate made of stiff material with holes filled by a relatively soft material (the domain containing a soft matrix can be both connected and disconnected). Two cases of asymptotic analysis are considered: one without pre-strain and the other with matrix pre-strain. In both cases, the total energy is in Von-Kármán regime ($\mathbf{O}(\varepsilon^5)$). A new splitting of the displacements is introduced to analyze the asymptotic behavior. The displacements are decomposed using the Kirchhoff–Love (KL) plate displacement decomposition. The use of a re-scaling unfolding operator allows for deriving the asymptotic behavior of the Green St. Venant's strain tensor in terms of displacements. The limit homogenized energy is shown to be of vK type with linear elastic cell problems, established using the Γ-convergence.

2.2. Disconnected stiff part

We focus on the simultaneous homogenization and dimension reduction of soft plates re-enforced with rigid substructure within the framework of non-linear elasticity when the thickness δ is comparatively smaller than the period ε i.e $\lim_{(\varepsilon,\delta)\to(0,0)} \frac{\delta}{\varepsilon} = 0$. The composite plate in its reference configuration consists of a connected periodic perforated plate made of a soft matrix with holes filled by 3D-printed rigid substructures (the domain containing the rigid part is disconnected). The total energy of the system is in the Kármán regime type, i.e., $\mathbf{O}(\varepsilon^2\delta^3)$, which is obtained by scaling the applied forces and using the decomposition of rod deformations. The limit behavior of the Green-St. Venant's strain tensor is determined using three types of unfolding operators. Using Γ-convergence, the limit homogenized energy is derived, and the existence of a minimizer is proven. The limit bending displacements satisfy the following $\partial_{12}\mathscr{U}_3 = 0$ and the limit membrane displacement $\mathscr{U}_m$ and the bending $\mathscr{U}_3$ are coupled by the non-linear isometry condition $e_{\alpha\beta}(\mathscr{U}_m) + \partial_\alpha\mathscr{U}_3\partial_\beta\mathscr{U}_3 = 0$.

3. Linearization

This work [3] investigates the homogenization, dimension reduction, and linearization of a composite plate subjected to external loading within the framework of a non-linear elasticity problem. The total elastic energy of the problem is of order $\sim h^2\varepsilon^{2a+3}$, where $a \geq 1$. The paper is divided into two parts: The first part presents the simultaneous homogenization, dimension reduction and linearization ($(\varepsilon,h) \to (0,0)$) of a composite plate. The second part consists of the rigorous derivation of linearized elasticity as a limit of non-linear elasticity with small deformation and external loading conditions. The results obtained demonstrate that the limit energy remains unchanged when first linearization ($h \to 0$) is performed, followed by simultaneous homogenization dimension reduction ($\varepsilon \to 0$) and when both limits approach zero simultaneously, i.e. $(\varepsilon,h) \to (0,0)$. The exact form of the limit energy(s) is obtained through the decomposition of plate deformations and plate displacements. By using the Γ-convergence technique, the existence of a unique solution for the limit linearized homogenized energy problem is demonstrated. These results are then extended to certain periodic perforated plates.

Acknowledgments

The research was funded by DFG, German Research Foundation, project number OR 190/10-1 and AIF project OptiDrape, both in the collaboration with the textile institute ITA in Aachen, Germany.

References

[1] Amartya Chakrabortty, Georges Griso, and Julia Orlik. "Dimension reduction and homogenization of composite plate with matrix pre-strain." Asymptotic Analysis Preprint (2024): 1-56.

[2] Amartya Chakrabortty, Georges Griso, and Julia Orlik. "Dimension reduction and homogenization for soft plates with printed disconnected rigid substructures." (In preparation).

[3] Amartya Chakrabortty, Georges Griso, and Julia Orlik. "Homogenization, dimension reduction and linearization for an elastic plate under small external loading." (Ready for submission).

ECCOMAS Thematic Conference and IACM Special Interest Conference
Highly Flexible Slender Structures (HFSS 2025)
22–26 September 2025, Kaiserslautern, Germany

Asymptotically based simulation and optimization of flow-induced deformation of textile filters

M. Krier [1], J. Orlik [1], R. Pinnau [2]

[1] Fraunhofer Institute for Industrial Mathematics, maxime.krier@itwm.fraunhofer.de, julia.orlik@itwm.fraunhofer.de
[2] Rheinland-Pfälzische Technische Universität, pinnau@rptu.de

Keywords: Fluid-Structure Interaction, Homogenization, Multi-Scale Optimization, Slender Yarns

1. Motivation

The flow-induced deflection of filters is a commonly encountered phenomenon in filtration applications with flexural filter media such as PET wovens. Since this deformation leads to locally increased pore sizes and open surface area, the local flow resistivity decreases. Common simulation approaches in filtration assume a rigid medium, thereby neglecting these effects. This causes potential discrepancies between simulation results and experimental measurements. Due to the drastically differing length-scales, the modeling of the flow-induced filter deformation and efficient numerical approaches to solve the coupled systems are challenging. The issues can be overcome by derivation of multi-scale systems by asymptotic approaches such as homogenization and dimension reduction.

2. Problem formulation and optimization approach

A multi-scale optimization problem with PDE constraints in a fluid-structure interaction (FSI) setting is considered. The microscale design of a woven filter, i.e. weaving type, weaving distances and utilized materials, is to be chosen such that a desired flow-induced displacement is attained. For the forward problem, Stokes flow through a channel is considered. The channel is split in half in main flow direction by the flexural filter of thickness and period ε. A depiction of the model domain with two separated fluid domains $\Omega_\varepsilon^\pm$ and filter domain Ω_ε^m is shown on the left-hand side of Figure 1. An effective macroscale FSI problem was derived and analysed in [1, 2, 3] by simultaneous homogenization and dimension reduction for $\varepsilon \to 0$. In the macroscale model, the deflection of the filter is governed by a permeable 2D Kirchhoff plate equation, with the jump of fluid stresses across the filter arising as a right-hand side load. In the non-stationary setting, fluid and plate velocity are back-coupled by a Darcy interface condition, while a no-slip condition at the fluid-structure interface is prescribed for the fluid velocity in the stationary setting.

The filter's microscale design is modeled by an abstract design variable $\mathbf{d}$, which in application is typically chosen in a compact subset of $\mathbb{R}^n$. The variable describes the topological appearance of the periodic representative unit of the filter domain, see the right-hand side of Figure 1, as well as elastic material properties and yarn-yarn contact stiffness. It enters the considered FSI problem through the Kirchhoff plate's effective fourth-order extensional, coupling and bending stiffness tensors, which are attained by solving auxiliary elasticity problems on the solid part $Y_\mathbf{d}^s$ of the periodic unit. In the microscale elasticity model, yarn-yarn contacts are modeled by a Robin-type interface condition. Moreover, the design variable influences the effective permeability tensor, attained from solving auxiliary Stokes flow problems in the fluid part $Y_\mathbf{d}^f$ of the periodic unit. In general, the influence of the design on the flow-induced filter deflection is non-trivial. As an intuitive example, decreasing weaving distances decreases the filter's permeability but on the other hand increases its bending stiffness. As a consequence, uniqueness of optimal designs can not be guaranteed.

Well-posedness of the considered optimization problem is verified by deriving the continuous dependence of the effective tensors on the design variable. For this purpose, a function space parameterization approach is followed. Moreover, a numerical optimization framework based on an ajoint-based approach is presented and exemplified for woven filter samples. First-order optimality conditions are derived which are used in gradient-based descent methods.

The complete numerical approach for the considered FSI problem is described in [5, 4]. On the microscale, a finite element formulation with Euler-Bernoulli beams, extended by a Robin-type contact condition, is em-

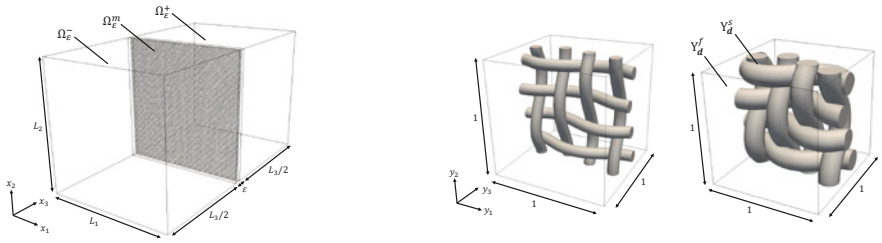

Figure 1: A depiction of the FSI model domain is shown on the left-hand side. The right-hand side shows representative periodic units of the woven filter for a varying design variable.

ployed for the computation of the filter's effective stiffness tensors. Exemplary solutions of the arising elasticity problems are depicted in the left-hand side of Figure 2. Due to the efficient implementation, the effective model parameters can be computed during the optimization iterations and do not require pre-computing. A finite volume solver is utilized for computation of the filter's design-dependent permeability tensor. On the macroscale, both forward and adjoint FSI systems are solved with a conforming finite element solver. For the two-way coupled non-stationary case, a monolithic formulation is employed. A solution of the FSI problem with displaced filter is depicted on the right-hand side of Figure 2. The adjoint-based optimization approach enables the computation of a gradient of the considered cost-functional, the latter is minimized using a sequential quadratic programming method.

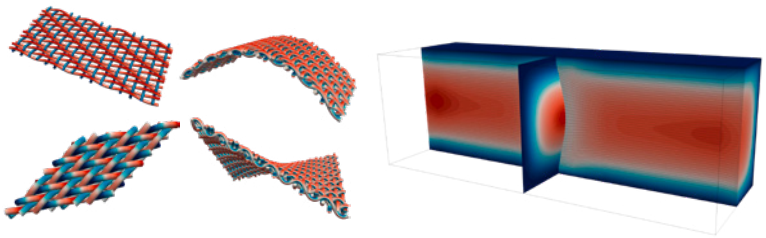

Figure 2: Solutions of tensile, bending, shearing and torsion auxiliary problems for a woven filter are shown on the left-hand side. The right-hand side shows a solution of the FSI problem with displaced filter in steady-state.

Acknowledgments

This project has received funding from the German Research Foundation, DFG-Project OR 190/6-3, in the department of Flow and Material Simulation of the Fraunhofer ITWM, which covers dimension reduction approaches on the yarn level for the FSI simulation with deterministic filter media.

References

[1] J. Orlik, G. Panasenko, R. Stavre. *Asymptotic analysis of a viscous fluid layer separated by a thin stiff stratified elastic plate*, Applicable Analysis, 100(3) (2021) 589–629

[2] M. Gahn, W. Jäger, M. Neuss-Radu. *Derivation of Stokes-plate-equations modeling fluid flow interaction with thin porous elastic layers*, Applicable Analysis, 101(12) (2022) 4319–4348

[3] M. Krier, J. Orlik. *Solvability of a fluid-structure interaction problem with semigroup theory*, AIMS Mathematics, 12 (2023) 29490–29516

[4] M. Krier, J. Orlik, G. Panasenko, K. Steiner. *Asymptotically Proved Numerical Coupling of a 2D Flexural Porous Plate with the 3D Stokes Fluid*, Multiscale Modeling & Simulation, 22(4) (2024) 1608–1645

[5] M. Krier, J. Orlik, R. Pinnau. *Multi-scale optimization problem for the flow-induced displacement of a periodic filter medium*, Optimization and Engineering, under review

ECCOMAS Thematic Conference and IACM Special Interest Conference
Highly Flexible Slender Structures (HFSS 2025)
22–26 September 2025, Kaiserslautern, Germany

Homogenization, dimension reduction and simulation of textiles

Maxime Krier[1], David Neusius [1], Julia Orlik [1], Konrad Steiner [1],

[1] Fraunhofer ITWM, julia.orlik@itwm.fraunhofer.de

Keywords: Plates of continuousfibers in contact, homogenization, dimension reduction, effective 2D models

1. Introduction

Geometrically, textiles are multi-scale materials possessing a periodic structure, locally consisting of thin, continuous beams in multiple contact with each other. In this paper, we will give an overview of 2D effective textile-plate models. The main modeling issue for textiles, especially in the non-crimp regime, is the contact between yarns, which changes the macroscopic behavior of the textiles. The reason for fabric folding is the coupling between effective tension, shear, bending, and torsion. It can arise due to the frictional coupling of yarns, as discussed in [BOP14], [OAA+17], or result from the non-linear behavior of the stretchable structural parts, see [GOW20b]. It can also be an effect of large bending under the isometry condition (preservin of the surface mesure) [FGO24].

In the impactful mathematical work [FJM06], all 2D isotropic plates were classified with respect to the magnitude of the forces, acting on them, relative to their stiffness and thickness. The plates provide different behaviors, starting from the linear elastic Kirchhoff plate. With increasing loading, the in-plane energy starts to be coupled with the bending angle, that leads to a folding in the compressed direction. In case of further increasing transverce load component, the plate comes into the large bending regime. Considering a complex loading, e.g., a penetration-puching-test, it finishes with the membrane behavior under large in-plane tension.
In our previous analysis works, we derived similar hierarchical models for textile materials by employing mathematical asymptotic homogenization and dimension reduction methods. The first works were about knitted

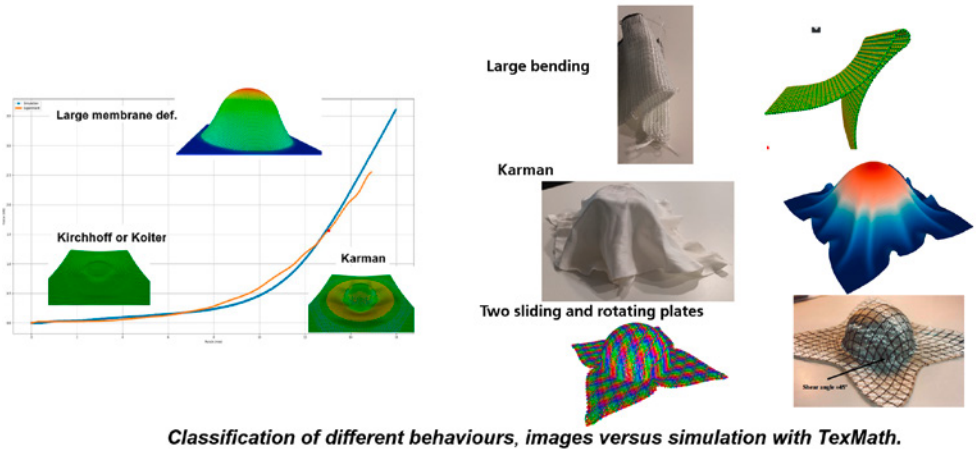

Classification of different behaviours, images versus simulation with TexMath.

fabrics made of thin, stretchable yarns. The effective textile behavior is a membrane in a large deformation regime [OPS16], [SO17], and the bending and shear effective stiffnesses are negligibly small. The next example deals with flexural rovings or preformed fiber bundles with a plane cross-section. These rovings or bundles can slide along each other almost without friction [GOW24]. They slide and rotate around the outer-plane axes until they meet some geometrical constraint. After that, they can either come out of the plane or the rovings can be slightly extended, as shown in Figure 1. The third example is a thin shell with a nearly isotropic structure and non-zero, but small, shear stiffness. It provides coupling between tension and bending (like a Karman plate [GOW20b]). The effective shell is bending-dominated, with only one fold [GOW24], and their position depends on the boundary fixation.
The focus of this paper is woven textiles. We analyse different effective 2D behaviours and, then simulate draping tests with them. For simulations, the software TexMath is employed. It is based on the homogenization and dimension reduction algorithms for shells, yarns, and contacts from [OPS16], [SO17], [GOW24], [GOW20b], [GOW24], [GOW20a].

2. Main physical parameters

The main textile properties influencing the effective textile behaviour are: the tex-tile pattern; the yarn's cross-sectional shape and size; the yarn's elastic properties and pre-strain (defining crimp); the friction coefficient between fibres.

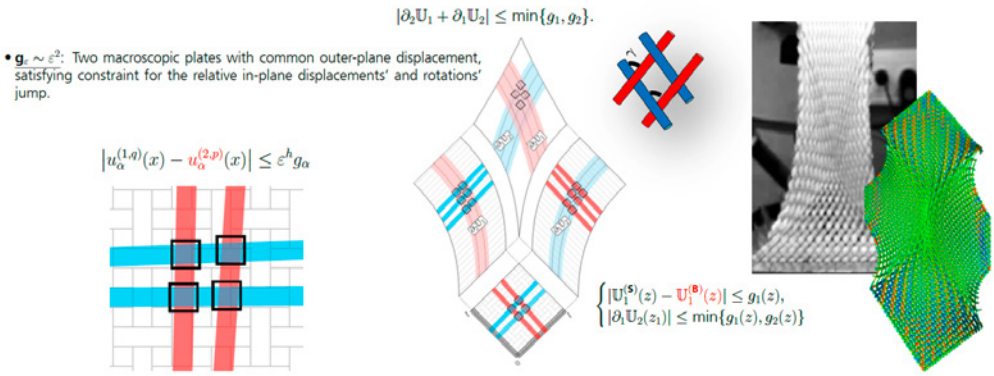

Figure 1: Sliding dominated shear behaviour (two effective plates)

The effective textile behavior depends more on the roving/fiber-bundle properties and cross-section than on the weaving type. Textiles, made of stretchable yarns, provide coupling between tension and transverse deflection for any type of textile patterns. This corresponds to the von Karman regim, [GOW20b], with the homogenized energy

$$\mathscr{J}_{vK}^{hom}(\mathscr{U}) = \frac{1}{2}\int_\Omega \left(a^{hom}_{\alpha\beta\alpha'\beta'}\mathscr{Z}_{\alpha\beta}\mathscr{Z}_{\alpha'\beta'} + b^{hom}_{\alpha\beta\alpha'\beta'}\mathscr{Z}_{\alpha\beta}\,\partial_{\alpha'\beta'}\mathscr{U}_3 + c^{hom}_{\alpha\beta\alpha'\beta'}\partial_{\alpha\beta 3}\,\partial_{\alpha'\beta'}\mathscr{U}_3\right)dx' - \int_\Omega f\cdot\mathscr{U}\,dx',$$

and $\mathscr{Z}_{\alpha\beta} = e_{\alpha\beta}(\mathscr{U}) + \frac{1}{2}\partial_\alpha\mathscr{U}_3\partial_\beta\mathscr{U}_3$. Without last quadratic strain terms, the in-plane and outer-plane energies are decoupled. The opposite type of textiles are those made of flexible yarns rather than stretchable ones. These textiles are bending-dominated and $\mathscr{Z}_{\alpha\beta} = 0$, the isometry condition, means the preserving of mean plane surface measure.

References

[BOP14] Bare, D. Z.; Orlik, J.; Panasenko, G.: Asymptotic dimension reduction of a Robin-type elasticity boundary value problem in thin beams; Applicable Analysis Band:93 (2014) H. 6, S. 1217–1238

[FGO24] Orlik, J., Falconi, R., Griso, G. (2023). Asymptotic behavior for nonlinear textiles with glued yarns. Analysis and Applications.

[FJM06] Friesecke, G., James, R. D., Müller, S. (2006). A hierarchy of plate models derived from nonlinear elasticity by gamma-convergence. Archive for rational mechanics and analysis, 180, 183-236.

[GOW20a] Griso, G.; Orlik, J.; Wackerle, S.: Asymptotic behavior for textiles; SIAM Journal on Mathematical Analysis Band:52 (2020) H. 2, S. 1639–1689

[GOW20b] Griso, G.; Orlik, J.; Wackerle, S.: Asymptotic behavior for textiles in von-Kármán regime Journal de Mathématiques Pures et Appliquées (2020), 144, 164–193

[GOW24] Orlik, J., Falconi, R., Griso, G., Wackerle, S. (2023). Asymptotic behavior for textiles with loose contact. Mathematical Methods in the Applied Sciences, 46(16), 17082-17127.

[OAA+17] Orlik, J.; Andrä, H.; Argatov, I.; Staub, S.: Does the weaving and knitting pattern of a fabric determine its relaxation time?; The Quarterly Journal of Mechanics and Applied Mathematics Band:70 (2017) H. 4, S. 337–361

[OPS16] Orlik, J.; Panasenko, G.; Shiryaev, V.: Optimization of textile-like materials via homogenization and beam approximations; Multiscale Modeling & Simulation Band:14 (2016) H. 2, S. 637–667

[SO17] Shiryaev, V.; Orlik, J.: A one-dimensional computational model for hyperelastic string structures with Coulomb friction; Mathematical Methods in the Applied Sciences Band:40 (2017) H. 3, S. 741–756

ECCOMAS Thematic Conference and IACM Special Interest Conference
Highly Flexible Slender Structures (HFSS 2025)
22–26 September 2025, Kaiserslautern, Germany

Modelling of nonsmooth frictional yarn-to-mandrel contact interactions for braiding simulation

Indrajeet Patil [1,2], Olivier Brüls [1]

[1] Department of Aerospace and Mechanical Engineering, University of Liège, Allée de la Découverte 9, 4000 Liège, Belgium, (ikpatil, o.bruls)@uliege.be

[2] Department of Mathematics for the Digital Factory, Fraunhofer Institute for Industrial Mathematics, Fraunhofer Platz 1, 67663, Kaiserslautern, Germany, indrajeet.krantikumar.patil@itwm.fraunhofer.de

Keywords: Multibody systems, Nonsmooth contact dynamics, Switching constraints, Braiding simulation.

1. Introduction

Braiding is the fundamental process in fabrication of preforms for composite production. On the one end, textile yarns flow from bobbin carriers in a controlled manner, driven by horn gears to form an interlocked mesh. On the other end, yarns undergo contact-friction interactions with the mandrel. The global process interactions are best captured by system-level models. Thus, we propose a multibody framework using Odin [1], where the carriers and the mandrel are modelled as rigid bodies, while the textile yarns are modelled as flexible beams. Phenomena such as tension compensation are modelled using judicious choices of kinematic joints, and carrier motions using switching bilateral constraints. In this work, we focus on the frictional yarn-to-mandrel contact interactions. For this investigation, the winding of a single yarn around the mandrel serves as a representative problem. Using nonsmooth models, the unilateral constraint can be expressed as a Signorini condition together with a Coulomb friction law.

2. Method

To solve the yarn-to-mandrel contact problem, two different approaches are considered in this work. Firstly, the mortar contact element proposed in [2] can be used provided that the yarns and the mandrel are both modelled as beams with circular cross-sections, and friction is neglected. The discrete quasi-static equilibrium is

$$\mathbf{f}^{\text{int}}(q(t)) + \mathbf{G}^T(q(t),t)\boldsymbol{\lambda}(t) = \mathbf{f}^{\text{ext}}(q(t)) \tag{1}$$

$$\mathbf{g}^{\overline{\mathcal{U}}}(q(t),t) = \mathbf{0}_{m\times 1} \tag{2}$$

$$\mathbf{0} \leq \boldsymbol{\lambda}^{\mathcal{U}}(q(t)) \perp \mathbf{g}^{\mathcal{U}}(q(t)) \geq \mathbf{0} \tag{3}$$

where q is the configuration on a Lie group, $\mathcal{U}$ denote the unilateral constraints, $\mathbf{g}^{\mathcal{U}}(q(t))$ is the contact gap, $\boldsymbol{\lambda}^{\mathcal{U}}$ is the normal contact forces, and $\overline{\mathcal{U}}$ are bilateral constraints. The Lagrange multipliers are defined as $\boldsymbol{\lambda} = \begin{bmatrix}\boldsymbol{\lambda}^{\mathcal{U},T} & \boldsymbol{\lambda}^{\overline{\mathcal{U}},T}\end{bmatrix}^T$. In the second approach, the mandrel is modelled as a rigid body, and proxy collision geometries represent the centerline of the yarn. Then, the Bullet library is exploited for collision detection. The time discrete equations are obtained using the nonsmooth generalized-α (NSGA) [3]. For instance at velocity level, the frictional contact problem in the tangential direction is expressed as

$$-(\mathbf{G}_T^j(q_{n+1})\mathbf{v}(q_{n+1}) + e_T^j\mathbf{G}_T^j(q_n)\mathbf{v}(q_n)) \in \partial\psi_{C(\Lambda_N^j(q_{n+1}))} \qquad \text{if } g_N^j(q_{n+1}) \leq 0, \tag{4}$$

where $\mathbf{v}$ is the velocity, $\mathbf{g}^j$ is the relative position for the contact j with the normal component g_N^j and tangential component $\mathbf{g}_T^j$, and e_T^j is the tangential restitution coefficient which is chosen as $e_T^j = 0$ for contact involving flexible bodies. Λ_N^j and $\boldsymbol{\Lambda}_T^j$ are the normal and tangential components of the Lagrange multiplier respectively representing the impulse, $\mathbf{G}_T^j$ is the tangential constraint gradient and $\psi_{C(\Lambda_N^j)}$ is the indicator function of the section of the Coulomb friction cone.

3. Simulation results for winding test

First, using the mortar method, we simulate the winding of a yarn around a cylindrical mandrel as shown in Figure 1a. The properties of the yarn are radius $r_y = 0.001$ m, length $l_y = 2.5$ m, $E = 110$ GPa, $\mu = 0.23$. The

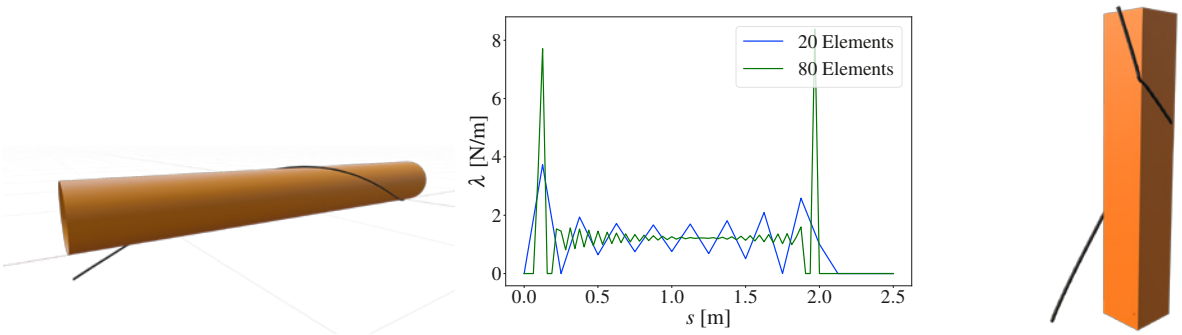

(a) (b) (c)

Figure 1: (a), (b) Winding test on cylindrical mandrel using frictionless mortar approach: mesh size variation for Lagrange multiplier λ. (c) Winding test on rectangular mandrel using the frictional collocation approach.

properties of the mandrel are radius $r_m = 0.03$ m, length $l_m = l_y = 2.5$ m, $E = 210$ GPa, $\nu = 0.21$. Both the yarn and the mandrel are discretized using 20 beam finite elements. The simulation consists of 650 load steps, with a load increment applied every 0.01 fraction of the total process. Figure 1b shows the resulting evolution of the normal contact Lagrange multiplier λ as a function of the arc length parameter s. Numerical oscillations are expected from a finite element discretization [2]. The mortar method can handle nonsmooth distributed contact forces, but at the cost of oscillations. We compare the results obtained by using mesh sizes of 20 and 80 elements. The amplitude of the oscillations in the Lagrange multipliers decreases significantly for the mesh size of 80 elements. For the moment, the mortar formulation is not combined with a collision detection procedure, which limits the applicability to larger problems. Also, our current implementation is limited to beams with cylindrical cross-section and frictionless contacts.

Second, using the collocation approach and proxy collision elements, one can further extend this analysis by considering general mandrel shapes (having convex and concave contours) and friction. For instance, Figure 1c shows a textile yarn winding around a rectangular mandrel.

4. Conclusion

The mortar method is a viable choice to solve the yarn-to-mandrel contact problem, but it requires some extension for the simulation of general cases. The collocation method with proxy collision elements can efficiently deal with frictional contact, arbitrary mandrel shapes, and can accomodate a high number of yarns.

Acknowledgments

This project has received funding from the European Union's Horizon 2020 research and innovation programme under the Marie Sklodowska-Curie grant agreement No 860124. The present paper only reflects the author's view. The European Commission and its Research Executive Agency (REA) are not responsible for any use that may be made of the information it contains.

References

[1] A. Cosimo, O. Brüls. *Odin*, GitLab repository, `https://gitlab.uliege.be/am-dept/odin`, 2022. `https://doi.org/10.5281/zenodo.7468114`

[2] A. Bosten, A. Cosimo, J. Linn, O. Brüls. *A mortar formulation for frictionless line-to-line beam contact*, Multibody System Dynamics, 54(1) (2022) 31–52.

[3] A. Cosimo, J. Galvez, F. J. Cavalieri, A. Cardona, O. Brüls. *A robust nonsmooth generalized-α scheme for flexible systems with impacts*, Multibody System Dynamics, 48(2) (2020) 127–149.

ECCOMAS Thematic Conference and IACM Special Interest Conference
Highly Flexible Slender Structures (HFSS 2025)
22–26 September 2025, Kaiserslautern, Germany

Geometric Algebra: a new Language for Flexible Multibody Dynamics and Robotics

Olivier A. Bauchau

University of Maryland, obauchau@umd.edu

Keywords: Geometric Algebra, Multibody Dynamics, Slender Structures

1. Introduction

Flexible multibody systems [1] are characterized by two distinguishing features: system components undergo finite motions and these components are connected by mechanical joints that impose restrictions on their relative motion. Clearly, kinematics plays a fundamental role in the analysis of these systems: it is required to describe the arbitrary motion of system components and is needed once again to evaluate the finite relative motion of these components where they are connected by mechanical joints. Hence, it is not surprising that numerous kinematics formulations have been used to describe multibody systems, in an effort to achieve simplicity of the formulation, freedom from singularities, and computational efficiency. The same remarks apply to robotics although many components of such systems are often assume to remain rigid.

2. Geometric algebra

Geometric algebra is a mathematical framework that provides an elegant, singularity free description of geometrical entities such as points, lines, and planes. These geometric entities can be moved in space via reflections, translations, rotations, and motions operations that are based on the "geometric product," a mathematical operation that involves algebraic manipulations only. Geometric algebra originates in the work of Grassmann [2] who introduced the concepts of vector spaces and wedge products. Clifford [3, 4] generalized the concepts introduced by Grassmann into what is now referred to as Clifford algebras and developed bi-quaternions [5] to handle rigid-body motions. Their work attracted little attention in the physics and engineering communities until Hestenes [6] showed the relevance of Clifford algebras to many problems of physics. Although it has received little attention in flexible multibody dynamics and robotics, geometric algebra is widely used in computer graphics.

Based on the work of Porteous [7], Selig [8] proposed a Clifford algebra of planes, lines, and points that can deal with rigid-body motion in an elegant manner. In fact, some of these concepts were already presented by Clifford [5]. The formalism was further refined by Gunn [9, 10] who called the algebra *Projective Geometric Algebra* (PGA) and underlined its numerous advantages.

Dorst et al. [11] studied *Conformal Geometric Algebra* (CGA) extensively. In CGA, circles and spheres are basic elements of the algebra in addition to planes, lines, and points but this generality comes at a price, the size of the algebra is doubled, together with computational and storage requirements. The analysis of typical multibody systems does not seem to call for the generality and complexity of CGA and hence, this paper focuses on the foundations of PGA. Dorst and De Keninck [12] provide a detailed description of PGA, which they call *Plane-Based Geometric Algebra*, rather than "projective geometric algebra." Finally, the same authors [13] have shown how PGA can be used to formulate rigid-body dynamics problems. Although it has received little attention in multibody dynamics and robotics, geometric algebra is widely used in computer graphics.

Plane-based geometric algebra brings together within the same formulation many tools that have been used previously in multibody dynamics such as quaternions and bi-quaternions or dual numbers and vectors. It provides a complete description of the kinematics of multibody systems and is already used in computer graphics and animation. All operations are performed using algebraic manipulations only and singularities are avoided altogether.

Cartan–Dieudonné's theorem, which states that orthogonal transformations are obtained from successive reflections, gives geometric algebra a sound mathematical foundation. Whereas traditional approaches to kinematics favor the geometric reasoning provided by Euler's theorem on rotation and Mozzi–Chasles theorem, geometric algebra emphasizes algebra over geometry. Recent papers by Bauchau [14, 15] have shown that geometric

algebra is a sound basis for describing the kinematics of multibody systems and for performing all required operations on the relevant geometric entities.

3. Flexible multibody dynamics with geometric algebra

This paper will present the finite element implementation of structural elements typically found in flexible multibody dynamics analysis tools. Throughout the formulation, the kinematics of the system is represented using geometric algebra. First, the formulation of each structural element is developed within the formalism of geometric algebra. Second, the governing equations for each structural element are expressed in terms of geometric algebra operations only. Finally, the finite element method in time is used to discretize the various elements in space and time simultaneously. It will be shown that the interpolation of motion is handled elegantly by the geometric algebra formalism.

A flexible multibody dynamics analysis tool based on the geometric algebra formalism will be presented and its predictions will be compared with those of more traditional analysis methods. In all cases, excellent correlation is observed. Clearly, geometric algebra is an ideal formalism for the description of the kinematics of flexible multibody systems, the derivation of the governing equations, and their finite element implementation.

References

[1] O. A. Bauchau. *Flexible Multibody Dynamics*, volume 176 of *Solid Mechanics and Its Applications*. Springer Netherlands, Dordrecht, 2011.

[2] J. Browne. *Grassmann Algebra. Vol. I: Foundations*. Barnard Publishing, Eltham, Australia, 2012.

[3] W. K. Clifford. *Mathematical Papers*. Macmillan, London, 1882. Tucker, R. (Ed.).

[4] D. J. H. Garling. *Clifford Algebras: An Introduction*, volume 78. Cambridge University Press, 2011. London Mathematical Society Student Texts.

[5] W. K. Clifford. A preliminary sketch of biquaternions. *Proceedings of the London Mathematical Society*, s1-4:381–395, 1871.

[6] D. Hestenes and G. Sobczyk. *Clifford Algebra to Geometric Calculus*. D. Reidel, Dordrecht, Boston, Lancaster, Tokyo, 1984.

[7] I. R. Porteous. *Topological Geometry*. Cambridge University Press, Cambridge, second edition, 1981.

[8] J. M. Selig. Clifford algebra of points, lines and planes. *Robotica*, 18(5):545–556, September 2000.

[9] C. Gunn. Doing Euclidean plane geometry using projective geometric algebra. *Advances in Applied Clifford Algebras*, 27(2):1203–1232, 2017.

[10] C. Gunn. Geometric algebras for Euclidean geometry. *Advances in Applied Clifford Algebras*, 27(1):185–208, 2017.

[11] L. Dorst, D. Fontijne, and S. Mann. *Geometric Algebra for Computer Science: An Object-oriented Approach to Geometry*. Morgan Kaufman, 2009.

[12] L. Dorst and S. De Keninck. Guided tour to the plane-based geometric algebra PGA (version 2.0), 2022. URL: bivector.net/PGA4CS.html.

[13] L. Dorst and S. De Keninck. May the forque be with you. Dynamics in PGA, 2023. URL: bivector.net/PGADYN.html.

[14] O. A. Bauchau. Geometric algebra for multibody dynamics. Part I: Elements of geometric algebra. *ASME Journal of Computational and Nonlinear Dynamics*, April 2025. On line: https://doi.org/10.1115/1.4067155.

[15] O. A. Bauchau. Geometric algebra for multibody dynamics. Part II: Applications. *ASME Journal of Computational and Nonlinear Dynamics*, April 2025. On line: https://doi.org/10.1115/1.4067156.

ECCOMAS Thematic Conference and IACM Special Interest Conference
Highly Flexible Slender Structures (HFSS 2025)
22–26 September 2025, Kaiserslautern, Germany

Finding Indicators for the Influence of Constraints Induced by Kinematic Assumptions Using the Example of the Euler-Bernoulli Hypothesis

Jonas Boungard [1], Jens Wackerfuß [1]

[1] Institute of Structural Analysis, University of Kassel, boungard@uni-kassel.de, wackerfuss@uni-kassel.de

Keywords: kinematic assumptions, constraint forces, nonlinear multi-points constraints, master-slave elimination

1. Introduction

Beam models rely on kinematic assumptions that restrict the possible deformations and describe the structural behaviour using a reduced set of parameters, i.e. the kinematics of the reference axis. While these assumptions allow for a drastic reduction in computational complexity, they also act as kinematic constraints. A beam model inherently satisfies these constraints, but when its results are compared to a more detailed continuum model without constraints, deviations can be observed. In many cases, these deviations remain within acceptable limits, and beam models provide an accurate and efficient representation of the structural behaviour. Yet, there are scenarios where the standard kinematic assumptions are ill suited, leading to significant errors [1]. Although this phenomenon is well known, no method has been developed to generally quantify the influence of the kinematic assumptions on the local and global structural behaviour. Such a method is of great interest because it allows the adequate selection of kinematic assumptions and the corresponding beam theory for each part of the structure. As a basis for the method, indicators for the influence of constraints induced by kinematic assumptions are required.

2. Objectives

The main objective of this contribution is to explicitly quantify the influence of constraints induced by kinematic assumptions and finding indicators to characterize this influence. For this, the study focuses on the kinematic assumptions of the Euler-Bernoulli hypothesis as a proof of concept.

3. Methodology

To measure the influence of constraints induced by kinematic assumptions in beam models, three different modelling approaches are compared in a numerical study: (1) a classical beam model following Euler-Bernoulli hypothesis, (2) a continuum model without additional constraints, serving as a reference solution, (3) a continuum model incorporating multi-point constraints to enforce one or more kinematic assumptions. These models are computed for both the geometrically linear and nonlinear case. Additionally, the following material models are varied: (a) linear isotropic elasticity, (b) hyperelasticity, (c) plasticity. Different sets of multi-point constraints are employed to model the three kinematic assumptions of Euler-Bernoulli hypothesis separately: ① cross-section keeps same dimensions, ② plane cross-section remains plane, ③ cross-section remains perpendicular to the beam's reference axis. These constraints are systematically varied and combined to analyse their individual and collective effects. The primary measure of constraint influence is the constraint forces induced in the continuum model. Since a large number of nonlinear constraints are introduced, an efficient master-slave elimination scheme is employed for their handling [2]. This approach reduces computational cost while maintaining accuracy. Furthermore, different indicators are introduced and their capability to systematically measure the impact of different kinematic assumptions is compared.

4. Results

As a prove of concept, a roll-up of a beam with rectangular cross section is used, see Fig. 1. The load is applied once via rotation control and once via load control. The beam is discretized using 40 geometrical exact planar Timoshenko beam elements as well as 40×4 geometrical nonlinear quadrilateral EAS elements. The kinematic assumptions ①, ② and ③ are modeled using multi-point constraints. The numerical results are depicted in Fig. 2 and 3.

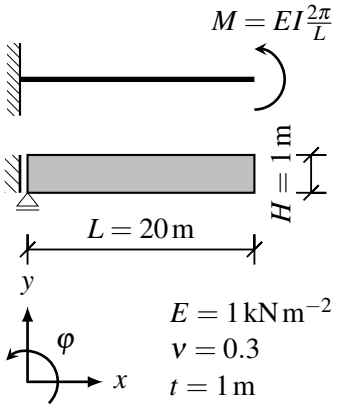

Figure 1: Geometry and parameters.

	Model						
	ana.	(1)	(2)	(3)	(4)	(5)	(6)
	load controlled, i.e. moment applied and rotation calculated						
$\varphi/2\pi$ [rad]	1	1.0000	1.0498	1.0497	1.0365	1.0365	1.0365
	rotation controlled, i.e. rotation applied and moment calculated						
M [kNm]	2.6180	2.6180	2.5049	2.5050	2.5320	2.5322	2.5321

Figure 2: Summary of results for load and rotation control. Model number see Fig. 3

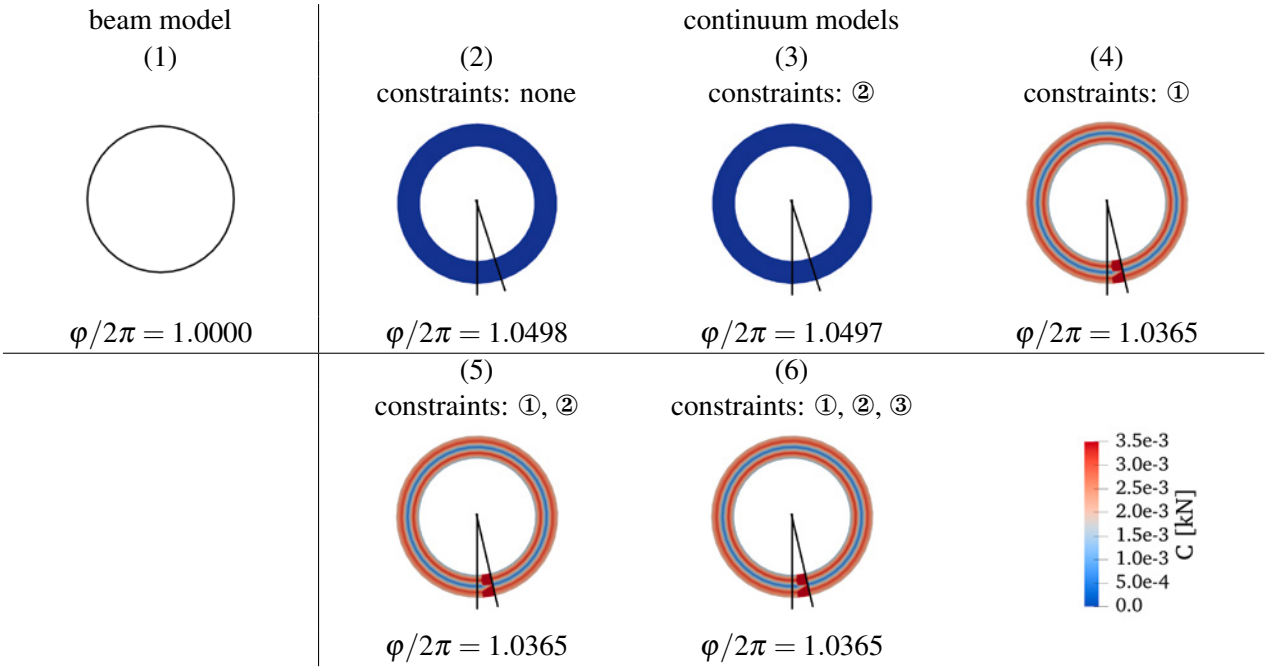

Figure 3: Deformed meshes and constraint forces $C = \sqrt{C_x^2 + C_y^2}$ for load control using different kinematic assumptions. The deep red part are artifacts due the modeling of the moment load.

Enforcing ② '*plane cross sections*' does not induce constraint forces. This shows that for pure bending moment, this kinematic assumption is valid. Enforcing solely ① '*inextensible cross sections*' as well as enforcing it mutually to other assumptions of Timoshenko respectively Euler-Bernoulli theory induces small constraint forces C. This illustrates that this kinematic assumption would be violated if it is not enforced. However, for pure bending it is of neglectable influence. For different types of loading, materials or cross section, the model could exhibit other constraint forces. The numerical results reveal that the constraint forces induced by enforcing kinematic assumptions of beam theories are an indicator for the validity of these assumption.

References

[1] P. Heylinger. *When beam theories fail*, Journal of Mechanics of Materials and Structures, 8.1 (2013) 15-35

[2] J. Boungard, J. Wackerfuß. *Master-slave elimination scheme for arbitrary smooth nonlinear multi-point constraints*, Computational Mechanics, 74.5 (2024) 955-992

ECCOMAS Thematic Conference and IACM Special Interest Conference
Highly Flexible Slender Structures (HFSS 2025)
22–26 September 2025, Kaiserslautern, Germany

A mixed finite element formulation for nonlinear elastodynamic beam structures with extensible directors: energy-momentum consistent scheme

Myung-Jin Choi [1*], Sven Klinkel [1], Simon Klarmann [1], Roger A. Sauer [2,3,4]

[1] Chair of Structural Analysis and Dynamics, RWTH Aachen University, Germany
[2] Institute for Structural Mechanics, Ruhr University Bochum, Germany
[3] Faculty of Civil and Environmental Engineering, Gdańsk University of Technology, Poland
[4] Department of Mechanical Engineering, Indian Institute of Technology Guwahati, India
∗ Corresponding author (choi@lbb.rwth-aachen.de)

Keywords: Beams, Extensible directors, Configuration constraints, Implicit dynamics, Cross-sectional warping

1. Introduction

We aim to develop an efficient and accurate beam model with cross-sectional deformations, and stability in long-term dynamics. Here, we present a numerical method for coupling beams at an arbitrary point along the axis. The beam kinematics is based on extensible directors along the transverse directions, which allow constant in-plane cross-sectional strains, and the associated three-dimensional stress state. The higher-order cross-sectional strains like warping can be enriched using an enhanced assumed strain method up to an arbitrary order, without increasing the number of global degrees-of-freedom (DOFs) [1, 2]. Here, for straightforwardly implementing various joint conditions in an algebraic manner, we further introduce independent rotation, translation, and stretching DOFs of the cross-section at a given arbitrary point along the axis. We present several numerical examples to verify the present method.

2. Theory

In the first-order beam kinematics, the current position of a material point is expressed by

$$\boldsymbol{x}(\zeta^1,\zeta^2,s,t) = \boldsymbol{\varphi}(s,t) + \sum_{\alpha=1}^{2} \zeta^\alpha \boldsymbol{d}_\alpha(s,t), \tag{1}$$

where $\boldsymbol{\varphi}(s,t) \in \mathbb{R}^3$ denotes the position of the axis, and the cross-section is spanned by two directors $\boldsymbol{d}_\alpha(s,t) \in \mathbb{R}^3$ ($\alpha \in \{1,2\}$) along which we define the transverse coordinates ζ^1 and ζ^2, and $s \in [0,L]$ denotes the arc-length coordinate of the initial axis whose length is L, and t denotes time. In order to have invariance of approximated strains under rigid body rotation, we directly approximate the director vectors, without any rotation parameters. For the discussion of objectivity, interested readers may refer to [2], and references therein. In order to implement joint conditions, we introduce new independent kinematic DOFs for the cross-section at an arbitrary point along the axis, which are the position vector, $\bar{\boldsymbol{\varphi}} \in \mathbb{R}^3$, the rotation tensor, $\bar{\boldsymbol{\Lambda}} \in \mathrm{SO}(3)$, and two logarithmic stretches $\bar{\boldsymbol{\mu}} = \left[\bar{\mu}^1, \bar{\mu}^2\right] \in \mathbb{R}^2$. It is based on a Lagrange multiplier method, which was also utilized for implementing an interface between beam and brick elements, see e.g., [3, Section 6.3]. At a given point $s = \bar{s}$ along the beam's axis, we have the following two constraints:

$$\begin{cases} \boldsymbol{\Phi}_0(\boldsymbol{\varphi},\bar{\boldsymbol{\varphi}}) := \boldsymbol{\varphi}(\bar{s}) - \bar{\boldsymbol{\varphi}} = \boldsymbol{0}, \\ \boldsymbol{\Phi}_\alpha(\boldsymbol{d}_\alpha,\bar{\boldsymbol{\Lambda}},\bar{\mu}_\alpha) := \boldsymbol{d}_\alpha(\bar{s}) - \lambda_\alpha(\bar{\mu}_\alpha)\bar{\boldsymbol{t}}_\alpha = \boldsymbol{0},\ \alpha = 1,2, \end{cases} \tag{2}$$

with the unit directors $\bar{\boldsymbol{t}}_\alpha \in \mathbb{R}^3$ parameterized by the rotation tensor $\bar{\boldsymbol{\Lambda}} \in \mathrm{SO}(3)$ at the joint, as

$$\bar{\boldsymbol{t}}_\alpha = \bar{\boldsymbol{\Lambda}}\boldsymbol{D}_\alpha(\bar{s}),\ \alpha = 1,2. \tag{3}$$

Here, $\boldsymbol{D}_\alpha(s) \in \mathbb{R}^3$ denotes the given initial unit director field, and the scalar function $\lambda_\alpha(\bar{\mu}_\alpha) := e^{\bar{\mu}_\alpha} > 0$ denotes the associated stretch ratios of the directors. Then, we define an augmented Lagrangian functional, considering the constraints in Eq. (2), as

$$\mathbb{L} := \mathcal{L} - \boldsymbol{\lambda}^0 \cdot \boldsymbol{\Phi}_0 - \sum_{\alpha=1}^{2} \boldsymbol{\lambda}^\alpha \cdot \boldsymbol{\Phi}_\alpha. \tag{4}$$

For the detailed expression of the Lagrangian $\mathcal{L}$, and the subsequent formulation, one may refer to [2].

3. Numerical example: Bending-twisting column in dynamics

We consider a bending-twisting column under an initial velocity condition, which consists vertical and horizontal beams, which are rigidly connected to each other. An initial velocity condition is applied along the vertical and horizontal beams, which are $\boldsymbol{V}_1 = 10^2 Z \boldsymbol{e}_1$ [m], and $\boldsymbol{V}_2 = 10^2 Y \boldsymbol{e}_1$ [m], respectively, where $\boldsymbol{e}_1$ denotes the global Cartesian basis along the X-axis, see Fig. 1a for the initial geometry and velocity. Here, we consider a St. Venant-Kirchhoff material with Young's modulus $E = 210\,\text{GPa}$, and Poisson's ratio $\nu = 0.3$. Fig. 1b shows the deformed configurations, and Fig. 2 shows the history of total energy, calculated using the present energy-momentum consistent (EMC) scheme, which shows the (algorithmic) conservation of total energy, using the uniform time increment $\Delta t = 0.1\,\text{s}$.

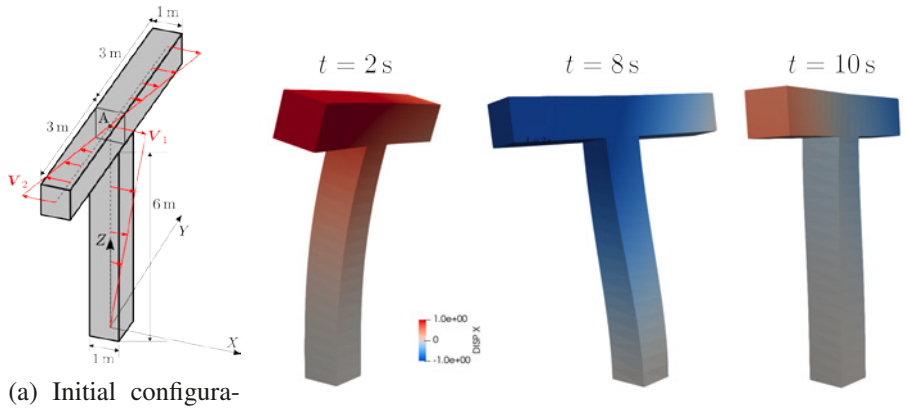

(a) Initial configuration

(b) Deformed configurations

Figure 1: Twisting column. Initial velocity field, and deformed configurations at several time instants.

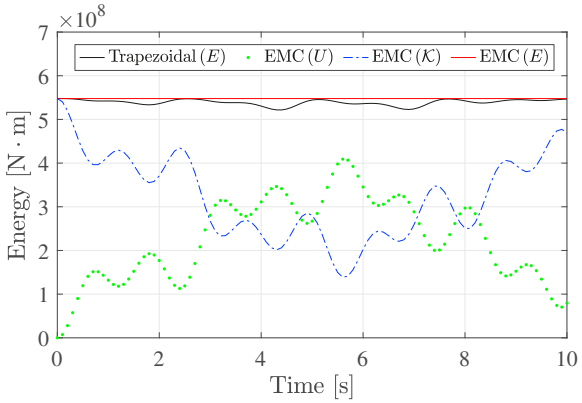

Figure 2: Time history of total energy. U, $\mathcal{K}$, and E denote the strain, kinetic, and total energies, respectively.

Acknowledgments

M.-J. Choi was supported by the German Research Foundation (DFG) - Project number 523829370.

References

[1] J Wackerfuß and F Gruttmann. A mixed hybrid finite beam element with an interface to arbitrary three-dimensional material models. *Comput Methods Appl Mech Eng*, 198(27-29):2053–2066, 2009.

[2] M.-J. Choi, S Klinkel, S Klarmann, and R A. Sauer. An objective isogeometric mixed finite element formulation for nonlinear elastodynamic beams with incompatible warping strains. *Multibody Syst Dyn*, pages 1–54, 2024.

[3] Simon Klarmann. Geometrisch und physikalisch nichtlineare mehrskalenmodellierung räumlicher stabtragwerke. Technische Universität Darmstadt, 2018.

ECCOMAS Thematic Conference and IACM Special Interest Conference
Highly Flexible Slender Structures (HFSS 2025)
22–26 September 2025, Kaiserslautern, Germany

Coupling of solid and beam elements with heterogeneous cross-sections

S. Klarmann [1], J. Wackerfuß [2], S. Klinkel [3]

[1] Lehrstuhl für Baustatik und Baudynamik, RWTH Aachen University, klarmann@lbb.rwth-aachen.de
[2] Institut für Baustatik und Baudynamik, Universität Kassel, wackerfuss@uni-kassel.de
[3] Lehrstuhl für Baustatik und Baudynamik, RWTH Aachen University, klinkel@lbb.rwth-aachen.de

Keywords: beam-solid coupling, heterogeneous cross-sections, warping, mixed finite elements

1. Introduction

The contribution deals with the coupling of a structural beam element with a continuum element. The objective of the contribution is a constraint-free transition between structure and continuum. In the frame of a substructure model, it offers the application of efficient beam elements in a broad range of the model while being able to resolve details with continuum elements [1]. A recent publication [2] picked up the topic and proposed an element formulation which acts only on the surface of the solid model. It covers layered cross-sections but requires the material properties from the point of view of the boundary of the continuum model. Our new approach aims to resolve the issue of heterogeneous cross-sections while maintaining the advantage of evaluating of the material law with the full strain state, such that any material can be applied at the interface. Furthermore, it is not required to know any information about cross-sectional properties as the provided information for the element is just the geometrical model and the assignment of the material properties.

2. Theory

To investigate the problem, we consider a mixed model with a 2D Timoshenko beam and 2D continuum elements. The difficulty connecting them lies in the different kinematic assumptions. The continuum theory at the solid side contains a full displacement state over the cross-section, while the beam theory allows for constant (in case of axial and tangential directions) and linear distributions (in case of axial direction) of the displacements only. In order to couple them and avoid spurious stresses at the interface, the 'beampart' of the deformations need to be enriched by suitable warping deformations. To achieve the coupling and allow the correct warping deformations, we use the following weak form of a mixed formulation in the transition zone:

$$g = \int_\Omega \underbrace{\delta\boldsymbol{\varepsilon}^g \cdot \boldsymbol{\sigma}^p}_{VI}\,\mathrm{d}\Omega + \int_\Omega \delta\boldsymbol{\sigma}^p \cdot \underbrace{\left(\varepsilon^B + \boldsymbol{\varepsilon}^\omega - \boldsymbol{\varepsilon}^p\right)}_{II}\,\mathrm{d}\Omega + \int_\Omega \delta\boldsymbol{\varepsilon}^p \cdot \underbrace{\left(\mathbf{C}\boldsymbol{\varepsilon}^p - \boldsymbol{\sigma}^p\right)}_{IV}\,\mathrm{d}\Omega$$
$$+ \int_\Omega \delta\boldsymbol{\sigma}^B \cdot \underbrace{\left(\boldsymbol{\varepsilon}^g - \boldsymbol{\varepsilon}^B\right)}_{I}\,\mathrm{d}\Omega + \int_\Omega \delta\boldsymbol{\varepsilon}^B \cdot \underbrace{\left(\boldsymbol{\sigma}^p - \boldsymbol{\sigma}^B\right)}_{V}\,\mathrm{d}\Omega + \int_\Omega \underbrace{\delta\boldsymbol{\varepsilon}^\omega \cdot \boldsymbol{\sigma}^p}_{III}\,\mathrm{d}\Omega.$$

Herein, $\boldsymbol{\varepsilon}^g$ are the geometric strains resulting from a linear interpolation between the continuum and beam displacements in the interface domain [1]. These geometric strains are bound to the beam strains $\boldsymbol{\varepsilon}^B$ enforced in an average way by the beam stress resultants $\boldsymbol{\sigma}^B$ (I). The beam strains determine the physical strain state $\boldsymbol{\varepsilon}^p$ by enriching them with additional warping strains $\boldsymbol{\varepsilon}^\omega$ (II). The physical stresses $\boldsymbol{\sigma}^p$ enforce the equality between these strains. Furthermore, the physical stresses should not introduce any additional work with the introduced warping strains (III). Classical material laws map the physical strains $\boldsymbol{\varepsilon}^p$ to the physical stresses $\boldsymbol{\sigma}^p$, here depicted for the linear elastic case (IV). The beam stress resultants $\boldsymbol{\sigma}^B$ can be calculated from the physical stresses $\boldsymbol{\sigma}^p$ (V) but are not required for the element formulation. Finally, the physical stresses $\boldsymbol{\sigma}^p$ enter the weak form of equilibrium (VI). They ensure the coupling between the continuum and the beam model and lead to the desired stress distribution over the height of the cross-section. The weak form is solved within the finite element method framework.

3. Numerical example

A layered beam as depicted in fig. 1 is considered to show the capabilities of the proposed transition element. Its left side is fully clamped and the right side is clamped, but can move in vertical direction. On the right side

a single force F is applied. The beam's cross-section consists of three layers with different heights h_1, h_2, and h_3. The material properties are choosen such that the core is much softer than the outer layers.

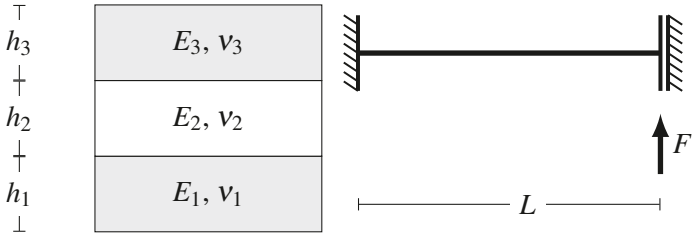

Figure 1: System and cross-section of a layered beam with load.

It is important to note that the structure is modelled with standard Q1 2D continuum elements. On both ends of the beam, the proposed transition element is used to apply the boundary conditions. Due to the system's structure and loading, both ends are subjected to a shear force and a bending moment. With the given material properties, both ends show a significant warping deformation.

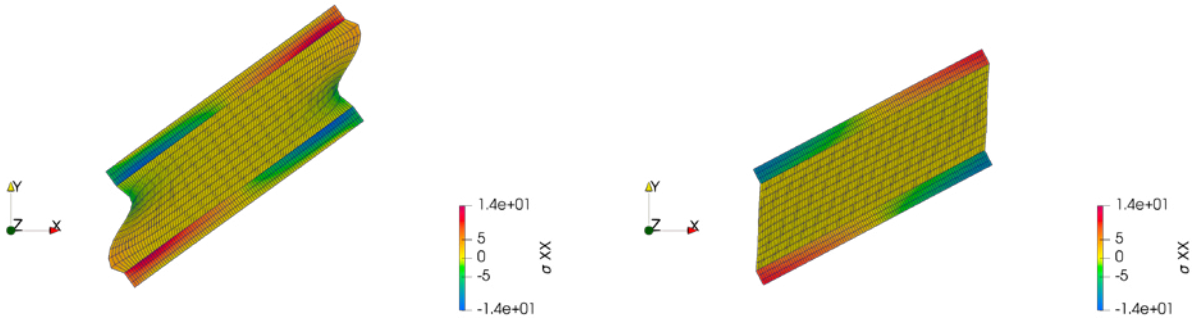

Figure 2: Comparison of [1] (left) and present transition element (right).

For $E_1 = E_3 = 10000$ and $E_2 = 10$, $\nu_1 = \nu_2 = \nu_3 = 0.3$, $h_1 = h_2 = 0.125$ and $h_3 = 0.75$ as well as $L = 2$, the deformed mesh with the normal stresses is depicted in fig. 2. On the left side, the results with the old interface element formulation [1] show a significant distortion on the boundary of the continuum elements. This impacts the quality of the approximation of the normal stresses and leads to wrong results. In contrast, the present formulation shows a much better approximation of the deformation state and represents the normal stresses in the expected way.

4. Conclusions

This contribution presents a modified version of the interface element presented in [1]. The present formulation has the advantage that the kinematic relations are more concise than in the previous approach and that warping shapes enrich the beam strains instead of introducing fictitious correction strains. The numerical example shows significant improvement in the case of heterogeneous cross-sections. In the present version, the use of nonlinear material laws within the interface element remains straightforward and the information provided by the user is the same as that of the classical continuum elements.

References

[1] S. Klarmann, J. Wackerfuß, S. Klinkel. *Coupling 2D continuum and beam elements: a mixed formulation for avoiding spurious stresses*, Computational Mechanics, 70 (2022) 1145-1166

[2] Francesc Turon, Fermin Otero, Alex Ferrer, Xavier Martinez . *Definition of a beam-like reduced order model element by means of a mixed dimensional coupling*, Computers and Structures, 302 (2024) 107466

ECCOMAS Thematic Conference and IACM Special Interest Conference
Highly Flexible Slender Structures (HFSS 2025)
22–26 September 2025, Kaiserslautern, Germany

Modelling of fibre-matrix bonding in cable-reinforced elastomer composites

Valentin Poussard [1], Damien Durville [2]

[1] Michelin, Research Center, valentin.poussard@michelin.com
[2] CentraleSupélec, ENS Paris-Saclay, CNRS, damien.durville@centralesupelec.fr

Keywords: Fibre-matrix bonding, Incompatible meshes, 3D-1D junction elements

1. Introduction

Cable-reinforced elastomer composites are used in various applications, such as tires or conveyor belts. Depending on the spacing between steel wires in the cable architecture, the elastomeric matrix may penetrate inside the cable reinforcement, endowing it with special properties. The mechanical response of such a composite is found to be strongly dependent on the behaviour of the small volumes of quasi-incompressible matrix enclosed between wires, called menisci, or enclosed in the core of the cable. Because of the very small dimensions of the matrix volumes between the wires, employing compatible 3D solid finite element meshes to discretise the matrix and the wires would result in simulations with prohibitive computational costs.

One potential solution to this issue involves the utilisation of 1D beam elements to model the steel wires, and standard 3D solid elements for the matrix. Using incompatible meshes for the wires and the matrix eliminates the need for meshing the geometrically complex interface between both components. Nevertheless, the bond between the wires and the matrix still needs to be taken into account. Previous approaches, for example using a mortar method to account for this bonding, have been proposed [1, 2]. The present approach, employing the general methodology developed for cables and fibrous structures, based on an implicit solver and implemented in the Multifil code [3], is based on the implementation of discrete structural elements, named junction elements. These junction elements are distributed on the surface of wires and couple two material particles, one attached to the wire and the other to the matrix.

2. Junction elements

The underlying principle of the method is to couple displacements of the wires and the matrix at the location of discrete junction elements by modelling a rigidity between the two material particles constituting the element, one attached to a wire, and the other to the matrix. The junction elements are evenly distributed on the contour of cross-sections at nodes of the beam elements (Figure 1.(a)). The I-th junction element is first defined by a material particle, denoted $\boldsymbol{\xi}_I^W$ located on the cross-section of a beam node, and the corresponding material particle $\boldsymbol{\xi}_I^M$ located at the same position in the initial configuration in the matrix is then looked for. For each element a penalty junction energy W_J is added to the system, expressed as:

$$W_J\left(\boldsymbol{\xi}_I^M, \boldsymbol{\xi}_I^M\right) = \frac{k_I}{2}\left(\boldsymbol{x}\left(\boldsymbol{\xi}_I^M\right) - \boldsymbol{x}\left(\boldsymbol{\xi}_I^M\right)\right)^2, \tag{1}$$

where $\boldsymbol{x}\left(\boldsymbol{\xi}_I^M\right)$ is the current position of particle $\boldsymbol{\xi}_I^M$ and k_I is the rigidity associated to the element.

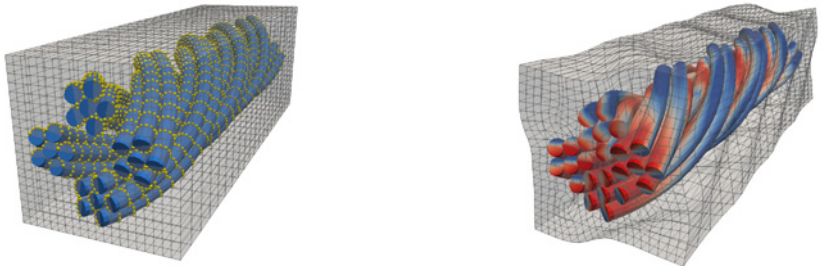

(a) (b)

Figure 1: (a) Initial configuration with junction elements (yellow spheres) – (b) Deformed configuration under a tensile load.

The location of these discrete junction elements, their number and their associated rigidity have large influence on the obtained results. These aspects will be discussed. In particular, it will be shown that excessive junction rigidities may induce locking phenomena in the matrix elements, depending on the dimensions of these elements with respect to the diameters of wires.

3. Identification of the rigidities of junction elements

As the rigidity of junction elements can significantly impact the results, a study was conducted to evaluate the appropriate value for this parameter. To this end, simulations were performed in which the displacement of a wire embedded in a volume of elastomer with fixed borders was analysed to determine the resistance of the matrix to this displacement, expressed in terms of rigidity (Figure 2.(a)). The variation of this rigidity as a function of the ratio of the elastomer volume width L to the wire diameter D was identified (Figure 2.(b)).

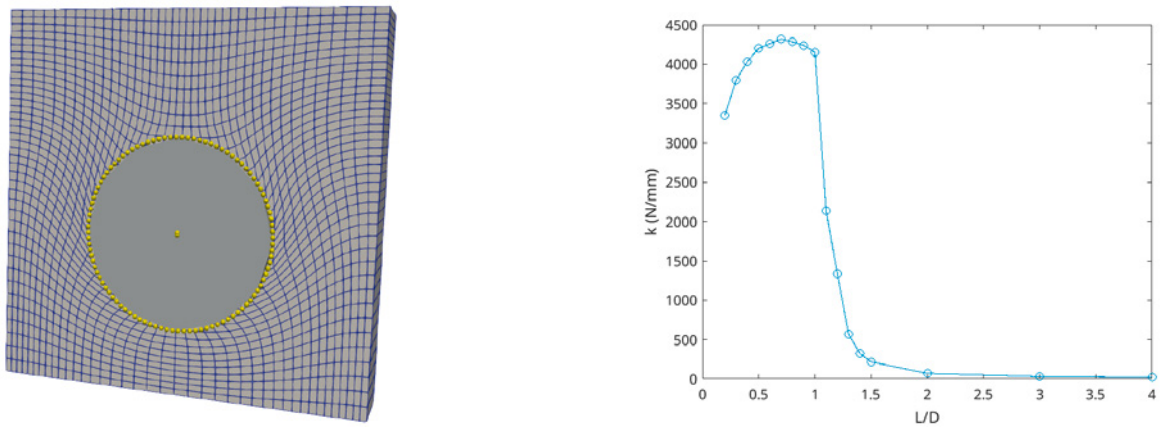

(a) (b)

Figure 2: (a) Displacement of a wire in a fixed elastomer volume – (b) Resistance to the wire's displacement as a function of $\frac{L}{D}$.

4. Results

The implementation of the identified junction rigidities allows the results of tensile tests (Figure 1.(b)) to be much less dependent on the discretisation size of the matrix mesh. Detailed results and comparisons with experimental measurements will be presented to discuss the validity of the present approach.

References

[1] Ivo Steinbrecher, Matthias Mayr, and Maximilian J. Grill. A mortar-type finite element approach for embedding 1d beams into 3d solid volumes. *Computational Mechanics*, pages 1377–1398, 2020.

[2] Ivo Steinbrecher, Alexander Popp, and Christoph Meier. Consistent coupling of positions and rotations for embedding 1d cosserat beams into 3d solid volumes. *Computational Mechanics*, 69:701–732, 2022.

[3] Damien Durville. Contact-friction modeling within elastic beam assemblies: an application to knot tightening. *Computational Mechanics*, 49:687–707, 2012.

ECCOMAS Thematic Conference and IACM Special Interest Conference
Highly Flexible Slender Structures (HFSS 2025)
22–26 September 2025, Kaiserslautern, Germany

Modeling and Simulation of the Winding Process for Electric Motor Rotors

Giacomo Crippa [1,2], Damien Durville [1]

[1] Université Paris-Saclay, CentraleSupélec, ENS Paris-Saclay, CNRS, LMPS - Laboratoire de Mécanique Paris-Saclay, 3 rue Joliot-Curie, Gif-sur-Yvette 91190, France,
{giacomo.crippa, damien.durville} @centralesupelec.fr
[2]Conception et développement des véhicules, moteurs et boîtes de vitesse, Technocentre Renault, 1 Av. du Golf, 78280 Guyancourt

---

Keywords: Finite Element Analysis, Winding, Copper Wire Deposition, Electrically Excited Synchronous Motor, Beam Model, Frictional Contact Interactions

1. Introduction

The transition to zero-emission vehicles by 2035 imposed by the European Union has intensified the need for sustainable electric motor technologies. A significant advancement in the field is the Electrically Excited Synchronous Motor (EESM) developed by Renault, which replaces permanent magnets in the rotor with a copper wire, wound with a nozzle that moves around the rotor core (ferromagnetic laminations stacks), depositing the wire and creating various layers that stack on top of each. High bending strains occur during deposition due to the wire being subjected to small curvature radii. This process reduces the reliance on rare earth materials, which are expensive and environmentally damaging. However, deposition presents challenges such as wire misalignment, gaps between layers, and plastic deformations, potentially leading to defects and efficiency loss. Currently, no specialized software exists to model this intricate process, leaving manufacturers reliant on costly and time-consuming trial-and-error methods. Existing simulation efforts demonstrated the feasibility of the approach but lacked detailed analysis of mechanical properties and complex deposition dynamics, struggling to capture critical factors like plastic strains, frictional contact, and the complexities of multilayer deposition.

2. Aim of the Study

As the observed windings' defects can be related to the effects of localized bending plastic strains and induced residual stresses, the goal of the study is to closely reproduce the deposition process to better understand the origins of the defects and try to optimize the deriving parameters of the process. To do so, this work aims to exploit Multifil's capabilities, an in-house software [1], which represents a modeling and numerical simulation approach based on an implicit solver for studying the behavior of entangled media and metallic cables. This research enhances the Multifil software's ability to simulate the winding process. By accurately modeling frictional contact and plastic deformations, also providing insights into wire tension, nozzle trajectory, and layer interactions, this study lays the foundation for optimizing rotor winding and improving motor efficiency.

3. Modeling

Multifil software was adapted to model the behavior of copper wire in the rotor winding process, using a 1D elastoplastic beam with the Chaboche law. Experimental stress-strain data provided by Renault were fitted to derive material parameters. The rotor core and guiding nozzle were modeled as moving rigid obstacles defined by analytical surfaces, allowing for controlled wire deposition. The nozzle's exit geometry was parameterized for accurate simulation. This geometry allows for the representation of the actual exit edge of the nozzle and thus permits the study of the radius of curvature of the wire at the exit from the nozzle. This region is important because a strong plasticization of the wire occurs, caused by the 90° bend the wire undergoes at this location. A parametric nozzle trajectory was implemented using MATLAB-defined control points, allowing flexible trajectory adjustments for future optimization studies. To model frictional contact interactions, projection algorithms were created to identify the normal direction of object surfaces to allow the definition of a gap function between the obstacle and the wire along that direction. A penalty method and a regularized Coulomb friction model were implemented to model wire-to-tool interactions, ensuring realistic contact and tangential

forces. A similar approach was used to model the contact between different wire regions. However, in this case, the contact was treated symmetrically between the two wire segments, using a proximity zone search algorithm that, after identifying the areas that could come into contact, creates intermediate entities that allow the problem to be modeled symmetrically, similar to what was previously described [1].

4. Results

Firstly, a simple test was created to measure the distance between the exit edge of the nozzle and the center of the wire bent by 90° at the exit of the nozzle (Fig. 1). The simulations well reproduced distance variations under different tension levels, although discrepancies with the experimental data, which will be the subject of further investigation, were observed.

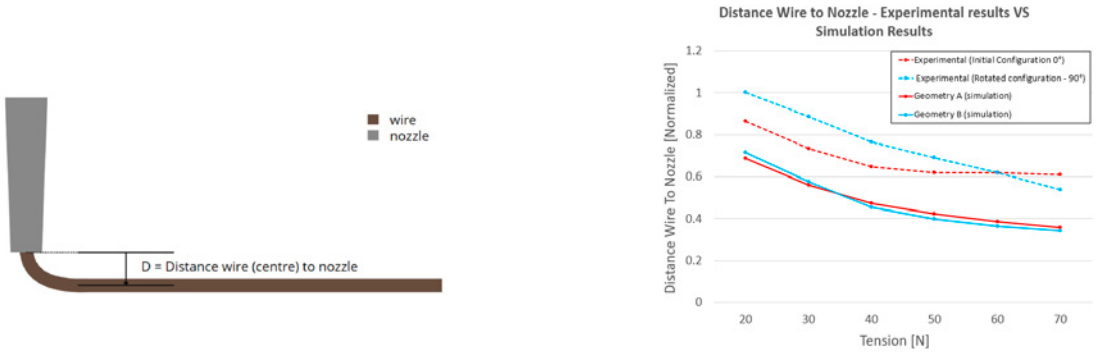

(a) The parameter studied in the experiments and Multifil simulations: distance from the wire centre to the nozzle exit edge in mm

(b) Comparison between the experimental test results (dashed lines) and the simulation results (continuous lines) for two geometrical configurations tested (in red geometry A, in blue geometry B)

Figure 1: Wire to nozzle distance test

The software was then successfully used to simulate single layer and overlapping winding scenarios, demonstrating its capability to model and quantify plastic deformations, contact interactions, and stress distribution (Fig. 2). While complete deposition simulations were not performed due to computational constraints, the results validate the feasibility of a full-scale study.

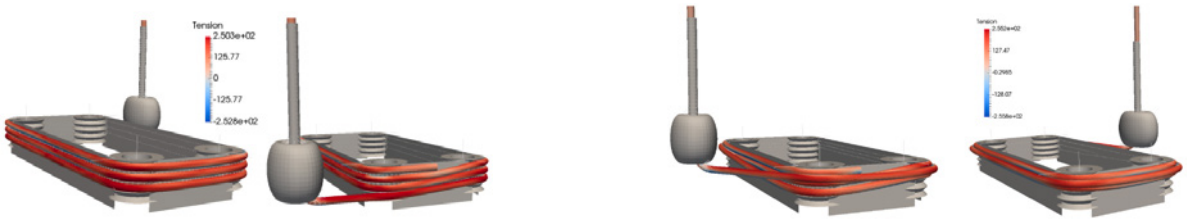

(a) Two side views of the stress distribution in the final step of depositing a single layer of 3 coils.

(b) Two side views of the stress distribution in the final step of a deposition in which a turn overlaps with a layer of two coils.

Figure 2: Stress distribution in two simplified deposition simulations

5. Conclusions

Multifil software proved to be a promising tool for simulating the rotor winding process, capturing key mechanical interactions and plastic deformations. Future work will focus on more accurate comparison with experimental results and on refining material models, optimizing trajectories, and reducing computational costs.

References

[1] Durville, D. (2012) *Contact-friction modeling within elastic beam assemblies: an application to knot tightening*, Computational Mechanics, 49 (6), 687-707

ECCOMAS Thematic Conference and IACM Special Interest Conference
Highly Flexible Slender Structures (HFSS 2025)
22–26 September 2025, Kaiserslautern, Germany

SE(3)-based shape and deformation representations for adaptive control of deformable objects

Louis Dehaybe, Olivier Brüls,

University of Liège, Belgium, [louis.dehaybe, o.bruls]@uliege.be

Keywords: Robotic manipulation, deformable objects, shape servoing, Lie group, sensor-based adaptive control

1. Introduction

The robotic manipulation of deformable objects (DOs) is a challenging research problem with applications in manufacturing (cables, sheets), robotic surgery (suturing, needle insertion), and household tasks (laundry folding), where slender structures are omnipresent. In this work, we focus on *shape servoing*, the task of controlling an object's deformations to achieve a desired shape, using a closed-loop adaptive control method. Given the infinite configuration space of DOs, a key challenge is designing a feedback signal that accurately captures the shape while remaining simple enough for real-time closed-loop control, making the shape representation a critical choice.

Previous works proposed various methods to approximate DOs' shape, such as object contours or simple geometric features like angles [1]. A standard approach, serving as our comparison baseline, is *position-based servoing* (PBS), which tracks the positions of an ordered set of object points [2]. However, in existing works, PBS representation of deformations is sensitive to rigid-body motions, such that linearized deformation models are not *invariant to the choice of the inertial frame*, thereby increasing their non-linearity.

Our work introduces an $SE(3)$-based servoing (SE3BS) approach which simultaneously combines several key properties that existing works partially fulfill: 1) *completeness* (i.e., being able to capture the object's pose in addition to its intrinsic shape), by representing the configuration through the pose of local frames attached to the DO, 2) *inertial frame invariance* of the deformation model, by expressing deformations as relative transformations between these frames, formulated in the Lie algebra $\mathfrak{se}(3)$, 3) *generality*, as local frames can represent any task and are not restricted to specific objects, and 4) *robustness to features choice*, which is notably improved by the integration of local frame orientations into the feedback loop. The proposed representation is integrated into an adaptive shape controller, evaluated through simulations of both single- and dual-arm manipulation of deformable linear objects (DLOs) and shells (Fig. 1a), and validated on our experimental platform with DLOs (Fig. 1b). A preliminary version of the approach was introduced in [3], demonstrated in limited simulations.

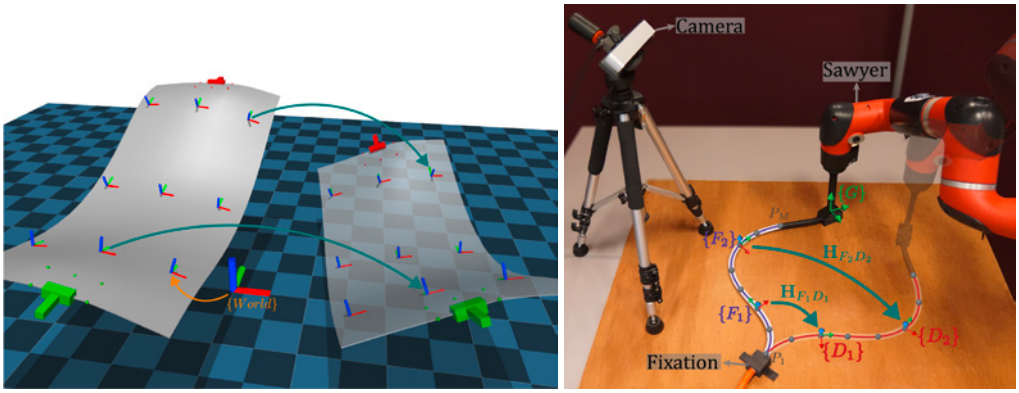

(a) (b)

Figure 1: SE(3)-based shape servoing: (a) Simulation with deformable surfaces, (b) Experimental setup with a DLO.

2. Shape servoing using an SE(3)-based representation of shapes and deformations

The current configuration of the DO is represented by the poses $\mathbf{H}_{F_i} \in SE(3)$ of N feature frames $\{F_i\}$ $(i = 1,\ldots,N)$, and we build the corresponding frames $\{D_i\}$ and their poses $\mathbf{H}_{D_i} \in SE(3)$ using the same points of the DO but on its desired configuration. Frames $\{F_i\}$ and $\{D_i\}$ are respectively indicated in purple and red

in Fig. 1b. We note $\mathbf{H}_F = \text{diag}(\mathbf{H}_{F_1}, \ldots, \mathbf{H}_{F_N}) \in SE(3)^N$, $\mathbf{H}_D = \text{diag}(\mathbf{H}_{D_1}, \ldots, \mathbf{H}_{D_N}) \in SE(3)^N$ and $\mathbf{H}_{RG} = \text{diag}(\mathbf{H}_{RG_1}, \ldots, \mathbf{H}_{RG_M}) \in SE(3)^M$, where $\mathbf{H}_{RG_m}$ denotes the m-th gripper pose with respect to the robot base frame. If the object exhibits elastic deformations only and if quasi-static manipulation is considered, the following linearization holds:

$$\mathbf{d}_F = \mathbf{J}(\mathbf{H}_{RG})\,\mathbf{d}_G \tag{1}$$

where $\mathbf{J}$ is the so-called *shape Jacobian* that relates robots motions to variations of the shape features. Indeed, in the SE3BS approach, we respectively represent *grippers displacements* from a configuration $\mathbf{H}_{RG}^{k_l}$ to a current configuration $\mathbf{H}_{RG}^{k}$ and *object deformations* from a shape $\mathbf{H}_F^{k_l}$ to a current shape $\mathbf{H}_F^{k}$ as $\widetilde{\mathbf{d}}_G^k = \log[(\mathbf{H}_{RG}^{k_l})^{-1}\,\mathbf{H}_{RG}^{k}]$ and $\widetilde{\mathbf{d}}_F^k = \log[(\mathbf{H}_F^{k_l})^{-1}\,\mathbf{H}_F^{k}]$, where the log map, which usually takes an element from $SE(3)$ to $\mathfrak{se}(3)$, is here adapted to $SE(3)^N$ or $SE(3)^M$, k indicates the current iteration and k_l is the last iteration at which the linearization was performed. $\mathbf{J}$ is not constant, and we use sensor feedback (see the camera in Figure 1b) and the Broyden update rule to constantly update its value according to past observations of the deformations. The shape error, computed as $\widetilde{\mathbf{e}}_F^k = \log\left((\mathbf{H}_F^k)^{-1}\mathbf{H}_D\right)$, is used to build a simple control law: $\mathbf{d}_G^* = \text{sat}(\hat{\mathbf{J}}^\dagger \mathbf{e}_F)$, which can be used to update grippers position. Stability of this controller can be proved using Lyapunov theory. This model-free adaptive control scheme can be applied to different objects and is resilient to external disturbances.

3. Experimental results

Fig. 2 illustrates a 2D manipulation task where a robot controls the position and orientation of a DLO's end. In Fig. 2a, black dots mark PBS feature points, while black arrows in Fig. 2b show SE3BS feature frames. This example illustrates how SE3BS solves the task with significantly fewer iterations (K), and lower total translation (Δx) and rotation ($\Delta\theta$) of the gripper. With PBS, the gripper can move in directions that temporarily decrease the features error by bringing the feature points closer to their target position (see yellow arrows in Fig. 2a and the error plot until iteration 33 in Fig. 2c). However, this comes at the cost of unintended deformations of the rest of the DLO, ultimately leading to a longer trajectory. SE3BS inherently prevents such unnecessary DLO deformations, as they would hinder the reduction of the rotational component of the shape error Φ_{SE3} (or even increase it). Our comprehensive simulation campaign confirms this tendency on a large number of tests in different situations, both in 2D and 3D. Additional benefits of SE3BS, such as reduced non-linearities of $\mathbf{J}$ and better robustness to features selection, are also observed.

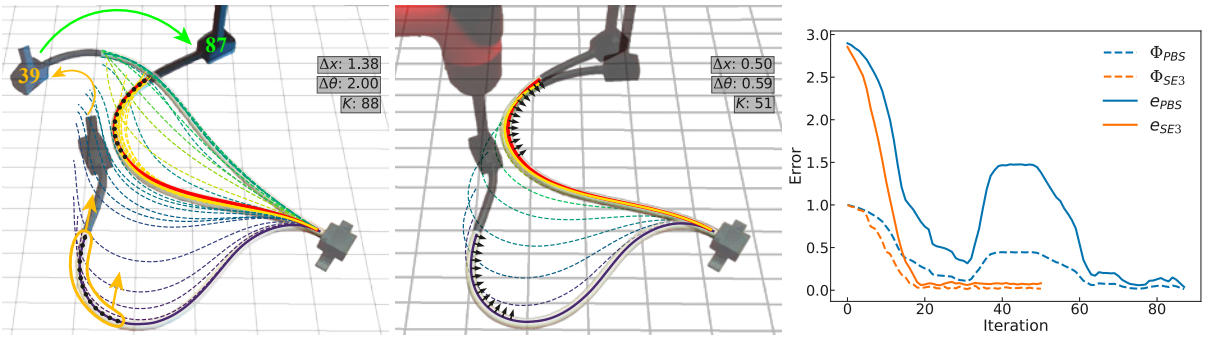

(a) (b) (c)

Figure 2: Comparison of trajectories obtained with (a) PBS and (b) SE3BS approaches. (c) Error plot, with $\Phi_{PBS} = \|\mathbf{e}_\mathbf{x}\|/\|\mathbf{e}_\mathbf{x}^0\|$ and $\Phi_{SE3} = \|\mathbf{e}\|/\|\mathbf{e}^0\|$, where $\mathbf{e}_\mathbf{x}^0$ and $\mathbf{e}^0$ are the initial shape errors of the features, and e is a common metric for both method.

References

[1] D. Navarro-Alarcón, Y. H. Liu, J. G. Romero, and P. Li. Model-free visually servoed deformation control of elastic objects by robot manipulators. *IEEE Transactions on Robotics*, 29(6):1457–1468, 2013.

[2] M. Yu, K. Lv, C. Wang, M. Tomizuka, and X. Li. A coarse-to-fine framework for dual-arm manipulation of deformable linear objects with whole-body obstacle avoidance. In *IEEE ICRA*, pages 10153–10159, 2023.

[3] L. Dehaybe and O. Brüls. An SE(3)-based formulation of the shape servoing problem. In *2nd Workshop on Representing and Manipulating Deformable Objects at the IEEE ICRA*, 2022.

ECCOMAS Thematic Conference and IACM Special Interest Conference
Highly Flexible Slender Structures (HFSS 2025)
22–26 September 2025, Kaiserslautern, Germany

Impact of Air Drag and Turbulence on Fiber Elongation in Melt Blowing

Dr. Manuel Ettmüller [1]

[1] Fraunhofer Institute for Industrial Mathematics ITWM, manuel.ettmueller@itwm.fraunhofer.de

Keywords: melt blowing, slender body theory, fiber dynamics, viscoelasticity, turbulent airflow

1. Introduction

Melt blowing is a widely used production method for nonwoven materials of polymer micro- and nanofibers. In the production of nonwovens, thousands of fibers are overlaid forming a chaotic structure, which is then bonded together either mechanically, thermically or chemically. Fabrics of meltblown nonwovens are widely used in the textile industry, for example as filters, hygiene products or battery separators. The meltblown process is an extrusion process in which the molten polymer is fed through small nozzles into a tangentially-flowing high-speed and highly turbulent air stream. The fibers are stretched by the airflow, cooled and laid down onto a conveyor belt. In this talk, we present an unsteady viscoelastic string fiber model to simulate melt blowing. The primary focus is on the modeling of the aerodynamic drag forces acting on the fiber, as it crucially influences fiber stretching and laydown.

2. Model

Similar to other fiber and nonwoven production processes, fibers produced by melt blowing are slender objects due to their small ratio of cross-sectional diameter to length indicated by the slenderness parameter $\varepsilon \ll 1$. Thus, their dynamics can be modeled by one-dimensional equations resulting from averaging three-dimensional balance laws over their cross-sections. For our melt blowing fiber model, we employ a unsteady viscoelastic string model in Lagrangian description, consisting of kinematic equations determining the fiber position and dynamic equations given by the balance laws for mass, momentum and energy. The viscoelastic material behavior is reflected by an upper convected Maxwell (UCM) description resulting in material laws for the stress σ and the pressure p.

$$\mathrm{De}\,\partial_t \sigma + \left(-\mathrm{De}(2\sigma + 3p) - \frac{\mu}{\theta}\frac{3}{\mathrm{Re}}\right)\frac{\boldsymbol{t}}{e}\cdot\partial_s \boldsymbol{v} + \frac{\sigma}{\theta} = 0, \tag{1}$$

$$\mathrm{De}\,\partial_t p + \left(\mathrm{De}\,p + \frac{\mu}{\theta}\frac{1}{\mathrm{Re}}\right)\frac{\boldsymbol{t}}{e}\cdot\partial_s \boldsymbol{v} + \frac{p}{\theta} = 0, \tag{2}$$

with dynamic viscosity μ, relaxation time θ, normalized fiber tangent $\boldsymbol{t}$, fiber elongation e and fiber velocity $\boldsymbol{v}$, as well as Deborah number De and Reynolds number Re. The momentum balance is given by

$$\partial_t \boldsymbol{v} - \partial_s\left(\sigma\frac{\boldsymbol{t}}{e}\right) - \boldsymbol{f}_g - \boldsymbol{f}_{\mathrm{air}} = \boldsymbol{0}, \tag{3}$$

with gravitational forces $\boldsymbol{f}_g$ and aerodynamic forces $\boldsymbol{f}_{\mathrm{air}}$. The dominant forces in melt blowing result from the air drag. The turbulent forces are incorporated by a turbulence reconstruction of the velocity fluctuations based on a k-ε turbulence description of the high-speed airflow, where the resulting air velocity is the sum of the mean velocity and the turbulent fluctuations [2, 3]. The aerodynamic forces $\boldsymbol{f}_{\mathrm{air}}$ can thereby be reduced to the dimensionless force function

$$\boldsymbol{F}(\boldsymbol{t},\boldsymbol{w}) = r_n(w_n, w_t)\boldsymbol{w}_n + r_t(w_n, w_t)\boldsymbol{w}_t, \tag{4}$$

with normal and tangential air resistance coefficients r_n and r_t, tangential velocity component $\boldsymbol{w}_t$ and normal velocity component $\boldsymbol{w}_n$. In [1], a sophisticated air drag model based on Oseen theory, Taylor heuristic and simulations was developed to calculate r_n and r_t that is universally valid for all Reynolds number regimes and incident flow directions. However, it showed that the employed regularization for tangential incident flow situations ($w_n \to 0$) with a with resistance coefficients only depending on the normal velocity component was underestimating the aerodynamic forces in near-tangential airflows. This is a particularly significant problem in

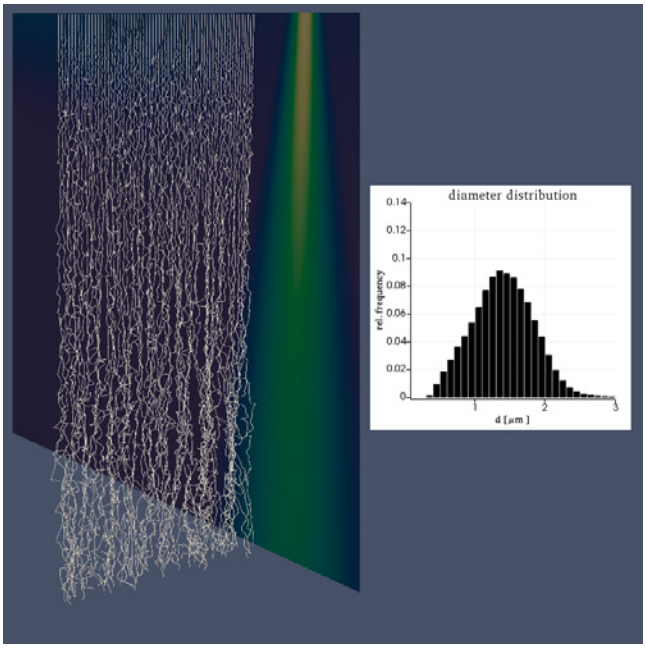

Figure 1: Simulation of the meltblown production process with resulting diameter distribution on the conveyor belt.

airflow-dominated processes such as melt blown resulting in reduced fiber elongations and incorrect diameter distributions on the conveyor belt. We therefore adapted the air drag model of [1] such that the tangential resistance coefficient for near-tangential incident flow situations ($w_n \leq w_0(w_t)/2$) is given by

$$r_t(w_t) = A v_t^{\alpha}, \qquad A > 0,\ \alpha > 0, \tag{5}$$

with boundary function w_0 chosen implicitly to match the air drag model for non-tangential incident flows.

3. Results

Figure 1 shows the results of an industrial meltblown process with a single row nozzle setup. The underlying airflow velocity is displayed behind the fibers as a 2D cross-section. The filaments exhibit a straight downward movement near the nozzle, where a significant amount of the elongation occurs. Further away from the nozzle, the effects of turbulence increase, leading to extensive fiber movement. This, in turn, contributes to the fiber elongation. The diameter distribution of the fibers on the conveyor belt mostly yields diameters in the range of one to two micrometers, which is in good agreement with experimental measurements.

4. Conclusions

Our proposed fiber model makes the simulation of industrial melt blowing processes with inclusion of turbulent and viscoelastic effects as well as temperature dependencies feasible. The simulations produce final fiber diameters of realistic order of magnitude due to the inclusion of turbulent effects acting on the fiber as well as the adaptation of the underlying air drag model for near-tangential incident flows. The provided simulation framework opens the field for simulation-based process design and material optimization.

References

[1] N. Marheineke, R. Wegener. *Modeling and application of a stochastic drag for fibers in turbulent flows.*, Int. J. Multiphase Flow, 37:136-148, 2011.

[2] F. Hübsch, N. Marheineke, K. Ritter, R. Wegener. *Random field sampling for a simplified model of melt-blowing considering turbulent velocity fluctuations.*, J. Stat. Phys., 150(6):1115–1137, 2013.

[3] M. Wieland, W. Arne, N. Marheineke, R. Wegener. *Melt-blowing of viscoelastic jets in turbulent airflows: Stochastic modeling and simulation.*, Appl. Math. Model., 76:558–577, 2019.

ECCOMAS Thematic Conference and IACM Special Interest Conference
Highly Flexible Slender Structures (HFSS 2025)
22–26 September 2025, Kaiserslautern, Germany

3D form board in the loop: interactive 3D flattening in the automotive wiring harness development process

Michael Koch , Daniel Dengel , Christian Loris , Oliver Hermanns

fleXstructures GbmH , [michael.koch, daniel.dengel, christian.loris , oliver.hermanns]@flexstructures.de

Keywords: wiring harness, flattening, simulation-based form board design

1. Introduction and industrial use case

Wiring harness development in automotive industry has gained significant importance in the recent years, driven by the growing number of driver assistance systems and comfort features. As a result, wiring harnesses are now rightly regarded as the nervous system of modern vehicles. This trend has been further accelerated by the electrification of the powertrain over the last decade and is expected to become even more important with the upcoming of autonomous driving and the growing importance of fuel cell technology as an alternative powertrain system. The development of harnesses is therefore one of the most complex and challenging tasks in automotive engineering. Currently, the development process is limited by a lack of synchronization points, information gaps and the limitations of conventional CAD software, which does not correctly map the real behaviour of flexible components such as wiring harnesses and high-voltage cables. Wiring harnesses are produced on form boards and therefore the realized design is an important development step. The transition from a harness designed in 3D to a configuration on a 2D form board is called flattening. Conventional flattening using CAD systems and 2D drawings led to a cost-intensive and iterative process step that took several months and, in some cases, still provided an unsatisfactory result for the design of the form boards.

Together with the research institutes Fraunhofer ITWM and Fraunhofer Chalmers Centre, fleXstructures GmbH and Industrial Path Solution AB have established IPS Cable Simulation [1], a technology on the market that eliminates the disadvantages of CAD systems and is widely used as a validation tool in wiring harness development. Based on IPS Cable Simulation, fleXstructures GmbH and Fraunhofer ITWM have initiated the BordNetzSim3D research project (for more information see [2]) to establish a simulation-based and fully digital end-to-end process for automotive wiring harness development. A central topic was the interactive flattening to identify the best configuration on a 2D form board. In [3], an automated flattening approach based on CAD systems was discussed, which already represents a first approach, but does not meet the requirements that were addressed and realized in BordNetzSim3D. The use of IPS Cable Simulation offers the possibility to investigate the influence of the form board design in the 3D environment in the vehicle, because typically the 3D configuration of the harness in the vehicle cannot be produced without shape-changing adjustments as a result of the form board layout. It is therefore very important for an efficient and cost-reduced development process that this possibility exists, which is why the authors refer to this possibility as “3D form board in the loop”. Figure 1 illustrates this concept using the example of a rear door wiring harness.

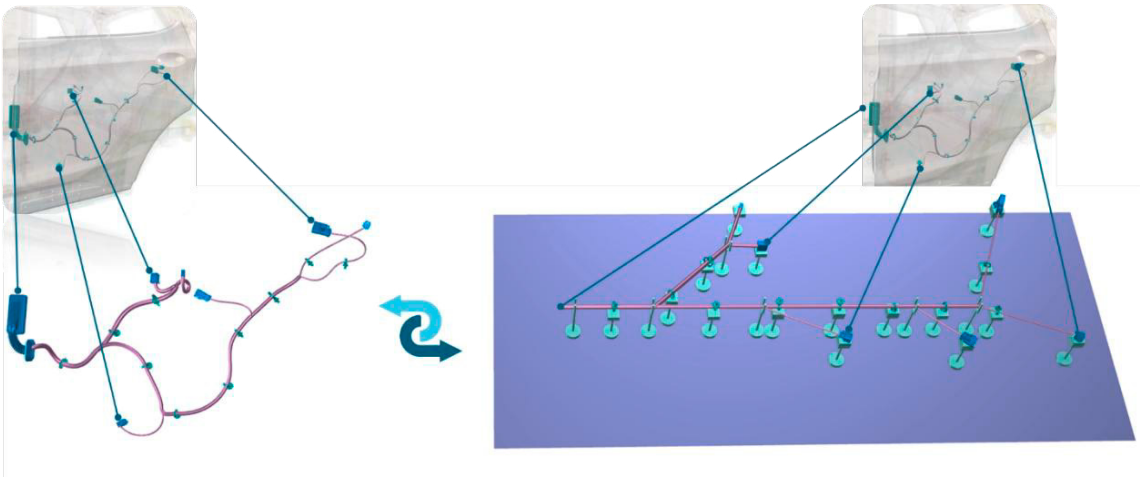

Figure 1. Comparison between 3D configuration in the vehicle and the 2D configuration on an exemplary production form board including possible manufacturing brackets for plugs and clips.

2. Methodical approach and industrial aspects for 3D flattening

The approach used for 3D flattening intelligently integrates information from the vehicle's wiring harness configuration, including the resulting torsional stress on wires and cable bundles, with design and ergonomic specifications derived from the form board layout, such as specifications for connector and clip mounts. As illustrated in **Figure 1**, connectors and connection points must remain fully accessible to the worker so that components and tasks, such as the application of protection features, e.g. the fixing of adhesive tape, can be carried out without obstruction. This combination is essential to produce a manufacturable and functionally robust wiring harness.

In addition to the boundary conditions regarding orientation and accessibility for the worker, an important requirement arises directly from the cables themselves: While the bending stresses are generally not critical, the configuration on the form board must ensure that the resulting 3D installation in the vehicle has minimal torsion. This torsion of the wiring harness in the vehicle is caused by the fact that although the wiring harness is produced without torsion on the form board, torsion is introduced into the vehicle during assembly.

The methodical approach will be presented and how to design the layout for the form board so that torsional stresses in the installed harness are minimized. The key advantage of this method is that designers can directly evaluate potential form board layouts and instantly see how changes affect the harness geometry in the vehicle. **Figure 2** illustrates the effects of realigning a branching direction in relation to the wiring harness configuration within the vehicle. The result achieved within the BordNetzSim3D project thus represents a coexistence of wiring harness design in the vehicle and of the form board and enables a synchronized and more efficient development process.

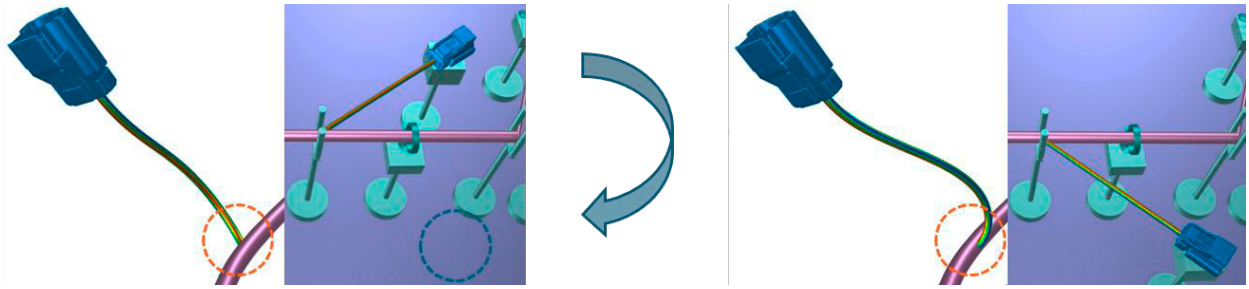

Figure 2. Effects on the vehicle configuration when changing the branch orientation direction on the form board.

Based on this, platform strategies for different vehicle classes can be realized in the future. This means that not only the configuration within a specific vehicle and on the corresponding form board can be optimized, but also the configurations across multiple vehicle derivatives. This means that a single form board layout can potentially be used to produce the same harness for multiple vehicle models. This concept is referred to as a multi-vehicle approach, which offers significant potential for the automation and scalability of future development processes.

References

[1] https://flexstructures.de/produkte/ips-cable-simulation/

[2] https://ecmiindmath.org/2024/03/18/simulation-based-design-of-cable-harnesses-and-digital-twin-of-the-wiring-system-process/

[3] T. van den Berg, G. La Rocca, M. J. L. van Tooren. *Automatic flattening of three-dimensional wiring harnesses for manufacturing*, ICAS2012 – 28th International Congress of the Aeronautical Sciences, 10 Pages, 2012.

ECCOMAS Thematic Conference and IACM Special Interest Conference
Highly Flexible Slender Structures (HFSS 2025)
22–26 September 2025, Kaiserslautern, Germany

Enhancing Cable Simulation with Flexible Clips and Mountings

Fabio Schneider-Jung [1], Michael Roller [1], Joachim Linn [1], Sudhanva Kusuma Chandrashekhara[1],

[1] Fraunhofer Institute for Industrial Mathematics ITWM, email:
fabio.julian.schneider-jung@itwm.fraunhofer.de, michael.roller@itwm.fraunhofer.de,
joachim.linn@itwm.fraunhofer.de, sudhanva.kusuma.chandrashekhara@itwm.fraunhofer.de

Keywords: Flexible clips, cable mountings, coupled simulation, flexible cables.

1. Introduction

Industry-standard software tools for CAD and virtual assembly frequently treat clips and mountings as rigid geometries, which does not accurately reflect their true nature. This limitation significantly narrows their range of applications, as many systems include critical components that are flexible and undergo deformation during assembly. As a result, there is an increasing demand for simulations that realistically depict deformations in slender flexible structures, as well as their interactions with flexible mountings, ideally in real-time for interactive purposes. Typical applications include the use of flexible clips and mountings such as rubber bushings and vibration isolators to accommodate the movement and deformation of cables and hoses in the automotive industry. We utilize the cable simulation from [3] and carry out coupled simulations with reduced models for the mounting elements. This approach enables us to include arbitrary geometries for these elements, resulting in more realistic interactions and practical assembly processes.

2. Methodology

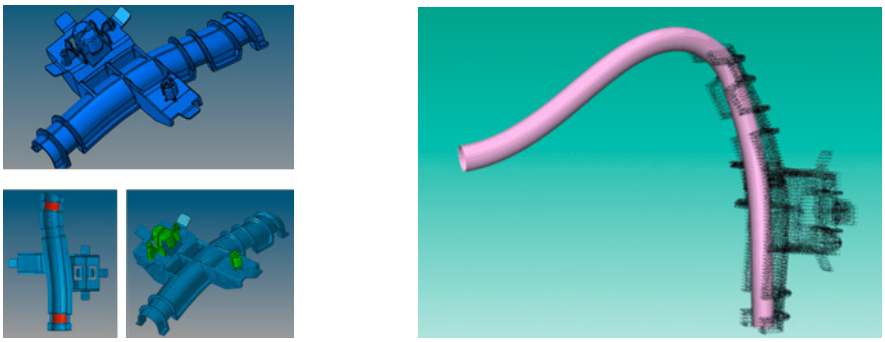

Figure 1: Cable with flexible mounting element.

In the preprocessing phase, we use ABAQUS to create a finite element model for the flexible mounting element, as shown in Figure 1(a). The substructure generator module in ABAQUS is employed to extract the condensed system equations. This module specifically carries out a Guyan reduction [1] for the flexible mount element, using the information from two categories of nodes: (1) Inner nodes (I) and (2) Retained nodes (R). For example, in Figure 1 (a), we have highlighted the retained nodes in green and red. The reduced system reads:

$$\begin{bmatrix} \mathbf{K}_{RR} & \mathbf{K}_{RI} \\ \mathbf{K}_{IR} & \mathbf{K}_{II} \end{bmatrix} \begin{bmatrix} \mathbf{u}_R \\ \mathbf{u}_I \end{bmatrix} = \begin{bmatrix} \mathbf{f}_R \\ \mathbf{0} \end{bmatrix}. \tag{1}$$

Applying Guyan reduction to equation 1, we obtain a simplified model dependent only on the retained nodes:

$$\left(\mathbf{K}_{RR} - \mathbf{K}_{RI}\left(\mathbf{K}_{II}\right)^{-1}\mathbf{K}_{IR}\right)\mathbf{u}_R = \mathbf{f}_R. \tag{2}$$

Now the potential energy and the reaction forces of the mounting element can be written as:

$$P\left(\mathbf{u}_R\right) = \frac{1}{2}\mathbf{u}_R^T\mathbf{K}\mathbf{u}_R, \tag{3}$$

$$\nabla_u P\left(\mathbf{u}_R\right) = \mathbf{K}\mathbf{u}_R, \tag{4}$$

where $\mathbf{K} = \mathbf{K}_{RR} - \mathbf{K}_{RI}\left(\mathbf{K}_{II}\right)^{-1}\mathbf{K}_{IR}$. For the coupled simulation together with the flexible mounting, we extend the energy minimization problem [2] with the energy potential of the clip and the coupling constraints for the cable and mounting. The extended system reads:

$$\min_{\mathbf{q},\mathbf{u}} \; E(\mathbf{q}) + P(\mathbf{u}) \tag{5}$$

$$\text{s.t. } \mathbf{g}(\mathbf{q}) = \mathbf{0}, \tag{6}$$

$$\phi\left(\mathbf{X}^{(0)}, \mathbf{q}\right) - \psi(\mathbf{u}) = \mathbf{0}. \tag{7}$$

where E is the potential energy of the cable, $\mathbf{q}$ represents the given deformed configuration, $\mathbf{u}$ represents the clip displacements, $\mathbf{g}$ represents the inner constraints, $\psi : \mathbf{u} \mapsto \mathbf{Y}$ maps local clip displacements $\mathbf{u}$ to global coordinates $\mathbf{Y}$, $\phi : \left(\mathbf{X}^{(0)}, \mathbf{q}\right) \mapsto \mathbf{Y}$ maps a given deformed cable state $\mathbf{q}$, local cable coordinates $\mathbf{X}^{(0)}$ to global coordinates $\mathbf{Y}$. Using equation (7), we can eliminate the dependence on clip displacements ($\mathbf{u}$) and formulate the optimization problem depending only on the cable configuration ($\mathbf{q}$) while preserving the system's dimensionality. This approach has been used for several complex geometry of clips. Its effectiveness and robustness will be showcased through a number of illustrative examples.

References

[1] S. Chen, H.H. Pan. *Guyan Reduction*, Communications in Applied Numerical Methods, 4 (1988) 549-556.

[2] J. Linn, T. Hermansson, F. Andersson, F. Schneider. *Kinetic aspects of discrete Cosserat rods based on the difference geometry of framed curves*, ECCOMAS Thematic Conference on Multibody Dynamics, 163-176, 2017.

[3] *IPS Cable Simulation*, Available at: https://flexstructures.com/products/ips-cable-simulation/

ECCOMAS Thematic Conference and IACM Special Interest Conference
Highly Flexible Slender Structures (HFSS 2025)
22–26 September 2025, Kaiserslautern, Germany

Simulation of spot welded assemblies using nonlinear shell theory

Samuel Lorin [1], Elias Börjesson [2], Lars Lindkvist [3], Kristina Wärmefjord [4], Rikard Söderberg [5], Fredrik Edelvik [6],

[1] Fraunhofer Chalmers Centre, samuel.lorin@fcc.chalmers.se
[2] Fraunhofer Chalmers Centre, elias.borjesson@fcc.chalmers.se
[3] Chalmers University of Technology, lars.lindkvist@chalmers.se
[4] Chalmers University of Technology, kristina.warmefjord@chalmers.se
[5] Chalmers University of Technology, rikard.soderberg@chalmers.se
[6] Fraunhofer Chalmers Centre, fredrik.edelvik@fcc.chalmers.se

Keywords: Variation Simulation, Spot Welding, Geometrically Non-Linear Shell Theory

1. Introduction

All manufacturing processes exhibit variations from nominal settings. These variations may arise from differences in material properties, leading to geometric deviations in manufactured parts. Additionally, part variation, along with inconsistencies in fixturing and tooling, contributes to deviations in the assembly process. Such geometric deviations can cause issues during assembly or result in a decline in the functional and aesthetic quality of the final product. Geometry assurance (GA) encompasses a series of activities throughout the product lifecycle aimed at ensuring the geometric quality of the manufacturing process. During the concept phase, design proposals are developed and evaluated in conjunction with manufacturing systems. This phase is followed by a verification stage, where inspection routines are established alongside virtual matching simulations. Finally, in the production stage, the focus shifts to process monitoring, deviation identification, and root cause analysis. The time and cost associated with design changes increase significantly as more product and manufacturing process decisions become finalized. Therefore, it is crucial to ensure that the product is highly likely to meet requirements and that those requirements are correctly defined from the early.

2. Locating system

Given a design proposal, the first step in GA is to develop a robust locating system. A locating system (LS) defines how a part is positioned in space using a fixture or relative to adjacent parts. It is represented as a set of triplets $(p_m, p_s, \boldsymbol{d})$, where p_m is the master point on the part, p_s is the slave point (a point on the mating surface), and $\boldsymbol{d}$ is a direction, typically the normal direction of the surface of the master point. The part is positioned by eliminating all gaps in the direction $\boldsymbol{d}$, as expressed by the equation:

$$\left(\boldsymbol{x}(p_m^i) - \boldsymbol{x}(p_s^i)\right) \cdot \boldsymbol{d} = t \quad \forall \quad i = 1, \quad \dots \quad n, \tag{1}$$

where $\boldsymbol{x}(p_m^i)$ and $\boldsymbol{x}(p_s^i)$ are the current positions of points p_m^i and p_s^i, respectively, t is the thickness of the shells here assuming the shells have the same thickness, and n is the number of positioning triplets. A robust locating system minimizes variations in key characteristics caused by deviations in the positions of the locating points $\boldsymbol{x}(p_m^i)$ and $\boldsymbol{x}(p_s^i)$. Therefore, designing a robust locating system is a key objective. From a design quality perspective, a robust locating system is fundamental, as it allows for wider tolerances.

3. Tolerance design

The next step is to define requirements for key design characteristics and assign appropriate tolerances. To achieve this, virtual tools play a crucial role in many industrial applications. These tools simulate how part variations propagate through the assembly process, ultimately affecting the final product.

Modern computer rendering also enables the evaluation of aesthetic attributes, helping to determine whether the requirements are appropriate or need adjustment. This allows designers to answer critical questions such as: Are these requirements sufficient, or do they need to be tightened or may they be widened?

4. Variation simulation

To ensure that design requirements are met and to verify that the assigned requirements are appropriate, variation simulation is used. Various techniques exist for variation simulation [1], but this discussion focuses on Monte Carlo simulation. In each iteration of a Monte Carlo simulation, deviations for all positioning points are randomly sampled based on their assigned probability distributions. An assembly function then calculates the resulting translations, rotations, and iterative adjustments based on the multi-step assembly process. Finally, deviations in key characteristics are recorded.

The finite element method (FEM) is typically used to model part deformations in variation simulations. However, Monte Carlo simulation requires solving numerous FEM models, necessitating efficient methods to handle multiple variations within a short time.

5. Spot welding

This paper focuses on variation simulation of spot-welded geometries. Spot welding is a widely used technique for joining sheet metal across various industries. In this process, a weld gun applies an electric current to heat and melt the plates, locally fusing them together to form what is known as a weld nugget. To model spot welding, linear FEM using shell elements is typically used [2] and it is often assumed that the geometric effects from heat can be neglected. The modeling steps are (1) Given initial deviations in the part and fixture, calculate the part's position and deformation by closing all positioning triplets. (2) At this stage, apply a spot weld plier to close any gap in the specified spot weld direction by enforcing the condition $(\boldsymbol{x}(s_m) - \boldsymbol{x}(s_s)) \cdot d = t$, where s_m and s_s are spot weld points. (3) While the plier forces are applied, constrain the relative position and rotation of points s_m and s_s. (4) Release the plier forces and compute the resulting spring-back effect. (5) If there are remaining spot welds, return to step (2). (6) Determine the position and deformation in the measurement fixture. To prevent geometric penetration in the modeling steps above, contact modeling is applied.

These models are typically solved using the Method of Coefficients (MIC) [3] where linear combinations of the effects from deviations are summed to model the resulting geometry. There are situations where the MIC is not ideal. For example, if a number of parts have been scanned in a pre-production series and it is necessary to model what the assembly might look like under different circumstances, it may be computationally more efficient to directly model the spot welding process without first calculating the sensitivity matrices.

6. Scope of the paper

In this paper, we have developed a model to simulate spot welding without using the standard MIC, often referred to as Direct-FEM. Using this model, we have investigated the consequences of assuming geometric linearity.

The shell model employed is based on the one proposed by Ibrahimbegovic [4, 5] and includes 6 degrees of freedom per node, including drilling rotation. The findings are used to provide recommendations on how to apply variation simulation to spot welding.

References

[1] R. Söderberg, L. Lindkvist, K. Wärmefjord, J. Carlson *Virtual geometry assurance process and toolbox*, Procedia Cirp, Elsevier, 3-12, 2016.

[2] S. Lorin, B. Lindau, L. Lindkvist, R. Söderberg *Efficient compliant variation simulation of spot-welded assemblies*, Journal of Computing and Information Science in Engineering, (2019).

[3] S. Liu, J, Hu. *Variation simulation for deformable sheet metal assemblies using finite element methods*, Journal of Manufacturing Science and Engineering, (1997).

[4] A, Ibrahimbegović. *Stress resultant geometrically nonlinear shell theory with drilling rotations—Part II. Computational aspects*, Computer Methods in applied mechanics and Engineering, 118 (1994).

[5] A, Ibrahimbegović. *Stress resultant geometrically nonlinear shell theory with drilling rotations—Part I. A consistent formulation*, Computer Methods in Applied Mechanics and Engineering, 1994.

ECCOMAS Thematic Conference and IACM Special Interest Conference
Highly Flexible Slender Structures (HFSS 2025)
22–26 September 2025, Kaiserslautern, Germany

Feasibility study for preliminary design of dynamic submarine power cables

Konstantina Ntarladima[1], Nikolaos Mavrodontis [2], Stylianos Koumlis [3]

Hellenic Cables, [[1]kntarladima,[2]nmavrodontis,[3]skoumlis]@hellenic-cables.com

Keywords: Feasibility Study, Submarine Cables

1. Introduction

This study proposes an approach for developing feasible preliminary designs for submarine power cables, particularly inter-array cables in floating offshore wind farms. A crucial component of these cables is the dynamic section, which spans between the floating platform and the seabed and is continuously subjected to environmental loading such as ocean currents, waves and platform motion induced loads.

Various dynamic configurations are evaluated to ensure structural integrity, efficiency, and long-term reliability. These include the catenary configuration, where the cable hangs freely between the floater and seabed; the lazy-wave configuration, incorporating buoyancy modules; and the tethered lazy-wave configuration, which adds an anchored tether for enhanced stability. Selecting the design—defined by key parameters such as cable length, buoyancy section length, and segment weights—is crucial for both safety and cost-effectiveness. While numerous methodologies have been explored, a comprehensive strategy remains an open challenge. This involves defining constraints, such as allowable seabed and surface clearance, and establishing evaluation criteria, including minimizing curvature and optimizing tension within defined ranges, in critical regions.

Existing works on preliminary design for dynamic submarine power cables propose various optimization criteria for selecting proper design characteristics. Several optimization frameworks, e.g. [1], [2], focus on curvature and tension distributions, applying structural constraints while others, e.g. [3], aim at cable length minimization satisfying constraints including bending radius and tension limits. The evaluation of multiple performance metrics such as the tension at the hang-off point, the optimized curvature in the sagging and buoyancy section, and the total cable length has also been considered [4]. Further contributions to the field, e.g. [5], propose fatigue-objective optimization algorithms. Furthermore, regarding objective function evaluation, existing works [4] perform optimization based solely on static analysis, or also conduct steady-state analyses under extreme environmental loading conditions [3], [2]. The work of Wang et al. [1] evaluates the objective function under both static and dynamic conditions, incorporating regular and irregular wave scenarios to assess performance robustness. Finally, for performing optimization researchers have used gradient-based numerical optimization algorithms such as the sequential least squares programming [3] and the gradient descent method [4], as well as genetic optimization algorithms [6], [1]. Despite advancements in optimization frameworks, challenges remain in defining generalized methodologies capable of balancing structural, cost, and operational constraints across diverse offshore environments.

2. Preliminary results

We investigate the design feasibility of a dynamic power cable in a lazy wave configuration, attached to a floating wind turbine at a water depth of 310 m. Initial cable lengths are based on industry experience for this depth. Using the simulation tool OrcaFlex [7], parameter variations are conducted via the API interface, with SIMA [8] considered for comparison. The study begins with a parameter variation of the buoyancy section length, assuming a nominal cable mass per unit length and an industry-standard ratio of buoyancy to cable submerged weight, $w_b/w = -1$, to achieve uniform curvature. A subsequent variation in the buoyancy section weight, see Figure 1 (left), identifies the configuration that minimizes maximum curvature and ensures allowable effective tension. The selected design is tested under three loading directions—near (0°), cross (90°), and far (180°)—to verify that curvature and effective tension remain within cable capacity, see Figure 1(right) and Figure 2. Notably, the maximum tension at the hang-off point is significantly reduced compared to a catenary configuration of the same cable.

The presentation will outline a feasibility strategy, incorporating dynamic and fatigue analyses to assess the

design's structural viability.

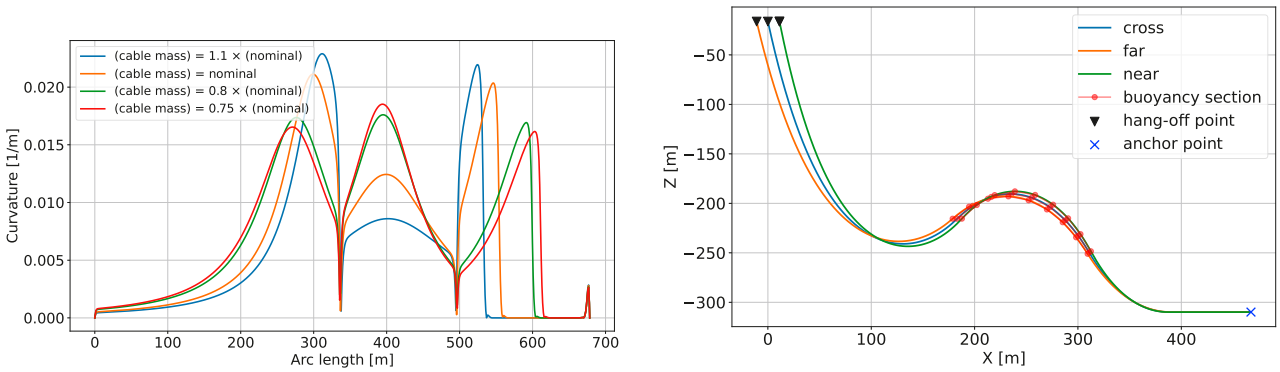

Figure 1: Curvature plots along arc length for varying cable mass per length (on the left), cable configuration under cross, far and near environmental loading (on the right).

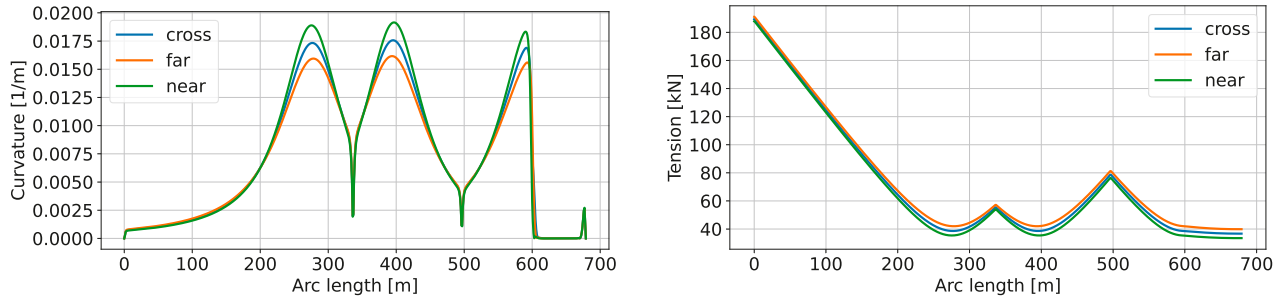

Figure 2: Curvature (on the left) and tension (on the right) along arc length for cross, far and near environmental loading.

References

[1] Y. Wang, F. Yan, Y. Du, H. Wang, S. Ai, and W. Wang. *A stepwise scheme for the optimization implementation of lazy wave dynamic cables*, Ocean Engineering, 311 (2024).

[2] I. B. Ahmad, A. Schnepf, M. C. Ong. *An optimisation methodology for suspended inter-array power cable configurations between two floating offshore wind turbines*, Ocean Engineering, 278 (2023).

[3] A. Schnepf, K. E. T. Giljarhus, Ø. Johnsen, C. Lopez-Pavon. *Dynamic power cable configuration design for floating offshore wind turbines using gradient-based optimization*, International Conference on Offshore Mechanics and Arctic Engineering, American Society of Mechanical Engineers, 2023.

[4] E. Guzman, *Dynamic Power Cable Optimized Configurations for Lazy Wave Riser Systems*, Université de Liège, Liège, Belgique, 2024.

[5] J. Yan, Q. Su, R. Li, J. Xu, Q. Lu, and Z. Yang, *Optimization Design Method of the Umbilical Cable Global Configuration Based on Representative Fatigue Conditions*, IEEE Journal of Oceanic Engineering, 48 (2023) 188-198.

[6] M. U. T. Rentschler, F. Adam, and P. Chainho, *Design optimization of dynamic inter-array cable systems for floating offshore wind turbines*, Renewable and Sustainable Energy Reviews, 111 (2019) 622-635.

[7] Orcina. *OrcaFlex*, Version 11.5, 2024. Available: `https://www.orcina.com/orcaflex/`

[8] SINTEF. *SIMA*, Version 4.8.1, 2024. Available: `https://www.sintef.no/en/software/sima/`

ECCOMAS Thematic Conference and IACM Special Interest Conference
Highly Flexible Slender Structures (HFSS 2025)
22–26 September 2025, Kaiserslautern, Germany

Interactive Simulation of Flexible Surface-like Parts as a Digital Support Function for Assembly Planning in the Automotive Pre-series Centre

Joachim Linn[1], Michael Roller[1], Muhannad Hawwash[1], Johan Ljunglide[2], Christoffer Cromvik[3]

[1] Fraunhofer ITWM, [joachim.linn, michael.roller, muhannad.hawwash]@itwm.fraunhofer.de
[2] Fraunhofer-Chalmers Research Center (FCC), Johan.Ljunglide@fcc.chalmers.se
[3] Industrial Path Solutions (IPS AB), christoffer.cromvik@industrialpathsolutions.com

Keywords: flexible surfaces, geometrically exact shells, static condensation, interactive simulation, assembly planning

1. Introduction on the industrial use case

In automotive development there is a growing demand for tools that enable the simulation of flexible surface-like components. In comparison to conventional software tools IPS already offers a fast simulation for specific flexible shell structures, like bellows and grommets or flexible flat cables [1]. For trim parts, interior and exterior panels there are currently no commercial software solutions that can support simulations in real time.

In a joint development project with a German OEM from automotive industry (Audi AG) a practically useful approach has been developed that provides an enormous computational speedup for flexible surfaces, enabling frame rates in the range of 50 – 90 Hz, which is sufficiently fast for interactive simulations in the IPS desktop. In our presentation some typical application examples like the one in *Fig. 1* below are shown. We expect that in the future this improved simulation technology will enable assembly simulations of flexible surface-like parts in virtual or extended reality (XR) environments.

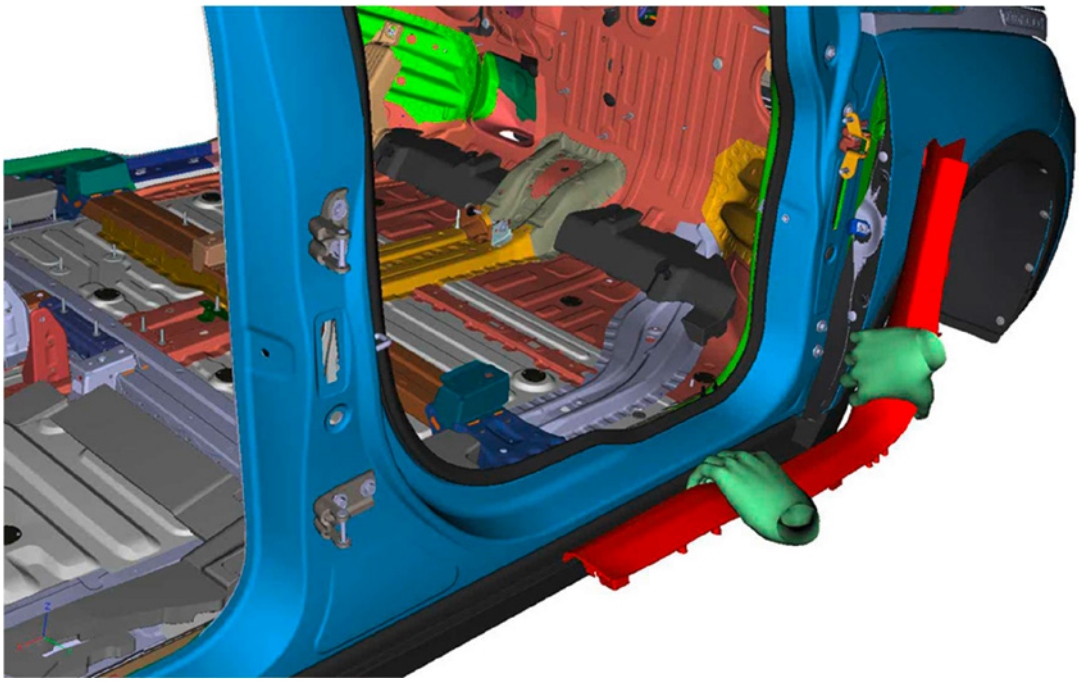

Figure 1. Screenshot taken from a “live” movie that shows an interactive assembly simulation of a flexible trim panel. During assembly the flexible part is grabbed by two hands and substantially deformed for fitting in its final position.

2. Methodical background and industrial application aspects

We will provide some background on the computational methods used for a speed-up of the full computational model [2] closely related to geometrically exact Cosserat shells [3], including an extended usage of a linearized shell model derived via static condensation (a.k.a. Guyan reduction, see Ch. 8 in [4]) for moderately large deformations in the "grey zone" between the geometrically linear and nonlinear domains.

For the industrial application it is important how such a simulation tool fits within the industrial workflow, considering the procedure to set up the model within the software framework, as well as the efforts spent and the type of information that an industrial user has to provide before being able to use the simulation tool. We will also outline such industrial application aspects which besides computational performance are very important for the user acceptance of such a digital support function.

Acknowledgements

Part of the research and development work was performed in a joint project activity with Audi AG, Neckarsulm. We acknowledge in particular the highly valuable contributions of Dipl.-Ing. (BA) Sarah Kreis and Dipl.-Ing. Jan Stanzel, and want to point the interested audience to their presentation [5].

References

[1] https://flexstructures.com/products/ips-bellows-grommets-and-ips-flat-cables/

[2] https://www.fcc.chalmers.se/technologies/comp/computational-structural-dynamics/

[3] Roller, M., Betsch, P., Gallrein, A., Linn, J. : *On the Use of Geometrically Exact Shells for Dynamic Tire Simulation.* In: Terze, Z. (eds) *Multibody Dynamics. Computational Methods in Applied Sciences*, vol **35**, pp. 205-236, Springer, Cham (2014). https://doi.org/10.1007/978-3-319-07260-9_9

[4] M. Géradin, A. Cardona: *Flexible Multibody Dynamics – A Finite Element Approach*. Wiley (2001)

[5] S. Kreis and J. Stanzel: *Development of a simulation method for real-time deformation of flexible vehicle parts*. 6th IPS Cable Simulation conference, June 25th – 26th 2025, Kaiserslautern, Germany: https://flexstructures.com/6th-ips-cable-simulation-conference-2025/.

ECCOMAS Thematic Conference and IACM Special Interest Conference
Highly Flexible Slender Structures (HFSS 2025)
22–26 September 2025, Kaiserslautern, Germany

Fiber Dynamics Simulation in Nonwovens Production Processes

Dr. Andre Schmeißer [1]

[1] Fraunhofer Institute for Industrial Mathematics ITWM, schmeiss@itwm.fraunhofer.de

Keywords: modeling, simulation, fiber dynamics, production process, nonwoven materials

1. Introduction

Nonwoven materials are a type of textile material made from thousands of thin fibers which are overlayed and bonded together by mechanical, thermal, or chemical processes, rather than being woven or knitted. They are typically produced in large sheets and can be used for a variety of applications, including hygiene, medical, automotive, and construction, showcasing their versatility and functional adaptability. The main types of industrial manufacturing processes are dry-lay processes such as Airlay, wet-lay processes, and extrusion processes, such as Spunbond or Meltblown. Full simulation of the production requires a complex chain of models dealing with the different aspects of the production, but allows creating Digital Twins [1] which can be used to analyze and optimize the process and resulting materials. We present 1d cross-sectional averaged models focusing on simulating the dynamics of such fibers as they are entangled in turbulent airflow and laid down to form nonwoven sheets, as well as results from industrial Spunbond and Airlay applications.

2. Methods

In a typical Spunbond process, raw polymer is molten and extruded through fine nozzles in a spinneret, producing jets of polymer melt. These are aerodynamically stretched and cooled to produce solidified fibers, which in turn are entangled by a turbulent airflow and laid down on a transport belt to form a nonwoven sheet. The dynamics of the fibers between drawing unit and deposition have a key influence on the final product, e.g. on homogeneity and in turn on mechanical properties. Due to the multi-phase and multi-scale nature of the problem, we use a model based on Cosserat-Rod theory for the fiber dynamics, where the long and slender fibers are described as one-dimensional objects with oriented cross-sections, obtaining one-dimensional balance laws of linear and angular momentum. Closing the system of equations by modelling the angular momentum and velocity, we arrive at a 1d string model without cross-sectional orientations [2]. Using a material model for elastic, inextensible fibers with constant diameter, we get the system of equations:

$$(\rho A)\,\partial_{\mathrm{tt}}\,\mathbf{r} \;=\; \partial_{\mathrm{s}}\left(T\;\partial_{\mathrm{s}}\,\mathbf{r} \;-\; \partial_{\mathrm{s}}\left((EI)\,\partial_{\mathrm{ss}}\mathbf{r}\right)\right) + \;\mathbf{f}_{ext}, \tag{1}$$

$$\|\partial_{\mathrm{s}}\,\mathrm{r}\| \;=\; 1. \tag{2}$$

Here $\mathbf{r}$ is the centerline of the fiber, (ρA) is the line density for density ρ and cross-section A, (EI) the bending stiffness for Young's modulus E and moment of inertia I. T is the tangential contact force of the fiber, which acts as a Lagrange multiplier for the algebraic inextensibility constraint (2). The sum of all external forces is denoted as $\mathbf{f}_{ext}$. Besides contact forces [3] and gravity, the dominant forces in Spunbond processes result from air drag. We model the turbulent forces using the results of a CFD simulation with a RANS-approach (Reynolds-Averages Navier Stokes), i.e.:

$$\mathbf{u}(\mathbf{x},t) = \;\bar{\mathbf{u}}(\mathbf{x},t) + \mathbf{u}'(\mathbf{x},t), \tag{3}$$

where the resulting air velocity $\mathbf{u}$ is the sum of the mean velocity $\bar{\mathbf{u}}$ and turbulent fluctuations $\mathbf{u}'$. The air drag then depends on the relative velocity between air and fiber with a corresponding model for the tangential and normal drag coefficients. Fiber fluctuations can be incorporated using a turbulence reconstruction model [4] or a white noise limit, leading to a system of randomized or stochastic PDEs respectively. Contact forces introduce another algebraic constraint, where h is an implicit function representing the contact surface [3]

$$\mathbf{f}_{contact} = \lambda\frac{h(\mathbf{r})}{\|h(\mathbf{r})\|}, \qquad (\lambda = 0 \;\wedge\; h(\mathbf{r}) \geq 0) \;\vee\; (\lambda > 0 \;\wedge\; h(\mathbf{r}) = 0) \tag{4}$$

with Lagrange multiplier λ for the constraint, leading to a system of stochastic partial differential-algebraic equations (SPDAE), which require great care in solving numerically. We semi-discretize the equation system in space, use Newton's method to solve the non-linear equations for each time step, and then use the implicit

Euler method to integrate in time. The corresponding boundary conditions for the free fiber end as well as the inflow boundary complete the system, while the inflow leads to a time-varying domain.

3. Results

Figure 1 (left) shows the result of an industrial Spunbond simulation for the process of Oerlikon Neumag, where hundreds of filaments filaments are overlayed to produce a nonwoven. Figure 1 (right) shows an Airlay process of Autefa Solutions [5]. In the airlay process, short staple fibers instead of endless filaments are used, but the same model for elastic, inextensible fibers is applied for the simulation. In both images, a 2D cross-section of the air flow velocity is displayed behind the fibers.

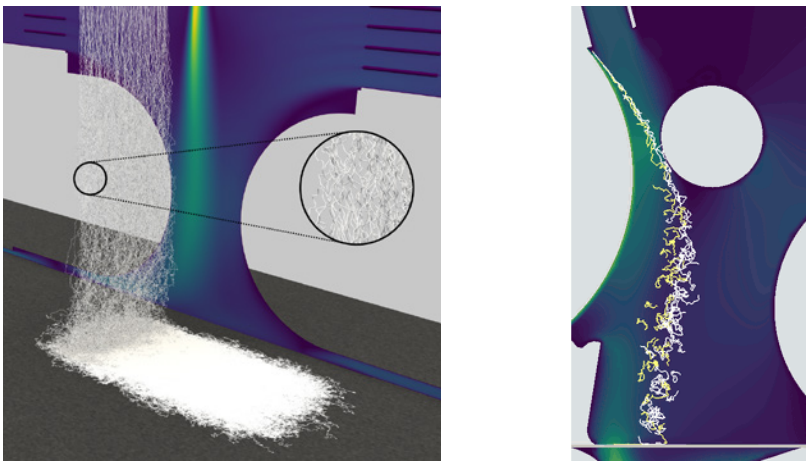

Figure 1. Simulation of Spunbond process of Oerlikon Neumage (left), simulation of Airlay process K12 of Autefa Solutions showing two kinds of fiber materials in white and yellow (right).

4. Conclusions

The simulation of nonwovens productions requires a complex chain of models for the different aspects of the production. We have focused on the entanglement and laydown of filaments and fibers in Spunbond and Airlay processes, modeling and simulating the dynamics of fibers in turbulent airflow. Due to the multiscale physics problem involved, a one-dimensional fiber with elastic material model is used resulting in a system of stochastic partial differential equations with algebraic constraints. Such simulations have important applications in industry, as they allow to virtually analyze and optimize the production process with respect to economics and material quality. Applying different numerics and material models, e.g. visco-elastic jets, simulations of other processes such as Meltblown are possible.

References

[1] R. Kirsch, A. Schmeißer. *From production process to operation: Digital twins for filtration*, F & S. Filtration and separation technologies. International edition, 1 (2023) 32-36

[2] A. Klar, N. Marheineke, R. Wegener. *Hierarchy of mathematical models for production processes of technical textiles*, ZAMM, 89 (2009) 941-961

[3] A. Schmeißer, R. Wegener, D. Hietel, H. Hagen. (2015). *Smooth convolution-based distance functions.* Graphical Models, 82 (2015) 67-76.

[4] M. Antoni, Q. Kürpick, F. Lindner, N. Marheineke, R. Wegener. *Reconstruction of inhomogeneous turbulence based on stochastic Fourier-type integrals. Part I: Modeling and analysis*. arXiv preprint (2023), arXiv:2311.09893

[5] S. Gramsch, A. Klar, G. Leugering, N. Marheineke, C. Nessler, C. Strohmeyer, R. Wegener. *Aerodynamic web forming: process simulation and material properties*. Journal of Mathematics in Industry, 6 (2016) 1-23.

ECCOMAS Thematic Conference and IACM Special Interest Conference
Highly Flexible Slender Structures (HFSS 2025)
22–26 September 2025, Kaiserslautern, Germany

Efficient NVH Analysis for Cables and Hoses

Fabio Schneider-Jung [1], Michael Roller [1], Joachim Linn [1]

[1] Fraunhofer Institute for Industrial Mathematics ITWM, [fabio.julian.schneider-jung, michael.roller, joachim.linn]@itwm.fraunhofer.de

Keywords: Cable simulation, NVH, Cosserat rod

1. Introduction

Vibrations along cables and hoses can transmit noise into the vehicle cabin and, there, it might annoy the occupants. This is particularly true for battery electric vehicles, due to the missing sound of the combustion engine. To assess the acoustic transmission properties in early, purely virtual development phases, an efficient simulation tool is desired, which is characterized by a low modelling effort and fast computations. In this contribution, we present a suitable methodology which enables NVH analysis already during the design phase.

2. Methodology

Based on a geometrically nonlinear rod model [1], the corresponding equations of motion are linearized and from the resulting system matrices the mechanical impedance matrix [2] – also called 'dynamic stiffness' – is computed. This is especially useful for easy assessments of the acoustic transmission properties and quick comparisons of variants of cable and hose assemblies.

To compute the mechanical impedance matrix, the degrees of freedom (DOF) of the cable or hose system are separated into *master* and *slave* DOF, such that we write the linearized equations of motion in the frequency domain as

$$\begin{bmatrix} \boldsymbol{f}_m \\ \boldsymbol{0} \end{bmatrix} = \left(-\omega^2 \begin{bmatrix} \boldsymbol{M}_{mm} & \\ & \boldsymbol{M}_{ss} \end{bmatrix} + \begin{bmatrix} \boldsymbol{K}_{mm} & \boldsymbol{K}_{ms} \\ \boldsymbol{K}_{sm} & \boldsymbol{K}_{ss} \end{bmatrix} \right) \begin{bmatrix} \boldsymbol{\Phi}_m \\ \boldsymbol{\Phi}_s \end{bmatrix} \tag{1}$$

and by eliminating the slave DOF, we arrive at

$$\boldsymbol{f}_m = \underbrace{\left(-\omega^2 \boldsymbol{M}_{mm} + \boldsymbol{K}_{mm} - \boldsymbol{K}_{ms} \left(-\omega^2 \boldsymbol{M}_{ss} + \boldsymbol{K}_{ss} \right)^{-1} \boldsymbol{K}_{sm} \right)}_{=\boldsymbol{Z}(\omega)} \boldsymbol{\Phi}_m \tag{2}$$

with mechanical impedance matrix $\boldsymbol{Z}(\omega)$. For simplicity, we ommitted damping in the above equations, but can be easily introduced on the level of equations of motion in frequency domain.

3. Application Example

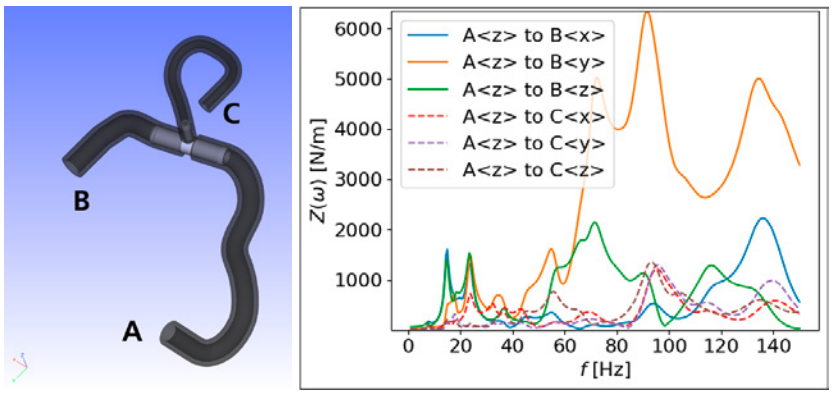

Figure 1: The example hose system (left) and its corresponding mechanical impedance matrix (right).

We demonstrate the method on a small hose system with three hose segments and a connector, as shown on the left in Figure 1. The computation of the corresponding mechanical impedance matrix is finished within

seconds and provides a quick indication to the potential noise transmission along the hose system. On the right of Figure 1, selected entries of the mechanical impedance matrix are plotted, in particular: transmission potential from hose end 'A', excited in 'z'-direction, to hose ends 'B' and 'C'.

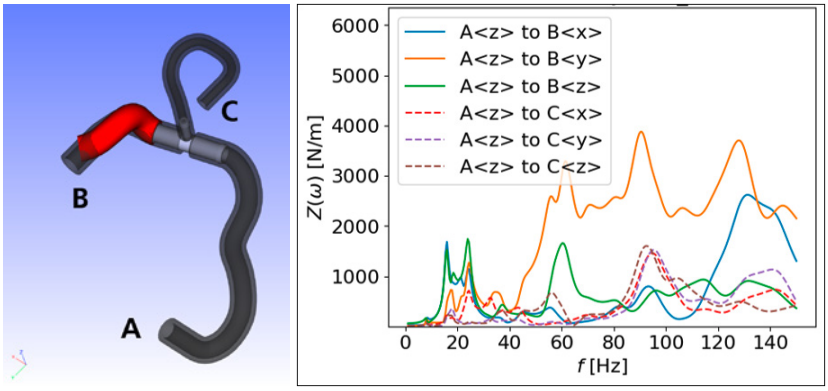

Figure 2: Modified hose system (left) with reduced noise transmission potential (right).

Now, by modifying the hose system - e.g. adjusting the preformation of one hose segment (see Figure 2, left) - one can efficiently find a configuration with reduced transmission potential (see Figure 2, right).

4. Conclusions

With the presented approach, it is possible to assess and improve the NVH performance of cable or hose routings already in the design phase. However, it is essential to provide the presented methodology in a easy-to-use software tool [3], such that already designers can include the NVH-analysis in their work, rather than CAE engineers.

References

[1] H. Lang, J. Linn, M. Arnold. *Multi-body dynamics simulation of geometrically exact Cosserat rods.* Multi-body Syst Dyn, 25 (2021), 285-312

[2] M. Géradin, A. Cardona. *Flexible Multibody Dynamics - A Finite Element Approach*, Wiley, 2001.

[3] https://flexstructures.com/products/ips-cable-simulation/